

# **Flow Visualization in 3D Printed PEM Fuel Cell Bipolar Plates**

by

Hossein Piri

B.A.Sc., Amirkabir University of Technology, 2013

A THESIS SUBMITTED IN PARTIAL FULFILLMENT OF THE

REQUIREMENTS FOR THE DEGREE OF

MASTER OF APPLIED SCIENCE

in

The Faculty of Graduate and Postdoctoral Studies

(Chemical and Biological Engineering)

THE UNIVERSITY OF BRITISH COLUMBIA

(Vancouver)

July 2017

© Hossein Piri, 2017

## Abstract

In recent years, due to the public concern on global warming, both increasing energy efficiency and developing green energy become crucially important. Fuel cells can be one of the most suitable clean energy solutions for the environment because of its high energy conversion efficiency and near zero emissions of criteria air pollutants at the use stage. To increase the energy efficiency of fuel cells, effectively utilize the Pt catalyst and increase the fuel cell durability, the uniform distribution of the reactants over the fuel cell active area is of great importance. Over the last decade, many researchers have focused on developing flow field design to homogeneously distribute the reactant and to decrease the pressure-drop in the bipolar plates. However, most of the previous studies are in the stage of numerical simulation, and the few experimental studies have used very simple flow field geometries. Not to mention that complex transport phenomena inside a fuel cell make even the numerical simulation challenging and time consuming, which hinders the quick screening of proposed modifications and new designs.

While the conventional fabrication techniques are expensive and time consuming, 3D printing is a very good rapid prototyping method that can be used both to validate the simulation results and to supplement the tedious simulation work. The question is whether the results from 3D printed flow fields could be as accurate and reliable as flow fields fabricated with conventional methods.

In the present research, we investigated the applicability of 3D printing in validating the simulation results and as a fast screening method. State-of-the-art designs for anode, cathode and water cooling BPPs proposed and fabricated using Polyjet 3D printing, SLA 3D printing and laser-cutter technologies and the pressure-drop and velocity profiles were measured for each plate. The results demonstrated that SLA 3D printing has great promises to serve as a screening tool in modifying the flow field design, as well as in validating the simulation results.

## Lay summary

In recent years, due to the public concern on global warming, developing green energy become crucially important. Fuel cells are devices for generating clean energy and can be one of the most suitable clean energy solutions for the environment. Numerous research works have focused on improving the fuel cell performance by modifying the bipolar plates, which are the key components of fuel cells. However, due to the high fabrication time and cost of the conventional bipolar plate fabrication methods, the fuel cell technology has not been widely commercialized. In this research, the applicability of 3D printing in prototyping the bipolar plates is assessed. Using 3D printing, a fast screening technique is introduced for evaluating the performance of any proposed design for the flow fields of bipolar plates. A novel flow field design is proposed and assessed using the introduced fast screening method.

## Preface

The work presented in this dissertation was completed by Hossein Piri under the supervision of Dr. Xiaotao Bi, with co-supervision of Dr.Hui Li and Dr.Haijiang Wang at the Department of Chemical and Biological Engineering at the University of British COLUMBIA. The experimental set-up used for the experiments presented in this thesis was designed and commissioned by Hossein Piri. The numerical simulation results presented in this dissertation was done by Dr.Hamidreza Sadeghifar. Hossein Piri prepared the initial and final drafts of this document, which was edited and approved by Professors Xiaotao Bi and Hui Li.

# Table of contents

<b>Abstract</b> .....	ii
<b>Lay summary</b> .....	iii
<b>Preface</b> .....	iv
<b>Table of contents</b> .....	v
<b>List of tables</b> .....	viii
<b>List of figures</b> .....	ix
<b>List of Symbols, Abbreviations and Nomenclature</b> .....	xiii
<b>Acknowledgments</b> .....	xviii
<b>1 Introduction</b> .....	1
<b>1.1 Functionalities of BPPs in FCs</b> .....	4
<b>1.2 Flow field design</b> .....	6
<b>1.2.1 Different channel configuration</b> .....	7
<b>1.2.2 Different flow field arrangement</b> .....	9
<b>1.3 Design and optimization strategy</b> .....	9
<b>1.3.1 Numerical simulation</b> .....	9
<b>1.3.2 Experiment for validating simulation results</b> .....	9
<b>1.4 Objectives of the present work</b> .....	10
<b>2 Literature review</b> .....	12
<b>2.1 PEMFC flow field design</b> .....	12
<b>2.1.1 Channel configuration</b> .....	12
<b>2.1.2 Optimizing flow channel geometrical features</b> .....	19
<b>2.1.3 Pressure-drop in flow field channels</b> .....	21
<b>2.1.4 The importance of BPP fabrication</b> .....	24
<b>2.2 Different fabrication techniques of BPPs</b> .....	24
<b>2.2.1 Machining of graphite plates</b> .....	24
<b>2.2.2 Molding graphite or carbon materials</b> .....	26
<b>2.2.3 Stamping metals</b> .....	26
<b>2.2.4 The problem of conventional fabricating techniques</b> .....	27
<b>2.3 Different rapid-prototyping techniques</b> .....	27
<b>2.3.1 3D printing</b> .....	28
<b>2.3.2 Laser-cutting</b> .....	40

2.4	Flow visualization .....	40
2.4.1	Particle image velocimetry (PIV).....	40
2.4.2	Laser induced fluorescence (LIF).....	42
2.4.3	Dye visualization.....	43
2.5	Knowledge gap .....	45
2.5.1	Strategies and scope of the present work.....	47
3	Experimental .....	49
3.1	Required experiments.....	49
3.2	BPPs fabrication .....	50
3.3	Geometry measurement.....	56
3.4	Transparent cell assembly.....	56
3.5	Flow rate measurement.....	58
3.6	Pumping system .....	60
3.7	Ensuring dynamic similarity .....	60
3.7.1	Determination of gas flow rates in anode and cathode BPPs .....	60
3.7.2	Determination of liquid flow rates in anode and cathode BPPs .....	62
3.7.3	Determination of flow rate in water-cooling BPP.....	65
3.8	Pressure-drop measurement .....	66
3.9	Flow visualization .....	67
3.9.1	Dye injection.....	67
3.9.2	Image capturing.....	68
3.9.3	Image processing and signal analysis .....	72
3.10	Statistical analysis .....	76
4	Results and discussion.....	77
4.1	Cross-section area of BPPs.....	77
4.1.1	BPPs with 0.4mm hydraulic diameter .....	78
4.1.2	BPPs with 0.635 mm hydraulic diameter .....	80
4.2	Pressure-drop in prototype BPPs.....	88
4.2.1	Pressure-drop in cathode BPPs.....	90
4.2.2	Pressure-drop in anode and water-cooling prototype BPPs .....	98
4.3	Velocity profiles in prototype BPPs .....	102
4.3.1	Velocity profiles in cathode BPPs .....	102
4.3.2	Velocity profiles in anode and water-cooling BPPs .....	138
5	Conclusion .....	148

5.1 Recommendations .....	151
References .....	153
Appendices .....	167
Appendix A .....	167
Appendix B.....	171
B.1 Introduction to 3D printers.....	171
B.2 Different 3D printing technologies.....	173
B.2.1 Solid based .....	174
B.2.2 Liquid Based .....	177
B.2.3 Powder based.....	182
Appendix C.....	189
C.1 Pumping system .....	189

## List of tables

Table 2-1. Summary of different 3D printing technologies. ....	30
Table 3-1: Different BPPs tested in the current research .....	54
Table 3-2: Thermodynamic properties of fluids consumed in the current research.....	61
Table 3-3: Air and hydrogen properties at BPP inlet condition. ....	61
Table 3-4: Summary of fluid type and flow rates applied in the experiments of current research. ....	66
Table 4-1: Channel cross-section size data for the studied BPPs .....	86
Table 4-2: Statistical analysis of pressure-drop data from 6 prototype BPPs versus the simulation results. .....	92
Table 4-3: Statistical analysis of velocity-profile data from 6 prototype cathode BPPs versus the simulation results.....	114
Table 4-4: Statistical analysis of velocity-profile data from anode and water-cooling BPPs.....	147

## List of figures

Figure 1-1: An exploded view of a PEM single cell. ....	3
Figure 1-2: Schematic diagram of a Polymer Electrolyte Membrane FC (reprinted from [4] with permission from Elsevier). ....	4
Figure 1-3: Different channel configurations of the gas flow field: a) Serpentine flow field channel (single); b) Straight-parallel flow field channel or Z-type parallel configuration; c) Interdigitated flow field channel; d) Pin-type flow field channel; e) Multi pass serpentine flow field (MSFF) channel (Drawn from [13] with permission from Elsevier). ....	7
Figure 2-1: Modified flow field arrangement of straight-parallel : a) separated inlets, b) neighbor inlets (reprinted from [12] with permission from Wiley). ....	14
Figure 2-2: Computer aided drafting drawing of cooling flow fields with (a) uneven flow and (b) even cooling flow. Circle identify the mixing zones in each design. The arrows denote the designated cooling inlets and outlets (reprinted from [42]with permission from Elsevier). ....	15
Figure 2-3: Effect of the Reynolds number: (a) relative flow rate distribution maps and (b) C.V value (reprinted [37] with permission from Elsevier.) ....	16
Figure 2-4: (a) Conventional parallel flow field design with single inlet/outlet, (b) Modified flow field design with three sections of channels: inlet, mid-section and outlet with single inlet/outlet (modified from [38] with permission from Elsevier). ....	17
Figure 2-5: Numerical results of mass flow rate across the flow field width: (a) conventional parallel flow field with single inlet/outlet, (b) modified parallel flow field with single inlet/outlet (modified from [38] with permission from Elsevier). ....	18
Figure 2-6: Metal and graphite BPPs (reprinted from [64]). ....	25
Figure 2-7: Minimum draft angle required for molds in fabricating molded graphite BPPs. ....	26
Figure 2-8: (a) Photograph of polypropylene flow plate with corresponding (b) SEM image (reprinted from [84]-Published by The Royal Society of Chemistry). ....	34
Figure 2-9: Representative cross-sectional XCT images of the MEA situated inside the 3D printed flow field fixture at dry and wet conditions. During FC operation in the wet state, the increased hydration of the membrane caused an increase in the membrane thickness and significant undulations of the CCM. The outline of the catalyst layers in orange has been included to better highlight changes seen in the membrane after swelling due to hydration (reprinted from [90], open access article). ....	35
Figure 2-10: Photograph of the finished BPP from [74] (reprinted from [74], open access article). ....	38
Figure 2-11: Typical images separated by $\Delta t$ , plus representative interrogation windows and cross-correlation function for interrogation windows in image 1 and image 2. $\Delta$ in the cross-correlation plot gives the average displacement of the image intensities between images and when divided by $\Delta t$ , provides a quantitative velocity vector centered at the center of the interrogation window (reprinted from [115] with permission from Elsevier). ....	42
Figure 2-12: Fluid velocity results from the numerical model for (a) CFF with uneven cooling flow and (b) CFF with even cooling flow. The incoming cooling flow rate is 2.67 mL s <sup>-1</sup> from the upper right corner. The CFF with even cooling flow has significantly fewer stagnant channels and more effective mixing regions. Images of dye mixing experiments for (c) CFF with uneven cooling flow after ~0.4 s of mixing and (d) CFF of even cooling flow after ~0.5 s of mixing. The incoming flow rate of cooling flow with blue dye is ~2.1 mL s <sup>-1</sup> . The scale bar is approximate. (reprinted from [42] with permission from Elsevier.)	44
Figure 3-1: Computer aided design of BPPs. ....	51

Figure 3-2: Different regions of active area in the cathode BPP. ....	52
Figure 3-3: Prototype BPPs studied in the current research. ....	55
Figure 3-4: Transparent cell schematic; a) Assembled transparent cell; b) Exploded view of transparent cell assembly. ....	57
Figure 3-5: Transparent cell components: a) Aluminum end plate; b) Bottom acrylic plate to match the grooves of aluminum end plate with that of BPP; c) Prototype BPP; d) Top acrylic plate to seal the prototype BPP and to enable flow visualization; e) Metal frame to uniformly distribute the tightening force over active area; f) Assembled transparent cell. The components come on top of each other in mentioned order to form the transparent cell assembly. ....	58
Figure 3-6: Actual flow rate versus rotameter percentage graph. ....	59
Figure 3-7: lightening system applied for uniform lightening with constant light intensity. ....	69
Figure 3-8: The setup applied for flow visualization and pressure-drop measurement in BPPs in the current research.....	70
Figure 3-9: Schematic of the setup applied for flow visualization and pressure-drop measurement in BPPs in the current research.....	71
Figure 3-10: Dye evolution in SLA 3D printed cathode flow field. a) $t=600\text{ms}$ ; b) $t=6800\text{ms}$ . ....	72
Figure 3-11: Schematic of the velocity measurement inside a flow channel. Since it takes some time for dye to travel from first yellow pixel on the left-hand side to the second yellow pixel on the right-hand side, the plot of intensity versus frame number for these two corresponding pixels would have a lag. Cross correlation of intensity versus frame number would inform us about the magnitude of this lag which can be translated to time with the knowledge of frame rate. ....	73
Figure 3-12: Intensity versus frame number graph for two corresponding pixels with different locations along the flow direction in a random channel of SLA 3D printed cathode plate with 0.635 mm hydraulic diameter.....	75
Figure 4-1: Resolution test taken under optical microscopy by Lyons et al. [128] (reprinted from [128] ). .....	81
Figure 4-2: Laser-cut BPP channel roughness. ....	81
Figure 4-3: Cross-section images of BPPs with 0.4 mm hydraulic diameter. ....	82
Figure 4-4: Polyjet 3D printed BPPs, with 0.4 mm diameter, before and after support removal. ....	83
Figure 4-5: Damaged Polyjet 3D printed BPPs during experiments. ....	84
Figure 4-6: Cross-section images of BPPs with 0.635 mm diameter .....	85
Figure 4-7: Channel cross-section area distribution in BPPs with 0.4 mm diameter. ....	87
Figure 4-8: Channel cross-section area distribution in BPPs with 0.635 mm diameter. ....	87
Figure 4-9: Effect of dissolved air of water on pressure-drop. ....	89
Figure 4-10: Pressure-drop in cathode BPPs with 0.635 mm hydraulic diameter.....	91
Figure 4-11: Pressure-drop in cathode BPPs with 0.4 mm hydraulic diameter.....	93
Figure 4-12: Pressure-drop in anode, cathode and water-cooling BPPs fabricated with covered SLA technology with 0.635 mm diameter. ....	100
Figure 4-13: Schematic of the fluid flow direction in different transition regions. ....	101
Figure 4-14: Velocity profile in cathode prototype BPPs with 0.635 mm hydraulic diameter, $Q=150$ ml/min.....	104
Figure 4-15: Velocity profile in cathode prototype BPPs with 0.635 mm hydraulic diameter, $Q=600$ ml/min.....	105
Figure 4-16: Velocity profile in cathode prototype BPPs with 0.635 mm hydraulic diameter, $Q=1300$ ml/min.....	106

Figure 4-17: Velocity profile in cathode prototype BPPs with 0.635 mm hydraulic diameter, Q=150 ml/min. There exist 13 points on the graphs of covered SLA, uncovered SLA and Polyjet such that point K (K=1:13) represents the average velocity of 5 channels with channel numbers 5K-4,5K-3,5K-2,5K-1,5K. .... 107

Figure 4-18: Velocity profile in cathode prototype BPPs with 0.635 mm hydraulic diameter, Q=600 ml/min. There exist 13 points on the graphs of covered SLA, uncovered SLA and Polyjet such that point K (K=1:13) represents the average velocity of 5 channels with channel numbers 5K-4,5K-3,5K-2,5K-1,5K. .... 108

Figure 4-19: Velocity profile in cathode prototype BPPs with 0.635 mm hydraulic diameter, Q=1300 ml/min. There exist 13 points on the graphs of covered SLA, uncovered SLA and Polyjet such that point K (K=1:13) represents the average velocity of 5 channels with channel numbers 5K-4,5K-3,5K-2,5K-1,5K. .... 109

Figure 4-20: Velocity profile in cathode prototype BPPs with 0.635 mm hydraulic diameter, Q=150 ml/min..... 110

Figure 4-21: Velocity profile in cathode prototype BPPs with 0.635 mm hydraulic diameter, Q=600 ml/min..... 111

Figure 4-22: Velocity profile in cathode prototype BPPs with 0.635 mm hydraulic diameter, Q=1300 ml/min..... 112

Figure 4-23: Velocity profile in cathode BPP with 0.635 mm hydraulic diameter in 150, 600, 1200 ml/min. a) Covered SLA 3D printed cathode BPP, b) Simulated cathode BPP. .... 113

Figure 4-24: Velocity profile in cathode prototype BPPs with 0.4 mm hydraulic diameter, Q=145 ml/min. .... 121

Figure 4-25: Velocity profile in cathode prototype BPPs with 0.4 mm hydraulic diameter, Q=338 ml/min. .... 122

Figure 4-26: Velocity profile in cathode prototype BPPs with 0.4 mm hydraulic diameter, Q=651 ml/min. .... 123

Figure 4-27: Velocity profile in cathode prototype BPPs with 0.4 mm hydraulic diameter, Q=145 ml/min. There exist 20 points on the graphs of laser cutter, SLA 3D printed and Polyjet 3D printed such that point K (K=1:20) represents the average velocity of 5 channels with channel numbers 5K-4,5K-3,5K-2,5K-1,5K. .... 124

Figure 4-28: Velocity profile in cathode prototype BPPs with 0.4 mm hydraulic diameter, Q=338 ml/min. There exist 20 points on the graphs of laser cutter, SLA 3D printed and Polyjet 3D printed such that point K (K=1:20) represents the average velocity of 5 channels with channel numbers 5K-4,5K-3,5K-2,5K-1,5K. .... 125

Figure 4-29: Velocity profile in cathode prototype BPPs with 0.4 mm hydraulic diameter, Q=651 ml/min. There exist 20 points on the graphs of laser cutter, SLA 3D printed and Polyjet 3D printed such that point K (K=1:20) represents the average velocity of 5 channels with channel numbers 5K-4,5K-3,5K-2,5K-1,5K. .... 126

Figure 4-30: Velocity profile in cathode prototype BPPs with 0.4 mm hydraulic diameter, Q=145 ml/min. .... 127

Figure 4-31: Velocity profile in cathode prototype BPPs with 0.4 mm hydraulic diameter, Q=338 ml/min. .... 128

Figure 4-32: Velocity profile in cathode prototype BPPs with 0.4 mm hydraulic diameter, Q=651 ml/min. .... 129

Figure 4-33: Velocity profile in cathode BPP with 0.4 mm hydraulic diameter in 145, 338, 651 ml/min. a) SLA 3D printed cathode BPP, b) Simulated cathode BPP. ....	130
Figure 4-34: pressure-drop profile in flow channels of cathode BPP with 0.4 mm hydraulic diameter before and after optimization; a) Near inlet, b) Near middle, 3) Near outlet. ....	135
Figure 4-35: Pressure-drop contour in flow channels of cathode BPP with 0.4 mm hydraulic diameter; a) Original design, b) Optimized design .....	136
Figure 4-36: Velocity-profile in flow channels of cathode BPP with 0.4 mm hydraulic diameter before and after optimization. ....	137
Figure 4-37 : Velocity contour in flow channels of optimized cathode BPP with 0.4 mm hydraulic diameter.....	137
Figure 4-38: Dye evolution in SLA 3D printed anode flow field. a) t=1637 ms; b) t=1738 ms.....	140
Figure 4-39: Dye evolution in SLA 3D printed water-cooling flow field. a) t=1717 ms; b) t=1745 ms. ....	141
Figure 4-40: Velocity profile in anode and water-cooling prototype BPPs with 0.635 mm hydraulic diameter, Q=150 ml/min; .....	142
Figure 4-41: Velocity profile in anode and water-cooling prototype BPPs with 0.635 mm hydraulic diameter, Q=300 ml/min; .....	143
Figure 4-42: Velocity profile in anode and water-cooling prototype BPPs with 0.635 mm hydraulic diameter, Q=600 ml/min; .....	144
Figure 4-43: Velocity profile in anode and water-cooling prototype BPPs with 0.635 mm hydraulic diameter, Q=1300 ml/min; .....	145
Figure 4-44: Effect of the total flow rate on the velocity profile of BPPs with 0.635 mm hydraulic diameter; a) Anode BPP, b) Water-cooling BPP.....	146
Figure B-1: (a) A solid CAD mode; (b) Meshed CAD file in .STL format. ....	172
Figure B-2: Schematic representation of the fabrication process in FDM 3D printer; Mixed fabrication process with two types of different filaments (yellow and blue) (reprinted from [77] with modified image caption, with permission from Elsevier). ....	174
Figure B-3: Self-retaining angle in FDM 3D printing. ....	176
Figure B-4: A typical type of laminated object manufacturing process (reprinted from [87] with permission from Elsevier). ....	177
Figure B-5: Schematic of the 3D printing process in Polyjet 3D printer. ....	178
Figure B-6: Schematic of the 3D printing process in SLA 3D printer (reprinted from [69], open access article). ....	180
Figure B-7: Stereolithography VS Digital light processing 3D printing (reprinted from [95]).....	181
Figure B-8: Samples plates created with the TS-3DP by Lyons et.al [68] (reprinted from [68])......	183
Figure B-9: Schematic of 3D printing process in SLS 3D printer. ....	185
Figure B-10: Schematic of 3D printing process in DMLS 3D printer (reprinted from [69] , open access article). ....	186
Figure C-1: House-made pulse dampener. The trapped air in the chamfer is a compressible medium and acts as a pulse dampener.....	191

# List of Symbols, Abbreviations and Nomenclature

## Nomenclature

A	Cell active area, cm <sup>2</sup>
A	Channel cross-section area, mm <sup>2</sup>
C <sub>p</sub>	Specific heat capacity, j/kgK
D <sub>h</sub>	Hydraulic diameter, mm
E <sup>o</sup>	Cell standard potential, volt
E <sub>avg</sub>	The percentage of average error, dimensionless
f <sub>f</sub>	Fanning friction factor, dimensionless
F	Faraday's constant, 96,485 sA/mol
<i>i</i>	Current density, A/cm <sup>2</sup>
<b><i>I</i></b>	Current, A
k	Friction factor of baffles and bends, dimensionless
L	Channel length, mm
m	Slope of the pressure-drop graph, dimensionless
<i><sup>o</sup>m</i>	Cooling water mass flow rate, kg/s
M	Molar mass, g/mol
n	Number of flow channels in the flow field, dimensionless
<i><sup>o</sup>n<sub>i</sub></i>	Substance i production/consumption rate, mol/s
N	Number of cells in the stack, dimensionless
Q	Fluid flow rate, ml/min
Re	Reynolds number, dimensionless

t	Time, s
T	Temperature, K
$U$	Fluid average velocity in flow channel, mm/s
$\bar{U}$	Mean average velocity, mm/s
$U'$	Fluid velocity in baffles and bends, mm/s
$V_a$	Actual cell voltage, volt
$V_{oc}$	Open circuit voltage, volt
$W_i$	Weight of standard error in experiment i, dimensionless
x	Pixel length, mm
$X_i$	Volumetric liquid fraction of i in mixture, dimensionless
$Y_i$	Volume fraction of i, dimensionless

### Acronyms

ABS	Acrylonitrile butadiene styrene
AM	Additive manufacturing
BPP	Bipolar plate
CAD	Computer aided design
CCM	Catalyst coated membrane
CCM	Compact camera module
CNC	Computer numerical control
COV	Coefficient of variation
DAQ	Data acquisition
DLP	Digital light processing
DMFC	Direct methanol fuel cell

DMLS	Direct metal laser sintering
FC	Fuel cell
FDM	Fused deposition modelling
GDL	Gas diffusion layer
HOR	Hydrogen oxidation reaction
LOM	Laminated object manufacturing
MEA	Membrane electrode assembly
MEMS	Micro-Electro-Mechanical processes
MFC	Microbial fuel cell
MPL	Micro porous layer
MSFF	Multi-pass serpentine flow field
OCT	Optical coherence tomography
ORR	Oxygen reduction reaction
PC	Polycarbonate
PEM	Polymer electrolyte membrane
PEMFC	Polymer electrolyte membrane fuel cell
PIV	Particle image velocimetry
PLA	Polylactic Acid
RP	Rapid prototyping
SE	Standard error
SEM	Standard error of the mean
SLA	Stereolithographic apparatus
SLS	Selective laser sintering
SM	Subtractive manufacturing

STL	Standard Tessellation Language
TS	Thermal spray
WLS	Weighted Least Squares
XCT	X-ray computed tomography

### Abbreviation

atm	Atmosphere
avg	Average
fps	Frames per second
glyc	Glycerin
max	Maximum
min	Minute
min	Minimum
mix	Mixture
OC	Open circuit
RH	Relative humidity
wat	Water
$\bar{y}_i$	Average of observations in point(i)
$y_{model}$	Expectation
2D	Two dimensional
3D	Three dimensional
:	Up to

### Greek letters

$\beta$	Correction factor in Darcy equation, dimensionless
---------	--

$\Delta P$	Pressure-drop, bar
$\lambda_i$	Stoichiometry of gas i, dimensionless
$\mu$	Fluid viscosity, Pa.s
$\nu$	Fluid kinematic viscosity, m <sup>2</sup> /s
$\rho$	Fluid density, kg/m <sup>3</sup>
$\Sigma$	Summation, dimensionless

## Acknowledgments

First and foremost, I would like to express my sincere gratitude to my kind supervisors, Dr. Xiaotao Bi and Dr. Hui Li, and outstanding supervision from Dr. Haijiang Wang for their mentorship over the past three years, for sharing their deep pool of knowledge, and their continued support, patience and trust. I am forever grateful to them for all the amazing opportunities they provided me with to grow as an individual and as a researcher. I would like to thank our group post-doc, Dr. Hamidreza Sadeghifar for all his help and support, for sharing his knowledge and simulation results by COMSOL Multiphysics software.

My most sincere thanks to Vivienne Jaehn-Kreibaum who volunteered for performing some of the experiments and spent long hours in the lab on weekends to speed up the experiments. The financial support of the project “PEM fuel cell architecture design” funded by the National Sciences and Engineering Research Council of Canada (NSERC) and H2E Co. is gratefully acknowledged and appreciated. I would also like to acknowledge and express appreciation to thank Dr. Jimmy Feng for providing us with high speed camera, Dr. Mark Martinez for providing us with OCT imaging apparatus and Masoud Daneshi to training me to use that, and Dr. Sheldon Green and Hatef Rahmani for providing us with the light source for flow visualization experiments.

I must express my very profound gratitude to my girlfriend, Shaghayegh Sadr Karimi for providing me with unfailing support and continuous encouragement throughout my years of study and through the process of researching and writing this thesis. This accomplishment would not have been possible without her. And finally, I would like to deeply thank my parents, Hassan and Mahi, and my brothers Afshar, Mehdi and Madjid for all their unconditional love and support who spend long hours on Skype day and night to motivate me to achieve more in life.

*To My parents*

*Hassan and Mahi*

*My brothers*

*Afshar, Mehdi & Madjid*

*And my lovely girlfriend*

*Shaghayegh*

# 1 Introduction

In recent years, due to the public concern about the global warming, depletion of fossil fuel reserves and environmental pollution, both increasing energy efficiency and developing green energy become crucially important. Fuel cells (FCs) can be one of the most suitable clean energy solutions for the environment. There are different types of FCs among which Polymer Electrolyte Membrane (PEM) FCs have drawn a great attention. PEM FCs (PEMFCs) have many advantages over other types of FCs, which make them reliable in many applications such as electric vehicles, aerospace applications, stationary power systems and submarines [1].

PEMFCs can be operated at different pressure ranges (1-6 atm), and different temperature ranges (50-90 °C). PEMFCs are able to rapidly respond to a quick start up in ambient and freezing conditions. They have a compact system volume that results in relatively high system efficiency and high power-density output [2]. Other advantages include light weight, zero pollution, easy implementation, robustness, soundness and long life-time.

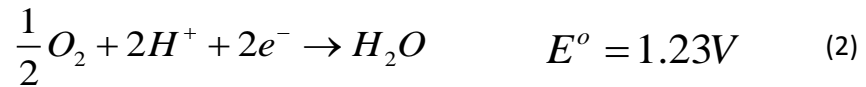
PEM single cells are comprised of different components, as shown in Figure 1-1, which are sandwiched together. The seven components of a PEMFC are: anode flow field with channels, anode gas diffusion layer (GDL), anode catalyst layer (ACL), proton exchange membrane, cathode catalyst layer (CCL), cathode GDL, and cathode flow field with channels. The inclusion of GDLs, catalyst layers and the membrane is referred to as Membrane Electrode Assembly (MEA) [3]. Sometimes GDL includes a microporous layer (MPL) to increase intimacy between the GDL and CL and to assist water removal. In some cases, catalyst layers are coated onto the two sides of the membrane which is called Catalyst Coated Membrane (CCM). The inclusion of the mentioned seven components together are forming a single cell, which are stacked together to build up the desired amount of power in a FC stack. The anode and cathode flow fields together in a stack are referred to as bipolar plates (BPPs). In the present

research, we also label the single anode and single cathode plates as “anode BPP” and “cathode BPP”, respectively.

In a FC stack, reactants are fed into each cell, inside which the following happens (Figure 1-2), hydrogen is fed through anode flow field channels and being distributed all over the GDL; GDL sub-distributes the hydrogen further over the catalyst layer where hydrogen molecules are being split based on the hydrogen oxidation reaction (HOR):



Protons are being transported through the polymer exchange membrane toward the cathode side, but electrons cannot and they travel through the external circuit [to the cathode side], generating electric power, as depicted in Figure 1-2. In the cathode side, the oxygen molecules together with the protons and electrons are participating in the oxygen reduction reaction (ORR):



The ORR is a sluggish reaction and its reactivity is much lower than that of the HOR, which necessitates the use of expensive platinum catalyst to accelerate the reaction rate. Based on the ORR and HOR half reaction, the overall reaction that is taking place in a PEMFC can be written as:



One can observe that the by-products of the above reaction are water and heat. The generated water at the cathode side is diffused through GDL to reach flow fields where it can be removed [3]. Despite the many advantages the PEMFCs have demonstrated, there are multiple drawbacks accompanied with PEMFCs because of which the large-scale commercialization of PEMFCs is still hindered. One of the issues with PEMFCs is the use of precious platinum catalyst which has dictated the high cost of PEMFCs;

secondly, the high volume, weight and price of BPPs prevent the high volumetric and gravimetric power-density, resulting in high cost of electricity generated from FCs; water management issue, expensive membrane and special fuel requirements are other problems. It is well known that PEMFCs have a narrow window of operational conditions and even a small deviation from set conditions can create a malfunction in PEMFCs.

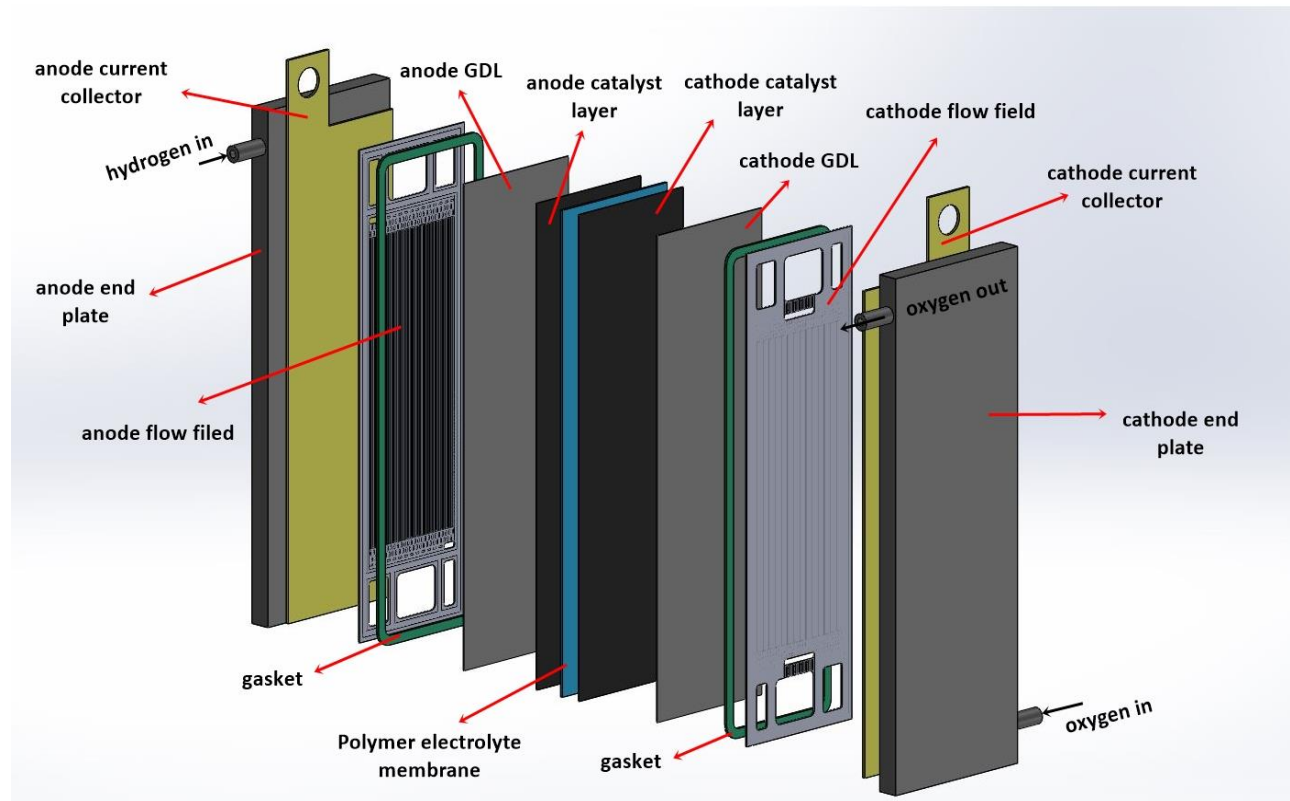


Figure 1-1: An exploded view of a PEM single cell.

There exist three types of overpotentials in PEMFCs that deviate the FC performance from its theoretical value. 1) Kinetic overpotential which is caused by the sluggish ORR, 2) Ohmic overpotential which is caused by the Ohmic resistance of the PEMFC stack including the Ohmic resistance of the membrane and BPPs, 3) Concentration overpotential because of the mass transfer of reactants to the reaction sites and the occupation of reaction sites by product water. Many researchers in recent years have tried to

increase the FC performance by minimizing various overpotentials and to pave the path toward wider commercialization of PEMFCs. There are various types of research works on each of the PEMFC components with aim to maximize the power-density and minimize the cost. One of the components that plays a vital role in PEMFCs is the BPP. Despite all the R&D efforts, the flow field design in the BPPs still needs to be improved in terms of both design efficiency and manufacturability. The following part discusses about the essential part of the BPPs in PEMFCs and the ways to optimize their performance.

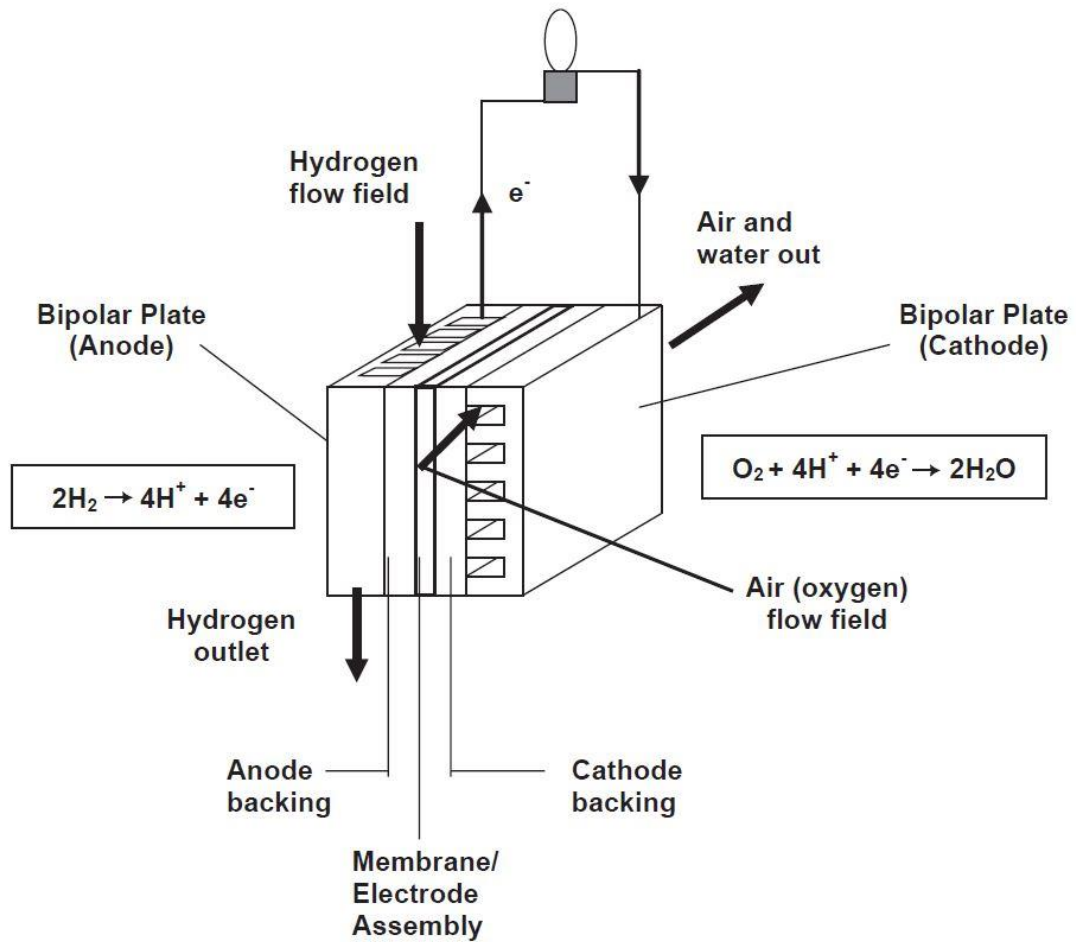


Figure 1-2: Schematic diagram of a Polymer Electrolyte Membrane FC (reprinted from [4] with permission from Elsevier).

## 1.1 Functionalities of BPPs in FCs

PEMFC stack design often comes down to BPP design which is in fact designing the flow fields on the surfaces of BPPs. Reactant flow fields are the core part of the PEMFCs and should serve number of

functions simultaneously in order to reach a high PEMFC stack performance. The BPPs supply the reactants through the flow field channels to the electrodes, but they should also transport the products away from the reaction sites. The product water is mostly in liquid form at the PEMFC working temperature, which must be effectively transported away or it will flood the reaction sites and clog the GDL pores. On the other hand, the membrane must remain hydrated to maintain good proton conductivity. Hence, the flow field design of BPPs must maintain an optimal water balance.

The BPPs remove away the product heat [5, 6]. BPPs electronically connect the cells together in the FC stack and an optimal flow field design is required to facilitate the transport of electrons by maximizing the contact area between the GDL and the BPPs. In addition, these plates provide structural support for the thin and malleable MEA [5-7].

To effectively serve their functions, BPPs need to distribute the fluids very uniformly over the active area to minimize concentration overpotential and to uniformly remove the product heat. BPPs should possess a high value of electronic conductivity for collecting the generated current, high mechanical strength to support PEMFC stack to be robust, high degree of impermeability to effectively separate fluids, high resistivity to corrosion in the harsh cell environment, inexpensive and lightweight materials, and easy manufacturability.

The DOE 2020 target for bipolar plate cost is US\$ 3 per kW, while its 2015 status is US\$ 7 per kW [8].

BPPs are currently responsible for around 60-85% of the PEMFC stack weight and 30-50% of its price[8, 4]. Hence, the cost, weight and volume of FC stacks need to be significantly reduced by an optimum flow field design and flow channel configuration. There exist significant BPP design and manufacturing challenges because of which design of more efficient flow fields has received great attention over the last decade.

## 1.2 Flow field design

The main purpose of a flow field design is to achieve uniform reactant concentration over the active area, as well as uniform cooling flow distribution, with a low pressure-drop in flow fields [9, 10].

Pressure-drop is directly related to the parasitic power required for circulating the reactants, which means an elevated pressure-drop will consume a higher fraction of the generated power. High pressure-drop would also dehydrate the membrane at the inlet region and cause flooding near outlet, and increase the chance of cross-flow and fluid leakage [11]. It would put the system under an elevated mechanical stress which could result in an uneven stress distribution over the active area.

As it is indicated from reaction kinetics, the reaction rate depends on the concentration of the reactants and the reaction temperature. In a PEMFC, ORR and HOR take place all over the active area. Therefore, the reactant pressure distribution and cooling flow distribution, which determines the reactant concentration and temperature distribution all over the active area, play a very important role in determining the reaction rate at different spots. An even reactant concentration distribution guarantees a higher utilization of Pt across the catalyst layer, provides the highest power output and prolonged stack lifetime. However, non-uniform concentration distribution results in non-uniform reaction rate which creates problems such as hot spot formation, membrane dehydration, flooding, material degradation and elevated thermal and mechanical stress [11].

Considering all these facts, designing reactant and cooling flow fields to achieve a low pressure-drop, and high pressure and flow uniformity is of significant importance. There are several design factors which could affect the pressure and flow distribution and pressure-drop in BPPs such as: flow channel path configuration, flow channel cross-section shape, channel to rib width ratio, channel height, channel aspect ratio (channel width to height ratio), channel length, number of channels, active area size, flow direction and many other factors. Numerous simulation and experimental research works have been done in each of these areas to optimize these factors.

The primary factor that determines the pressure and flow distribution and pressure-drop over the active area is flow path configuration. None of other factors could help significantly if channel configuration fails to provide a uniform flow and pressure distribution. Hence, most researchers focus on optimizing the flow path configuration. In the following part, different possible channel configuration, flow field arrangement (which is the inlet/outlet positions relative to each other), and characteristics corresponding to each configuration are discussed.

### 1.2.1 Different channel configuration

Possible flow field configurations are pin type, straight-parallel, single serpentine, multi-pass serpentine flow field (MSFF) and interdigitated, as it is illustrated in Figure 1-3. Here we discuss each type in detail.

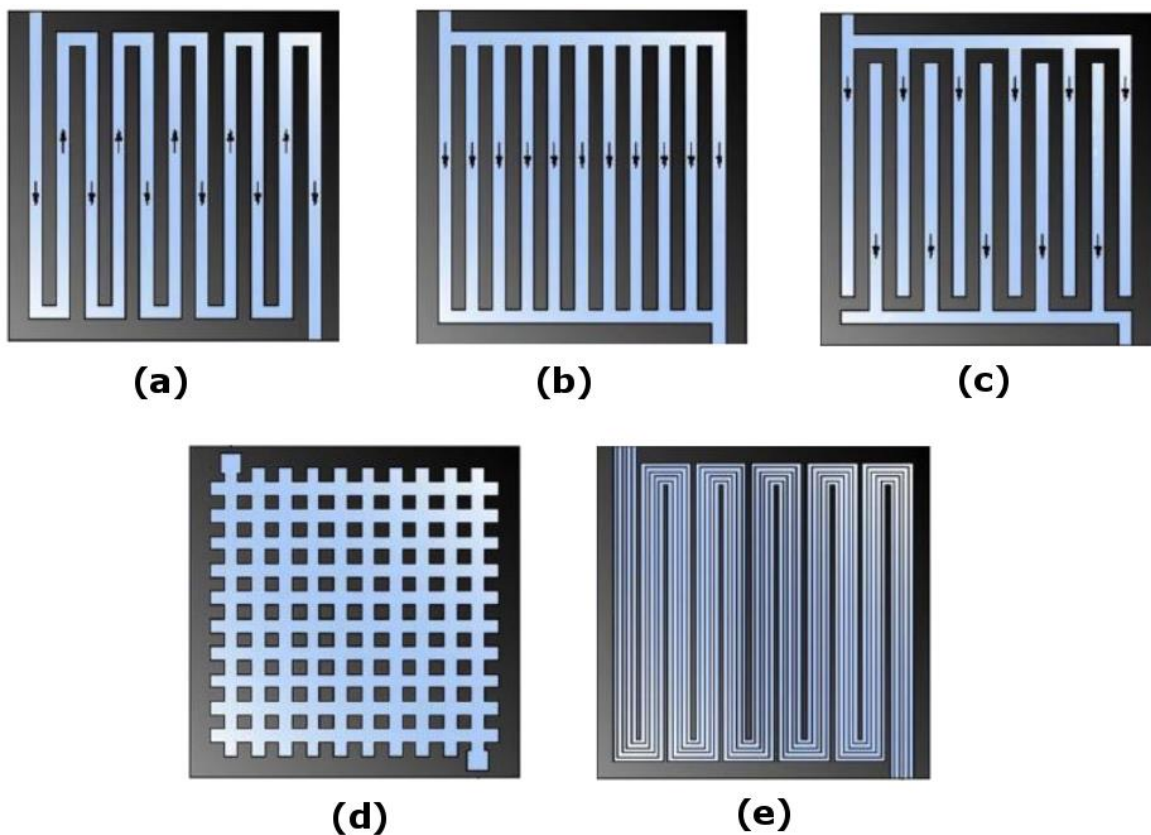


Figure 1-3: Different channel configurations of the gas flow field: a) Serpentine flow field channel (single); b) Straight-parallel flow field channel or Z-type parallel configuration; c) Interdigitated flow field channel; d) Pin-type flow field channel; e) Multi pass serpentine flow field (MSFF) channel (Drawn from [13] with permission from Elsevier).

### *1.2.1.1 Pin type*

The pin-type flow field consists of a network of circular or cubical pins which are arranged in a particular pattern. Pin type usually demonstrates a highly non-uniform flow distribution and very low pressure-drop.

### *1.2.1.2 Straight-parallel*

The straight-parallel channel configuration is the simplest channel configuration which divides the inlet flow into several parallel paths. The parallel configuration demonstrates a small pressure-drop and non-uniform flow distribution (better than pin-type). Straight-parallel channels can be fabricated very easily which makes the FC stack manufacturing less expensive.

### *1.2.1.3 Single Serpentine*

The single serpentine channel configuration forces the fluid to flow through a single path, which in turn increases the speed and pressure-drop of the flow. The single serpentine channel configuration forces the reactant into gas diffusion layers and demonstrates a very good flow uniformity [14–18]. However, the pressure-drop associated with single serpentine configuration is in the order of thousands of times higher than that of straight-parallel configuration [12].

#### *1.2.1.3.1 Multi-pass serpentine*

A tradeoff between straight-parallel and single path serpentine flow channels is achieved by multi path serpentine flow field (MSFF) configuration. The pressure-drop and flow uniformity of this configuration is between those of straight-parallel and single path serpentine flow fields. Wang and Wang [11] reported that pressure-drop in MSFF is two degree of magnitude lower than that of single path serpentine.

#### **1.2.1.4 Interdigitated**

The interdigitated flow field is based on a dead-ended channel design that forces the under-rib convection. This configuration increases the reaction rate by forcing reactants to GDL and assists the water removal [19–21]. However, a very large initial pressure (more than that in a single path serpentine) is required to push the reactants through GDL.

#### **1.2.2 Different flow field arrangement**

Bases on the location of flow inlet and outlet, straight-parallel flow channels can have U-type arrangement, as shown in Figure 1-3, or Z-type arrangement, as shown in Figure 2-1-a.

### **1.3 Design and optimization strategy**

As discussed, optimizing the flow field design is very important and the goal of flow field design is to produce a uniform pressure, temperature and velocity profile over the active area, to ensure uniform reaction rate, and meanwhile to balance the parasitic power requirements of pumping fluids through the flow fields. Here are the different methodologies commonly used for optimizing the flow fields.

#### **1.3.1 Numerical simulation**

In numerical works, usually a theoretical network model based on mass and momentum conservation is developed for finding the flow distribution and pressure-drop, which would help to optimize the flow channels geometrical features and configuration. The numerical simulation of PEMFCs is a challenging task since several transport phenomena as well as chemical reaction and electrochemical interaction should be considered in developing the governing equations. The numerical simulation is usually carried out using computational fluid dynamics (CFD).

#### **1.3.2 Experiment for validating simulation results**

While the BPPs can be designed by CFD, the complicated nature of PEMFCs makes it necessary for the numerical simulation to be tested and verified in practical experiments to assess their pragmatic

efficiency. To evaluate the rigor of numerical work in predicting the flow and pressure-drop distribution, flow field channels should be fabricated and flow visualization and pressure-drop experiments should be carried out on real BPPs. However, the complexity of the flow field design sometimes hinders their fabrication by the conventional manufacturing techniques. This, along with the long fabrication time and high cost of the conventional fabrication methods, highlights the urgent need for an alternative manufacturing technique that could enable us to evaluate the optimization ideas practically with a reasonable time and cost. RP techniques provides the path for such an approach and have been utilized in many FC researches. 3D printing is a RP technique that has lots of advantages over other manufacturing techniques and could be quite beneficial for this application. The use of 3D printing in different branches of science is becoming a very important topic and it has a great potential to revolutionize the FC industry. A few research groups in recent years have tried to utilize 3D printing for fabricating different components of FCs especially BPPs. The question remains is that whether results from 3D printed prototype BPPs can be as good as the results from real graphite or metal BPPs.

#### 1.4 Objectives of the present work

The general objective of the present work is to increase the PEMFC stack energy output through optimizing the flow fields design. We aim to increase the flow distribution uniformity without increasing the total pressure-drop in the BPP flow fields. The current research proposes a flow field design for cathode, anode and water-cooling BPPs, tests its performance and optimizes the design for cathode BPP.

Specifically, the present work aims to investigate the applicability of 3D printing as a RP technique in fast-screening of the proposed flow field designs and in validating the simulation results. Moreover, the current research aims to investigate the pros and cons of different RP methods specially in manufacturing of flow fields, with focus on 3D printing, which could assist future researchers in selecting

right 3D printing method for a desired application. A novel prototype BPP with enclosed channels is fabricated which serves as a reliable tool in flow field design assessment.

## 2 Literature review

This chapter will discuss previous works on the following topics: (1) PEMFC flow field design, with a focus on modifying the straight-parallel channels to achieve an elevated flow uniformity. Then, we will introduce the different techniques applied for manufacturing of BPPs, and discuss about the benefits of (2) RP techniques, with a focus on 3D printing. We have reviewed different 3D printing technologies and pros and cons of each method in more detail in Appendix , a summary of which will be presented in this chapter. To the best of our knowledge, it is for the first time that such an instructive review has been done, which can help future researchers to select the right 3D printing technology for their desired application. In the rest of this chapter we will briefly discuss (3) Different flow visualization techniques. At the end, we will present the identified knowledge gap and the scope of the present work.

### 2.1 PEMFC flow field design

As it was mentioned in chapter 0, flow field design is the key method to increase the PEMFC efficiency and to maximize the power output. Many research groups have tried to develop flow fields with maximum pressure and fluid distribution uniformity and minimum pressure-drop by optimizing the channel configuration, and optimizing the flow channel geometric features. Here we summarize previous works in each of these two categories, and present the mathematical model for the pressure-drop in flow channels.

#### 2.1.1 Channel configuration

Numerous research groups have studied the performance of different channel configuration and flow field layout on the PEMFC performance [22-31]. Straight-parallel flow channels are not able to uniformly distribute the fluids [34], because of which they have not been paid attention by researchers in the past, and most of the research works have focused on serpentine and interdigitated flow channels. However, straight-parallel flow channels can easily be fabricated and are more cost effective than other

designs. Hence, it is very beneficial to focus on optimizing straight-parallel flow channels to obtain a more uniform flow pattern. The following discusses the research works conducted in recent years to modify the straight-parallel flow fields [35-38].

Barreras et al. [35] derived the velocity distribution in commercial straight-parallel channels with Z-type flow field arrangement, both by flow visualization experiment and by simulation. Their results revealed that in Z-type flow field arrangement, the flow has high tendency to go through side channels and lower tendency to go from middle part. They conducted experiment in two different Reynolds number (68 and 154), and reached the conclusion that the flow distribution is not dependent on Reynolds number and total flow rate.

Bi et al. [39] modified the straight-parallel flow channels by inserting flow-restrictors at the inlet region of the flow field. The addition of baffles increases the pressure-drop which in turn facilitates the product water removal and mitigates flow maldistribution. Their proposed design successfully alleviated the flow instability caused by negative-slope pressure-drop in horizontal two-phase flow. The advantage of the research work by Bi et al. [39] is that they have presented experimental results for supporting the functionality of their proposed novel flow field design.

Wang and Wang [12] introduced the parameter of *ratio of channel area to intake header* and suggested that decreasing this parameter boosts the flow uniformity. They reduced this parameter by applying two inlets/outlets and separating the flow field active area into two parts, as shown in Figure 2-1.

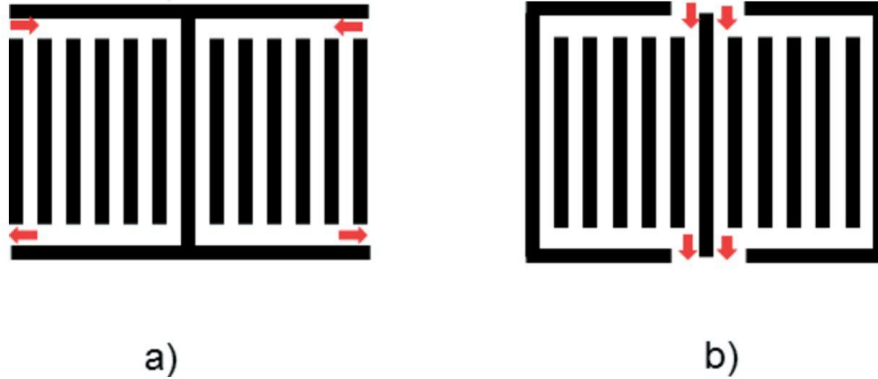


Figure 2-1: Modified flow field arrangement of straight-parallel : a) separated inlets, b) neighbor inlets (reprinted from [12] with permission from Wiley).

Imbrioscia et al. [40] simulated the hydrogen flow through BPPs with 20 straight-parallel flow channels, with  $40 \times 40 \text{ mm}^2$  active area. They modified several geometric properties of the conventional straight-parallel flow channels including width, depth and channel configuration, and obtained the velocity and pressure distribution in response to each modification. They applied channel fins to lead the flow into different regions. Investigating 8 different designs, Imbrioscia et al. concluded that increasing the collector area width, as well as bottom and top areas of the flow fields can boost the uniformity of the fluid distribution.

Gould et al. [36] used the cooling flow channels model proposed in [41], and improved the model by rotating the baffles  $90^\circ$  from those in the original design. Figure 2-2 shows the original and the modified design. Using numerical simulation, Gould et al. [36] demonstrated a more uniform cooling flow distribution in the modified design. Uneven flow distribution results in low degree of mixing and formation of stagnant areas especially behind the baffles. Uniform flow, however, eases this problem such that Gould et al. have reported a stagnation-free pattern in the modified design. They reported 2/27 channels to be stagnant in the modified design due to the sudden  $180^\circ$  turn of flow. Gould et al. [36] used qualitative experiments and used these experiments as a support for their simulation. However, they did not mathematically analyze the experimental results to demonstrate an experimental

velocity profile. Additionally, Gould et al. [36] did not take into consideration the fluid distribution in cathode and anode flow fields.

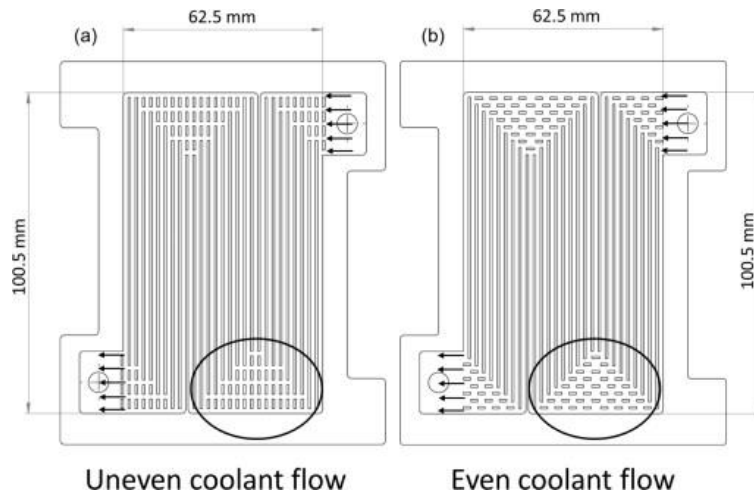


Figure 2-2: Computer aided drafting drawing of cooling flow fields with (a) uneven flow and (b) even cooling flow. Circle identify the mixing zones in each design. The arrows denote the designated cooling inlets and outlets (reprinted from [42] with permission from Elsevier).

Xu et al. [37] simulated the gas velocity distribution in Z-type straight-parallel flow channels and revealed that Z-type arrangement results in less flow from middle and more flow from the side channels, as shown in Figure 2-3. This observation is in agreement with the velocity profiles obtained by Barreras et al. [35]. However, the results by Xu et al. [37] suggest that in Z-type flow field arrangement, flow tends to become more non-uniform as the total flow rate (Reynolds number) increases, which contradicts the conclusion of Barreras et al. [35]. Xu et al. [37] further reported that the flow non-uniformity increases with increasing the channel number. They reasoned that the more channels are connected in parallel, the more the resistance of side channels decreases. Hence, Xu et al. [37] recommended an increased flow resistance in side channels in order to make the flow more uniform in Z-type flow field arrangement.

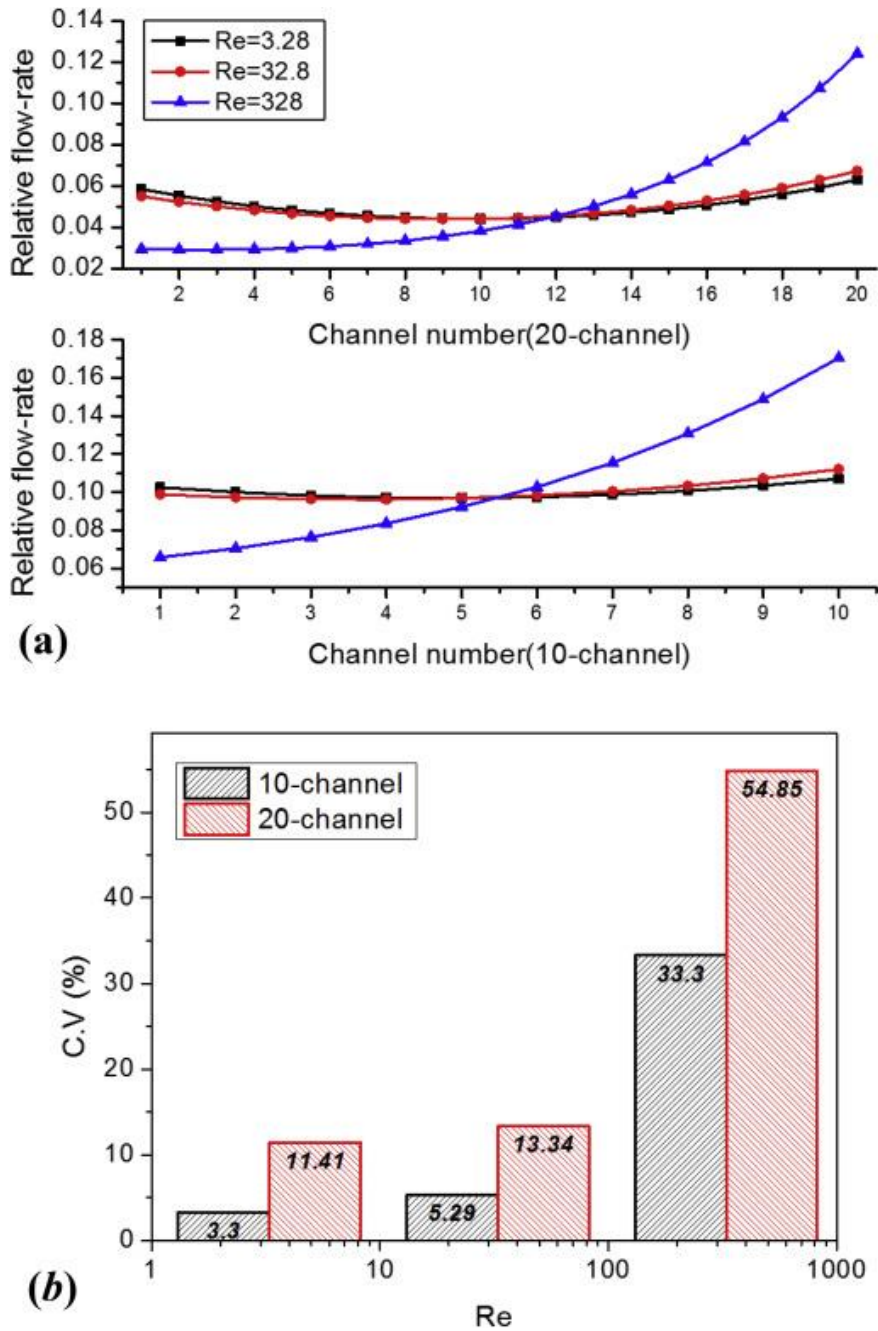


Figure 2-3: Effect of the Reynolds number: (a) relative flow rate distribution maps and (b) C.V value (reprinted [37] with permission from Elsevier.)

In another numerical simulation work, Lim et al. [38] applied the following modifications to the conventional straight-parallel flow channels in order to uniform the fluid flow. They divided the channels into multiple stages such that channel width was reduced from inlet to mid-section of the channel, and

then the channel width was increased in the outlet area. The outlet region acts as an accumulation region and increases the pressure-drop from inlet to outlet and assists both water management and flow uniformity. Figure 2-4 [38] demonstrates both conventional straight-parallel and modified straight

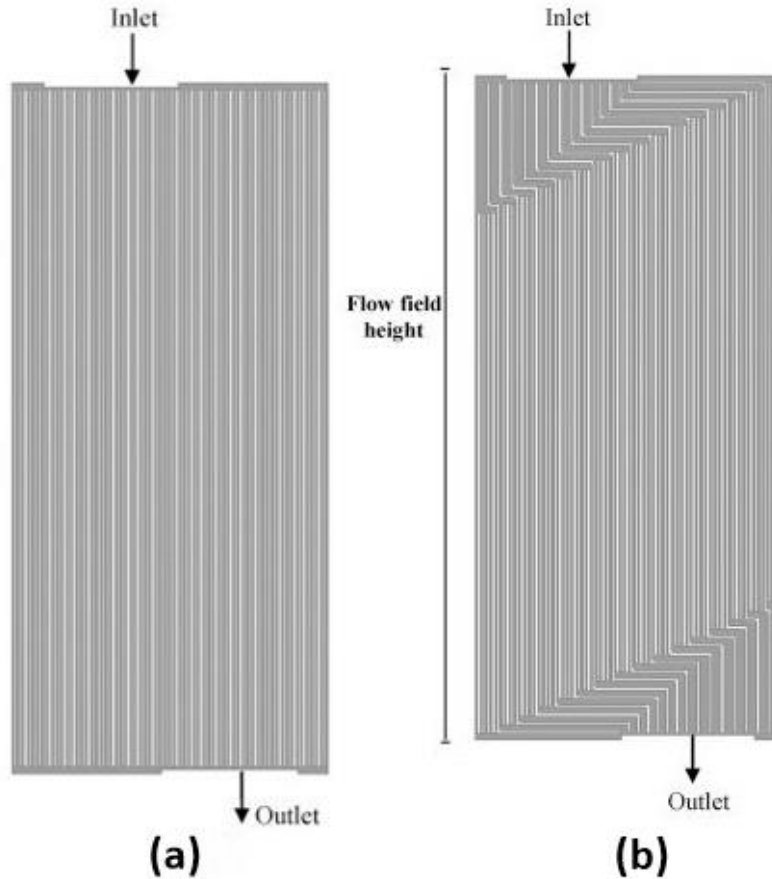


Figure 2-4: (a) Conventional parallel flow field design with single inlet/outlet, (b) Modified flow field design with three sections of channels: inlet, mid-section and outlet with single inlet/outlet (modified from [38] with permission from Elsevier).

parallel flow channels studied by Lim et al. [38]. The channel width varies from 1 mm to 3 mm, the rib width is 1 mm and the total active area is 129 mm×305 mm. Channel width of 3 mm is the main disadvantages of their proposed design since it would cause MEA intrusion into the channel, which could in turn decrease the FC stack life time. The simulation results by Lim et al. [38] demonstrated that the modified flow fields gave a more gradual pressure gradient from inlet to outlet and distributed the

reactants more uniformly than conventional design, as shown in Figure 2-5 [38]. The results by Lim et al. [38] also demonstrated that single inlet/outlet design performed better than double inlet/outlet design. This is due to the varying-length channels in double inlet/outlet channels, which deteriorates the flow uniformity and reduces the active area. This opposes the idea that one of the means for evenly distributing the fluids over the active area is leading the fluid to active area through multiple inlets.

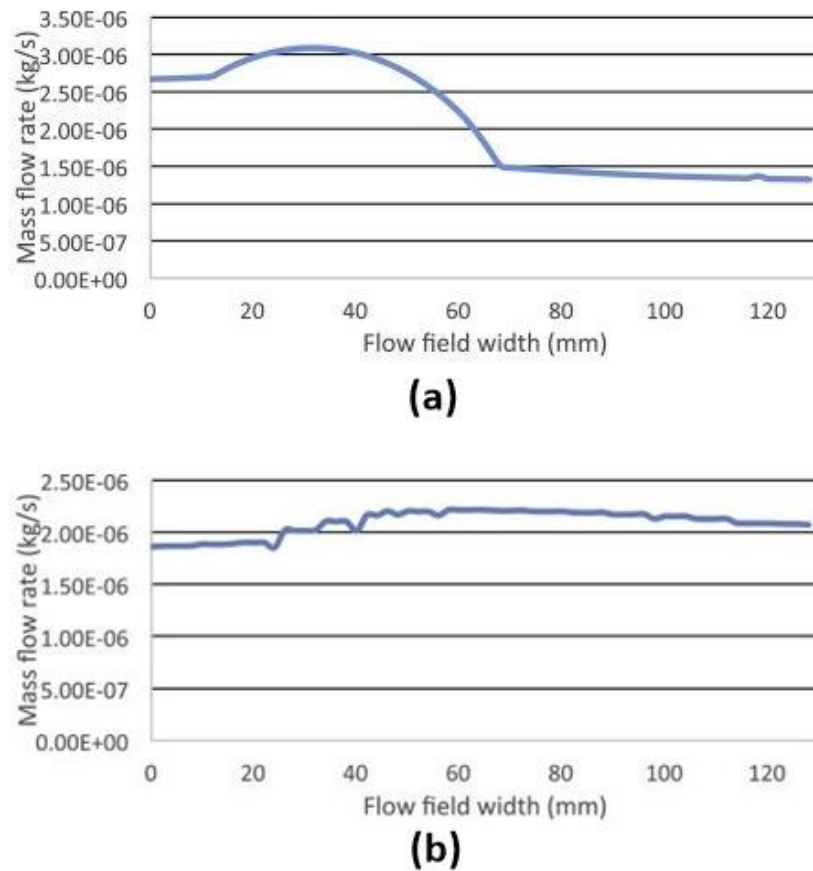


Figure 2-5: Numerical results of mass flow rate across the flow field width: (a) conventional parallel flow field with single inlet/outlet, (b) modified parallel flow field with single inlet/outlet (modified from [38] with permission from Elsevier).

### 2.1.1.1 Taking advantage of the non-uniform flow distribution

Since it is not possible to achieve a 100% uniform flow, it is important to detect the regions that flow has higher tendency to go through in anode, cathode and cooling BPPs, and then to try to align these

regions. The anode region with higher hydrogen concentration would generate more heat and electrons, and would require higher cooling flow to maintain the plate in a uniform temperature. It is also important to match the cathode side with higher oxygen concentration to that part of anode side, in order to balance the electron generation and consumption rate, and to avoid in-plane electron transfer, that would otherwise result in higher Ohmic resistance.

Wilkinson and St-Pierre [43] reported that non-uniform cooling flow distribution could be even beneficial to overall FC performance if it is well-matched with reactant flow distribution. If the cooling and reactant flow field design could be manipulated such that temperature would increase from inlet to outlet, then water saturation pressure would also increase and would cause alleviated flooding. Results from an earlier work [44] suggests that concurrent flows of cooling and reactant air, in combination with countercurrent flows of hydrogen and reactant air, results in an elevated FC performance in comparison with cooling, reactant air, and hydrogen concurrent flow. Similar results are reported by Kang et al. [43], with concurrent flows of cooling and reactant air and countercurrent flows of reactant air and hydrogen.

### 2.1.2 Optimizing flow channel geometrical features

Several geometric features of the flow channel affect the FC stack performance, which are reviewed and discussed below.

#### 2.1.2.1 *Channel and rib width*

Several studies have demonstrated the effect of channel and rib size on PEMFC [45-46]. Wider channels give smaller pressure-drop which is beneficial in terms of parasitic power loss. However, small pressure-drop increases the flow non-uniformity and disables the flow to push out the product water. Moreover, wider channels increase the chance for MEA intrusion which may reduce the cell life time. On the other hand, changing channel width would inevitably change the rib width, which also affects the FC performance. Smaller rib size would reduce the landing area for electron transfer and increase the

Ohmic overpotential. While larger rib size (smaller channel size) would decrease the GDL porosity underneath the landing area and would create mass transport overpotential. The optimum channel and rib width should be determined for each case, and there is not a specific rule for applying to all cases.

Scholta et al. [44] numerically analyzed the optimal channel and rib width in parallel flow channels, applying the values of 0.7 mm and 1 mm for both channel and rib width in 100 cm<sup>2</sup> active area. They suggested that narrow channels are appropriate for higher current loads, while wider channels are better for lower current loads. Similar results were reported by Zamel and Li [47], and they concluded that the rib to channel ratio of 1:2 is optimal. Shimpalee and Van Zee [48] reported that narrow channels with wider ribs present slightly better performance due to the locally non-uniform distribution of the reactants in the wider channel configuration. The global distribution was the same. Wang et al. [45], however, mentioned that in straight-parallel flow channels the main transport mechanism of reactant into GDL is diffusion and an increased channel width would assist this transport, although they did not consider the effect of flow uniformity. Wang et al. [49] indicated that at high current densities, the reduced channel size increases the fluid velocity, assists reactant mass transport into GDL and accelerates water removal, with a channel size of 0.535 × 0.535 mm<sup>2</sup> to be the optimum size.

In short, smaller channel width with rib to channel ratio of 1:1 performs better in terms of the flow uniformity, electron transfer and GDL porosity. However, smaller channel is hard for being manufactured and increases the pressure-drop; optimum channel size is dependent on the specific application. FCs utilizing air as an oxidizing agent require smaller rib width than FCs utilizing pure oxygen [13].

#### *2.1.2.2 Channel aspect ratio*

Channel aspect ratio (height to width ratio) is the other factor that could influence the PEMFC performance. As the channel height decreases, the channel cross-section also decreases which in turn increases the pressure-drop. This could slightly increase the cell performance by removing the

accumulated water in channel outlet. Results of Choi et al. [50] highlighted that increasing the channel width would decrease the cell voltage much more significantly than increasing the cell height. Smaller aspect ratio would cause membrane dehydration, and at the same time would increase reactant mass fraction in under rib areas.

Manso et al. [51] numerically investigated the effect of channel aspect ratio in 10 different height to width ratios ranging from 0.07 to 15. They reported that designs with higher aspect ratio demonstrated more even current distribution with higher global cell performance. They suggested 10:6 aspect ratio for an optimal cell performance. They did not consider, however, the fact that higher aspect ratio would decrease the rib mechanical strength which may impact more on FC long-term durability, and it might not be the best from mechanical strength view point to select channel height twice as its width.

Wang et al. [52] found that at low current densities, the aspect ratio of channel is not influencing the FC performance, while at high current densities decreasing the aspect ratio would increase the channel velocity and improve the cell performance by an elevated under rib convection. Wang et al. [53] also found that in straight-parallel channels, decreasing the aspect ratio increases the water removal and boosts the cell performance. For interdigitated channels, they suggested an aspect ratio of 1 with 1mm×1mm channel cross-section.

### 2.1.3 Pressure-drop in flow field channels

As mentioned before, one of the factors that is very important to be considered in flow field is the pressure-drop, since it is directly related to the parasitic power loss and determines the energy output fraction required for circulating the fluids. It should be noted that although small values of pressure-drop along the channels are desired, pressure-drop has a close interaction with water management ability and flow distribution uniformity, which dictates a tradeoff between pressure-drop and flow uniformity. As mentioned previously, one of the roles of BPPs is to remove the product water, since

stagnant water would block the flow channel and would deteriorate the reactant gas distribution. To ensure that flow channels are efficiently removing the product water, a high pressure-gradient along the channel is required. Numerous research groups have studied the pressure-drop in PEMFC BPPs [3, 54-61]. Here some representative results will be discussed.

The pressure-drop of an incompressible flow in a pipe can be modeled using Darcy-Weisbach equation:

$$\Delta P = f \frac{L}{D_h} \rho \frac{U^2}{2} \quad (4)$$

Where L is the flow path length,  $D_h$  is the hydraulic diameter of flow path cross-section,  $\rho$  is the density of the incompressible fluid, and U is the average fluid velocity. The Fanning friction factor,  $f_f$ , for a square channel cross-section in the laminar flow regime ( $Re < 2,100$ ) can be calculated from the eq.(5):

$$f_f = \frac{14.2}{Re} [62] \quad (5)$$

Where:

$$Re = \frac{\rho U D_h}{\mu} \quad (6)$$

Where  $\mu$  is the fluid viscosity. The pressure-drop in flow fields of a non-operating (cold) FC with straight-parallel flow channels can be modeled by adding a second term to Darcy-Weisbach equation, as shown in eq. (7):

$$\Delta P = f \frac{L}{D_h} \rho \frac{U^2}{2} + \sum k \rho \frac{U^2}{2} \quad (7)$$

Where k is local flow resistant (baffle, bend) and U' is the average flow velocity in the place of the local resistant. Substituting (6) and (5) into (7), one obtains:

$$\Delta P = 28.4\mu L \frac{U}{D_h^2} + \sum k \rho \frac{U^2}{2} \quad (8)$$

Eq.(8) reveals that in the first term, which is the dominant term when  $\sum k$  is small, pressure-drop dependency on flow velocity is of first order, and on channel dimension is of reciprocally second order. This highlights that in small channel dimensions, even small deviation from expected cross-sectional area could result in a high deviation from the expected pressure-drop. Eq.(8) further reveals that when  $\sum k$  is small, the relation between pressure-drop and fluid velocity is linear in small fluid velocity, while at higher velocities the second term becomes dominant and the relation becomes quadratic.

In an operating PEMFC, the pressure-drop in BBPS shows further deviations from linear pattern. As the reactants pass through the channels, they participate in chemical reaction and this changes the volumetric flow rate. Moreover, the water is being generated as a reaction by-product which turns the single-phase gas flow into two-phase flow, and disturbs the pressure-drop obedience from linear pattern. The other factor responsible for non-linear pressure-drop is the BPP geometry. The presence of baffles and turns in the flow field changes the flow field geometry from that of a pipe and violates the assumption of small  $\sum k$ . More importantly, the presence of GDL and under-rib convection add to the pressure-drop and further deviates it from the linear pattern.

Zhang et al. [61] experimentally calculated the single-phase pressure-drop in a single channel inside which a strip of GDL was used to simulate the PEMFC flow channels. They demonstrated that pressure-drop in the mentioned channel with a single phase laminar flow follows the linear relationship. They further investigated the two-phase pressure-drop in flow channels and very well modeled the two-phase flow pressure-drop in flow fields.

Anderson [3] studied the pressure hysteresis in two-phase flow in PEMFC BPPs with parallel channels and found that pressure-drop hysteresis is due to the liquid water accumulation in the cathode flow channels during the descending approach.

Other researchers [3, 54–61] also studied the gas-liquid two-phase flow pressure-drop in PEMFC flow channels and demonstrated the non-linear nature of pressure-drop in the presence of water in the flow channels. The focus of these studies was to improve the existing mathematical models for predicting the pressure-drop in PEMFCs based on valid and realistic experimental data. They conducted pressure-drop experiments to study the onset of flooding and to use it as a tool for better water management. These studies will assist future researchers to design flow channels with a reasonable pressure-drop and maximized flow uniformity.

#### **2.1.4 The importance of BPP fabrication**

So far, we introduced some of the previous works on optimizing the flow field design. Despite the many research works on this topic, they are mostly numerical simulations and suffer from lack of experimental data to validate those simulations. The first step in practical assessment of proposed flow field designs is to fabricate the proposed design models. The following section discusses different fabrication techniques of BPPs and pros and cons of each method.

### **2.2 Different fabrication techniques of BPPs**

There are three types of materials used for fabricating BPPs: graphite, metal and carbon-polymer composite, each of which suitable for one of the following fabrication methods.

#### **2.2.1 Machining of graphite plates**

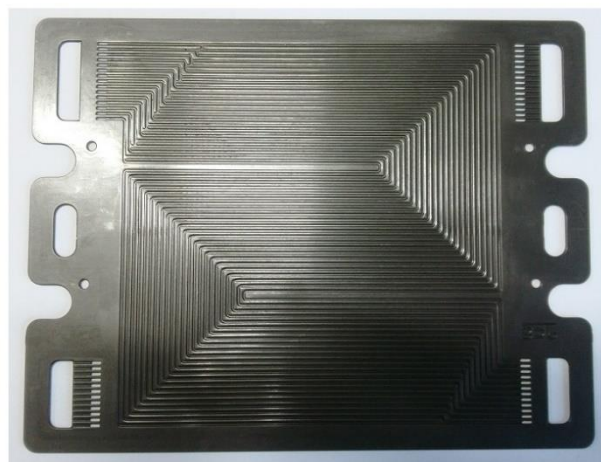
The first method for fabricating BPPs is CNC machining of graphite plates, the high precision of which makes it interesting for most research works. To the best of our knowledge, CNC machining is able to subtract channels with as small as 0.2mm×0.2mm cross-section. Using micro drill bits, CNC machining

has even the theoretical capability of machining smaller channel cross-sections. Figure 2-6-b demonstrates an example of machined graphite BPP.

CNC machining of graphite plates is a very difficult process because of the flaky microstructure and irregular geometry of graphite [63]. Moreover, brittleness of graphite plates adds to its fabrication difficulty and hinders its applicability in experimental and real automotive applications. These problems also limit the flow field design to simple planar geometry, and increasing the design complexity would drastically add to the CNC machining cost. The high cost also prevents the applicability of this method to high-volume production, which is a must in automotive industry. One solution could be CNC machining of a mold and using that mold for high-volume production using the following method.



**(a) Metal bipolar plate.**



**(b) Graphite bipolar plate.**

*Figure 2-6: Metal and graphite BPPs (reprinted from [64]).*

### 2.2.2 Molding graphite or carbon materials

In this method, a graphite slurry is molded inside a high-precision die under high temperature and pressure. Onishack et al. [65] fabricated molded graphite bipolar separator plates and reported an equivalent performance with the state-of-the-art machined graphite plates.

In order to easily take out the molded graphite plate, a draft angle of at least  $15^\circ$  is needed for the flow channels, as shown in Figure 2-7. Moreover, there exist a minimum thickness requirement for the molded graphite plates, which in turn increases the FC stack weight and volume.

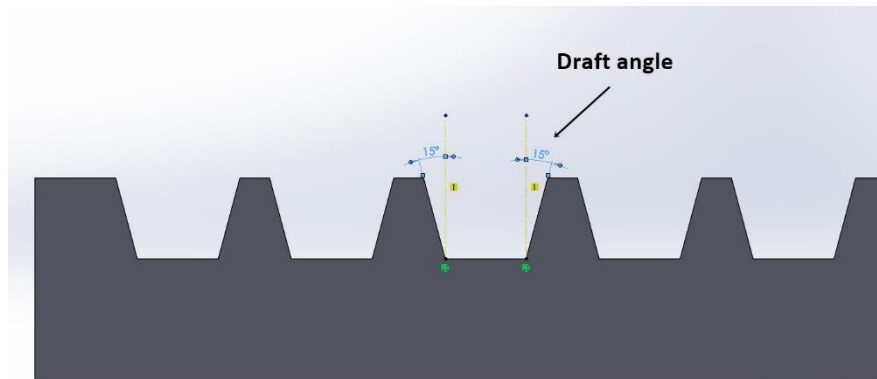


Figure 2-7: Minimum draft angle required for molds in fabricating molded graphite BPPs.

### 2.2.3 Stamping metals

BPPs were traditionally being fabricated by CNC machining of graphite or by molded graphite composites, but now FC industry is moving toward stamped metal BPPs. Applying metals for fabricating BPPs enables the production of cheap and light-weight FC stacks. Metal BPPs can have much lower thickness and rib width which allows designing more complex fluid flow fields. A sample metal BPP is shown in Figure 2-6-a. Additional advantages of metal BPP include malleability, resistivity to shock and vibration, lower cost and lower fluid cross over. Metal BPPs could be recycled after their lifetime, which is an important consideration. However, metal BPPs suffer from lower thermal conductivity. The thermal conductivity of graphite composite material that is mostly used for BPP fabrication is 20-50

W/mK, while that of metal is 16.3 W/mK [66]. Another severe problem with metal BPPs is the necessity for making them corrosion resistant. The byproducts of metal corrosion prevent the water transport within the MEA, and many research works have been done to overcome this drawback [67,68].

#### 2.2.4 The problem of conventional fabricating techniques

These three mentioned fabrication methods are time-consuming and expensive and limit the designs to simple planar ones. Hence, we need to consider faster and cheaper prototyping techniques that would enable us to fabricate experimental prototypes to evaluate the ideas and to quickly analyze their weaknesses and strengths, which would pave the path toward rapid screening of initial ideas. The following part will introduce the alternative fabrication techniques that can be utilized for practical testing of the complex flow field designs with a reasonable time and cost.

### 2.3 Different rapid-prototyping techniques

Rapid-prototyping (RP) is a machine-based technology for fabricating 3D prototypes, that can manufacture near-net shape designs from a computer aided design (CAD) model. RP dates back to 1980s, and was first used to create models [69]. Two important class of RP techniques are subtractive manufacturing (SM) and additive manufacturing (AM). SM is referred to a process within which 3D parts are manufactured with subtracting (cutting) material away from a solid block of material to achieve the desired pattern. The main limitation of SM is that it dictates planar design. CNC machining, drilling, milling, grinding and more recent technology of laser-cutting of plastic parts are some popular examples of SM.

AM is referred to a process within which fabrication takes place by powder consolidation, solidification of fluids or addition of materials layer by layer. These techniques are also called freeform fabrication or layered manufacturing [69,70]. The fabrication accuracy can be manipulated by controlling the amount of material added in each increment. Unlike SM, AM is capable of manufacturing complex designs such as hollow parts, undercuts, internal cavities, pipes, overhangs, lattice structures, parts with oriented

internal pore structure and many other complex geometries that conventional fabrication techniques are not able to create. Due to the high cost and high fabrication time of the conventional fabrication techniques, RP techniques are of great interest for many researchers since they provide the platform for fast and cost-effective fabrication, which is a must in research environment. Particularly for FC applications, AM brings us the opportunity to change the design of a specific part of FC without the necessity for changing the entire setup design. The application of metals, ceramics and composites has widened the spectrum of parts that can be fabricated by RP [69].

As mentioned by Dudek et al. [69], it should be noted that RP techniques are not meant to supplant other fabrication methods, especially the ones being used for high-volume production. The main point of RP is to eliminate tooling and reduce the cost for short run fabrication. RP is also useful for creating parts designed for specific purposes such as custom parts, or creating parts for the purpose of product development in the laboratory [71].

### 2.3.1 3D printing

3D printing is the most useful and most beneficial AM technique. 3D printing has been very popular in industry and research environment in recent years and it has shown great promises for RP of complex designs. After expiration of 3D printing patents and the wide applicability of CAD models, 3D printing service is nowadays an affordable RP route for instant testing of many ideas.

3D printing has a great potential for revolutionizing the FC industry, where cost and weight reduction are essential toward FC economic viability. 3D printing has been advertised as a method for RP of BPPs as well as many other FC components. With eliminating the necessity for tooling, 3D printing could help assessing the BPPs performance in a negligible time and cost compared to other fabrication techniques. 3D printing enables fabricating single-piece BPPs without the need for welding, with non-planar geometries such as internal passages [72], that could decrease the number of parts, sealing requirement and complexity of assembly.

In a recent work, Dudek et al. [69] introduced different 3D printing techniques with the focus on 3D printing advantages for mobile applications and aerial researches. They have provided the readers with very good information on how each technology works and the materials being used in each 3D printing method. However, the work by Dudek et al. [69] lacks information about the accuracy, minimum feature size and cost of each method. Furthermore, Dudek et al. [69] does not provide us with information about how each method is beneficial compared to other methods, and does not lead us toward technology selection. In other words, one cannot decide about the appropriate technology for a specific purpose based on the work by Dudek et al. [69].

In the present work, Appendix provides detail information on 3D printing process and discusses each 3D printing technique. The information in Appendix is based on recent catalogues from famous 3D printing companies, and based on author's personal experience in 3D printing, as well as previous works from literature, which aims to help researchers decide the right 3D printing technique for their specific research needs.

Herein, we shortly summarize different 3D printing techniques and discuss the previous works done with each 3D printing method to prototype BPPs.

#### *2.3.1.1 Summary of different 3D printing techniques*

The following table summarizes different 3D printing techniques that is discussed in Appendix . Please note that we did not compare the 3D printing time since all 3D printers can prototype the part in a negligible time in comparison with other RP and fabrication techniques, and time is not a factor that could affect our decision in selecting the right technology for our specific purpose.

Table 2-1. Summary of different 3D printing technologies.

3D Printing Method	X/Y Plane Accuracy (mm)	Layer Thickness (mm)	Minimum Feature Size (mm)	3D printing Cost (US\$) Per Gram	Apparatus Price ×1000 US\$	Materials	Suggested Temperature (°C)	Notes	Summary
FDM	0.127-0.200	0.127-0.508	1.000	0.075	1-8	ABS, PLA	100°C <	Requires pre-fabrication and post fabrication steps.	Real world thermoplastics that are unmatched in mechanical, thermal and chemical strength.
Polyjet	0.100	0.016	0.200	0.750	24-350	Vero series resins	100°C <	Slightly out of shape in <0.5 mm features	Highly detailed parts built with precision and speed, in a wide variety of build materials, Non-stable materials.

Table 2-1. Continued

SLA	0.051	0.051-0.102	0.635	1.650	2-500	Acrylic, Epoxy	100°C <	Perfect and very sharp cross-section in small dimensions	Resin based 3D printing ideal for high detail large parts and concept models that require painting & finishing.
SLS	0.762-1.270	0.102-0.152	1.000	1.050	10-350	Nylon, Ceramic	150°C <	High Thermal Resistivity and mechanical strength in comparison with SLA, Polyjet, FDM	Accurate and functional parts that are durable enough for end use low volume production.
DMLS	0.300-0.400	0.020-0.040	0.100-0.200	20.000	250-500	Ti-alloy, Al, SS	Less than 60% of the printed metal melting point.	Appropriate for 3D printing functional metal BPPs in one piece without the need for welding.	Functional metal parts appropriate for end use.
DLP	0.025-0.065	0.025-0.150	0.200	0.900	2-300	Resins	100°C <	Faster than SLA	-----
LOM	NA	0.100	NA	NA	NA	NA	NA	Not widely applied	-----

### 2.3.1.2 Previous works on prototyping BPPs by different 3D printing technologies

#### 2.3.1.2.1 Solid based

##### 2.3.1.2.1.1 Fused deposition modelling (FDM)

One of the early works that has applied 3D printing to fabricate FC components is done by Chen et al. [80]. They used FDM 3D printing with ABS material for prototyping a miniature FC stack with 6 cm×6 cm×0.9 cm volume. Chen et al. [80] developed an air-breathing 10 cell planar array stack design within which they took advantage of the pin-point precision of FDM 3D printers in order to achieve a high power-density. Chen et al. [80] compared the fabrication time of FDM technology with other technologies for fabricating miniature FCs. The two alternative methods to prototype such miniature FC stacks are CNC machining and micro-electro-mechanical processes (MEMS). The fabrication time of each method are as follow; FDM: 1h, CNC: 2h, MEMS: 12-36 h. In addition to saving time, FDM would bring the chance to fabricate the parts which can be very challenging with CNC machining, although current FDM technology is still too far from the CNC precision. Chen et al. [80] reported that the power-density of their prototype FC stack is comparable to that of state-of-the-art planar array FC stack, and concluded that this fast inexpensive fabrication method has the promises for successful prototyping of FC components, and can be further developed in the future.

Chen et al. [81] tried to demonstrate the feasibility of RP technology for FC applications. They employed FDM 3D printing with ABS material for fabricating honeycomb-shaped methanol reservoir and cathode structure of an air-breathing direct methanol FC (DMFC), with 5×5 cm<sup>2</sup> active area. Chen et al. [81] compared the performance of the conventional air-pumping DMFC and that of rapid-prototyped air-breathing DMFC, and proved the applicability of FDM 3D printing in fabricating complex BPP design of DMFC stacks, which is not feasible with CNC machining. In another part of their study, Chen et al. [81] used FDM 3D printing with ABS material to fabricate flow fields of air-breathing monopolar PEMFC stack with 6×6×3 cm<sup>3</sup> volume, and reported a power-density of 123 mW/cm<sup>2</sup>, which is close to literature

(100-120 mW/cm<sup>2</sup>) [82]. Although Chen et al. [81] have mentioned that their flow field design was impossible to be fabricated with CNC subtractive manufacturing, they did not show the design of their PEMFC flow fields and we cannot comment on the complexity of their designs. Their honeycomb methanol reservoir is not complicated to be fabricated by 3D printing.

In a more recent work, Di Lorenzo et al. [83] utilized FDM 3D printing with polycarbonate acrylonitrile butadiene styrene (PC/ABS) material to fabricate a small scale microbial FC (MFC). They incorporated FC components while 3D printing the MFC, which eliminated the need for any fitting and sealing. Using 3D printing, Di Lorenzo et al. [83] were able to further miniaturize their MFC, which helped them to fabricate stack of multiple units and arrangement of multiple miniature MFC single cells.

In another application, in order to tackle the cost, weight and manufacturability challenges in water electrolysis, Chishlom et al. [84] fabricated flow plates for water electrolysis by applying two layers of silver coating on a 3D printed flow plates. They used a FDM 3D printer with polypropylene material for RP of flow plates with 12.96 cm<sup>2</sup> active area and 0.9×0.9mm<sup>2</sup> flow channels cross-section, shown in Figure 2-8. Chishlom et al. [84] reported that silver coated 3D printed plates are 4 times lighter than conventional titanium plates, and cost less than 1/4 of titanium plates. However, their costs evaluation does not seem to be realistic. They have reported US\$ 1.54 per kg of polypropylene, while one kg polypropylene 3D printing filament costs around \$US 60. Chishlom et al. [84] evaluated the performance 3D printed flow plates in water electrolysis and reported an acceptable performance in terms of overall efficiency, overall electric resistance and polarization curves. The research by Chishlom et al. [84] is a valuable research as the first work to present a new fabrication paradigm for water electrolysis application. However, the geometry and dimensions used by them are not applicable in state-of-the-art electrochemistry researches. Other 3D printing techniques with more accuracy and capability to fabricate smaller features are recommended for the future research.

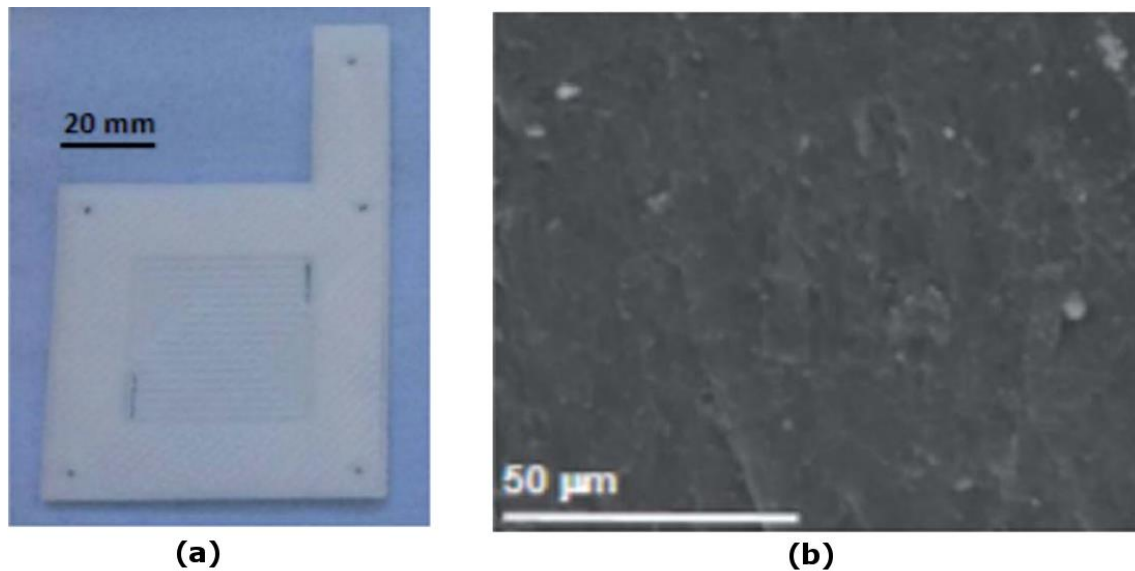


Figure 2-8: (a) Photograph of polypropylene flow plate with corresponding (b) SEM image (reprinted from [84]-Published by The Royal Society of Chemistry).

#### 2.3.1.2.2 Liquid Based

##### 2.3.1.2.2.1 Polyjet

In a recent research, White et al. [90] utilized objet30 desktop 3D printer, which is a popular version of Polyjet 3D printers, for fabricating a housing fixture for water imaging application in PEMFCs. They 3D printed a cell with two flow channels with half-circular cross-section, each having 0.5 mm radius and 10 mm length, with an active area of 0.24 cm<sup>2</sup>. One of the valuable steps in their research is that they have demonstrated X-ray computed tomography (XCT) images of channel cross-section of 3D printed channels, as shown in Figure 2-9 [90]. Such images can be used to evaluate the ability of different 3D printing techniques to fabricate all the details of small features. White et al. [90] reported that 3D printing enabled them to fabricate a fixture small enough to ensure a reasonable signal-to-noise ratio for commercial XCT scanners, which conventional fabrication techniques were unable to fabricate such a design. They chose a 3D printing material with lower X-ray absorbance than metal and graphite and no noticeable gas permeation. Their overall results highlight that with novel material selection and design

miniaturization, 3D printing method could demonstrate many advantages for being used in non-invasive imaging of PEMFCs.

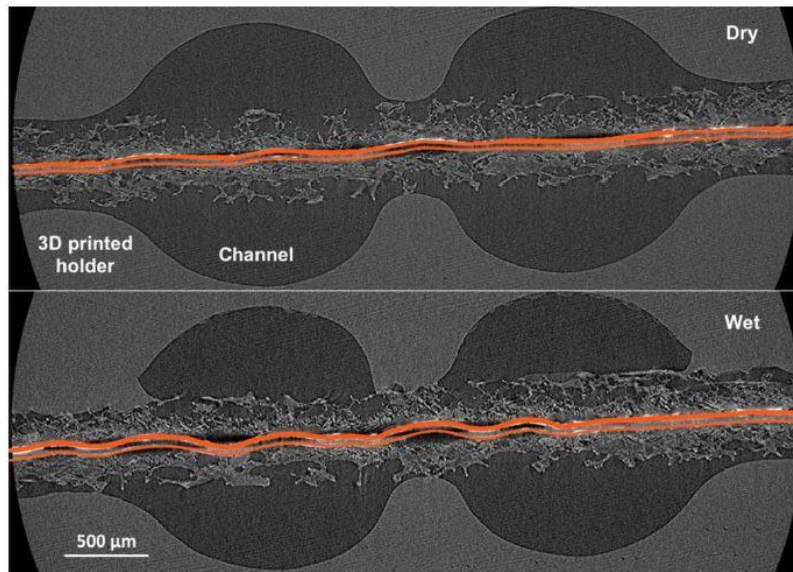


*Figure 2-9: Representative cross-sectional XCT images of the MEA situated inside the 3D printed flow field fixture at dry and wet conditions. During FC operation in the wet state, the increased hydration of the membrane caused an increase in the membrane thickness and significant undulations of the CCM. The outline of the catalyst layers in orange has been included to better highlight changes seen in the membrane after swelling due to hydration (reprinted from [90], open access article).*

#### 2.3.1.2.2.2 Stereolithography (SLA)

Papaharalabos et al. [94] used SLA and FDM 3D printing in developing a small MFC for power generation and waste water treatment. They developed three MFCs using ABS, PC-ISO and RC25 materials. They used SLA for 3D printing RC25 and FDM for 3D printing ABS and PC-ISO materials. Papaharalabos et al. [94] compared the performance of three 3D printed FCs with a control cell, and reported that all three 3D printed cells demonstrated improved single cell performance, with the following order of elevated performance: Pc-Iso, RC25, ABS. The research by Papaharalabos et al. [94] highlights the different performance of 3D printing materials that could help researchers working in the MFC area to choose their desired material. However, the difference in performance is related to the nano-structure and biocompatibility of materials, and does not directly correspond to the 3D printing

apparatus performance. Hence, it could not help us determine the accuracy and applicability of these 3D printing techniques for 3D printing of BPPs and other FC components.

#### 2.3.1.2.2.3 Digital light processing (DLP)

Gould et al. [36] used ZBuilder Ultra 3D printer, which is a popular class of DLP 3D printers, for prototyping cooling flow fields, in order to validate their numerical results on cooling flow distribution in flow channels. They used ZCorp's SI500 plastic for 3D printing cooling flow field plates that had a depth of 0.5 mm, width of 1.5 mm, and rib width of 0.75 mm. The aim of Gould et al. [36] was just to qualitatively validate their numerical data. Although this method of 3D printing satisfies their need, Gould et al. [36] have not answered the question that whether plastic 3D printed plates can be a good candidate for precise flow visualization experiments. Furthermore, they did not investigate whether 3D printed plates match their desired size, and whether any possible inaccuracy or imperfection in fabrication is acceptable. A further step can be to compare the results from 3D printed plates with that of real graphite/metal plates, and then based on this comparison to determine the applicability of 3D printing.

#### 2.3.1.2.3 Powder based

##### 2.3.1.2.3.1 Powder bed and inkjet head 3D printing

Lyons et al. [68] introduced a RP technique using powder bed Inkjet 3D-printing followed by thermal spray (TS) deposition, in order to reduce PEMFC stack cost, reduce fabrication time and increase flow field design flexibility. They first 3D printed gypsum patterns of BPPs with 500  $\mu\text{m}$  channels, using ZCorp Z310 3D printer which has +/- 250  $\mu\text{m}$  accuracy [97]. Then, they took advantage of the high temperature stability of gypsum 3D printing material, and deposited metals on gypsum patterns using a hybrid TS deposition equipment, creating metallic gas flow plates. Their final step was removing 3D printed part in order to have a pure metal body of BPP. Figure B-8 demonstrates their 3D printed-TS BPPs. Lyons et al. [68] have reported fabrication time of 20 min per four 3D printed pattern, and 30 min for TS deposition.

This fabrication time, however, does not seem to be realistic for conventional BPPs. Although they reported the fabrication cost of US\$ 5 per plate, and asserted this as a significant cost advantage, they have not specified their plate size which prevents us from assessing the cost effectiveness of coupled 3D printing-TS technology. Lyons et al. [68] just tested their proposed 3D printing-TS method for a basic geometry as shown in Figure B-8 , and have not demonstrated the applicability of this method to more intricate designs, or have not shown the minimum size requirements of this method. Although most 3D printing and RP techniques are having high nominal accuracy, they fail to realize the intricate features of the part in practice, resulting in some degree of discrepancy between prototype and real part results.

#### 2.3.1.2.3.2 Selective laser sintering (SLS)

Chen et al. [63] applied indirect SLS for fabricating PEMFC BPPs. They mentioned that SLS of carbon composite materials satisfies both material and procedure selection requirements for the fabrication of PEMFC BPPs. The procedure used by Chen et al. [63] involves laser sintering of powder followed by two further steps (binder carbonization and epoxy filtration), in order to make the plates to meet DOE targets. Chen et al. [63] reported that the BPPs they fabricated in their research were satisfactory and they further improved the conductivity of plates to meet all the DOE 2005 targets. In another work, Guo and Leu [105,104] applied SLS of graphite with a binder to prototype several BPPs, and showed that their 3D printed BPPs performed similar to injection molded BPPs.

#### 2.3.1.2.3.3 Direct metal laser sintering (DMLS)

Netwall et.al [112] used DMLS method to prototype 40mm×80mm single-piece BPPs with 21cm<sup>2</sup> active area, with embedded flow channels, using Ti-alloy. They used these DMLS 3D printed plates to study how to decrease the surface roughness of BPPs to reduce contact resistance. Netwall et al. [112] mentioned that in a state-of-the-art PEMFC, minimizing the Ohmic resistant is of great importance since Ohmic resistant is responsible for 55% of the total I<sup>2</sup>R losses and energy is converted to heat rather than electricity with I<sup>2</sup>R relation.

In another study, Gould et al. [74] used single cells from [112], as shown in Figure 2-10, in a 40-cell stack. They first compared the polarization curve of single cell with DMLS 3D-printed BPPs to that of carbon BPPs, and reported similar performance in the kinetic region. In the mass transfer region, they observed improved performance in the case of DMLS BPPs due to the differences in hydrophobicity of carbon and Ti-alloy. In the Ohmic region, however, Netwall et al. reported relatively lower performance for Ti-alloy BPPs in comparison to graphite plates. They attributed this lower performance to the increased contact resistance across the BPP-GDL interface in 3D printed BPPs.

Although Gould et al. [74] applied polishing and then coating on 3D printed parts to alleviate the distortion from flatness, they could not eliminate the plate height difference completely and reported 20% less than expected power because of  $44 \pm 25 \mu\text{m}$  deviation from flatness. This is one example that imperfection in 3D printing limits its applicability for FC stacks. Gould et al. [74, 114] suggested that researches should be done toward modification of flatness and feature size, as well as surface finish to prototype parts with higher accuracy in both XY and Z-direction.

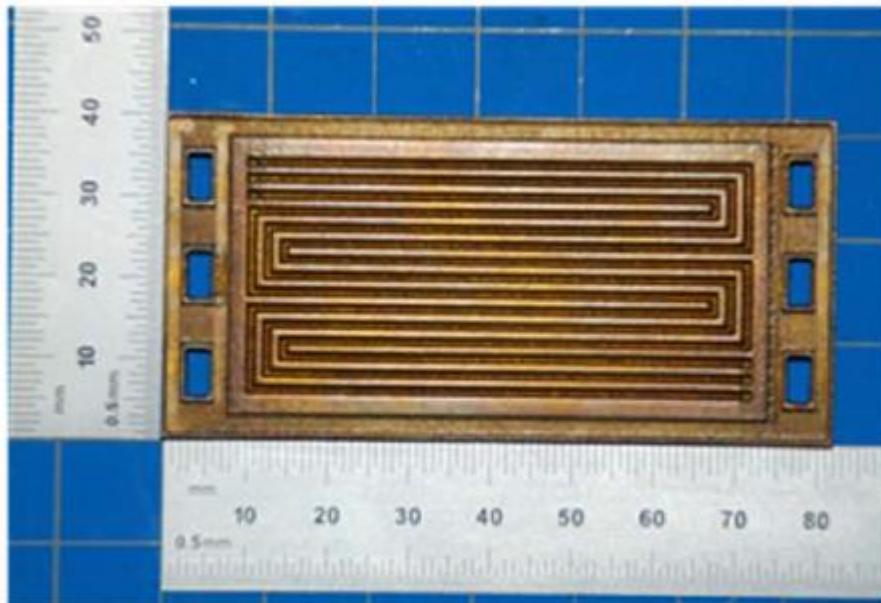


Figure 2-10: Photograph of the finished BPP from [74] (reprinted from [74], open access article).

Gould et al. [74, 109, 114] asserted that DMLS 3D printing would lower cost and fabrication time, and reported their fabrication time to be in the order of a few hours. Although this makes sense in case of single cells, it might not be valid in case of 40-cell stack. Increasing the fabrication volume in conventional fabrication methods would decrease the fabrication cost and time for 40-cell stack, while with 3D printing the cost and volume relation is linear. Hence, detailed financial analysis is needed to provide the reader with a sense of how DMLS could be beneficial both financial-wise and time-wise. Gould et al. [74] used channel and rib width of  $\sim 1$  mm. However, recent BPP designs are moving toward small channel dimensions in the order of a few tenth of millimeters, such that current 3D printing technologies are unable to prototype the detailed features of the new designs with an acceptable precision. The research by Gould et al. [74] does not provide us with the information on the minimum channel dimensions could be 3D printed with DMLS technology.

It should be noted that both Gould et al. [74] and Lyons et al. [70] have focused on fabricating functional prototypes using 3D printing and AM, and they have both asserted that their methods offer reduced fabrication time and cost. Although the time reported by Lyons et al. [70] (20 min per four plates) seems much lower than the time for DMLS, Lyons et al. [70] have not specified their plate size. It is obvious that higher accuracy will require higher 3D printing time, and since the accuracy of the DMLS method (100 micros) is higher than the accuracy of powder-binder 3D printers (250 micros), it would result in higher 3D printing time. We believe that 3D printing most 3D printing technique would meet the timing requirement for RP, and the determining factors would be accuracy, complexity and number of post fabrication steps. Gould et al. [74] mentioned that 100 micron feature size has a detrimental effect in Ohmic resistance and applied three polishing and coating steps to improve the surface roughness, which would undoubtedly add to total prototyping time. While Lyons et al. [70] did not believe that even 250 micron accuracy would affect their desired research intention, and applied the 3D printed patterns for TS deposition. We believe that method introduced by Lyons et al. [70] would be less complex and pricy

than method of Gould et al. [74]. However, we can have finer and much precise features with DMLS, and one should decide between different methods based on the research intention.

### 2.3.2 Laser-cutting

Laser-cutting is a SM technique within which, first the desired planar design is cut on paper. Then the paper is glued onto a plastic piece, e.g. acrylic glass, to cover the areas which does not need to be cut. Laser beam is then applied on the plastic which melts down the uncovered areas and forms the aimed design. The depth of cut can be controlled by changing the power of the laser beam. We could not find a previous work in the literature which has applied laser-cutter technology for prototyping BPPs.

## 2.4 Flow visualization

Flow visualization is a method for investigating the fluid flow behavior with flow tagging. When a fluid is running through a flow field, flow is being tagged and images of the fluid flow are being captured usually by a compact camera module (CCM). Analyzing the captured images enables us to study the fluid behavior. The most common fluid flow visualization techniques are discussed below.

### 2.4.1 Particle image velocimetry (PIV)

PIV is a method for obtaining instantaneous velocity fields. In this method, a fluid is seeded with small enough tracer particles such that the particles follow the streamlines of the flow. Then two consecutive laser pulses with a time gap in the order of micro seconds activates the tracer particles, and the corresponding images are recorded using a high speed CCM camera. Figure 2-11 [115] demonstrates an example of the two consecutive images captured in a PIV experiment. The time delay between two images allows slight displacement of the tracer particles in the second image relative to the first image. Then in *interrogation process*, each of the two images are divided into many small regions that cross correlation analysis between these regions determines the planar displacement of the particles. Dividing

the displacement with the time gap between two images, one can calculate the velocity in each region and construct the 2D velocity field [116].

Feser et al. [116] employed PIV to measure the 2D velocity distribution in the flow channels of interdigitated and serpentine flow channels. They carried out PIV in acrylic plates with 15 cm<sup>2</sup> active area with 5 channels, each having 9×9 mm<sup>2</sup> cross-section. Their setup was scaled up and water was used instead of air, with maintaining geometric and dynamic similarities. The scaled-up system allowed them to use large particles with 20-40 μm size range which simplifies illumination and particle tracking. The PIV measurement helped them to confirm that in interdigitated and single serpentine flow channels, a significant portion of the reactant fluid travels from under rib region.

Yoon et al. [115] performed gas phase PIV in a single straight channel as well as in a serpentine flow field, with two channels having 1:1 channel to rib ratio, with 1 mm channel width. The Reynolds number in their experiments was 70. They suggested that tracer particles with dimensions smaller than 1 μm is needed to accurately follow the stream lines. However, smaller particles require close lens focus to distinguish small particles, which in turn decreases the view field. Small field of view will force researchers to do experiment in a single channel at a time and to work with small Reynolds number (low fluid velocity). Considering these two facts, PIV might not be a suitable method for studying the flow behavior in large number of channels related to each other, nor in channels with very high fluid velocity.

Hecht et al. [117] investigated the convective and diffusive flow transport pattern inside the multi-pass serpentine BPPs of a simplified FC model using PIV and LIF simultaneously (see the following part for LIF). PIV method has mostly been used for liquid phase velocimetry which allows measuring local velocity distribution with high spatial resolutions. Hecht et al. utilized PIV for the liquid phase flow visualization, and LIF for the gas phase, with matching Reynolds number. The combination of LIF and PIV enabled them to separate diffusive and convective transport. To simulate the fluid transport through GDL in real FCs, Hecht et al. [117] put 100 μm gap between channel rib and covering glass. They used 2

$\mu\text{m}$  Rhodamine-B particles for performing the PIV. The results of Hecht et al. [117] showed that part of the gas flow is transported perpendicular to channel structure. Although their experimental method has served as a proof of concept for the applicability of these techniques in FC researches, the more realistic models need to be studied with these techniques to further evaluate the applicability of the method.

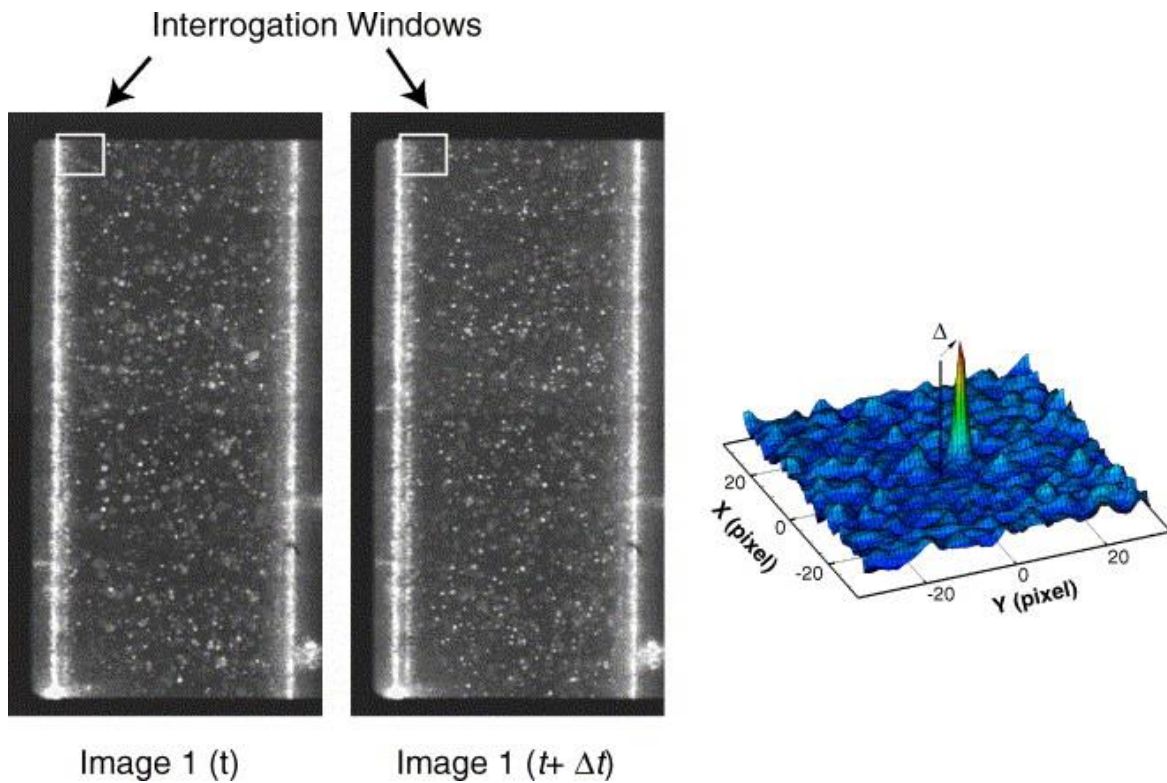


Figure 2-11: Typical images separated by  $\Delta t$ , plus representative interrogation windows and cross-correlation function for interrogation windows in image 1 and image 2.  $\Delta$  in the cross-correlation plot gives the average displacement of the image intensities between images and when divided by  $\Delta t$ , provides a quantitative velocity vector centered at the center of the interrogation window (reprinted from [115] with permission from Elsevier).

## 2.4.2 Laser induced fluorescence (LIF)

In this technique, liquid is circulated through the flow field over a period of time until the flow reaches steady state. Then at a certain time, fluorescent dye is injected in pulses in the upstream, in synchronization with laser pulses and appropriate image acquisition system. The fluorescent dye is capable of being excited with laser beam, allowing us to trace the flow. Sulforhodamine-B is a typical

dye being used for this purpose. Appropriate lenses are required to scatter the laser beam on a desired view field. Furthermore, filters are being applied to construct a good contrast between the dye illumination and background lights. This is a very useful technique for flow visualization in FC applications. However, the setup complexity along with several adjusting steps makes it a challenge to be widely utilized in FC experiments. Especially, when large number of experiments are required, it is preferred to find alternative simpler techniques to perform flow visualization experiments.

Barreras et al. [35] used LIF to study the flow distribution in commercial straight-parallel flow fields. The BPPs consist of 16 channels, each having 3 mm width with 1 mm rib width, with 50 cm<sup>2</sup> active area. In another research by Barreras et al. [118], LIF was used in the same procedure with their previous work [35] to study the fluid dynamic performance in three different anode flow fields. Their flow fields consist of 32 channels of 2mm width with 1 mm ribs, with a total active area of 49 cm<sup>2</sup>.

Barreras et al. [35, 118] suggested that because of the difficulties accompanied by gas flow visualization, performing the flow visualization in liquid phase while maintaining the dynamic similarity could be quite useful to circumvent many challenges. For instance, Barreras et al. [35] mentioned that UV lasers are required to activate the fluorescence property of the typical vapor tracers. Moreover, organic vapors are not compatible with many plastics, and quartz window is needed to seal the BPP.

### 2.4.3 Dye visualization

Dye visualization is similar to LIF, except that regular dye is utilized instead of fluorescent dye, and the colored dye is used to determine the flow front. The setup is simpler since the dye does not need laser activation, and filters, additional exposure and scattering lenses are not required. This deletes the necessity for utilizing special dyes, and synchronizing the laser pulse with dye injection. The regular dye visualization technique is suitable for visualization of the flow in macro scale, e.g. for determining the

flow distribution among channels, while PIV and LIF are mostly suitable for visualizing the flow behavior in micro-scale, e.g. flow profile within a single channel.

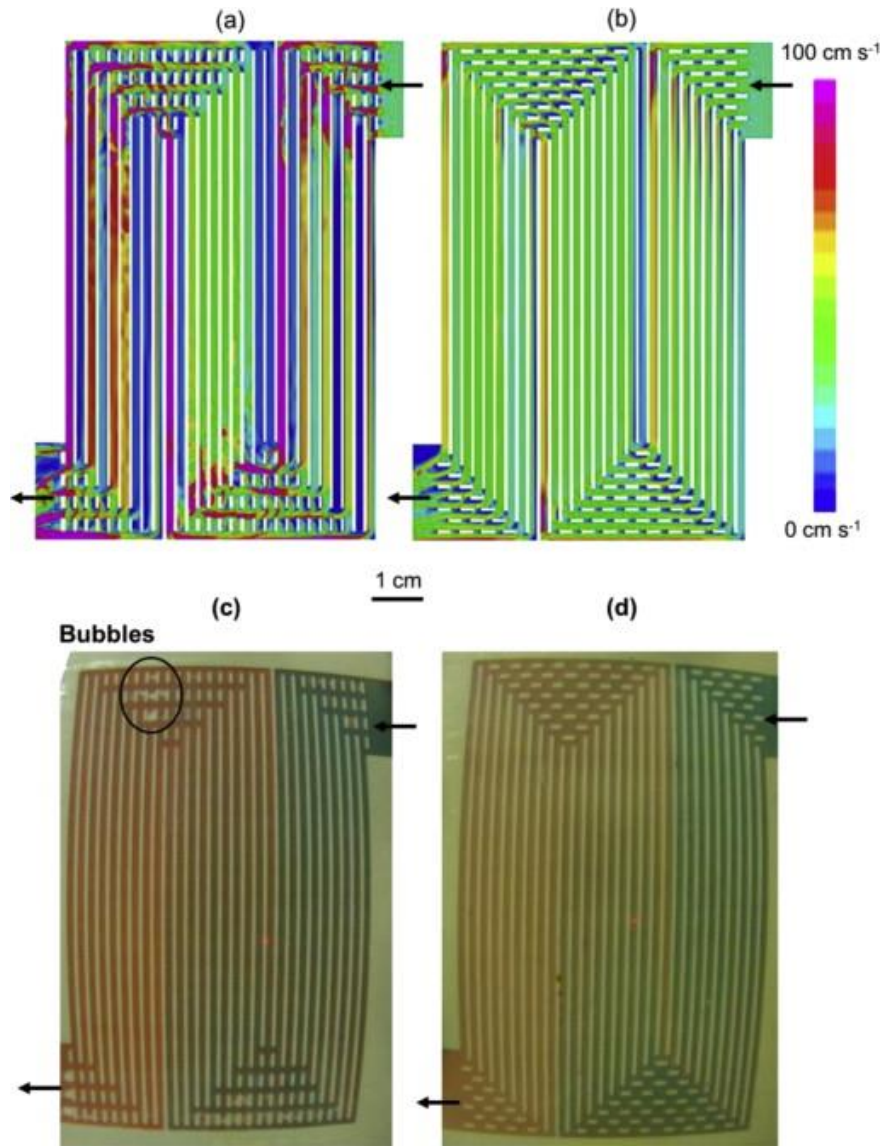


Figure 2-12: Fluid velocity results from the numerical model for (a) CFF with uneven cooling flow and (b) CFF with even cooling flow. The incoming cooling flow rate is  $2.67 \text{ mL s}^{-1}$  from the upper right corner. The CFF with even cooling flow has significantly fewer stagnant channels and more effective mixing regions. Images of dye mixing experiments for (c) CFF with uneven cooling flow after  $\sim 0.4 \text{ s}$  of mixing and (d) CFF of even cooling flow after  $\sim 0.5 \text{ s}$  of mixing. The incoming flow rate of cooling flow with blue dye is  $\sim 2.1 \text{ mL s}^{-1}$ . The scale bar is approximate. (reprinted from [42] with permission from Elsevier.)

Gould et al. [36] used the following method to determine the flow distribution in their cooling flow fields. They ran the red water through channels, and suddenly changed the liquid supply of the pump to

blue water using a three-way valve. Then they took an image of the flow  $\sim 0.5$ s after switching the water supply, as shown in Figure 2-12, and analyzed the image qualitatively. They translated purple color to interpret mixing and concluded that channels with purple color are experiencing faster fluid flow, while channels with red color are having slower flow. Although their method could be quick in getting a qualitative idea of flow distribution, it will be impractical to apply this method for validating numerical results. A detailed image processing and signal analysis is required to quantify flow velocity within each channel. To show the rigor of the simulation work, and to decide how realistic the proposed method will be, one needs to perform quantitative experiments to compare the “data”.

## 2.5 Knowledge gap

Despite the many research works on BPP optimization, they are still not used in FC industry. As we reviewed, numerous research groups have focused on developing PEMFC flow fields with uniform flow and pressure distribution, with low pressure-drop. However, most of these research groups have addressed the problem through numerical simulation, but have not validated simulation results by experimental data. More importantly, most of the ideas proposed for improving the flow field performance either cannot be fabricated, or if fabricated, suffer from various problems that the authors have not taken into account. Hence, there exists a great interest to experimentally validate the simulation results by running flow visualization and pressure-drop experiments over physically fabricated BPPs. A few research groups have attempted to run experiments on flow field channels to lend support to their numerical simulations. However, because of the huge time demand and high cost of the conventional fabrication techniques, and the complexity of flow visualization experiments, most of previous experimental studies have focused on the flow dynamic behavior through flow visualization techniques in commercial or very simple flow fields. The use of over-simplified and non-realistic geometries is far away from state-of-the-art realistic BPPs. The flow fields in the current study are aiming at more complex geometries with small channel dimensions (0.4 mm). Although some of

previous papers have used small channel dimensions ( $<0.5$  mm) [3, 119-122], they have performed experiments in only one or a few channels (e.g. 3 channels), and have not considered the fluid dynamic performance in flow field of realistic number of channels ( $>50$  channels). Not to mention that some numerical models cannot even be manufactured with conventional fabrication techniques.

These facts highlight the necessity for finding new fabrication and manufacturing routes that could enable us to fabricate the complex designs. There is also a great benefit if we can find a RP technique and fast screening experiment method that could enable us to test the design ideas very quickly without the need to numerically simulate them, because numerical simulation is a very challenging and time-demanding task. 3D printing is a new AM technology that has many advantages and has shown many potentials to revolutionize many branches of the science. However, 3D printing technology is not matured enough and its applicability in prototyping BPPs and its ability in 3D printing small state-of-the-art channels is still a question. A few research groups in recent years have utilized 3D printing in FC researches, especially in prototyping BPPs. But those researches have just used 3D printing for prototyping a simple BPP design with relatively large channels, and based on those limited work, they concluded the applicability of 3D printing method for BPPs. In the best case, 3D printing was used for qualitatively validating the simulation data of a basic flow field geometry. We could not find any work that has used 3D printing for prototyping state-of-the-art BPPs with realistic number of channels with  $<0.5$  mm channel size. There is thus a need to determine whether 3D printing is an appropriate technology for fabricating prototypes of the state-of-the-art **real** BPPs. Furthermore, what limitations 3D printing might have for such an application and how reliable the technology is in terms of feature resolution and data accuracy need to be evaluated. Ultimately, which 3D printing technology is most suitable for a specific application should be identified.

One of the other problems of the previously mentioned research works is that simulation and experiment are usually run on a relatively small active area, but automotive applications usually require

high power output, which requires a large active area. Optimizing the flow distribution becomes more challenging when tests need to be carried out over a large active area. Only in the simulation of Lim et al. [38] an active area size in the range meeting the automotive industry requirements was used, although their simulation results have not been validated experimentally.

All of the previous works have focused on just one of the BPP flow fields, either anode, cathode or cooling flow field. To the best of our knowledge, none of the previous works has considered all three flow fields together. FC performance is dependent on the simultaneous performance of anode, cathode and cooling plates. As we discussed previously, and mentioned by Wilkinson et al. [43], even if there exists a flow non-uniformity, taking advantage of this non-uniformity and managing it could be beneficial too.

In terms of flow visualization, not many works have been done to visualize the flow velocity distribution in the BPPs. A few studies have been done by PIV and LIF techniques on very simple channel geometries with large channel sizes. However, many problems arise in flow fields of realistic number of flow channels, with small channel dimensions, which might never be revealed in large channel dimensions. In addition, the mentioned techniques are usually very challenging to work with in which sometimes the work complexity hinders producing acceptable amount of data. The complexity of the mentioned methods also prevents quick evaluation of the BPP models experimentally.

### **2.5.1 Strategies and scope of the present work**

As discussed in chapter 0, the general objective of the current research is to develop flow field designs and to optimize their performance. To develop and modify a design, several steps of trial and error are required to find the optimum value of different parameters such as: channel/rib width, channel aspect ratio, number of channels, channel configuration, channel arrangement etc. To successfully optimize the mentioned parameters, first the validity of simulation results need to be confirmed with experimental data, which requires physical manufacturing of BPPs, and then trial and errors on numerical simulation.

However, the numerical simulation process is both complex and time-consuming which might hinder the development of an optimum flow field design. This highlights the necessity for a fast-screening experimental method which could not only validate the simulation results, but also could be utilized as an alternative to numerical simulation when required.

In the present research, based on the previous suggestions from literature, state-of-the-art flow field design for cathode, anode and water-cooling BPPs will be proposed, which has an active area of 187 cm<sup>2</sup>, with 0.4×0.4 mm<sup>2</sup> cross-section area of flow channels. Numerical simulations will be first performed using COMSOL Multiphysics to assess the design performance, and then flow visualization and pressure-drop experiment will be carried out to validate the simulation results. As mentioned in chapter 0, the specific objective of the present work is to investigate the applicability of 3D printing as a RP technique in fast-screening of proposed flow field designs and in validating the simulation results. Hence, the prototype BPPs will be fabricated using several 3D printing technologies, which allows (1) to experimentally evaluate the fluid dynamic behavior of 3D printed BPPs, in order to validate the simulation results; (2) to compare the suitability of several novel 3D printing technologies in prototyping the flow fields with complex designs and small feature size; and (3) to assess the applicability and limitations of 3D printing in fabricating prototype and real BPPs.

Measured flow velocity distribution and pressure-drops from experiments will be compared with COMSOL results. The following chapter will describe our fabrication techniques and design of the experiments.

## 3 Experimental

In this chapter, we will discuss about the experimental setup, apparatus selection and fabrication methods for running the experiments. We will first discuss about the required experiments and then will talk about the novel methods we have used in the experiment setup.

### 3.1 Required experiments

To perform experiments on BPPs, the first step required is to physically fabricate them. Here we have utilized novel RP techniques to manufacture the fluid flow fields. Prior to running any fluid mechanics experiments, care must be taken toward the dimension accuracy, and the real dimensions should be known after the fabrication. Hence, the first set of experiments is to measure the geometry of the fabricated plates.

As it was discussed in the chapter 1, flow through the GDL depends on the pressure profile in the BPP. However, it should be noted that the uniformity of the flow distribution does not necessarily ensure a homogeneous reactant distribution over the active area. Take as an instance the single serpentine flow field, where the equal amount of flow passes through channels, but the concentration of reactants is non-uniformly distributed over the catalyst layer. The near inlet region with higher pressure forces more reactant into GDL, while outlet region experiences lower concentration of the reactants [118].

Hence, the flow field design target is to achieve **uniform pressure distribution** over the catalyst layer, which in gas phases is equivalent to uniform reactant distribution. However, extracting the pressure profile experimentally is a very challenging task where adding pressure sensors all over the active area would disturb the flow. Only pressure-drop along the flow fields can be measured experimentally. On the other hand, although uniform velocity profile does not ensure uniform reactant concentration, a non-uniform flow distribution will more likely result in non-uniform reactant distribution which would deteriorate the FC performance. Especially in the case of present work, the preliminary simulation

results suggested a near-uniform velocity profile to ensure a uniform pressure distribution. Therefore, it is very important to measure the velocity profile in the flow fields. In the present work, we measure the pressure-drop and velocity distribution over the active area, and then using these parameters we assess the simulation results. If the numerical modelling validated, we can rely on numerical simulation to figure out the pressure distribution over the active area.

### 3.2 BPPs fabrication

CAD of the BPP were made using SOLIDWORKS 2014 x64 Edition. To fabricate the CAD models, SOLIDWORKS files have been converted to STL files, which is the file type known by 3D printers and laser-cutter apparatus. The 327 mm×98 mm×2 mm cathode, anode and water-cooling BPP comprises straight-parallel fluid flow channels with an electrode active area of 186.4 cm<sup>2</sup>, with flow channels which have 0.4 mm×0.4 mm square cross-sectional area. Small depth of the flow channels would decrease the BPP thickness which in turn decrease the FC stack total volume and weight. A solid model of the BPPs is shown in Figure 3-1, within which the fluid flow is being directed toward different straight-parallel channels by inserting baffles in the inlet region of the flow field (transition region), as shown in Figure 3-2. Addition of baffles increases the resistant in certain direction and assists the uniform distribution of the flow.

Single-piece BPPs were fabricated using 3D printing and laser-cutter technologies. It is for the first time that laser-cutter technology is used for the BPP fabrication. It enables us to compare two RP technologies, 3D printing and laser-cutter, together and to provide the future researchers with information on the applicability of each technology. We have utilized two state-of-the-art 3D printing technologies, SLA and Polyjet 3D printing, for 3D printing the BPPs and to compare the technologies together. The reason we chose these two technologies of 3D printing is that they offer the best combination of price and accuracy. Although we could 3D print with higher accuracy in Z-axis using DMLS, the price would be much higher, as discussed in Table 2-1.

The channel cross-section area in the original design is 0.4 mm×0.4 mm. However, due to the minimum feature size recommended for SLA 3D printing by FORECAST 3D Ltd. for SLA 3D printing [123], some of the plates were fabricated with 0.635 mm×0.635 mm channel cross-section.



(a) Cathode.



(b) Water cooling.



(c) Anode.

Figure 3-1: Computer aided design of BPPs.

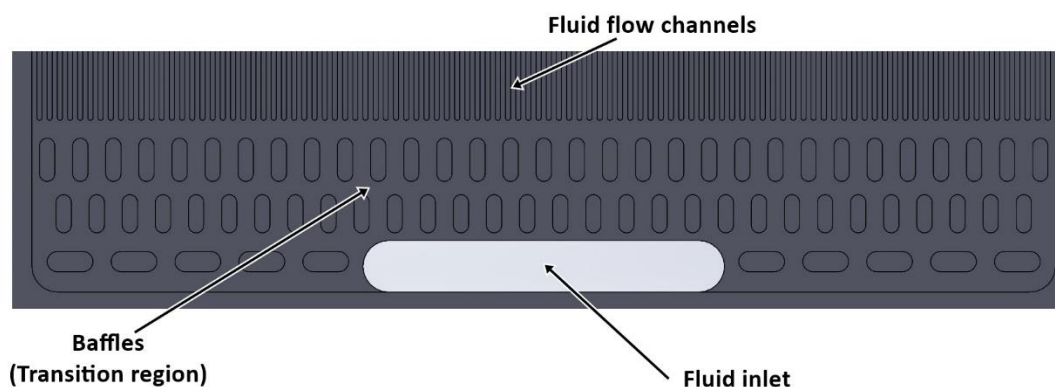


Figure 3-2: Different regions of active area in the cathode BPP.

In addition to the original CNC machined graphite plate, two cathode BPPs with 0.4 mm×0.4 mm cross-section was fabricated using Polyjet and laser-cutter technology (BPP#2,7 from Table 3-1), which enables us to compare these methods together. Based on the preliminary results from Polyjet plates, the fluid crossflow between the channels, as well as the compression and deformation of the flow channels due to the tightening in the transparent cell, were concerns. To eliminate the errors caused by these factors, a novel idea of 3D printing of enclosed channels was proposed. However, neither Polyjet nor powder-based technologies can 3D print such channels. As discussed in detail in section 2.3.1.20, those technologies 3D print hollow parts with support materials which can be removed after fabrication. However, in the case of BPPs in the current experiments, removing support materials from 101 long channels with 0.4×0.4 mm<sup>2</sup> cross-section was impossible. Theoretically, SLA 3D printing can 3D print such enclosed channels, but even SLA 3D printing requires challenging post-fabrication steps. After trial and error 3D printing for more than 6 months on 30 different designs, eventually a cathode BPP with enclosed channels was fabricated. Two cathode BPPs were fabricated using SLA 3D printing technology, to investigate the cross flow between channels, and to compare SLA technology with Polyjet. The two SLA cathode plates were designed identical except that in one of the two plates, a transparent layer was 3D printed on top of the channels to enclose them (BPP#5,6 from Table 3-1). We denote these two

plates as “covered SLA” (BPP#6) and “uncovered SLA” (BPP#5). It is for the first time that such novel enclosed channels are 3D printed, which has lots of promises for future researches. It would increase the similarity between simulation and experiment geometries since enclosed channels ensure that the cross flow between channels as well as the plate deformation under stress are eliminated, which in turn assists researchers to investigate the effect of other parameters rather than geometry. Since the minimum recommended feature size for SLA technology is 0.635 mm, the two SLA cathode plates (BPP#5,6 from Table 3-1) were 3D printed with 0.635 mm×0.635 mm cross-section area. Moreover, to evaluate the SLA ability in 3D printing the features below the minimum recommended size, another cathode plate with 0.4 mm×0.4 mm cross-section was 3D printed with SLA technology (BPP#4 from Table 3-1). The latter cathode plate also enables comparing the geometric accuracy of SLA, laser-cutter and Polyjet together, as well as with that of the real graphite BPP. Due to the preliminary results from cathode plates, anode and water-cooling plates were also fabricated with 0.635 mm×0.635 mm cross-section area using SLA technology with a 3D printed cover on top of the channels (BPP#8,9 from Table 3-1). Two other anode and water-cooling plates were fabricated without a layer on top for cross-section imaging purpose. Table 3-1 and Figure 3-3 summarizes all the prototype BPPs tested in the current research.

For Polyjet 3D printing, Objet Eden 500 in HD mode was used; Resolution = 0.00063” Z, 0.012” XY; Tolerance = ± 0.005” or ± 0.001” whichever is greater; Minimum feature size = 0.012”. For SLA 3D printing, SLA 5000 SOLID IMAGING SYSTEM by 3D Systems Ltd. was used. Its standard dimensional variation is typically within ±0.007” for the first inch and ±0.003” for every inch thereafter; XY resolution= 0.008 - 0.012”; Minimum feature size = 0.025”. Laser-cutting was done by Unlimited Design Ltd. located in Vancouver.

Table 3-1: Different BPPs tested in the current research

BPP #	Technology	BPP type	Number of Channels	Cross-section (mm <sup>2</sup> )	Purpose
1	CNC machining	Cathode	101	0.4×0.4	Reference
2	Polyjet 3D printing	Cathode	101	0.4×0.4	To compare Polyjet with Laser-cutter
3	Polyjet 3D printing	Cathode	64	0.635×0.635	To compare SLA with Polyjet
4	SLA 3D printing	Cathode	101	0.4×0.4	To evaluate SLA capability in small features
5	SLA 3D printing	Cathode	64	0.635×0.635	Uncovered SLA cathode
6	SLA 3D printing	Cathode	64	0.635×0.635	Covered SLA cathode A layer was 3D printed on top of the channels to enclose them
7	Laser-cutter	Cathode	101	0.4×0.4	To introduce a new RP technology
8	SLA 3D printing	Anode	64	0.635×0.635	To compare the flow behavior in anode, cathode and water-cooling BPPs
9	SLA 3D printing	Water-cooling	64	0.635×0.635	To compare the flow behavior in anode, cathode and water-cooling BPPs



Figure 3-3: Prototype BPPs studied in the current research.

### 3.3 Geometry measurement

To measure the channel dimensions of the prototype BPPs, cross-section images of all flow channels of all BPPs are taken. Images are taken using optical coherence tomography (OCT), OCTG-1300 model M003220179 by THORLABS. The dimensions are measured with ImageJ version 1.51k. To investigate the channel cross-section size variation across the BPP, all channels of a BPP are measured. Channel cross-section size of different BPPs are compared to study the accuracy and ability of different prototyping technologies in manufacturing small features.

### 3.4 Transparent cell assembly

The most common technique to observe flow field flow is to use a transparent FC. In the current research, the transparent cell consisted of: one 1" house-made anodized aluminum end plate on top of which components were placed to assemble the transparent cell; a bottom acrylic plate; bipolar plate; a top acrylic plate that comes on top of the BPP to serve as viewing window; and a metal frame to hold the system together. Figure 3-4 and Figure 3-5 show the transparent cell components along with the assembled transparent cell. The transparent cell was assembled by placing the components on the aluminum end plate to clamp the BPP between two ½" thick pieces of acrylic sheet. To provide uniform clamping pressure with minimum bowing, and to visualize the flow, a ½" stainless steel frame with 6 viewing windows was designed. 10 Grade-8, 5/16" bolts were placed around the outside of the BPP through the aluminum end plate and the metal frame, and were tightened in a star pattern in 3 steps. First, the bolts were pre-tightened using 4.5 Nm torque, followed by tightening up to 6.5 Nm, and finally tightening force increased to 9 Nm. The reason 9 Nm was chosen as tightening force is that based on preliminary dye visualization tests, the tightening force below 9Nm results in a gap between top acrylic glass and channel ribs which in turn reduces the pressure-drop along the BPP. However, the tightening force above 9 Nm causes BPP deformation which results in further pressure-drop. Silicon ribs were used under the bars of the metal sheet to provide additional clamping pressure to the center of the flow field.

O-ring was used to seal the edge of the flow field. Since the 3D printed BPPs are susceptible to deformation under clamping pressure, a wide-range micrometer screw gauge is used to measure any possible deformation.

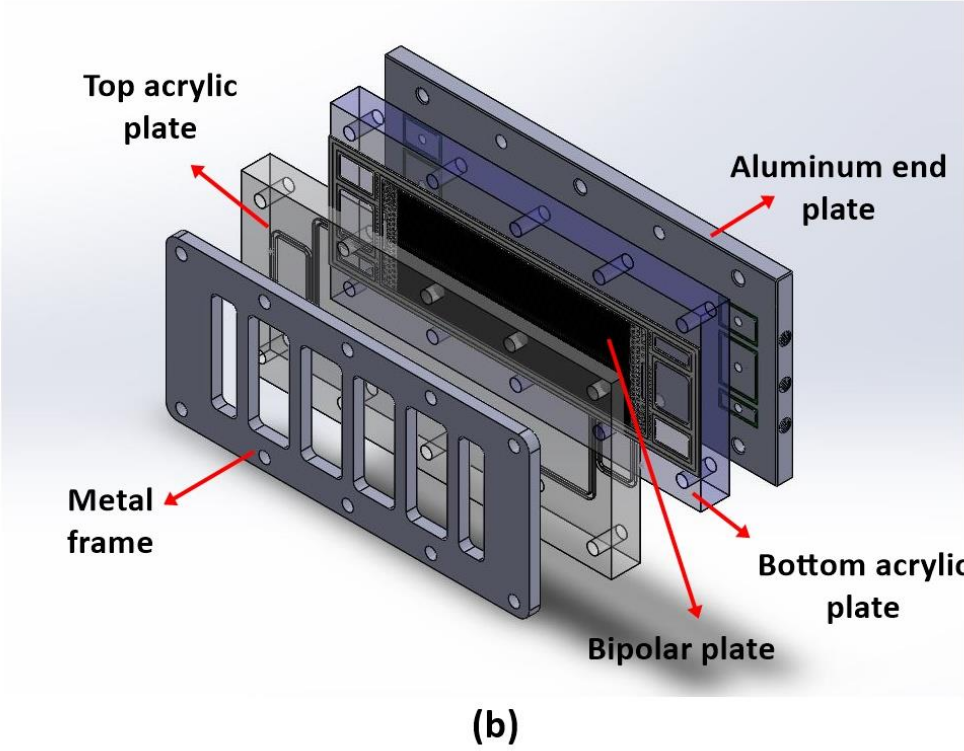
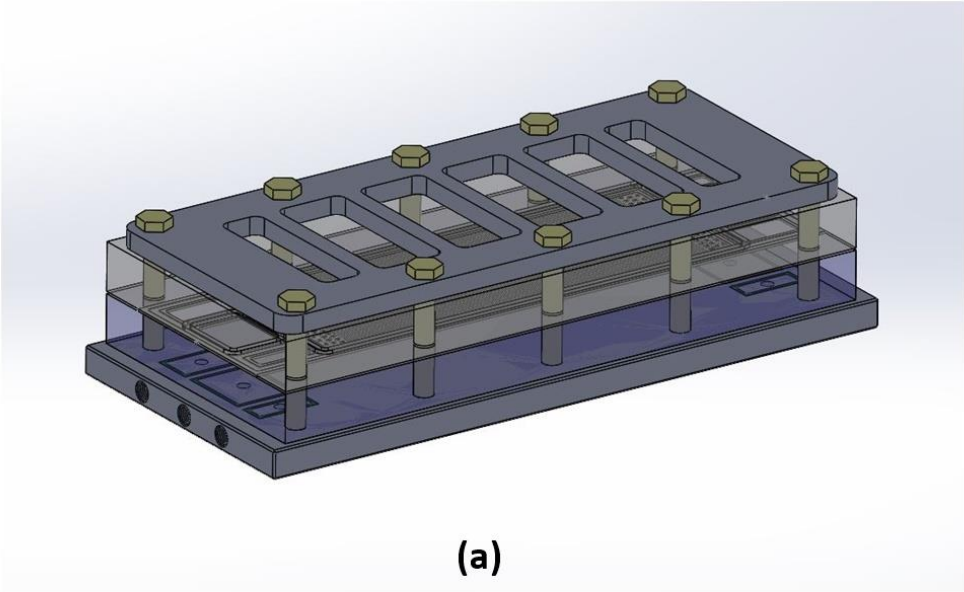


Figure 3-4: Transparent cell schematic; a) Assembled transparent cell; b) Exploded view of transparent cell assembly.

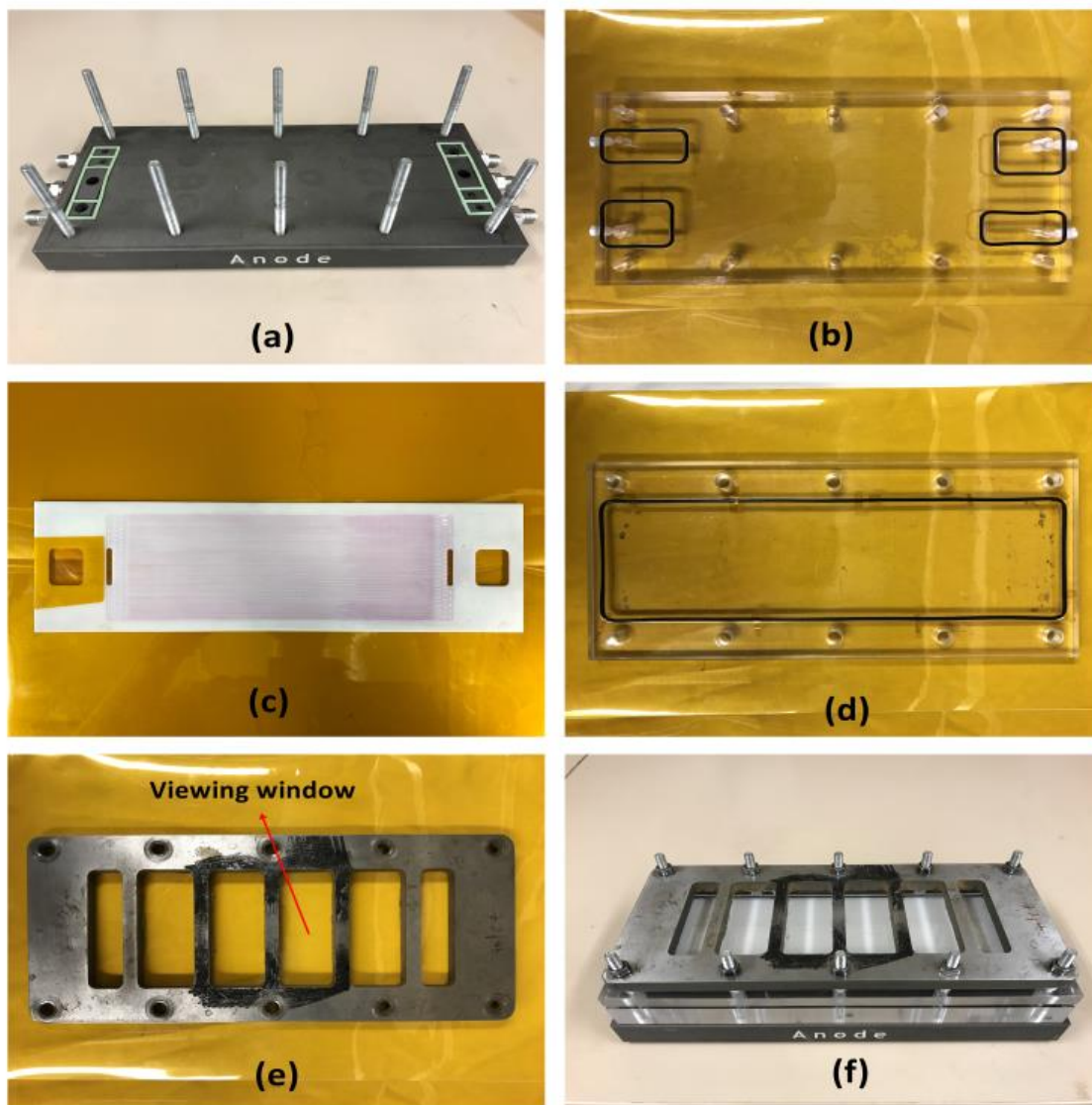


Figure 3-5: Transparent cell components: a) Aluminum end plate; b) Bottom acrylic plate to match the grooves of aluminum end plate with that of BPP; c) Prototype BPP; d) Top acrylic plate to seal the prototype BPP and to enable flow visualization; e) Metal frame to uniformly distribute the tightening force over active area; f) Assembled transparent cell. The components come on top of each other in mentioned order to form the transparent cell assembly.

### 3.5 Flow rate measurement

A 10"-long linear rotameter type 6A 1110 by INSTRUMENT CANADA, which shows the flow rate as a percentage of the maximum measurable flow, was used for measuring the flow rate. The maximum flow

could be measured with this rotameter is 700 ml/min. The pump driver controller combined with manual flow measurement was used for higher flow rates.

Due to the high inaccuracy (5%) accompanied with the rotameter, the rotameter was calibrated using manual flow measurement. At each flow rate, the flow rate shown by rotameter was recorded and then the deaerated water was collected for 10 minutes for measuring the precise flow rate. The “actual flow” versus “rotameter percentage” was plotted as shown in Figure 3-6, which is a calibration graph for acquiring the precise flow rate at each percentage. The precision of flow measurement in this method is high and error is smaller than 2% of the measured flow.

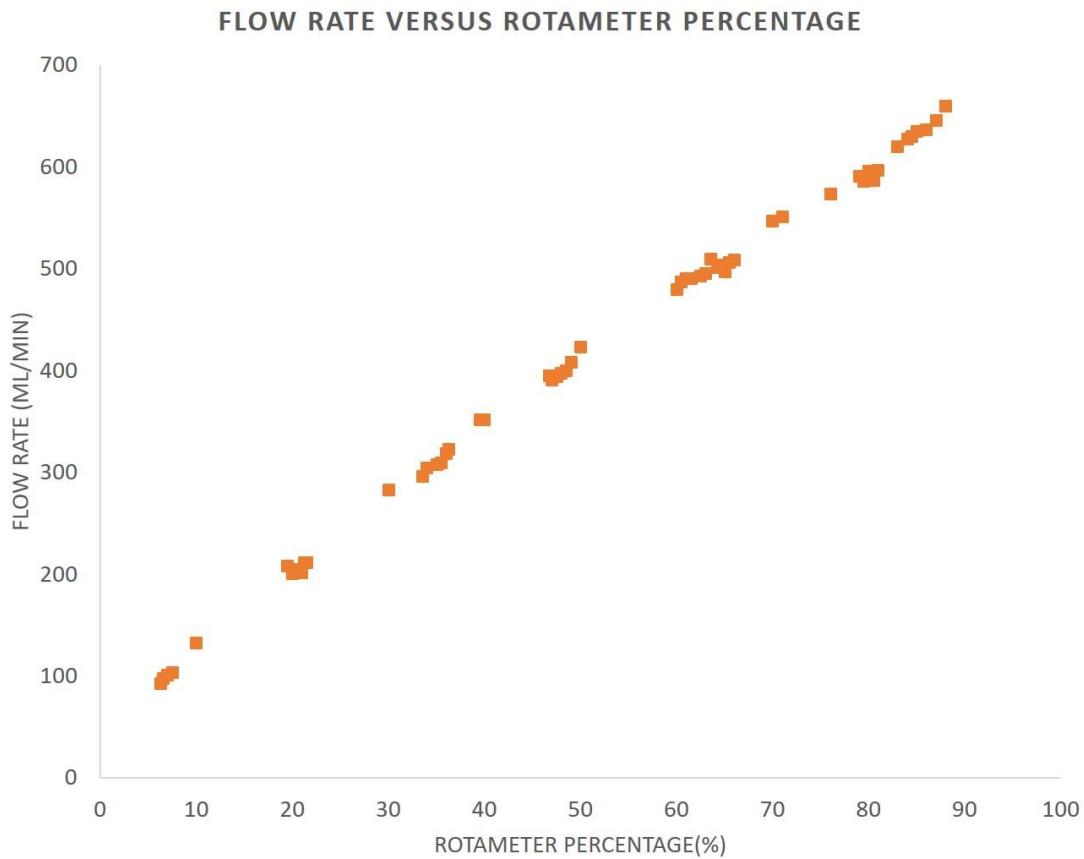


Figure 3-6: Actual flow rate versus rotameter percentage graph.

### 3.6 Pumping system

A COLE-PARMER 7553-20 pump drive, with COLE-PARMER 7518-00 pump head, with COLE-PARMER 7553-71 speed controller, with “C-Flex tubing (50 A), L/S 15,25ft “tube was used. A house-made pulse dampener was used to alleviate the flow fluctuation at small flow rates. The pumping system is discussed in more detail in Appendix .

### 3.7 Ensuring dynamic similarity

As it was discussed in Chapter 2, flow visualization in gas phase is accompanied with lots of challenges which directs the researchers to visualize the fluid flow in liquid phase. In the current research, we conducted the flow distribution and pressure-drop experiments in liquid phase, with same Reynolds number as gas phase flow to maintain the dynamic similarity. The dimensionless Reynolds number for a fluid flowing through a channel equals  $\frac{\rho U D_h}{\mu}$ , where  $\rho$  is the fluid density in  $\text{kg/m}^3$ ,  $U$  is the fluid mean velocity in  $\text{m/s}$ ,  $D_h$  is the channel hydraulic diameter in  $\text{m}$ , and  $\mu$  is the fluid absolute viscosity in  $\text{Pa}\cdot\text{s}$ .

#### 3.7.1 Determination of gas flow rates in anode and cathode BPPs

For the target 30kw PEMFC stack, the following conditions are considered: temperature ( $T_{\text{avg}}$ )= 80°C, relative humidity (RH) = 100%, air stoichiometry ( $\lambda_{\text{air}}$ ) =1.8, hydrogen stoichiometry ( $\lambda_{\text{H}_2}$ ) =1.3, total pressure ( $P_{\text{total}}$ )=170.25 kpa. The main physical properties of hydrogen, air and water at atmospheric pressure (1atm) and typical PEMFC working temperature of 80°C are provided in the Table 3-2 [125,126,35].

Table 3-2: Thermodynamic properties of fluids consumed in the current research.

Fluid	Temperature (°C)	Kinematic Viscosity $\nu$ (m <sup>2</sup> /s)	Absolute Viscosity $\mu$ (Pa s)	Density $\rho$ (kg/m <sup>3</sup> )	Molar mass (g/mol)
Air	80	$2.086 \times 10^{-5}$	$2.065 \times 10^{-5}$	0.9900	28.970
Hydrogen	80	$1.558 \times 10^{-4}$	$1.050 \times 10^{-5}$	0.0674	2.015
Water	20	$1.007 \times 10^{-6}$	$1.005 \times 10^{-3}$	998.2000	18.010
Glycerin	20	$6.150 \times 10^{-4}$	0.7601	1236	NA

Since the inlet pressure is greater than the atmospheric pressure, Table 3-3 represents the fluid properties at inlet condition. We assume, however, that change in pressure is not changing the water and glycerin properties, nor air and hydrogen absolute viscosity.

Table 3-3: Air and hydrogen properties at BPP inlet condition.

Fluid	Temperature (°C)	Pressure (kpa)	Kinematic Viscosity $\nu$ (m <sup>2</sup> /s)	Absolute Viscosity $\mu$ (Pa s)	Density $\rho$ (kg/m <sup>3</sup> )
Air	80	170.25	$1.223 \times 10^{-5}$	$2.07 \times 10^{-5}$	1.682
Hydrogen	80	170.25	$9.267 \times 10^{-5}$	$1.05 \times 10^{-5}$	0.113

In a PEMFC stack, the reactant consumption rate can be calculated using eq.(9) and eq.(10) [127], where

$\dot{n}_{air}^o$  and  $\dot{n}_{H_2}^o$  are the molar air and hydrogen consumption rates in mol/s,  $i$  is the current density in A/cm<sup>2</sup>, A is the BPP active area in cm<sup>2</sup>, N is the total number of cells in the stack,  $\lambda_{air}$  and  $\lambda_{H_2}$  are air

and hydrogen stoichiometry,  $F$  is the Faraday's constant and equals 96,485 sA/mol,  $y_{O_2}$  is the oxygen fraction in air and equals 0.2095.

$$n_{air}^o = \lambda_{air} \frac{iAN}{4Fy_{O_2}} \quad (9)$$

$$n_{H_2}^o = \lambda_{H_2} \frac{iAN}{2F} \quad (10)$$

To obtain the 30KW power, considering the minimum degradation, the current density ( $i$ ) of  $1 \text{ A/cm}^2$  is considered. With substituting the mentioned values in eq.(9) and eq.(10), the values of  $4.273 \times 10^{-3} \text{ mol/s}$  and  $1.293 \times 10^{-3} \text{ mol/s}$  are obtained for the air and hydrogen molar consumption rates, respectively. Eq.(11) can be used to convert molar reactant consumption rate to reactant volumetric flow rate, where  $M$  is the fluid molar mass in  $kg/mol$ , and  $\rho$  is the fluid density in  $kg/m^3$ . By substituting the hydrogen and air properties at inlet condition from Table 3-3 in eq. (11), the values of 0.0736 lit/s and 0.0230 lit/s are obtained for the air and hydrogen volumetric flow rates, respectively.

$$Q = \frac{nM}{\rho} \quad (11)$$

### 3.7.2 Determination of liquid flow rates in anode and cathode BPPs

To replace the gas flow with water flow, the dynamic similarity should be maintained between two systems, which is possible through maintaining the equality between Reynolds numbers. Therefore, the Reynolds number of air flow at inlet condition through cathode channels should be equal to that of water flow through cathode channels, and similarly the Reynolds number of hydrogen flow through anode channels at inlet condition should be equal to the that of water flow through anode BPP. Using eq.(12), if the same plate is used, eq.(13) results from simple calculation.

$$\frac{\rho_1 U_1 D_{h1}}{\mu_1} = \frac{\rho_2 U_2 D_{h2}}{\mu_2} \quad (12)$$

$$Q_{water} = \frac{V_{water}}{V_{air}} Q_{air} \quad (13)$$

Substituting the air and hydrogen volumetric flow rates in eq.(13) results in values of 363 ml/min and 15 ml/min for water flow rate through cathode and anode BPPs, respectively. Please note that the channel hydraulic diameter is assumed to be 0.4 mm in these calculations. In BPPs with 0.635 mm dimension, however, the channel dimension difference should be considered. The volumetric flow rate in the parallel identical channels can be calculated using eq.(14), where  $Q$  is the volumetric flow rate in  $m^3 / s$ ,  $n$  is the number of channels,  $A$  is the single channel cross-section area in  $m^2$ , and  $\bar{U}$  is the average mean fluid velocity inside each channel in  $m / s$ .

$$Q = nA\bar{U} \quad (14)$$

To maintain the dynamic similarity between two BPPs with  $n_1$  and  $n_2$  channels, with channel dimensions  $D_1$  and  $D_2$ , using the same liquid, the eq.(15) should be satisfied. Using the values of  $n_1 = 101$  and  $n_2 = 64$  channels, with channel dimensions of  $D_1 = 0.4mm$  and  $D_2 = 0.635mm$ , results in  $Q_2 = 1.006Q_1$ , which highlights that approximately similar water flow rates should be used in BPPs with 0.4 mm and 0.635 mm hydraulic diameter.

$$Q_2 = \frac{n_2}{n_1} \frac{D_2}{D_1} Q_1 \quad (15)$$

### 3.7.2.1 Determination of liquid flow rate in cathode BPP

Above calculations suggest that to maintain the dynamic similarity, water flow rate of 363 ml/min is required for cathode BPP experiments. The value is also scaled up and down to investigate the system capability in higher and lower flow rates.

Since in cathode BPPs with 0.4 mm cross-section, the maximum pressure-drop that could be measured by pressure sensor was occurring in around 650 ml/min of water, the value of 650 ml/min is used as the maximum flow for both velocity distribution and pressure-drop experiments. Moreover, the value of 150 ml/min which is almost half of the 363 ml/min, is used as scaled down flow for the velocity distribution experiments in cathode plates. However, in cathode BPPs with 0.635 mm dimension, the maximum pump ability, 1300 ml/min, is used as the above limit of velocity distribution experiments, and half as well as 1/8 of 1300 ml/min are used as two other flow rates. In pressure-drop experiments, the flow rates are varied from minimum pump ability up to maximum pressure sensor ability.

### 3.7.2.2 Determination of liquid flow rate in anode BPP

For anode experiments, the calculated value of 15 ml/min for water flow not only is below the pump ability, but also the liquid flow will be largely disturbed by dye injection. Based on suggestion of Barreras et al. [35], a mixture of water and glycerin is used to increase the liquid kinematic viscosity to overcome this problem. The mixture composition can be calculated using the methodology described in [125] applying the following equations:

$$v_{mixture} = \frac{\mu_{water}^{X_{water}} \mu_{glycerin}^{X_{glycerin}}}{\rho_{mixture}} \quad (16)$$

$$\rho_{mixture} = X_{water}\rho_{water} + X_{glycerin}\rho_{glycerin} \quad (17)$$

$$X_{liquid} = \frac{V_{liquid}}{V_{mixture}} \quad (18)$$

Where  $X_{liquid}$  represents the volumetric liquid fraction in the mixture, and  $V$  represents the volume.

Using eq.(13), the volumetric flow rate is directly proportional to the fluid kinematic viscosity. Therefore,

using  $v_{mix} = 20v_{wat}$  would result in liquid volumetric flow rate of  $Q_{mix} = 20Q_{wat} = 300ml / min$ , which

enables running the experiments in liquid phase in anode plate as well as cathode plate. Using the value

of  $X_{glyc} = 0.47$  and  $X_{water} = 0.53$  would result in a mixture with such kinematic viscosity. Considering these, the anode velocity experiments are carried out in 150, 300, 600 ml/min of water-glycerin mixture.

### 3.7.3 Determination of flow rate in water-cooling BPP

In PEMFCs, the cooling water consumption rate can be calculated with setting eq.(19) equal to eq.(20) [127], where  $\dot{Q}$  is the heat production rate in  $J/s$  (Watt),  $V_{oc}$  is the open circuit voltage of cell and equals 1.25 volt for PEMFCs,  $V_a$  is the actual cell voltage and equals 0.6 volt in the current stack,  $I$  is the total current output of a single cell in Amps,  $\dot{m}$  is the water mass flow rate in  $kg/s$ ,  $C_p$  is the specific heat capacity of water and equals 4,184  $J/kgK$ , and  $T_{in}$  and  $T_{out}$  are the inlet and outlet water temperatures in kelvin. Setting eqs. (19) and (20) equal results in eq.(21), which can be used to calculate the water mass consumption rate.

$$\dot{Q} = (V_{oc} - V_a)I \quad (19)$$

$$\dot{Q} = \dot{m} C_p (T_{in} - T_{out}) \quad (20)$$

$$\dot{m} = \frac{(V_{oc} - V_a)I}{C_p (T_{in} - T_{out})} \quad (21)$$

Using the values of  $T_{in} = 70^\circ C$  and  $T_{out} = 85^\circ C$ , the value of  $\dot{m} = 0.002095 kg/s$ , which is equivalent to  $Q_{wat} = 125 ml/min$ , is obtained for the water flow rate. Using a mixture of 13% glycerin and 87% water in velocity experiments in water-cooling BPPs, the  $Q_{wat} = 125 ml/min$  would be equivalent to  $Q_{mix} = 300 ml/min$  in terms of Reynolds similarity. The velocity experiments are carried out in 150, 300, 600 ml/min of water-glycerin mixture in water-cooling BPPs. Although the value of mixture flow rate is same in velocity experiments of both anode and water-cooling BPPs, the

composition of the water-glycerin mixture is different. The pressure-drop experiments in anode and water-cooling BPPs are done using pure water same as cathode plates. These bring the opportunity for further performance comparison of anode and water-cooling plates. Table 3-4 summarizes the fluid flow rates used for flow visualization experiments in different BPPs.

Table 3-4: Summary of fluid type and flow rates applied in the experiments of current research.

BPP type	Hydraulic Diameter (mm)	Velocity distribution experiments					Pressure-drop experiments
		Fluid composition	Flow rates (ml/min)	Reynolds number	Flow regime	Current density (A/cm <sup>2</sup> )	Fluid composition
Cathode	0.4	$X_{\text{wat}}=1, X_{\text{gly}}=0$	Q1:150 Q2:363 Q3:650	Re1=62 Re2=149 Re3=266	Laminar	1	$X_{\text{wat}}=1, X_{\text{gly}}=0$
Cathode	0.635	$X_{\text{wat}}=1, X_{\text{gly}}=0$	Q1:150 Q2:600 Q3:1300	Re1=61 Re2=245 Re3=529	Laminar	1	$X_{\text{wat}}=1, X_{\text{gly}}=0$
Anode	0.635	$X_{\text{wat}}=0.53, X_{\text{gly}}=0.47$	Q1:150 Q2:300 Q3:600	Re1=3 Re2=6 Re3=12	Laminar	1	$X_{\text{wat}}=1, X_{\text{gly}}=0$
Water-cooling	0.635	$X_{\text{wat}}=0.87, X_{\text{gly}}=0.13$	Q1:150 Q2:300 Q3:600	Re1=26 Re2=53 Re3=106	Laminar	1	$X_{\text{wat}}=1, X_{\text{gly}}=0$

### 3.8 Pressure-drop measurement

To measure the pressure-drop, the PX750-150DI differential pressure transmitter by OMEGA LTD. is used, which can measure the differential pressure-drop in 0"-150" H<sub>2</sub>O range by 0.25% span accuracy.

The pressure sensor translates the 0"-150" H<sub>2</sub>O pressure-drop linearly to 4-20 mA current output, which is then converted linearly to 1-5 VDC using a house made amp-to-volt convertor. The voltage output is then converted to digital voltage input of the computer using a Labjack U3-HV data acquisition (DAQ) device.

The pressure-drop measurement was carried out in different flow rates in 60-1500 ml/min range, from minimum pump ability up to maximum pressure sensor ability. The pressure-drop for each BPP was measured in 5 sets, each set at two approaches: ascending and descending flow rate, each approach at least at 8 different flow rates. Hence, each data point is the average of at least 10 measurements. The 8 different flow rates for measuring the pressure-drop was selected based on the relevant stoichiometry for each BPP. Although the system gets steady state very fast, the flow was circulated in the system for at least 10 min before recording the pressure-drop. The ascending and descending approaches are selected to figure out if there exist any pressure-drop hysteresis in the single-phase flow.

### 3.9 Flow visualization

The flow visualization experiment has been carried out in different BPPs with loading them into the transparent cell. The deaerated water was circulated in BPPs inside the transparent cell for 5 min to stabilize the flow in stationary condition. After this time, dye was pulse injected in synchronization with the image acquisition. Flow was visualized by tracking the evolution of the dyed fluid front. For each flow field plate, the flow distribution was tested at least at 3 different flow rates as mentioned in Table 3-4 , and each flow-rate was tested 3 times. The following discusses each step of flow visualization experiment in detail.

#### 3.9.1 Dye injection

As a useful dye injection strategy, Barreras et al [35] suggested the dye injection location to be 40×diameter in the upstream before the channel inlet in 45° angle. We have used their suggestion for

the location of dye injection. However, the 15° angle has been used between the dye injecting tube and the main stream tube. The dye injection system is made of a 1ml syringe connected with a 1/16" ID tube to the main stream. The dye was pulse injected and the dye volume was chosen small enough to not disturb the flow stream and not to be invasive. For low flow rates (<150 ml/min), 0.5 ml black dye is used, and for high flow rates (>150 ml), 0.7 ml dye is used.

Different dyes were tested to visualize the flow front. The dyes were selected based on the criteria of low diffusivity, low toxicity, non-reactivity and high contrast. Potassium permanganate, sodium fluorescein activated with UV light, and black dye named Ebest Black AR3 provided by European OGD LTD. were examined. Potassium permanganate was reactive and changed the color of the 3D printed plates to brown. Sodium fluorescent did not provide enough light intensity and hindered us from visualizing multiple channels simultaneously. The Ebest Black AR3 demonstrated non-reactivity and high contrast and was used for the flow visualization experiments in this study. To investigate the dye diffusivity, the dye was injected into the flow channels with stagnant water, and the time for dye to travel the entire channel was measured. The measured time was greater than 1 min, which is significantly greater than the time required for the dye to travel the channel when water flows through those flow channels (< 3 seconds). The diffusion-induced dispersion of the selected dye was therefore neglected in the data analysis.

### 3.9.2 Image capturing

A high-speed camera model MS70KDMG2 by MEGA SPEED with a resolution of 504×504 pixels, with a 55 mm TELECENTRIC lens was placed perpendicular to the BPPs for image acquisition. The camera can capture images up to 4,500 frames per second (fps), and it has the capacity for storing 16,000 frames. Therefore, if recording with e.g. 4,000 fps, capturing can be done for maximum 4 seconds. Images have been recorded for a field of view of 87 mm×87 mm with a spatial resolution of 0.1732 mm/pixel. To illuminate the view field, a large light source was used as shown in Figure 3-7. When capturing images

with high frame rate, the regular light sources show intensity fluctuations which adversely affects the experiments. Hence, it is important to utilize a light source with constant lightening, that the mentioned light source successfully provided the plate with non-variant-intensity lightening. To distribute the light uniformly over the flow field, two house-made light diffuser sheets located consecutively 5 cm,10 cm after the light source, as shown in Figure 3-7. Figure 3-8 and Figure 3-9 depicts the whole setup used for this research.

The flow visualization technique in our proposed research is simpler than the one performed by Barreras et al. [35], without the use of laser setup, scattering lenses and fluorescent dye. Furthermore, in contrast to the work by Barreras et al. [35], we have utilized image processing and signal analysis techniques to determine the velocity in a very complex geometry with much smaller channel size, which will be discussed now in more detail.



*Figure 3-7: lightening system applied for uniform lightening with constant light intensity.*

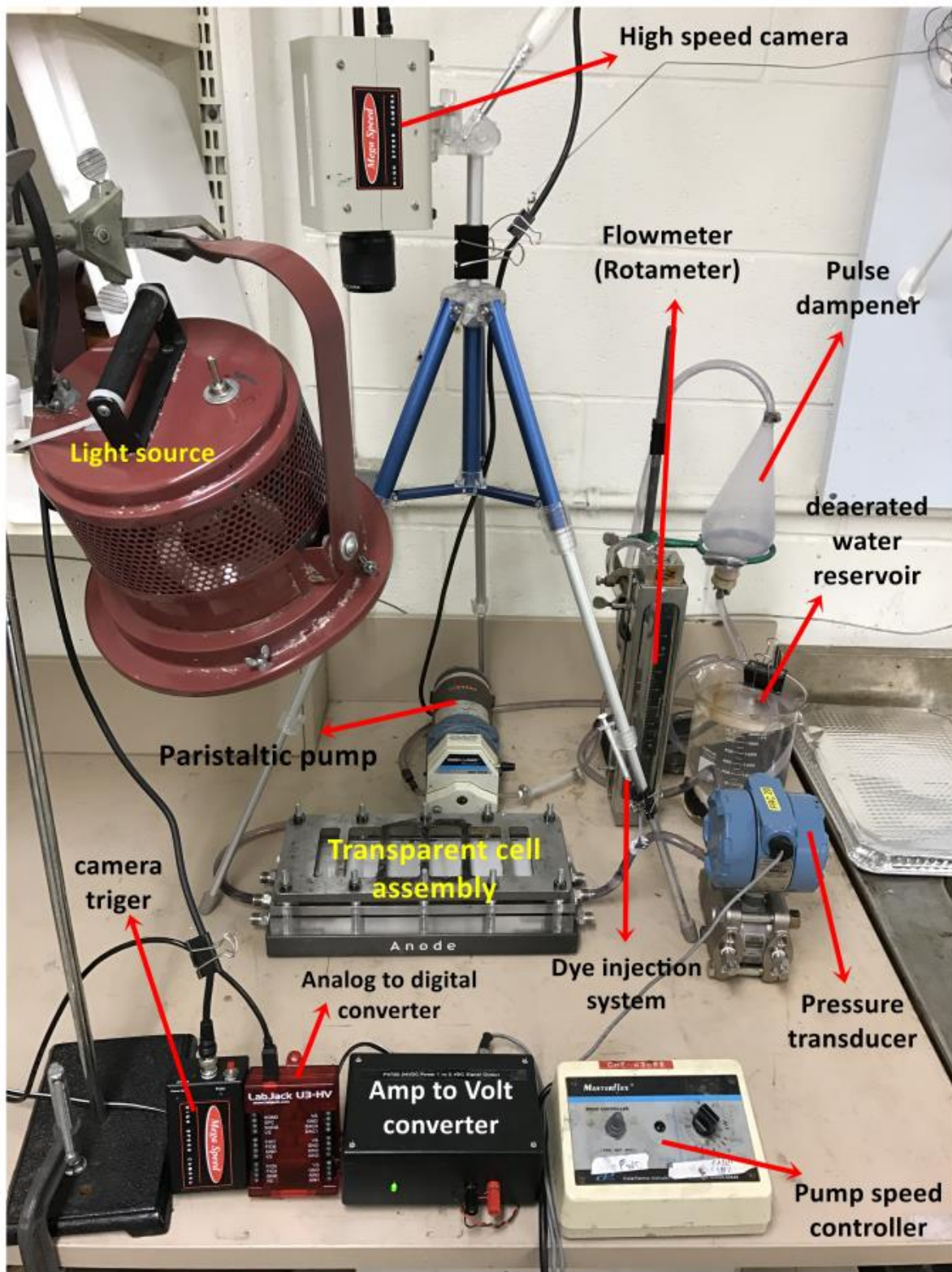


Figure 3-8: The setup applied for flow visualization and pressure-drop measurement in BPPs in the current research.

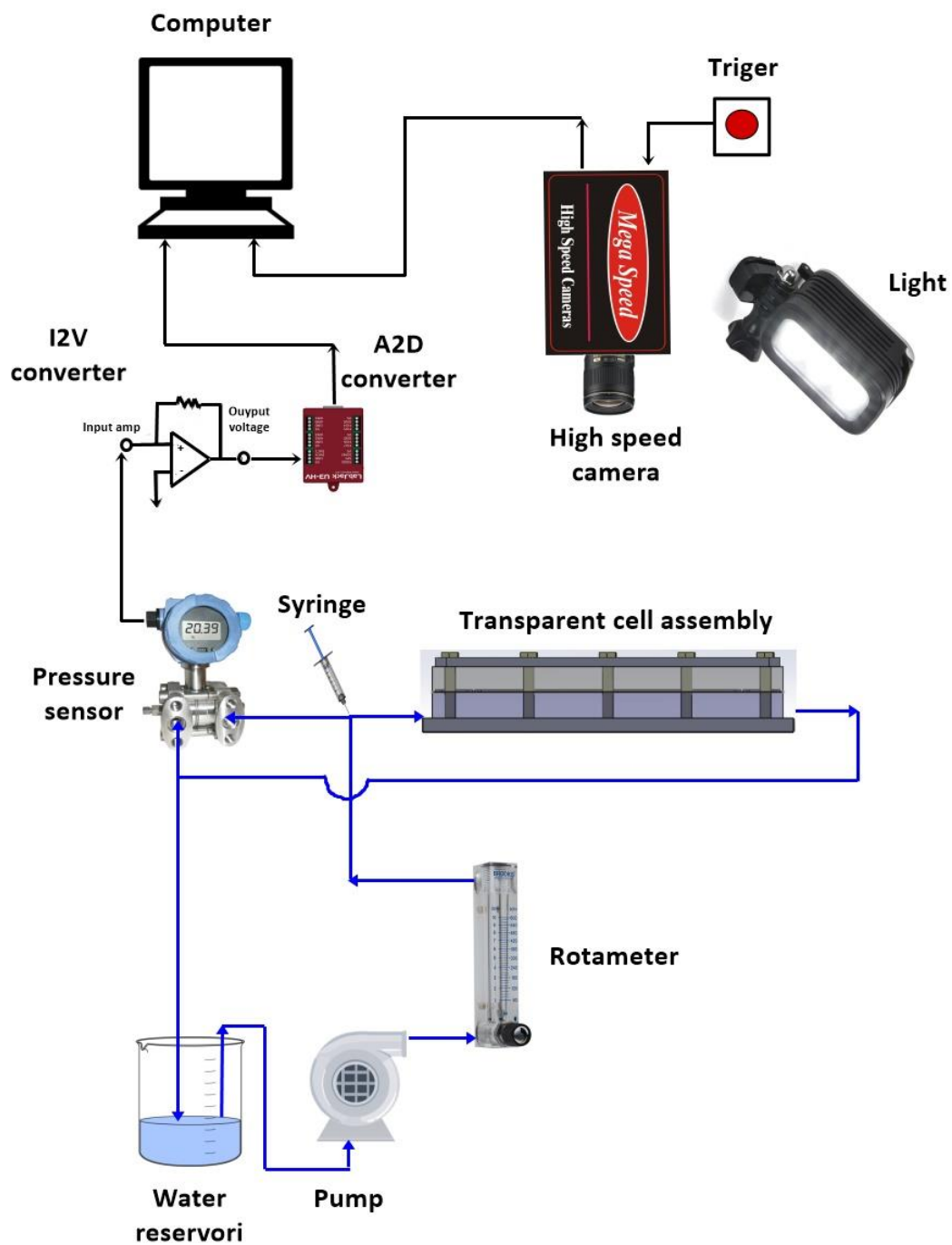


Figure 3-9: Schematic of the setup applied for flow visualization and pressure-drop measurement in BPPs in the current research.

### 3.9.3 Image processing and signal analysis

After the tracer dye was injected in the deaerated water flow, image capturing was immediately started and 16,000 images were taken of the dyed fluid evolution. The velocity distribution between the flow channels has been measured by tracking the evolution of the dyed liquid, as shown in Figure 3-10, and analyzing the captured images with the following method.

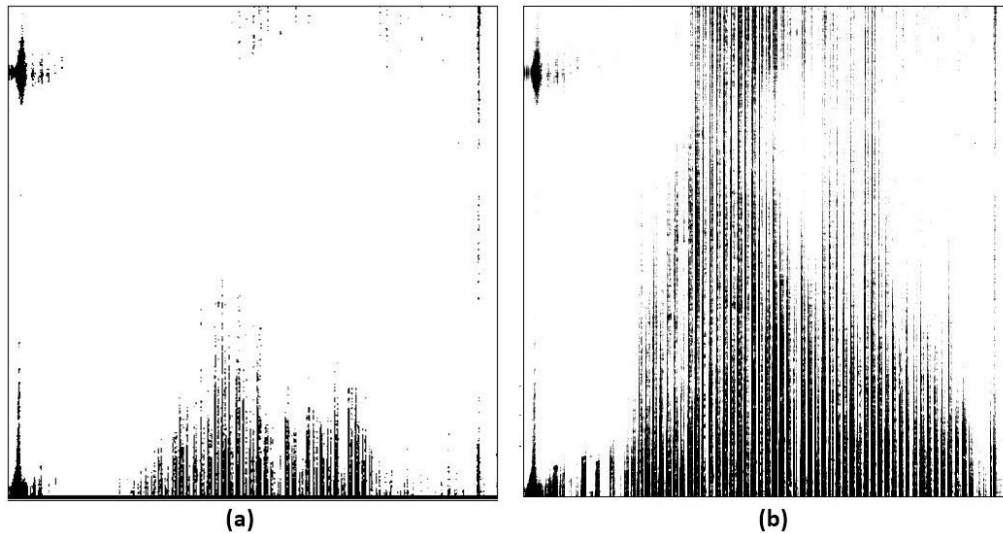
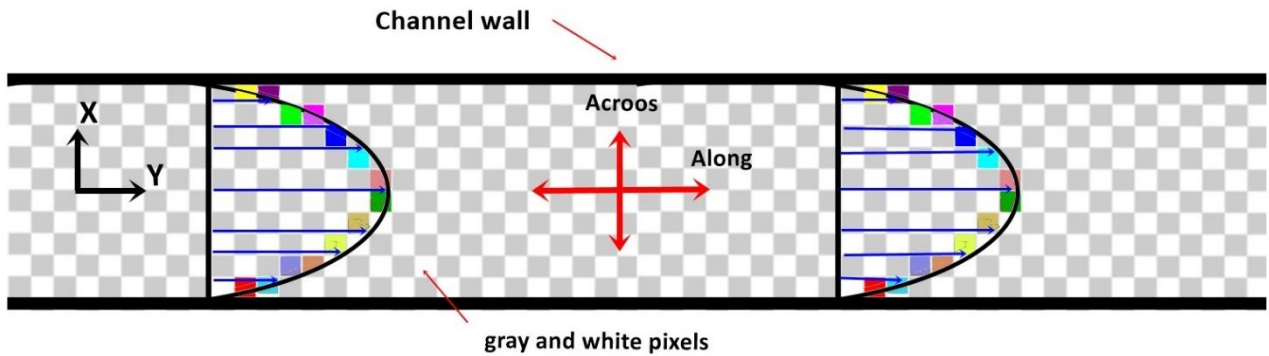


Figure 3-10: Dye evolution in SLA 3D printed cathode flow field. a)  $t=600\text{ms}$ ; b)  $t=6800\text{ms}$ .

A MATLAB R2015a code, which is shown in Appendix A, is developed for extracting the velocity distribution profile among the flow channels. The code reads and analyzes all the 16,000 images, each image consists  $504 \times 504$  pixels. For calculating the fluid velocity in each channel, corresponding pairs of pixels are selected across the channels, as shown in Figure 3-11. The corresponding pairs of pixels within each channel refer to pixels which are in the same distance from the channel wall (Same X-coordinate if the plate is exactly vertical). The corresponding pair of pixels are identically colored in Figure 3-11. The vertical distance between two corresponding pixels of each pair is known with *reading* the images in MATLAB. The idea for measuring the required time for the dye to travel from one pixel to another one, e.g. from the yellow pixel in left hand side to yellow pixel in the right-hand side in Figure 3-11, is based on the fact that when the dye enters a certain pixel, the intensity of that pixel is being

decreased, since black dye has lower intensity than deaerated water. Therefore, the plot of Intensity-Frame number is expected to have a sharp valley since the intensity is constant until the dye enters to that certain pixel, and then suddenly decreases followed by a gradual increase as the dye goes out. Figure 3-12 demonstrates the intensity versus frame number for two corresponding pixels within a random channel of an SLA 3D printed channel with 0.635 mm width. The lag between blue and red graphs in Figure 3-12 is attributed to the time which takes for the dye to travel from one pixel to another pixel. This frame lag is calculated using cross-correlation analysis in MATLAB and is converted to time by the knowledge of frame rate. The velocity is then calculated by dividing the vertical distance between two pixels by the calculated time from cross-correlation analysis.



*Figure 3-11: Schematic of the velocity measurement inside a flow channel. Since it takes some time for dye to travel from first yellow pixel on the left-hand side to the second yellow pixel on the right-hand side, the plot of intensity versus frame number for these two corresponding pixels would have a lag. Cross correlation of intensity versus frame number would inform us about the magnitude of this lag which can be translated to time with the knowledge of frame rate.*

At each channel width (X-coordinate), at least 10 pairs of corresponding pixels with different heights (Y-coordinates) was selected, as shown in Figure 3-11, and the velocity of the flow streamline at that certain width (X-coordinate) was obtained with taking average of all the velocities calculated at that certain X-coordinate. Then at each channel, velocities at different channel width (X-coordinate) was

averaged to calculate the mean channel velocity. Therefore, the reported velocity at each experiment for each channel is the average of 10×number of pixels across the channel, which varies based on the channel width and field of view.

The frame rate was manipulated based on the flow rate. If the fluid flow rate of 1400 ml/min is used, the fastest fluid velocity will be in the channels of the BPPs with 0.4 mm×0.4 mm cross-section. The average mean velocity in the flow channels of a BPP with identical channels can be calculated from eq.(22), where  $Q$  is the total flow rate in ml/min,  $A$  is the cross-section of a single flow channel in mm<sup>2</sup>,  $n$  is number of channels,  $U$  is the mean fluid velocity inside a channel in mm/s, and  $\bar{U}$  is the average mean velocity of all the flow channels in mm/s. Please note that “mean” velocity is used to denote the mean velocity inside one channel, while “average” refers to average velocities of all the flow channels which here we call “average mean velocity”.

$$Q = 0.06nA\bar{U} \quad (22)$$

Using eq.(22), the average mean velocity inside the flow channels of a BPP with 101 flow channels and 0.4 mm×0.4 mm cross-section, with 1400 ml/min flow rate would be 1.443 m/s. The preliminary simulation results demonstrated that the highest mean velocity inside the flow channels is not more than 2 times the average mean velocity. Therefore, in all the velocity measurement experiments the mean velocity is smaller than 2.164 (=1.443×1.5) m/s. Correspondingly, 4,000 fps was chosen for most of the velocity profile experiments. Using such a frame rate, the uncertainty in the velocity measurement can be derived using eq.(23), where  $U$  is the mean velocity inside the flow channel,  $x$  is the distance travelled by the dye frontier, and  $t$  is the time needed for travelling distance  $x$ .

$$dU = \frac{1}{t} dx - \frac{x}{t^2} dt \quad (23)$$

$dt$  is the uncertainty in time, which with 4,000 fps equals  $\frac{1}{4000} = 2.5 * 10^{-4} s$ .  $dx$  is the pixel size

which is 0.1732 mm/pixel. Substituting these values into eq. (23) will give  $dU = 10$  mm/s. Therefore, the

uncertainty in velocity calculation would be  $\frac{dU}{U} * 100 = 0.46\%$ , which is very small. Since at lower flow

rates it takes relatively longer time for the dye to go through the channels, the video capturing was

performed for a longer time (more than 4 seconds) to track the dye displacement all along the flow field.

Therefore, the frame rate was decreased to 1,000 fps at 60 ml/min and 2,000 fps at 150 ml/min. The

uncertainty, however, remained low since the flow rate was much lower than 1400 ml/min.

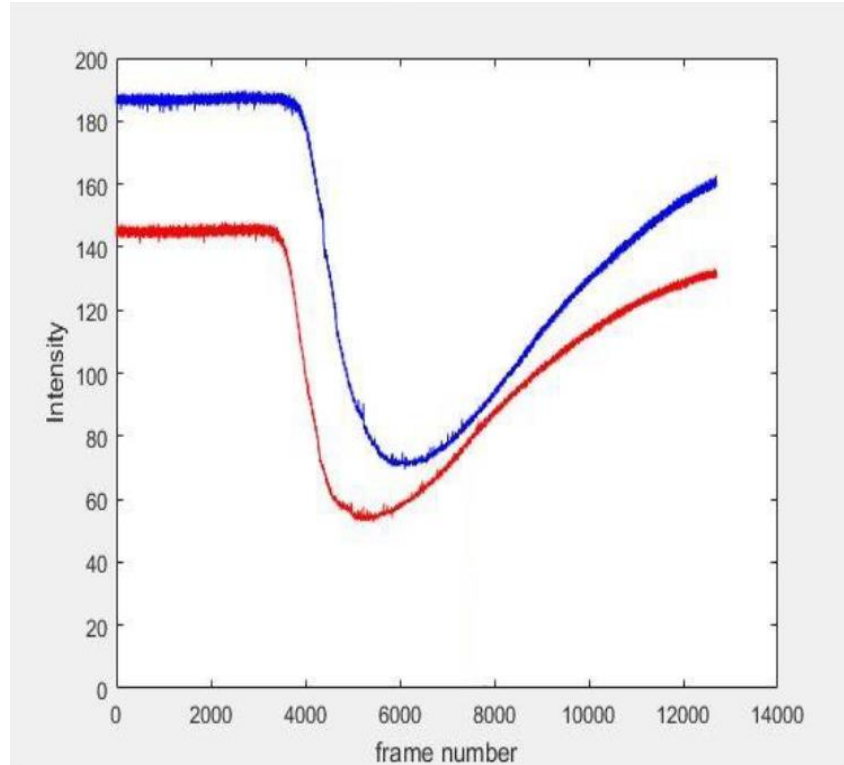


Figure 3-12: Intensity versus frame number graph for two corresponding pixels with different locations along the flow direction

in a random channel of SLA 3D printed cathode plate with 0.635 mm hydraulic diameter.

### 3.10 Statistical analysis

To compare the agreement of different graphs together, the goodness of fit was performed. To decide whether graph-1 or graph-2 is closest to expectation, the goodness of fit was tested with weighted least squares (WLS), where the reciprocal of standard error is used as weight. To find out the discrepancy between graph-*i* (*i*=1,2) and expectation (model), the errors between each two corresponding points is calculated using eqs. (24) and (25), where  $y_i$  is the average of observations in point(*i*),  $y_{model}$  is the expectation, and  $SE_i$  is the standard error of the mean (SEM) which equals the sample standard deviation divided by square root of sample size. After the matrix of error,  $E=[E_i]$  (*i*=1:*n*) *n*=# of channels, is extracted for both graphs, the p-value is calculated with less than alternative hypothesis to determine whether there exists a significant difference between the errors from two graphs. The significance level is assumed to be 5%.

$$E_i = w_i (y_i - y_{model})^2 \quad (24)$$

$$w_i = \frac{\frac{1}{SE_i}}{\sum \frac{1}{SE_i}} \quad (25)$$

In validating the simulation results, to test the discrepancy between two graphs (experiment VS simulation), the percentage of average error is calculated using eq. (26), where *n* is the number of data points on graph. In velocity experiments, in addition to error, the skewness of the graphs is also compared to each other to decide about the symmetry of results.

$$E_{avg} = \frac{100}{n} \sum_1^n \frac{|y_{expected} - y_{observed}|}{y_{expected}} \quad (26)$$

Please note that in the current research whenever it is necessary for comparing the mean of two sets of data, p-value is calculated to decide the significance of difference between two data sets.

## 4 Results and discussion

This chapter represents the experimental results obtained from pressure-drop and velocity distribution measurements using different prototype BPPs. First, the cross-section images of the prototype BPPs are captured to evaluate the quality of different fabrication methods. This is followed by measured pressure-drop data as well as velocity distribution data for different prototype BPPs to shed light on pros and cons of each RP technique.

### 4.1 Cross-section area of BPPs

As given in Table 3-1, nine different BPPs were manufactured with different fabrication techniques. To visualize the fabrication method precision, and to measure the channel cross-sectional area, images of the channel cross-section were captured using OCT method. Comparing to Figure 4-1, which represents the cross section image of 3D printed BPP from [128], the cross section images of BPPs made in the current study in Figure 4-2 demonstrate that the images captured by OCT method in the current research are much more clear and precise than the cross-section images captured in previous studies [128] by optical microscopy, which needs to either break the plate or 3D print only a small sample, because this method needs to be carried out perpendicular to the channel cross-section. While OCT can capture images when the plate is perpendicular to the imaging apparatus, which allows the BPP to be simply put under the OCT apparatus lens.

Figure 4-3 and Figure 4-6 show the OCT images of channel cross-section of different BPPs in the present study. Cross-section images are captured from all the channels of each BPP, which allows the cross-sectional area for each single channel to be calculated. Table 4-1 summarizes the statistical data of average channel cross-sectional area for each BPP, in conjunction with Figure 4-7 and Figure 4-8, which demonstrate the channel size distribution graphs of the studied BPPs. It is noted that the data in Table 4-1 are calculated based on all the channels of a BPP, with each channel being studied in channel inlet,

channel middle part and channel outlet region. Also noted is that in order to compare the size distribution of different plates, the graphs in Figure 4-7 and Figure 4-8 are shifted to the origin.

#### 4.1.1 BPPs with 0.4mm hydraulic diameter

Visual analysis of Figure 4-3-a reveals that CNC machining results in identical channels with sharp square cross-section of channels. This observation is confirmed by Table 4-1 (BPP#1), where statistical analysis of all channels of graphite plate with consideration of random and systematic errors shows a coefficient of variation (COV) less than 5% for CNC machining and a size slightly (1.9%) lower than the expected size. Figure 4-7 also demonstrates a very sharp distribution histogram for the channel cross-sectional size of graphite plate, which confirms that channels are quite identical in real fuel cell stacks.

Taking graphite channels as the reference, it can be concluded from COV data of Table 4-1 and size distribution histograms of Figure 4-7 that channel size distribution is much more uniform in SLA 3D printed and laser-cut BPPs (# 4 and #7 in Table 3-1), than Polyjet 3D printed BPP (#10). The non-uniformity of channels in Polyjet printed BPP can be observed in Figure 4-3-d, where some channels are even clogged. The channel size distribution is approximately similar in SLA 3D printed and laser-cut BPPs, and both have less uniform channel size distribution than CNC machined BPP.

Although the same CAD file is used for fabricating all BPPs with 0.4 mm hydraulic diameter, it can be seen from Figure 4-3 and Table 4-1 that the resulting average channel size differs from different fabrication methods. CNC machining and SLA 3D printing produce channels with expected average channel size, with rectangular channels. We attribute the difference in expected and measured average channel size to the random and systematic errors. Laser-cutter technology (BPP#7), however, produces trapezoidal channels which are on average 20% larger than the expected channels. This is because that the depth in laser-cutting is controlled with the power of the laser which melts the plastic, and that is done by trial and error and is fraught with errors. The average depth of laser-cut channels is 0.5 mm.

One of the major problems of the laser-cutter technology is the rough channel bottom surface resulting from melting the plastic to create the channel, as shown in Figure 4-2, which would increase the pressure-drop and adversely affect the accuracy of fluid dynamic studies.

#### *4.1.1.1 Effect of support materials on Polyjet 3D printing quality*

Figure 4-3-d and Table 4-1 (BPP #10) demonstrate that the resulting average channel size from Polyjet 3D printing is almost half of the expected channel size, and the channel cross-section is semi-circular rather than rectangular. This is because of the support material used between channels to lend support to channel walls during the fabrication in Polyjet 3D printing. Although these support materials are supposed to be removed after fabrication in support cleaning process, the small channel size prevents the full cleaning of support materials from between channels. After we received the 3D printed BPP with 0.4 mm diameter from the manufacturing company, we could see lots of support materials still remaining in between the channels. Some of these remaining support materials were cleaned manually from a few channels, as shown in Figure 4-4-a, which illustrates the amount of support materials available in channels after support cleaning process.

We developed and followed the following protocol for cleaning the support materials in order to remove almost 100% of the support materials: The Polyjet 3D printed BPPs were soaked in 4% NaOH in an ultrasound bath for 4 hours. Figure 4-4-b and Figure 4-4-c demonstrate the OCT images of channel cross-section before and after applying the support removal procedure, respectively. The statistical data of Polyjet 3D printed plate after support removal in Table 4-1 (BPP#2) suggest that removing the support materials increases the average channel size by 38% and reduces the channel cross-section size variation by 5%. But still there exists a large discrepancy between expected and actual average channel size, and the COV is much higher than other BPPs. These observations suggest that despite the high nominal accuracy of Polyjet technology presented in Table 2-1 (0.1 mm), it is not a suitable method for 3D printing features below 0.5 mm.

The other problems accompanied with Polyjet 3D printing is that BPPs 3D printed with Vero white (the most famous Polyjet material) are not robust and are prone to damage and deformation during the experiment. Polyjet materials have less mechanical strength in comparison with FDM, SLA and SLS materials which cause numerous problems in experiments. As in some instances in Figure 4-5, the channel walls get damaged when washing the plates, and the materials get deformed when exposed to water, opposite to SLA plates. The Polyjet material gets contaminated by dyed water after a few repeated experiments, while SLA materials completely get washed out of dye.

#### 4.1.2 BPPs with 0.635 mm hydraulic diameter

Figure 4-6 shows the OCT images of channel cross-section of BPPs with 0.635 mm hydraulic diameter. Figure 4-6-a along with Table 4-1 (BPP#2 and 3) shows that applying Polyjet 3D printed parts with larger features ( $>0.5$  mm) is not improving the consistency of channels since the COV is the same between BPP#2 and BPP#3. This is also true for SLA 3D printer, where the COV is the same for SLA 3D printed BPPs with 0.4 mm and 0.635 mm diameter. This highlights the inconsistency in 3D printing which is not related to the channel size. However, the Polyjet 3D printed BPPs with 0.635 mm diameter have near square channels and show 15% improvement in terms of closeness to the average expected channel cross-section area, which confirms that Polyjet printing accuracy increases at dimensions above 0.5 mm.

Figure 4-6 along with Figure 4-8 and Table 2-1 presents a few points about SLA 3D printing. First, they represent that SLA 3D printing outperforms Polyjet in terms of channel consistency, closeness to expected average channel size and channel cross-section geometric shape. Moreover, it can be concluded that SLA performs consistently in 3D printing different plates, since the images and the statistical data of SLA 3D printed cathode, anode and water-cooling BPPs with 0.635 mm diameter are very similar. In particular, the perfect square cross-section of the SLA BPPs shown in Figure 4-6-b,c,d is exemplary. That we cannot see further improvement in the average channel size closeness to the expected size from BPP#4 to BPP#5 in Table 4-1 suggests that SLA 3D printing performs with the same

fabrication quality in small (<0.5 mm) features as well as in large features (>0.5 mm). Note that since in the novel SLA enclosed cathode plate (BPP#6 in Table 4-1) a layer was 3D printed on top of the channels, OCT was unable to capture images of channel cross-section in this case. Therefore, we assume that the channel cross-section size in covered SLA cathode plate (BPP#6) is the same as uncovered SLA cathode plate (BPP#5).

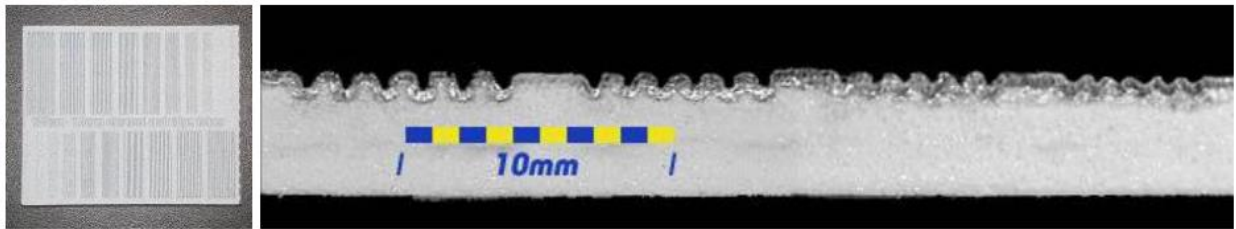


Figure 4-1: Resolution test taken under optical microscopy by Lyons et al. [128] (reprinted from [128]).

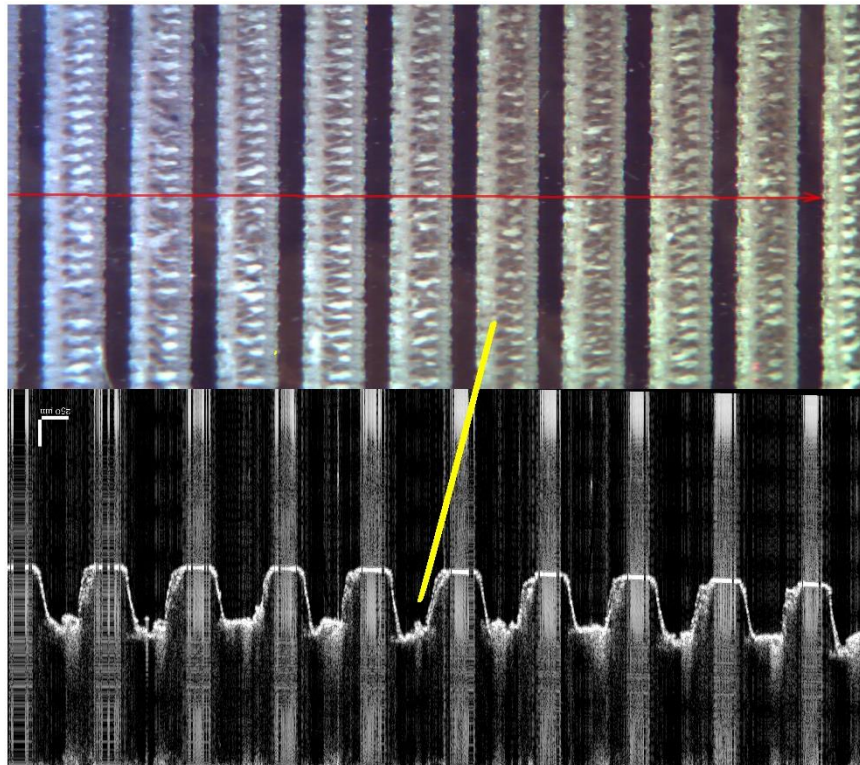
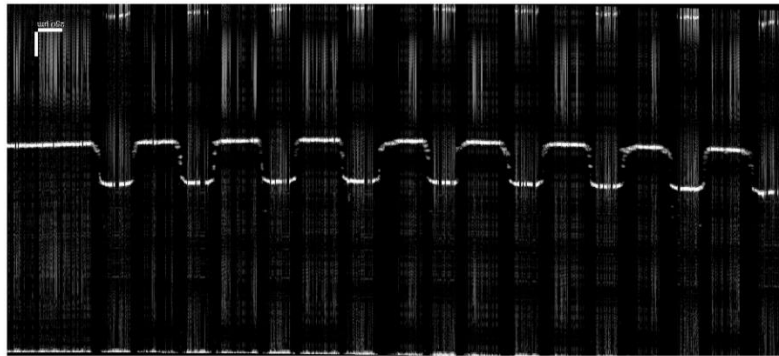
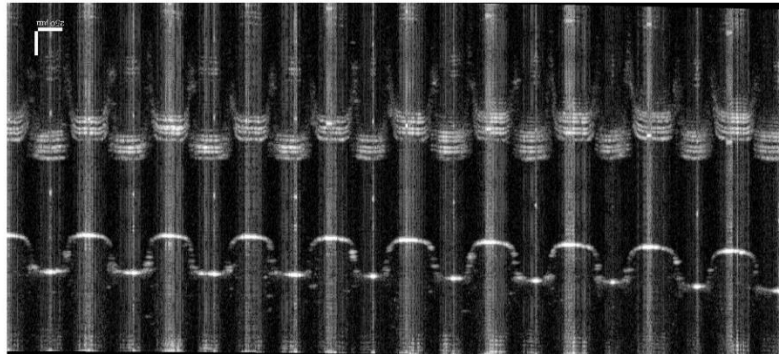


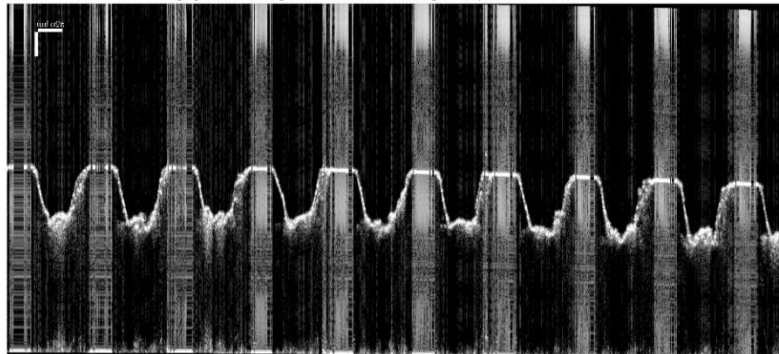
Figure 4-2: Laser-cut BPP channel roughness.



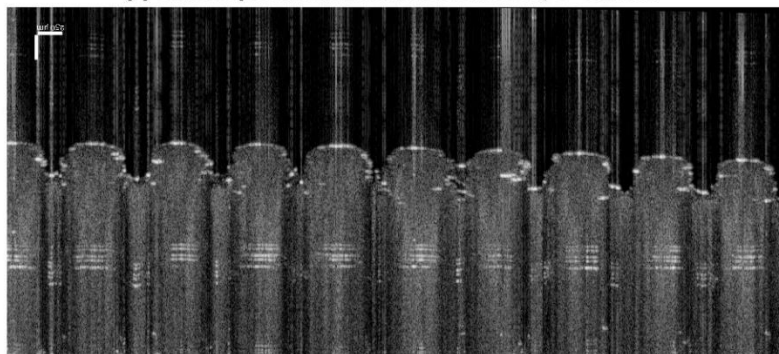
**(a) CNC machined graphite cathode plate, D=0.4mm.**



**(b) SLA 3D printed cathode plate, D=0.4mm.**



**(c) Cathode plate fabricated with laser cutter, D=0.4mm.**

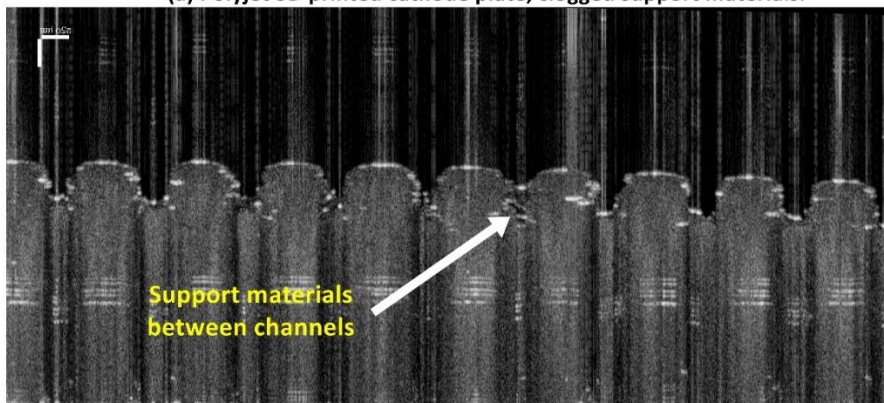


**(d) Polyjet 3D printed cathode plate, Before support removal, D=0.4mm.**

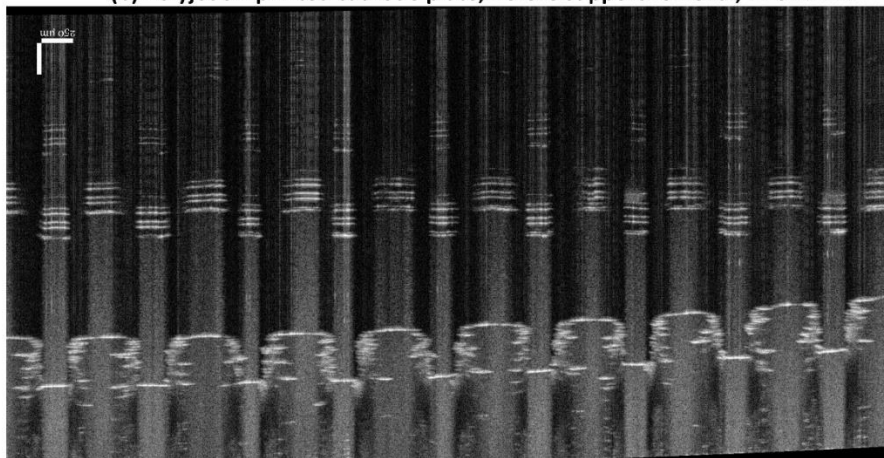
*Figure 4-3: Cross-section images of BPPs with 0.4 mm hydraulic diameter.*



(a) Polyjet 3D printed cathode plate, clogged support materials.



(b) Polyjet 3D printed cathode plate, Before support removal,  $D=0.4\text{mm}$ .



(c) Polyjet 3D printed cathode plate, After support removal,  $D=0.4\text{mm}$ .

Figure 4-4: Polyjet 3D printed BPPs, with 0.4 mm diameter, before and after support removal.



**(a) Damaged channel walls during washing.**

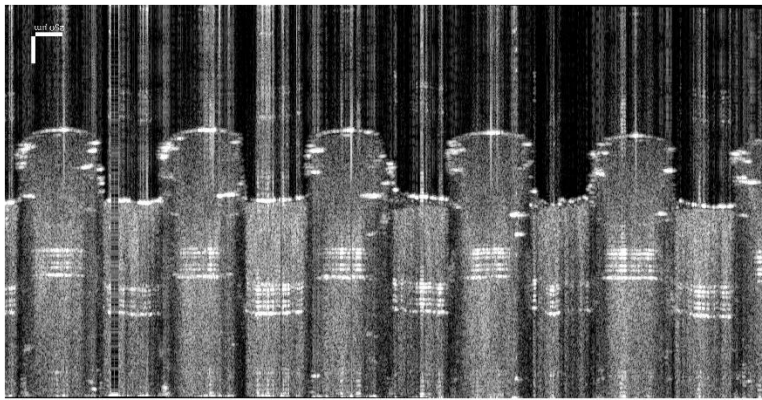


**(b) Deformed polyjet 3D printed BPP.**

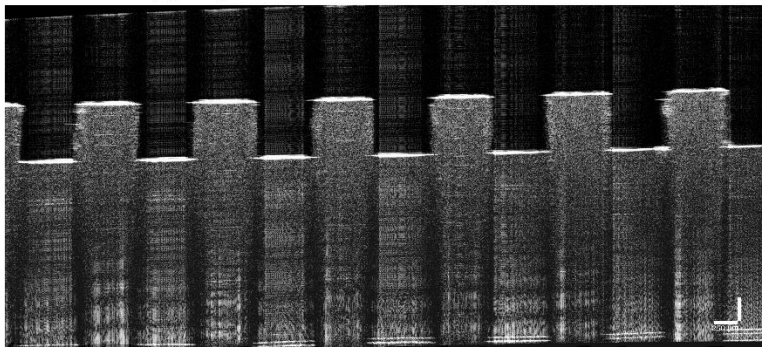


**(c) Polyjet 3D printed BPP colored with dyed water.**

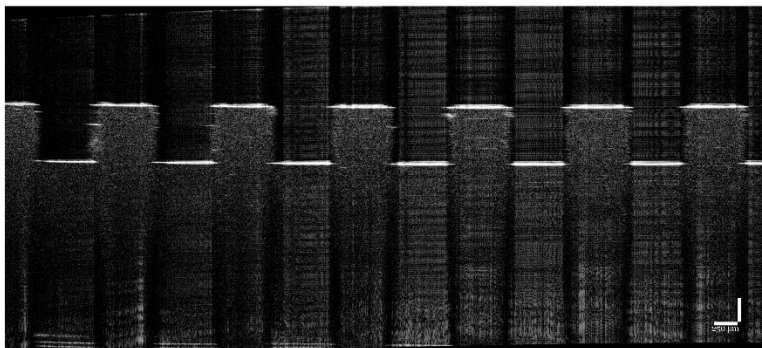
*Figure 4-5: Damaged Polyjet 3D printed BPPs during experiments.*



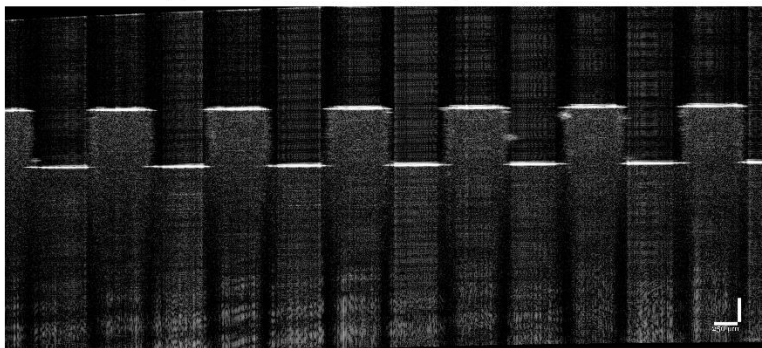
**(a) Polyjet 3D printed cathode plate,  $D=0.635\text{mm}$ .**



**(b) SLA 3D printed cathode plate,  $D=0.635\text{mm}$ .**



**(c) SLA 3D printed anode plate,  $D=0.635\text{mm}$ .**



**(d) SLA 3D printed water cooling plate,  $D=0.635\text{mm}$ .**

*Figure 4-6: Cross-section images of BPPs with 0.635 mm diameter*

Table 4-1: Channel cross-section size data for the studied BPPs

BPP #	Technology	BPP type	Number of channels studied	Expected cross-section area (mm <sup>2</sup> )	Actual mean cross-section area (mm <sup>2</sup> )	Expected cross-section/ Actual cross-section	Standard Deviation (mm <sup>2</sup> )	Coefficient of variation (%)	Average size discrepancy from expectation (%)
1	CNC	Cathode	101	0.1600	0.157	1.019	0.00756	4.82	1.90
2	Polyjet	Cathode (After support removal)	101	0.1600	0.124	1.290	0.01890	15.20	22.64
3	Polyjet	Cathode	64	0.4032	0.373	1.080	0.05740	15.40	7.60
4	SLA	Cathode	101	0.1600	0.156	1.021	0.01190	7.61	2.09
5	SLA	Cathode (Uncovered)	64	0.4032	0.389	1.037	0.01570	4.05	3.63
6	SLA	Cathode (Covered)	64	0.4032	NA	NA	NA	NA	NA
7	Laser-cutter	Cathode	101	0.1600	0.193	0.829	0.01190	6.18	20.65
8	SLA	Anode	64	0.4032	0.395	1.021	0.01960	2.11	2.11
9	SLA	Water-cooling	64	0.4032	0.393	1.024	0.01670	4.25	2.43
10	Polyjet	Cathode (Before support removal)	101	0.1600	0.099	1.790	0.01830	20.40	44.04

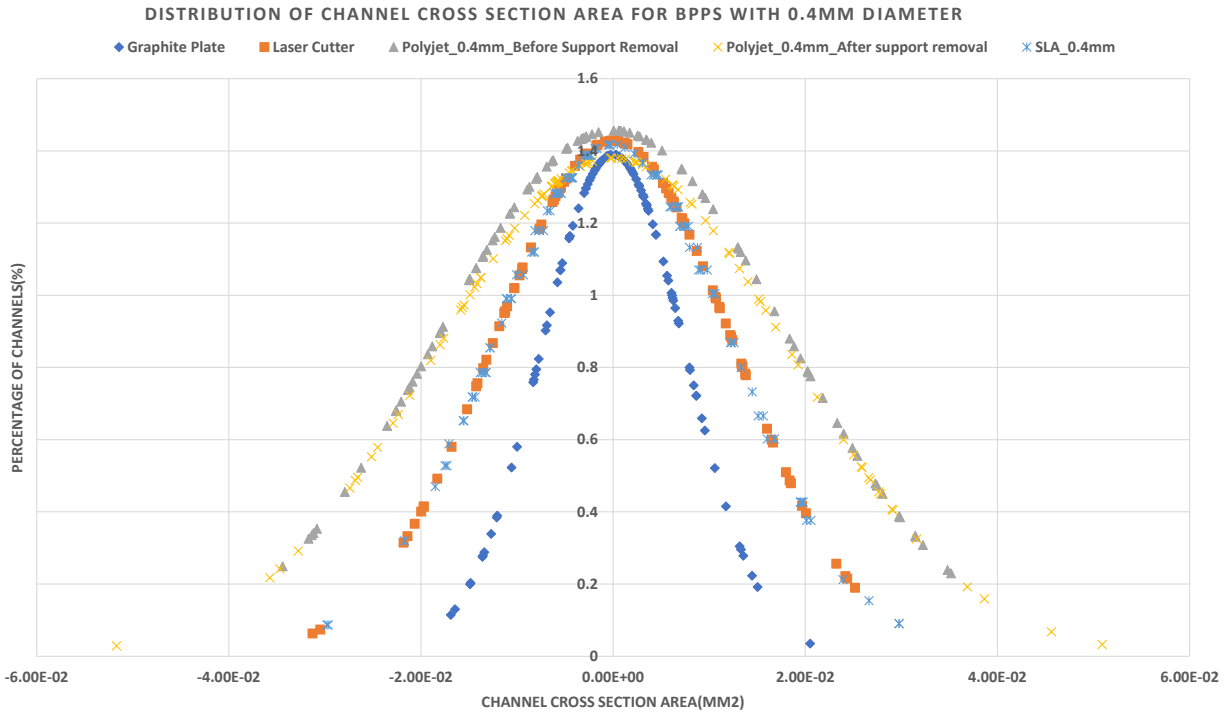


Figure 4-7: Channel cross-section area distribution in BPPs with 0.4 mm diameter.

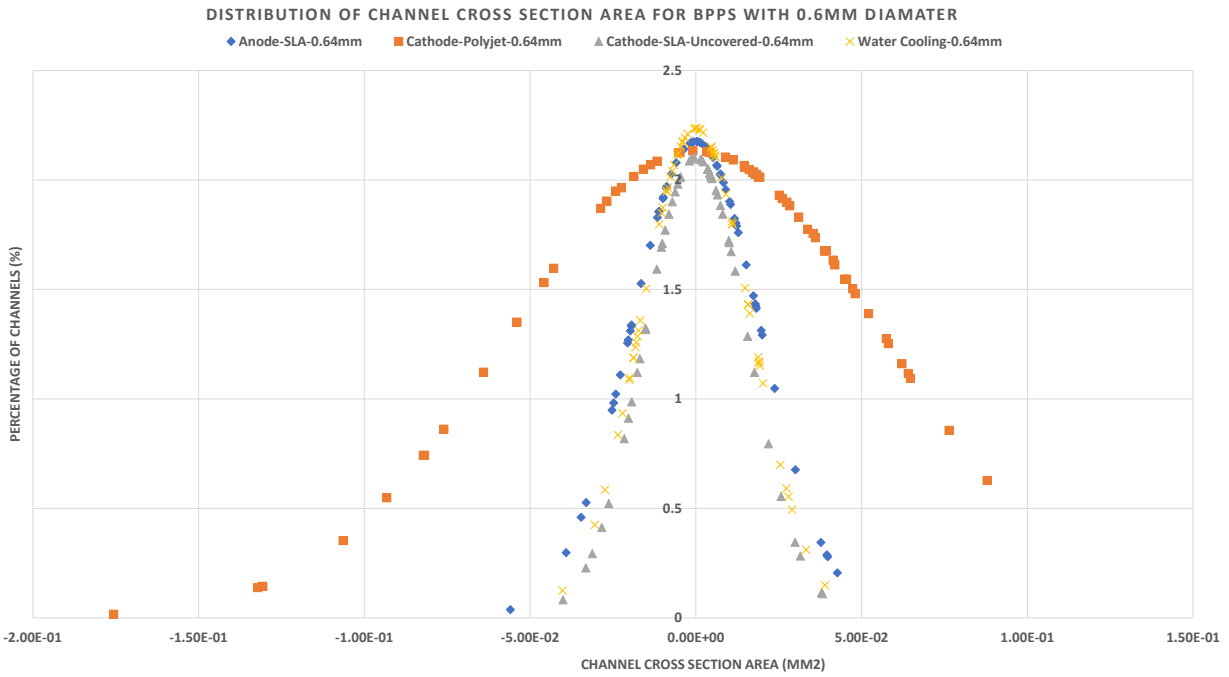
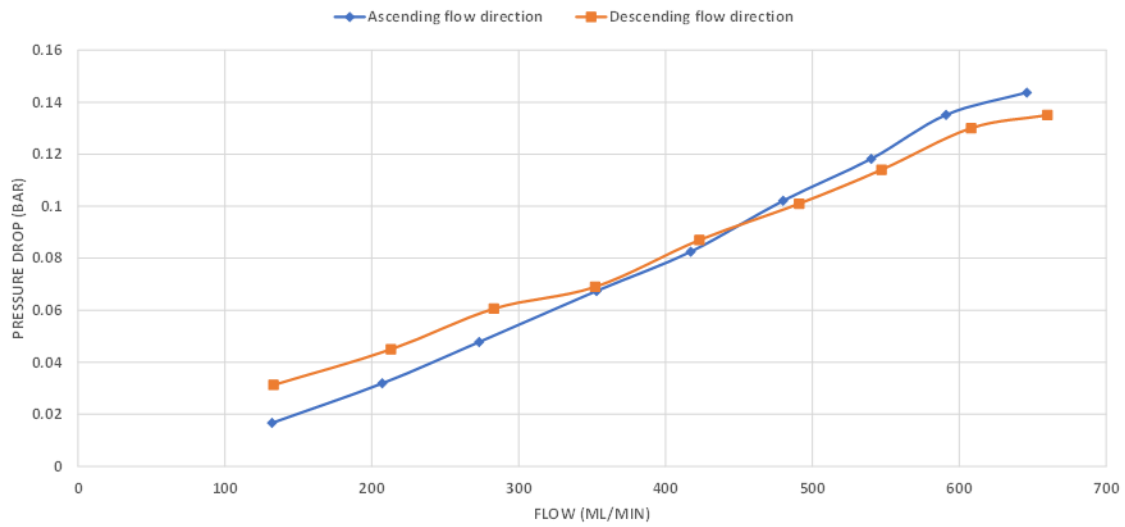


Figure 4-8: Channel cross-section area distribution in BPPs with 0.635 mm diameter.

## 4.2 Pressure-drop in prototype BPPs

This part presents the results of pressure-drop experiments in prototype BPPs. First, we present the effect of de-aerated water on pressure-drop experiment to justify why de-aerated water is used in this research. Figure 4-9 depicts the effect of dissolved air bubbles available in tap water on pressure-drop. As it can be seen in Figure 4-9-a, the dissolved air bubbles result in different pressure-drop curves depending on the direction of the flow rate change. If we start from low flow rate and increase the flow rate (ascending direction), the pressure-drop is more linear than in the descending direction, and the graphs of ascending and descending flows do not match each other. One reason for this observation is that the existence of air bubbles violates the incompressible flow assumption made in Darcy equation, which would change the value of pressure-drop. Moreover, the air bubbles in the tap water accumulate in the pressure sensor diaphragm, and this accumulation is more significant at higher flow rates. Hence, starting from higher flow rates caused more air bubbles to accumulate in the pressure sensor diaphragm and its sudden release caused a breakdown in the pressure-drop curve, as demonstrated in Figure 4-9-a (descending flow direction). However, Figure 4-9-b confirms that pressure-drop is not a function of the change in flow direction, which suggests the elimination of fine bubbles with the use of de-aerated water in the experiments. Figure 4-9-b reveals that there does not exist pressure-drop hysteresis in single-phase flow.

**(A) PRESSURE DROP IN UNCOVERED SLA CATHODE PLATE IN INCREASING AND DECREASING FLOW DIRECTIONS USING TAP WATER**



**(B) PRESSURE DROP IN UNCOVERED SLA CATHODE PLATE IN INCREASING AND DECREASING FLOW DIRECTIONS USING DEAERATED WATER**

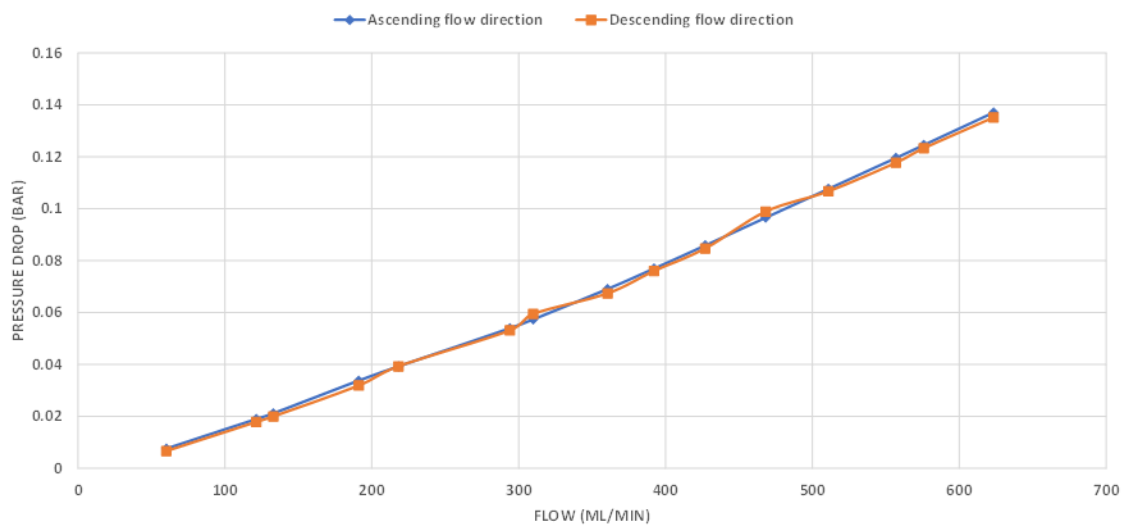


*Figure 4-9: Effect of dissolved air of water on pressure-drop.*

#### 4.2.1 Pressure-drop in cathode BPPs

As discussed in part 4.1, the SLA 3D printed BPPs demonstrate the highest agreement with the expected geometry, and hence have the potential to be used as a reference to validate the simulation results.

However, all the SLA plates (except BPP#6) were tightened in the transparent cell assembly which might deviate the plate from ideal shape. The only plate which was not tightened in the active area and could maintain its geometry was BPP#6, on top of which a layer is 3D printed to have the channels sealed. A piece of acrylic glass is located (but not tightened) on the plate to prevent any possible channel swelling due to water flow. Considering these facts, the covered SLA cathode plate with 0.635 mm diameter would be the closest to the ideal geometry during the experiment.

##### 4.2.1.1 *Pressure-drop in cathode BPPs with 0.635 mm hydraulic diameter*

Figure 4-10 exhibits the pressure-drop versus flow-rate in cathode BPPs with 0.635 mm diameter. As it is shown, there exists a good agreement between the simulated pressure-drop data and measured from covered SLA plate (BPP#6), and the average and maximum discrepancy between data points are only 6.0% and 23.1%, respectively. This observation both validates the simulation results and suggests that covered SLA cathode plate performs very close to design. It should be worthwhile reminded that graphite plates are highly brittle and expensive, and we aim to replace conventional graphite plates with a plate made by RP technique to run the fast screening experiments. This observation recommends that novel design of covered SLA cathode plate enables it to serve as a rapid fabrication method for at least testing the pressure-drop in any novel BPP design.

Figure 4-10 indicates that the pressure-drop from uncovered SLA and Polyjet cathode plates with 0.635 mm diameter (BPP#3,5) deviate from the expected pressure-drop based on design dimensions, and it is more significant for the case of Polyjet. As it is shown in Table 4-2, the average and maximum discrepancy between the pressure-drop of Polyjet plate and numerically simulated plate are 25.25% and

45.25%, respectively, and 13.6% and 32.5% for uncovered SLA. The possible reason for this discrepancy will be given after the pressure-drop of prototype BPPs with 0.4 mm diameter is presented.

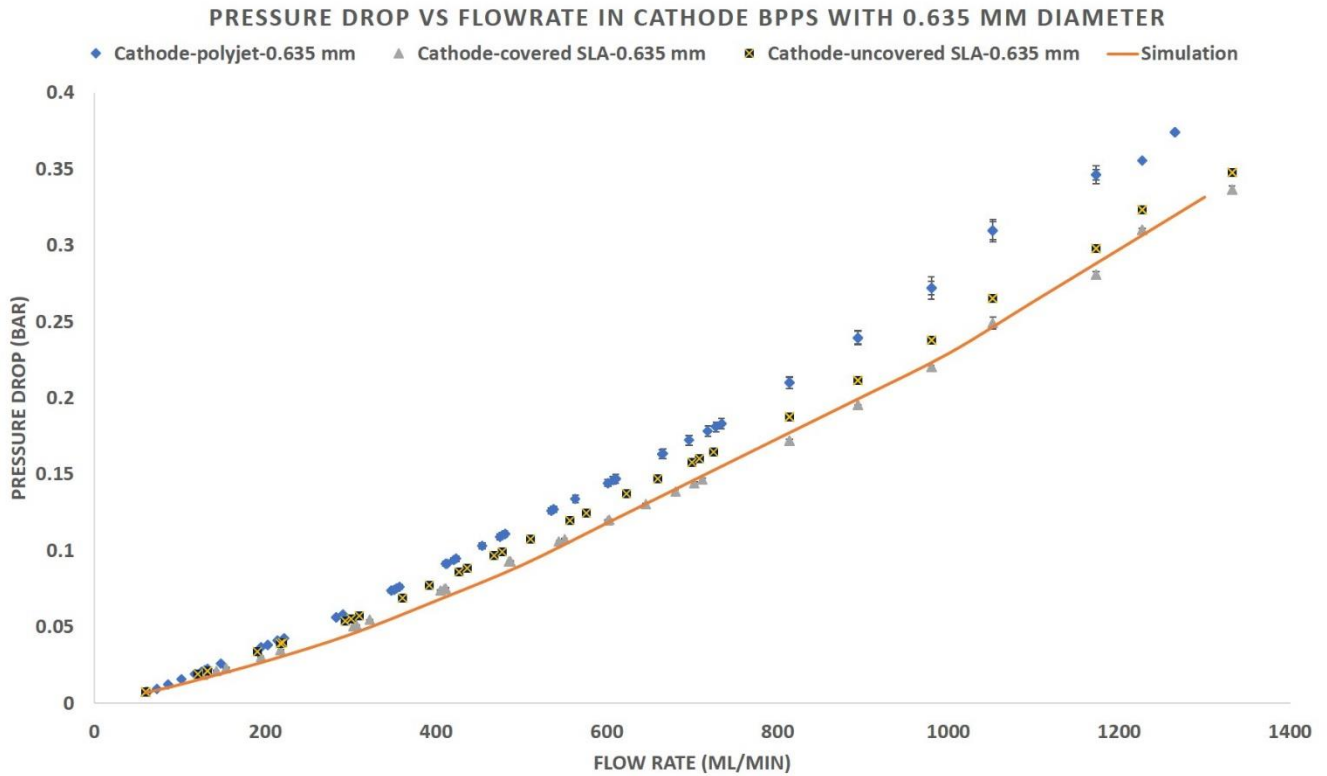


Figure 4-10: Pressure-drop in cathode BPPs with 0.635 mm hydraulic diameter.

#### 4.2.1.2 Pressure-drop in cathode BPPs with 0.4 mm hydraulic diameter

Figure 4-11 exhibits the pressure-drop data versus flow rate in cathode BPPs with 0.4 mm hydraulic diameter. As it is observed, there exists a good agreement between pressure-drop data of SLA and numerically simulated cathode plate of 0.4 mm diameter, where the average and maximum discrepancy between the two curves are 8.0% and 18.0%, respectively. Again, this validates the simulation results and highlights the reliability of SLA as a RP technique. On the other hand, the laser-cut prototype has less pressure-drop than expectation where average and maximum discrepancy between pressure-drop data of measured and simulated are 22.0% and 29.1%, respectively. Pressure-drop data from Polyjet plate with 0.4 mm diameter show a huge difference from expectation, where the average and maximum

discrepancy between measured and simulated results are 147.2% and 180.7% respectively. The following section explains the very diverse behavior of different BPPs.

Table 4-2: Statistical analysis of pressure-drop data from 6 prototype BPPs versus the simulation results.

BPP #	Technology	BPP type	Number of channels	Average discrepancy from simulation (%)	Maximum Discrepancy From Simulation (%)	Slope of Pressure-drop graph In linear region (bar.min/ml)	Slope of BPP divided by slope of relevant simulation ( $m_{exp} / m_{model}$ )
2	Polyjet	Cathode (After support removal)	101	147.26	180.13	0.001320	2.03
3	Polyjet	Cathode	64	25.25	45.25	0.000251	1.58
4	SLA	Cathode	101	8.01	17.74	0.000725	1.12
5	SLA	Cathode (Uncovered)	64	13.60	32.50	0.000209	1.32
6	SLA	Cathode (Covered)	64	6.17	23.25	0.000192	1.22
7	Laser-cutter	Cathode	101	22.15	28.42	0.000510	0.79
11	Simulation1	Cathode	64	0.00	0.00	0.000158	1.00
12	Simulation2	Cathode	101	0.00	0.00	0.000650	1.00

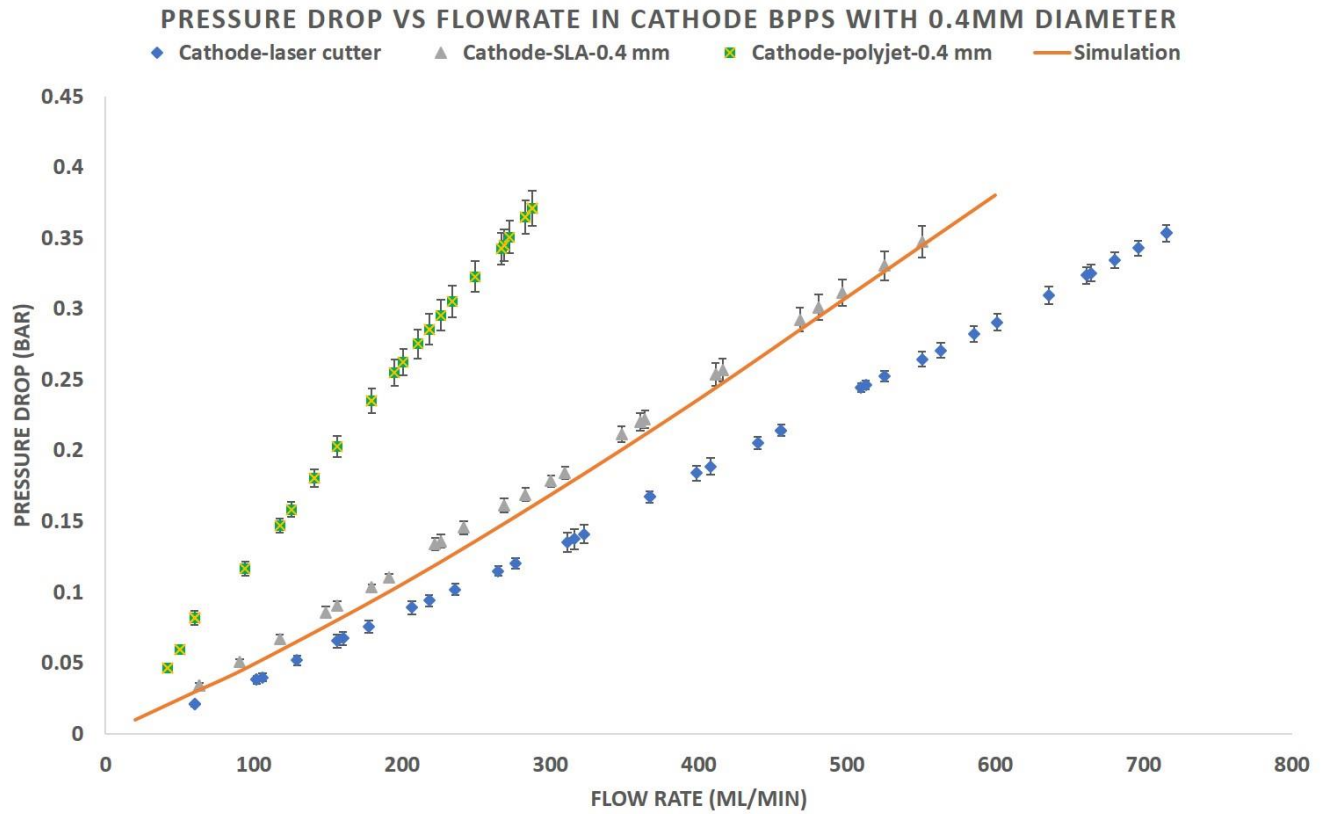


Figure 4-11: Pressure-drop in cathode BPPs with 0.4 mm hydraulic diameter.

#### 4.2.1.3 Explaining pressure-drop behavior of cathode BPPs with 0.635 mm hydraulic diameter

At small fluid velocity, the second term in eq. (8) can be neglected, which implies that the pressure-drop in flow channels maintains a linear relationship with the fluid velocity at low flow rates. Considering the low Reynolds number calculated in Table 3-4 for all the experiments in the current research, we assume a linear relationship between pressure-drop and fluid velocity in flow channels, which is compatible with simulation where results from COMSOL Multiphysics suggest that the pressure-drop in flow channels of the BPPs is dominant and the pressure-drop in two transition regions together counts for approximately 20% of the total pressure-drop at high flow rates. Substituting eq. (14) into eq. (8) with the assumed linearity of pressure-drop curve will result in eq.(27), from which eq.(28) can be derived with  $D_h^2 = A$ .

$$\Delta P = \frac{28.4\mu L}{nAD_h^2} Q \quad (27)$$

$$\Delta P = \frac{28.4\mu L}{nA^2} Q \quad (28)$$

Eq.(28) predicts the linearity of the pressure-drop vs. flow rate curve in low flow rates, with the slope of  $\frac{28.4\mu L}{nA^2}$ . All the pressure-drop graphs in Figure 4-10 and Figure 4-11 demonstrate linearity in low flow rates, with a small curvature at high flow rates which is a result of the increasing effect of pressure-drop in transition region at high flow rates. Since we work in the low Reynolds number region ( $Re < 530 \ll 2100$ ), the curvature of the pressure-drop graphs is unlikely related to the deviation from laminar flow. As mentioned, the slope of the pressure-drop vs. flow rate is proportional to  $\frac{1}{nA^2}$ , which suggests that the small deviation from expected channel cross-section area could result in high deviation of pressure-drop graph from expectation. The slope of pressure-drop vs flow rate is calculated in the linear region as given in Table 4-2.

To test the proportionality of pressure-drop slope to  $\frac{1}{nA^2}$ , the following calculations are performed on the simulation results. Dividing the slope of simulated cathode plate with 0.4 mm diameter with that of simulated cathode plate with 0.635 mm diameter (BPP#11 and 12 in Table 4-2) results in a value of 4.113 ( $\frac{m_{12}}{m_{11}} = \frac{0.000650}{0.000158} = 4.113$ ). On the other hand, the ratio of expected slopes from BPP#11 and BPP#12 is 4.024, as calculated in eq. (29). The discrepancy between 4.113 and 4.024 is only 2%, which confirms the proportionality of pressure-drop slope with  $\frac{1}{nA^2}$ .

$$\frac{m_{12}}{m_{11}} \propto \frac{1/n_{12}A_{12}^2}{1/n_{11}A_{11}^2} = \frac{64 * 0.635^4}{101 * 0.4^4} = 4.024 \quad (29)$$

As mentioned before, covered SLA cathode plate with 0.635 mm hydraulic diameter (BPP#6) has the closest geometry to expectation. Error for this plate, which is the difference between actual and expected slopes of the pressure-drop graph, is calculated below and the error value of 13% is obtained.

$$\frac{m_{actual}}{m_{expected}} = \frac{m_6}{m_{11}} = 1.215 \quad (30)$$

$$\frac{A_{expected}}{A_{actual}} = 1.037 \quad (31)$$

$$Error = \frac{|1.037^2 - 1.215|}{1.037^2} * 100 = 13\% \quad (32)$$

Since the covered SLA cathode plate is closest in geometry to expectation and was not compressed in transparent cell assembly, we attribute this 13% to the error of measurement and experiments and deviations from the assumptions that we have made. In the case of uncovered SLA cathode plate with 0.635 mm diameter (BPP#5), this error is 23% which is attributed to the compaction and deformation of the plate in transparent cell assembly. One useful study is to compare the results from covered and uncovered SLA plates, which would provide us with the degree of deformation in SLA plate. The ratio of

cross-section area after clamping in transparent cell is 1.043 ( $\frac{A_{covered}}{A_{uncovered}} = \sqrt{\frac{m_5}{m_6}} = 1.043$ ), which shows

that SLA plates experience almost 4% deformation in surface area when tightened in the transparent cell assembly. It should be noted that the calculated deformation of SLA plates is with considering all the errors and assumptions we have made, which highlights that SLA plates possess a good mechanical strength and can be utilized in FC studies.

The difference of expected and actual slope (error) in the case of Polyjet printed cathode BPP with 0.635 mm diameter (BPP#3) is 35% which shows a higher degree of deformation in Polyjet plates than SLA.

Comparing uncovered SLA and Polyjet cathode plates with 0.635 mm (BPP#3 and #5) will enable us to determine the difference in deformation of SLA and Polyjet plates. The difference in the ratio of cross-section area of BPP#3 and BPP#5, before and after tightening in the transparent cell, is calculated by eq.(33), which demonstrates that Polyjet BPPs have 5% less mechanical strength than SLA BPPs.

$$\frac{\sqrt{\frac{m_3}{m_5} - \frac{A_5}{A_3}}}{\frac{A_5}{A_3}} * 100 = 5.22\% \quad (33)$$

#### 4.2.1.4 Explaining pressure-drop behavior of cathode BPPs with 0.4 mm hydraulic diameter

In cathode BPPs with 0.4 mm diameter, the slope of the pressure-drop in SLA cathode BPP (BPP#4) differs by 7% from expectation, and we attribute this to the errors of the experiment and deviation from assumptions. It should be worth mentioning that although SLA cathode plate with 0.4 mm is clamped in the transparent cell, its agreement with expected values is even more than that of covered SLA plate with 0.635 mm diameter (BPP#6). This is either because of the minor errors in simulation results, or because of the high mechanical strength of the SLA plates based on the following assumption that covered and uncovered SLA plates have the same cross-section area when not clamped onto the transparent cell assembly. It was reported in the previous section that lumped difference between cross-section areas of covered and uncovered SLA plates with 0.635 mm (BPP#5 and 6) is 4% and we interpreted this as deformation of SLA plate. However, the 4% difference could result not from the deformation but from the minor difference in the cross-section area of covered and uncovered SLA plates, which could happen from 3D printing the additional layer in the case of BPP#6. Hence, it seems to be reasonable to attribute a high mechanical strength to the SLA plates.

As it was mentioned previously, in Figure 4-11 there exists a significant difference between the data of Polyjet cathode plate with that of other plates. A part of this discrepancy can be justified by considering

the large difference in cross-section area of BPP#2 with expectation ( $\frac{A_2}{A_{expected}} = 0.775$ ). However, eq.(34) reveals that the squared ratio of expected to actual cross-section area before tightening is 1.66, while the ratio of actual over expected slope is 2.03, and there still exists 22% discrepancy between expected and actual slope of pressure-drop graph from BPP#2. Similar to BPP#3, this discrepancy could be attributed to the deformation of Polyjet BPP due to the clamping force in the transparent cell assembly. Another useful point is to compare the ratio of cross-section area, from Polyjet and SLA cathode plates of 0.4 mm diameter channels, before and after tightening in transparent cell assembly, as done by eq. (35). Eq. (35) demonstrates that Polyjet BPP possess 6.79% less mechanical strength than SLA BPP plate, and agrees with previously calculated difference in mechanical strength of two prototype BPPs (5%).

Finally, the pressure-drop curve of BPP fabricated with laser-cutter method demonstrates a 15% discrepancy from expected slope. Laser-cut BPP is fabricated with acrylic glass, the Young's modulus for which is  $3.2 \times 10^9$  pa. The initial studies of pressure-drop in BPPs revealed that pressure-drop in laser-cut BPP is not relevant to the clamping force, which could be interpreted as that acrylic glass has a good resistant to deformation in the clamping force range applied (4.5-15 N.m). With the assumption of resistivity to deformation and the error of around 7% in the BPPs with 0.4 mm diameter, the remaining 8% deviation from the expected slope can be attributed to the high roughness of flow channels in lase-cut plate, as demonstrated in Figure 4-2.

$$\left(\frac{A_{expected}}{A_2}\right)^2 = 1.66 < \frac{m_2}{m_{expected}} = 2.03 \quad (34)$$

$$\sqrt{\frac{m_2}{m_4} - \frac{A_4}{A_2}} * 100 = 6.79\% \quad (35)$$

#### 4.2.2 Pressure-drop in anode and water-cooling prototype BPPs

The pressure-drop experiments were also carried out in anode and water-cooling BPPs. Since the length of flow channels in water-cooling and anode BPPs are different from each other and from the cathode plates, the pressure-drop was calculated per unit length in mentioned BPPs. Figure 4-12 demonstrates the pressure-drop per meter vs. the flow rate in anode, cathode and water-cooling BPPs with 0.635 mm hydraulic diameter, fabricated with SLA technology with enclosed channels (BPP#6, 8 and 9 in Table 3-1). Although the number of channels, channel cross-section size (Table 4-1), distribution of channel cross-section size (Figure 4-8) and fabrication technology are exactly same for all those BPPs, and channel lengths are approximately equal, the pressure-drop curve are significantly different. The values for the slope of the pressure-drop curve in the linear region are 0.000192, 0.000339, 0.000584 for cathode, anode and water-cooling BPPs, respectively. Moreover, the pressure-drop from water-cooling and anode plate possess higher curvature than that of cathode plate.

This deviation from linear behavior gives the hint for reasoning the significant difference of pressure-drop from three plates; More curvature demonstrates that channels are experiencing higher fluid velocity. The source of this significant difference is the different configuration layout of anode, cathode and water-cooling BPPs, as demonstrated in Figure 3-1, which could result in different velocity profile distribution. Since the velocities at different flow channels of a certain BPP are not equal, eq. (8) indicates that the pressure-drop values would be also different in different flow channels, and the channel with highest value of pressure-drop (highest velocity) controls the total pressure-drop in each BPP.

Hence, eq. (28) should be modified by a correction factor  $\beta$ , which is the ratio of fluid velocity in fastest channel over the average fluid velocity, as shown in eq. (36). The introduction of such a correction factor to eq. (28) yields eq.(37). It should be worth noting that this equation was needs to be used for formulating the pressure-drop in cathode plates as well. However, since all previously studied BPPs are

cathode, with identical flow field configuration, the correction factor could be assumed equal for all cathode prototypes. Because we were interested in the ratio of pressure-drops between different cathode BPPs,  $\beta$  would cancel out in the equations. But the effect of  $\beta$  needs to be considered in comparing the pressure-drop graphs of anode, cathode and water-cooling BPPs.

$$\beta = \frac{\max(U_i, i = 1:n)}{\frac{Q}{nA}} \quad (36)$$

$$\Delta P = \frac{28.4\mu L}{nA^2} \beta Q \quad (37)$$

In addition to fluid velocity variation among different channels, the transition region configuration and position of the inlet are two other factors that could be responsible for different pressure-drop behaviors in anode and water-cooling BPPs. Although the configuration of transition region is the same in anode and cathode plates, the position of the inlet is different in two plates which causes the fluid stream lines to form different angles with baffles in the transition region, as demonstrated in Figure 4-13-a, b. In the case of water-cooling BPP, the transition region constitutes only one row of baffles, which decreases the total area available for movement of fluid in the transition region that could add to the pressure-drop. In addition, there exist short transition channels in the water-cooling BPP, as shown in Figure 4-13-c, and manual calculations demonstrated that these short channels could add 21% to the total pressure-drop. To further comment on the very diverse behaviors of anode, cathode and water-cooling BPPs we need to obtain the velocity profiles in three plates to acquire an approximate value for  $\beta$ .

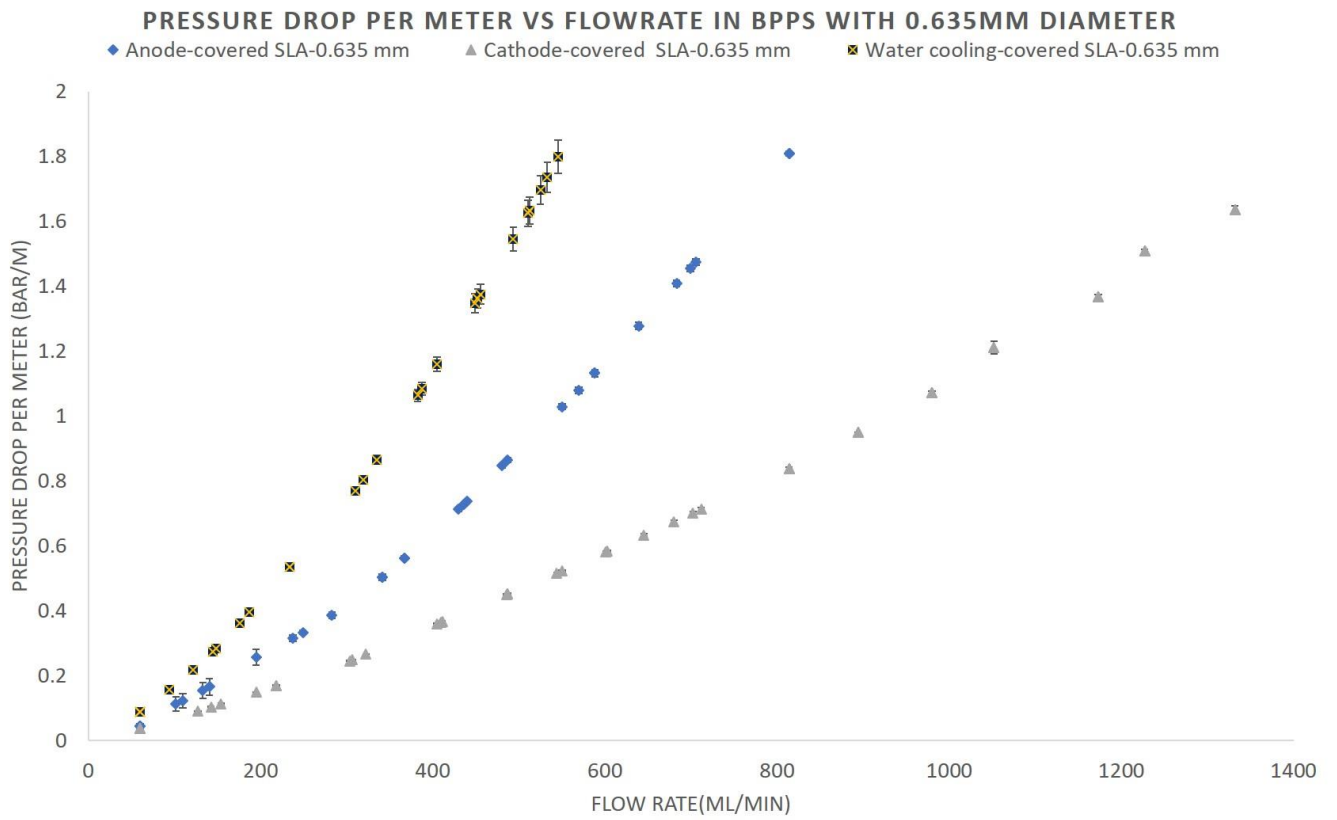
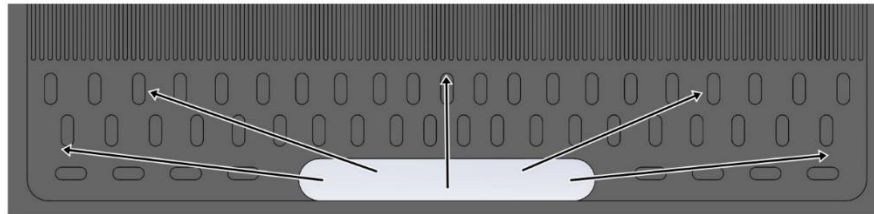
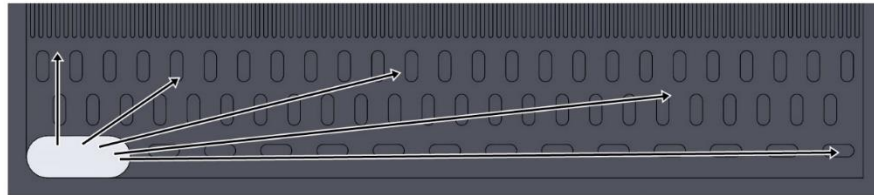


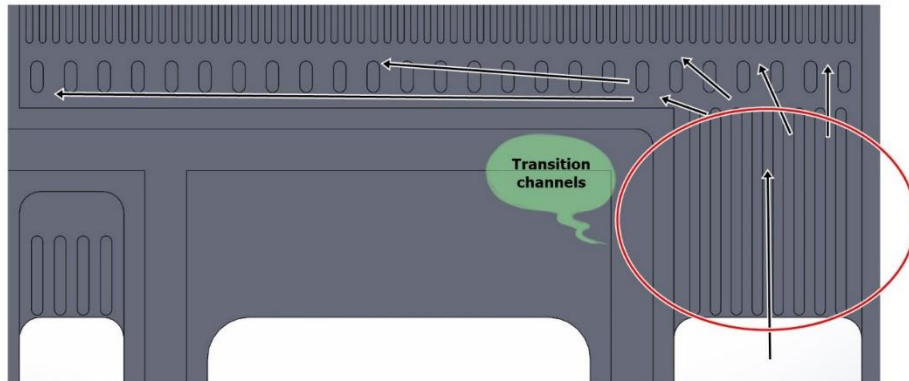
Figure 4-12: Pressure-drop in anode, cathode and water-cooling BPPs fabricated with covered SLA technology with 0.635 mm diameter.



(a) Cathode BPP transition region.



(b) Anode BPP transition region.



(c) Water cooling BPP transition region.

Figure 4-13: Schematic of the fluid flow direction in different transition regions.

### 4.3 Velocity profiles in prototype BPPs

This section presents the results of velocity profile experiments in prototype cathode BPPs, followed by the results from prototype anode and water-cooling BPPs.

Eq. (14) reveals that the mean average fluid velocity in flow channels is reciprocally related with the channel cross sectional area. As shown in Table 4-1, actual channel cross-sectional area differs from expectation, which is also tightened in the transparent cell that causes further deviation from expected surface area. Hence, using a fixed fluid flow rate, the mean average fluid velocity would be different for each BPP, which makes the comparison difficult. To overcome this issue, the fluid velocity in all channels are normalized to compare the results from different BPPs with simulation results. The value of mean average fluid velocity in each BPP is then used to validate the velocity measurement technique and to determine the degree of deformation in each BPP. To determine the uniformity of flow distribution between flow channels of a particular BPP, the coefficient of variation (COV) as suggested by Xu et al. [37], as well as  $\beta$  are calculated.

#### 4.3.1 Velocity profiles in cathode BPPs

As exhibited in Figure 3-1-a, the inlet and outlet regions of the BPP are centered in cathode BPP, and the flow is directed toward different flow channels by the baffles in the transition region. The high fluid flow resistant of flow channels compared to that of transition region could increase the flow uniformity since it could let the flow to be distributed in the transition region and then to move uniformly along the channels. The results of flow visualization in prototype BPPs are analyzed and the velocity profile in each prototype plate is demonstrated. First, the velocity profiles of BPPs with 0.635 mm hydraulic diameter are presented, followed by the velocity profiles of BPPs with 0.4 mm hydraulic diameter. Each BPP is tested at low, medium and high fluid flow rates.

#### 4.3.1.1 *Velocity profile in cathode BPPs with 0.635 mm hydraulic diameter*

Figure 4-14, Figure 4-15 and Figure 4-16 demonstrate the velocity profile in cathode BPPs with 0.635 mm hydraulic diameter in total fluid flow rates of 150, 600, 1300 ml/min, respectively. The tested BPPs are: SLA 3D printed cathode BPP with a layer 3D printed on top of the channels (BPP#6,  $D_h=0.635$  mm), SLA 3D printed cathode BPP without such a 3D printed layer (BPP#5,  $D_h=0.635$  mm), and Polyjet 3D printed cathode BPP (BPP#3,  $D_h=0.635$  mm). Since the results for BPPs#3, #5 and #6 are plotted together in Figure 4-14, Figure 4-15 and Figure 4-16, and each line consists of 64 data points, the figures are crowded, which makes the comparison difficult. To ease the comparison of the graphs visually, two groups of additional graphs are plotted using the data from Figure 4-14, Figure 4-15 and Figure 4-16. The first group contains Figure 4-17, Figure 4-18 and Figure 4-19 where the velocity of every 5 channel is represented with a single number, which is the average velocity of those 5 channels. The second group contains Figure 4-20, Figure 4-21 and Figure 4-22 where the results from each BPP are plotted individually along with the simulation results. Please note that the experimental data points in velocity profiles are connected to each other to help the reader to follow the trends. The results from velocity profiles are statistically compared with simulation results in Table 4-3.

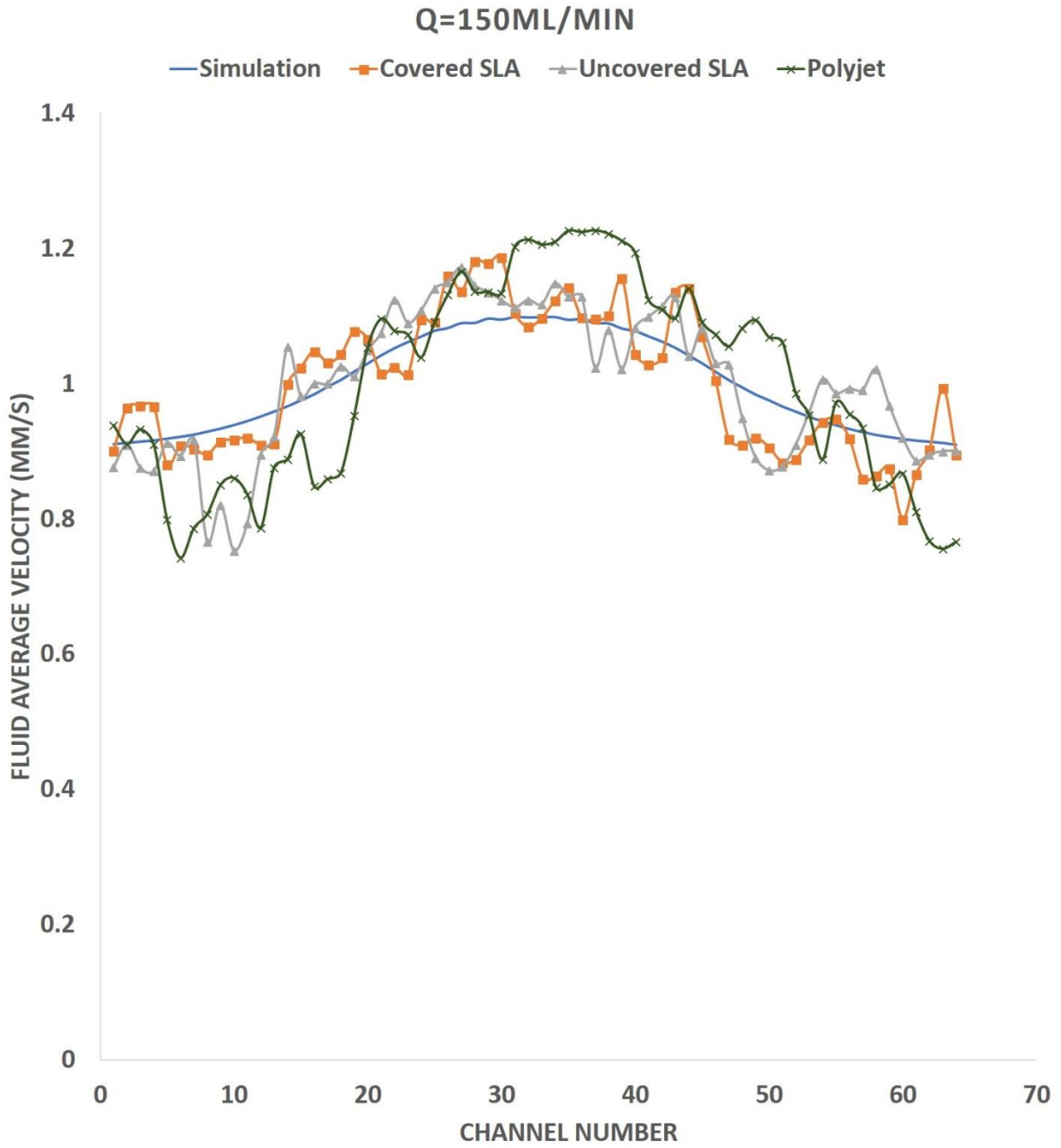


Figure 4-14: Velocity profile in cathode prototype BPPs with 0.635 mm hydraulic diameter, Q=150 ml/min.

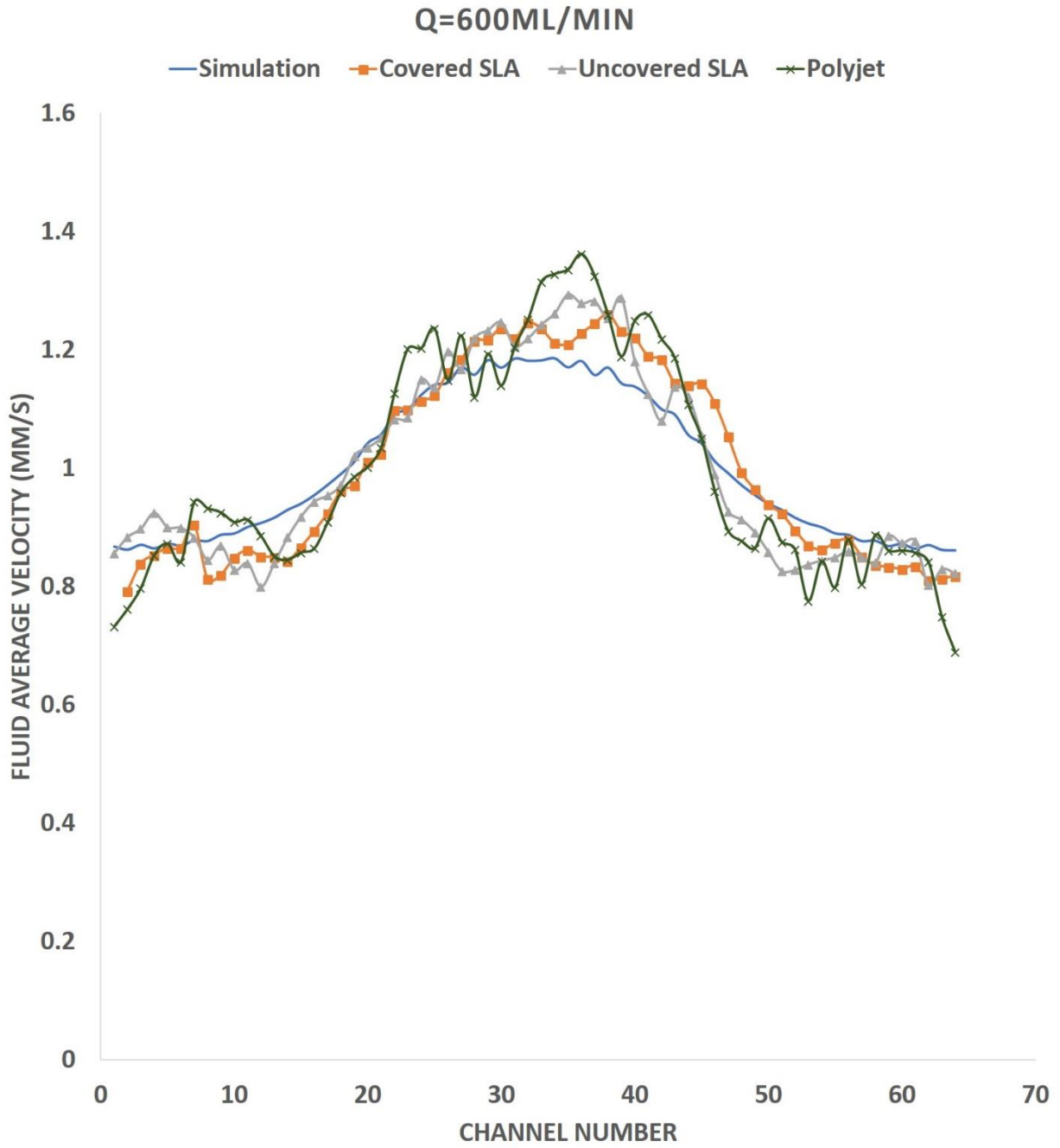


Figure 4-15: Velocity profile in cathode prototype BPPs with 0.635 mm hydraulic diameter, Q=600 ml/min.

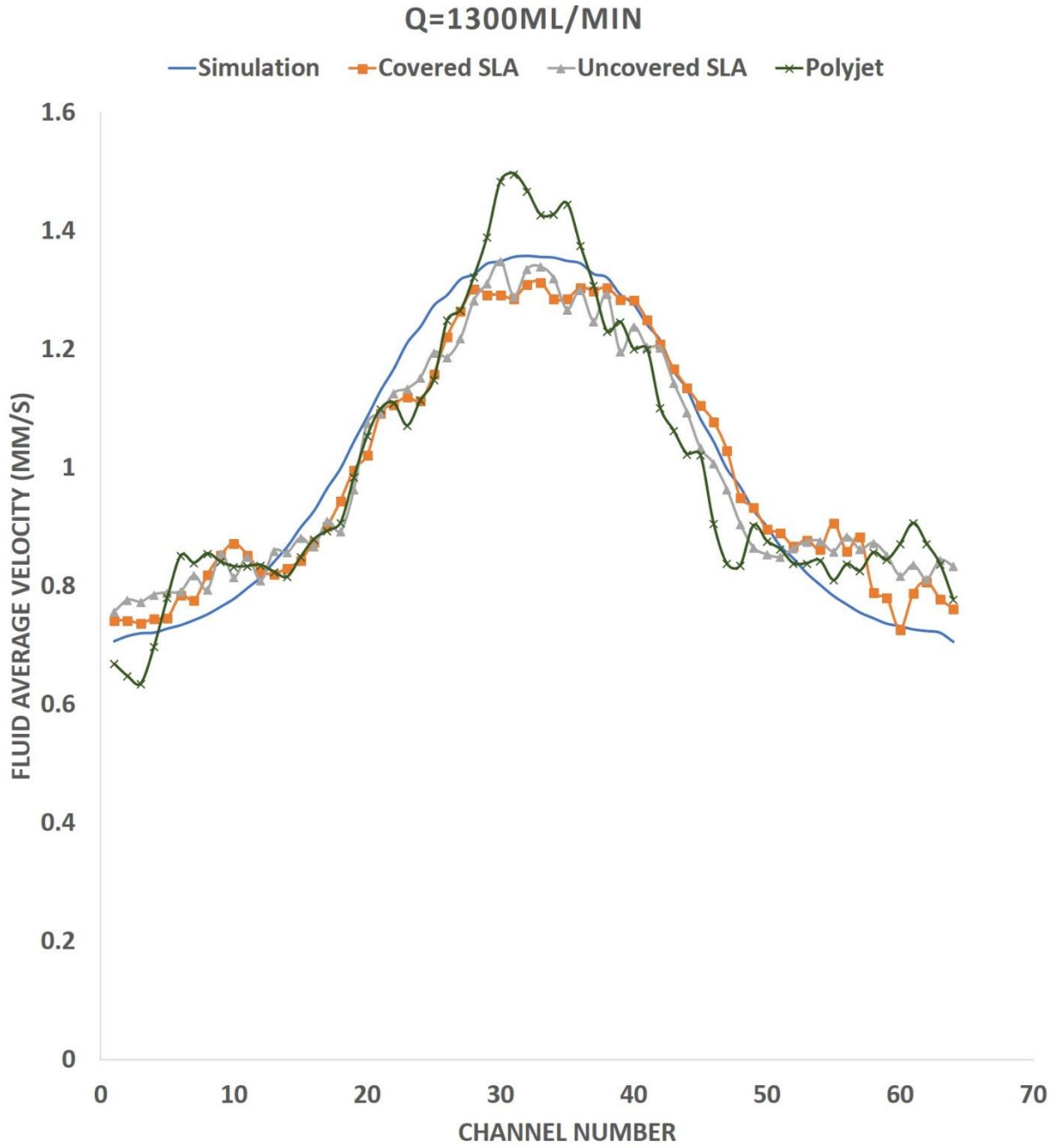


Figure 4-16: Velocity profile in cathode prototype BPPs with 0.635 mm hydraulic diameter, Q=1300 ml/min.

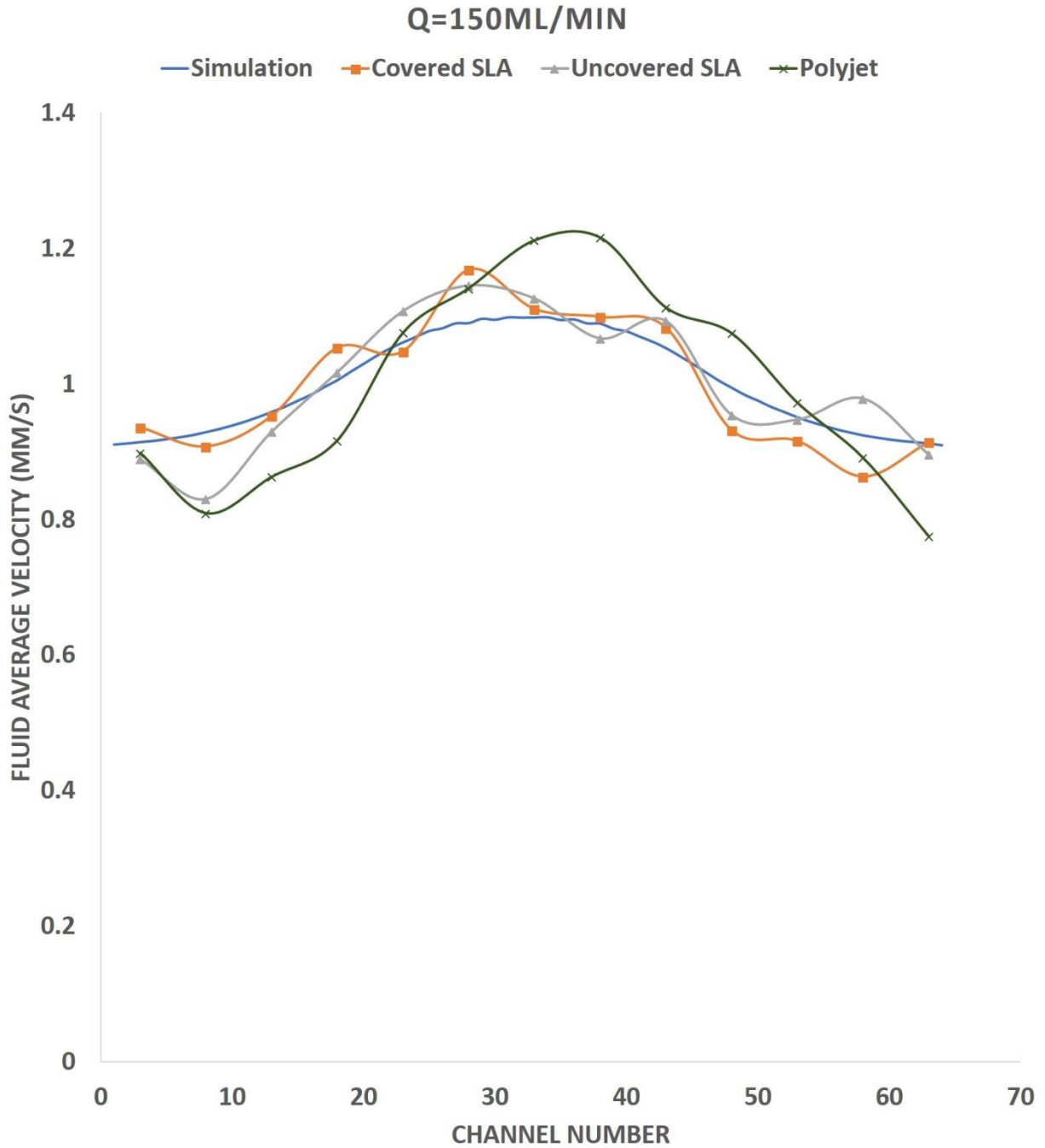


Figure 4-17: Velocity profile in cathode prototype BPPs with 0.635 mm hydraulic diameter, Q=150 ml/min. There exist 13 points on the graphs of covered SLA, uncovered SLA and Polyjet such that point K (K=1:13) represents the average velocity of 5 channels with channel numbers 5K-4,5K-3,5K-2,5K-1,5K.

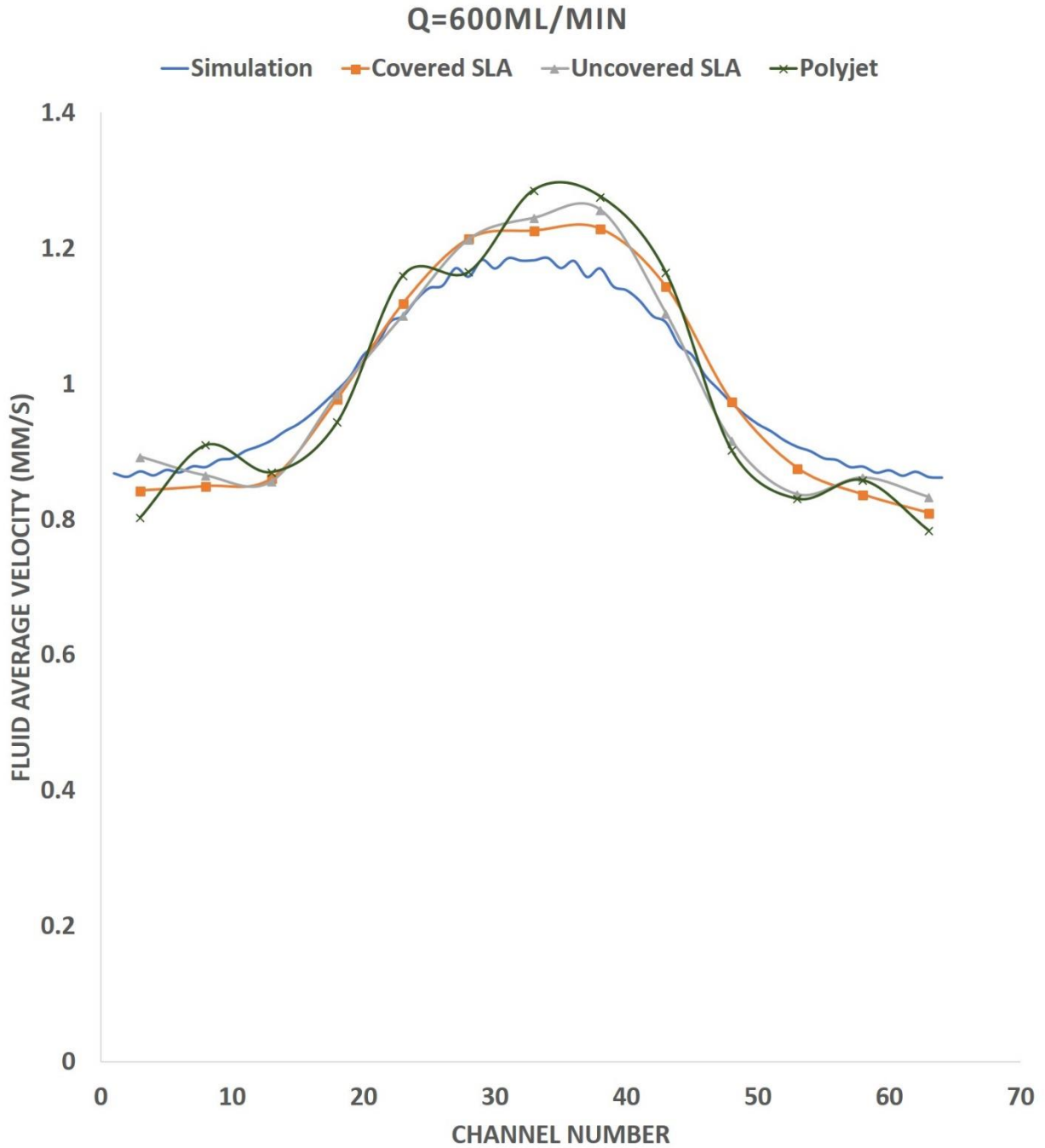


Figure 4-18: Velocity profile in cathode prototype BPPs with 0.635 mm hydraulic diameter, Q=600 ml/min. There exist 13 points on the graphs of covered SLA, uncovered SLA and Polyjet such that point K (K=1:13) represents the average velocity of 5 channels with channel numbers 5K-4,5K-3,5K-2,5K-1,5K.

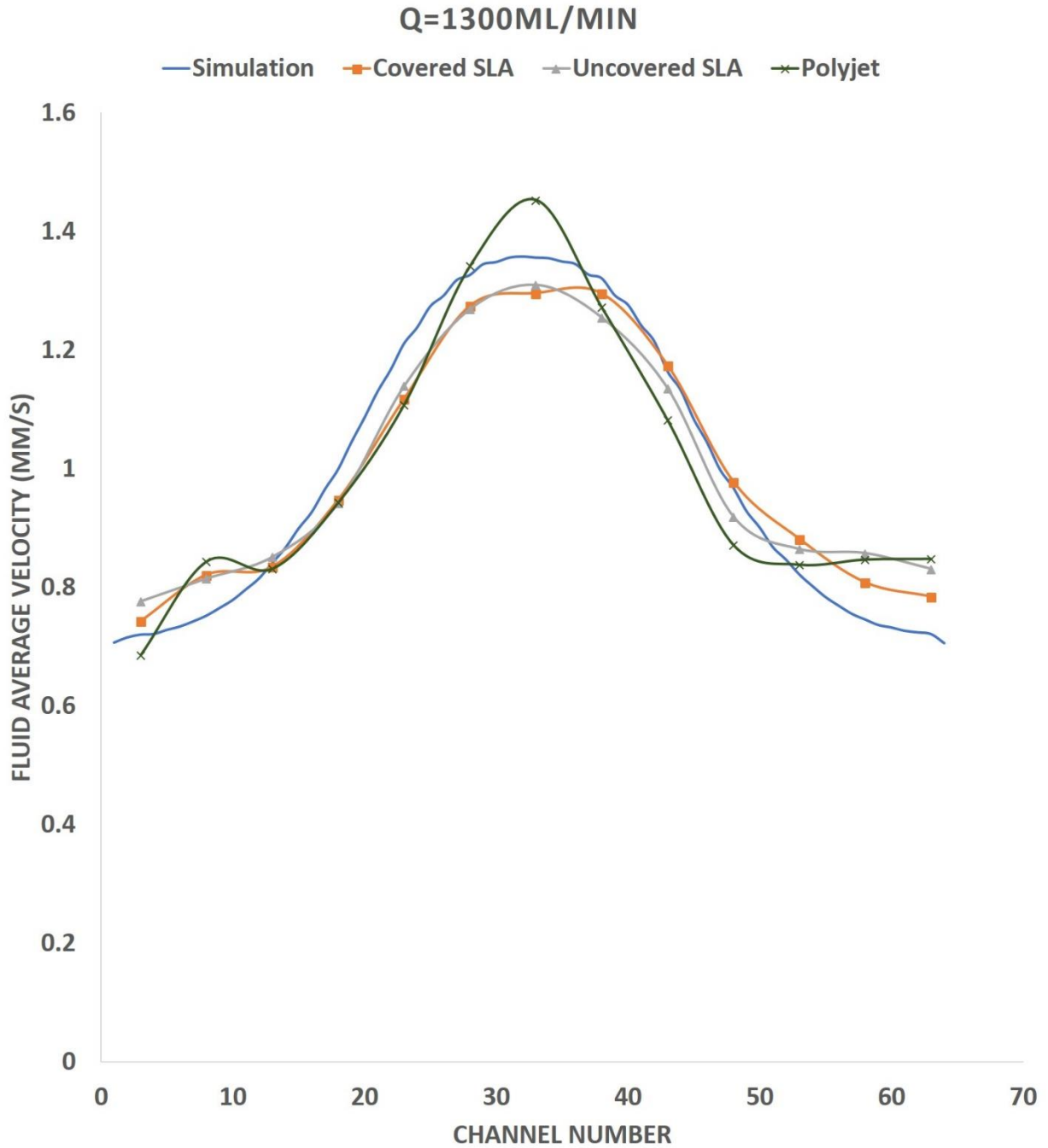


Figure 4-19: Velocity profile in cathode prototype BPPs with 0.635 mm hydraulic diameter, Q=1300 ml/min. There exist 13 points on the graphs of covered SLA, uncovered SLA and Polyjet such that point K (K=1:13) represents the average velocity of 5 channels with channel numbers 5K-4,5K-3,5K-2,5K-1,5K.

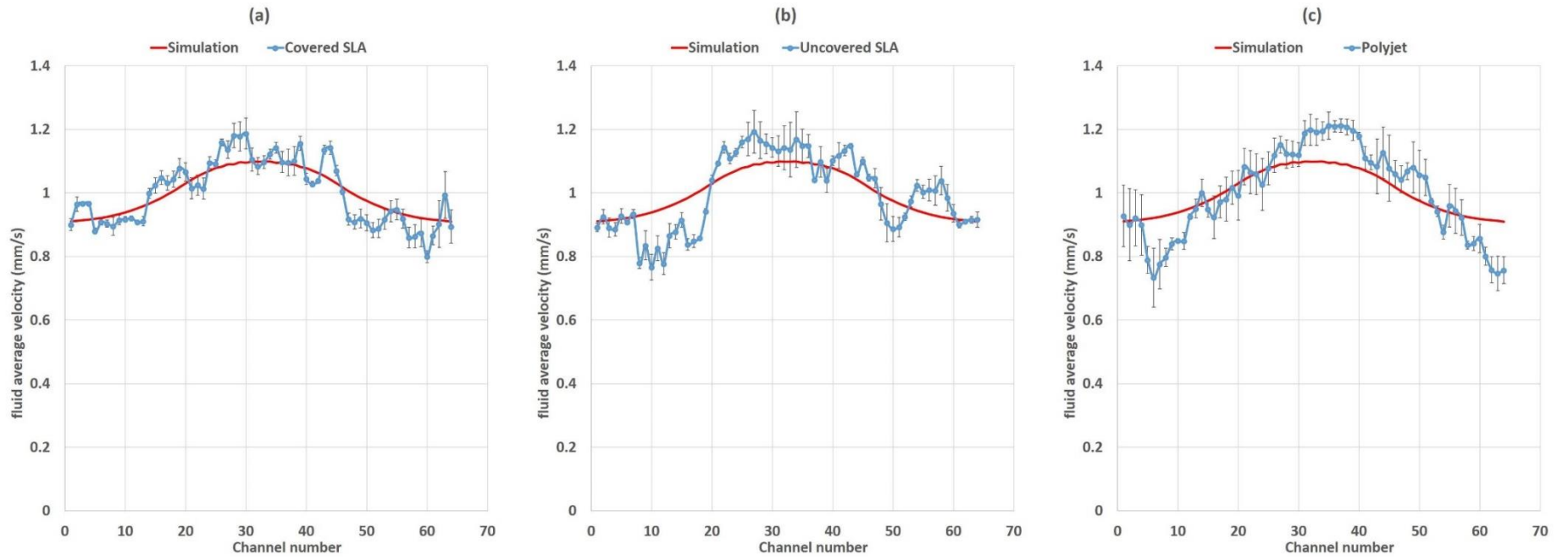


Figure 4-20: Velocity profile in cathode prototype BPPs with 0.635 mm hydraulic diameter,  $Q=150$  ml/min.

a) SLA with a layer 3D printed on top of channels, b) SLA 3D printed without a layer 3D printed on top of the channels, c) Polyjet 3D printed.

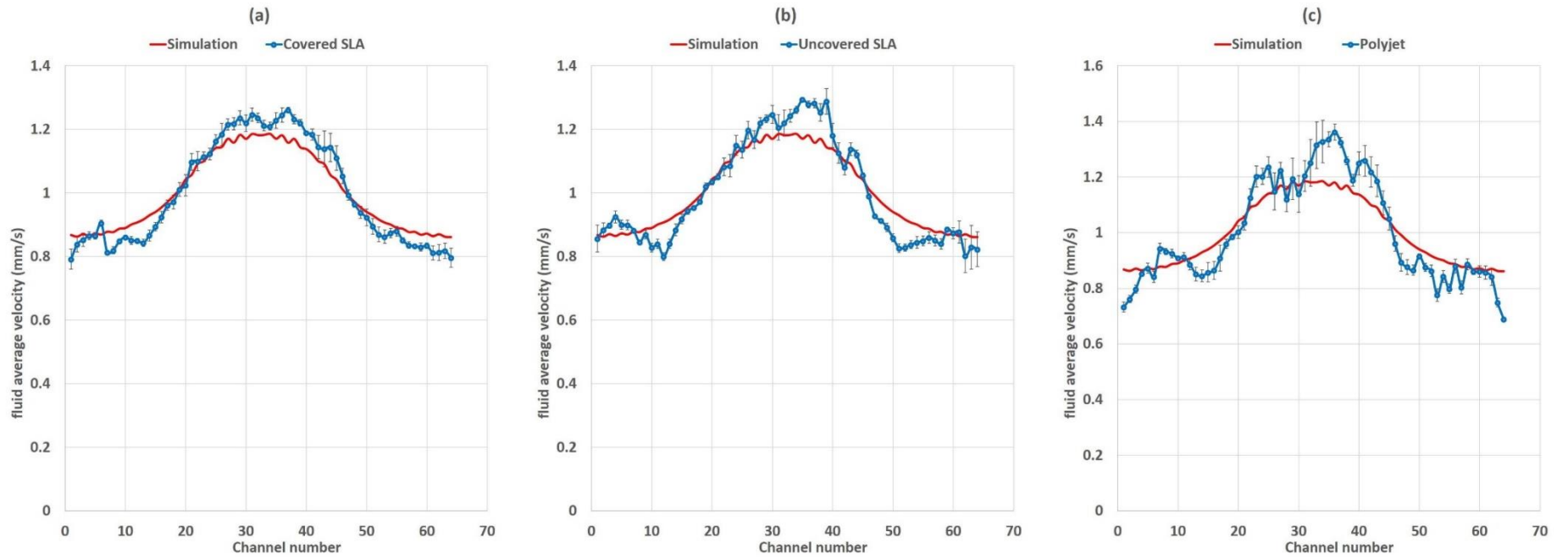


Figure 4-21: Velocity profile in cathode prototype BPPs with 0.635 mm hydraulic diameter,  $Q=600$  ml/min.

a) SLA with a layer 3D printed on top of channels, b) SLA 3D printed without a layer 3D printed on top of the channels, c) Polyjet 3D printed.

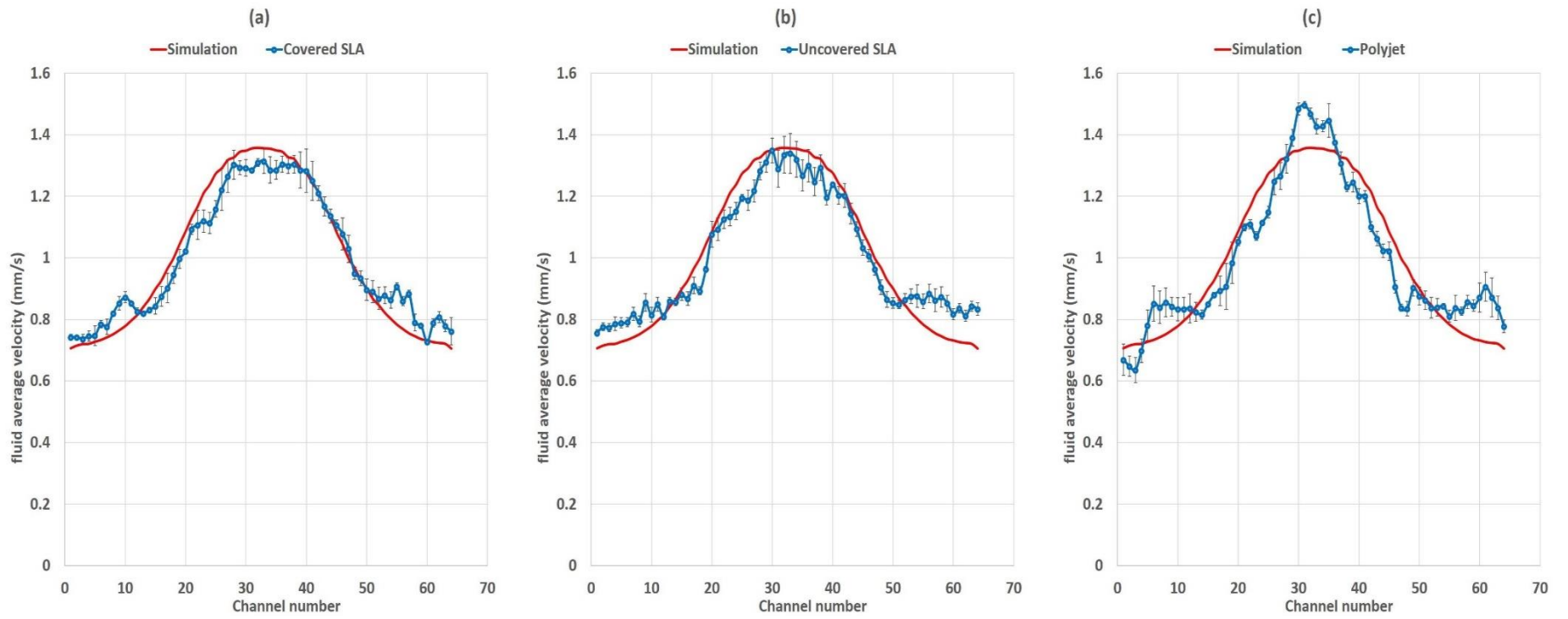


Figure 4-22: Velocity profile in cathode prototype BPPs with 0.635 mm hydraulic diameter,  $Q=1300$  ml/min.

a) SLA with a layer 3D printed on top of channels, b) SLA 3D printed without a layer 3D printed on top of the channels, c) Polyjet 3D printed.

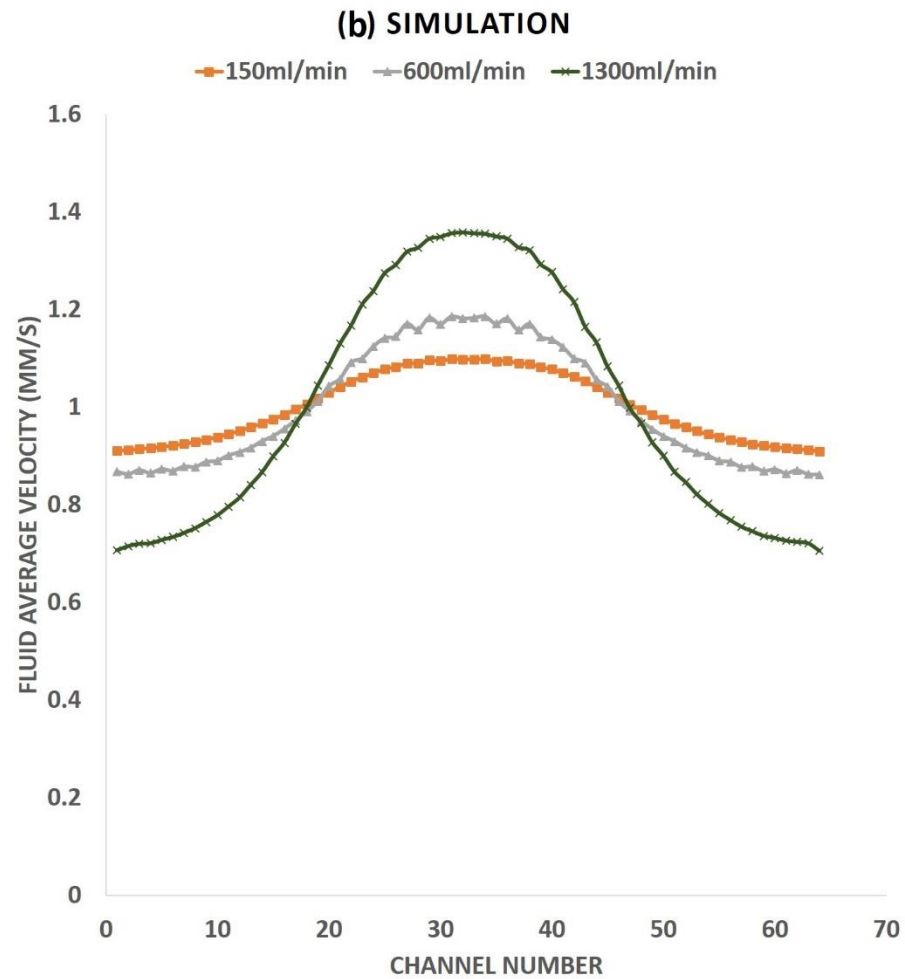
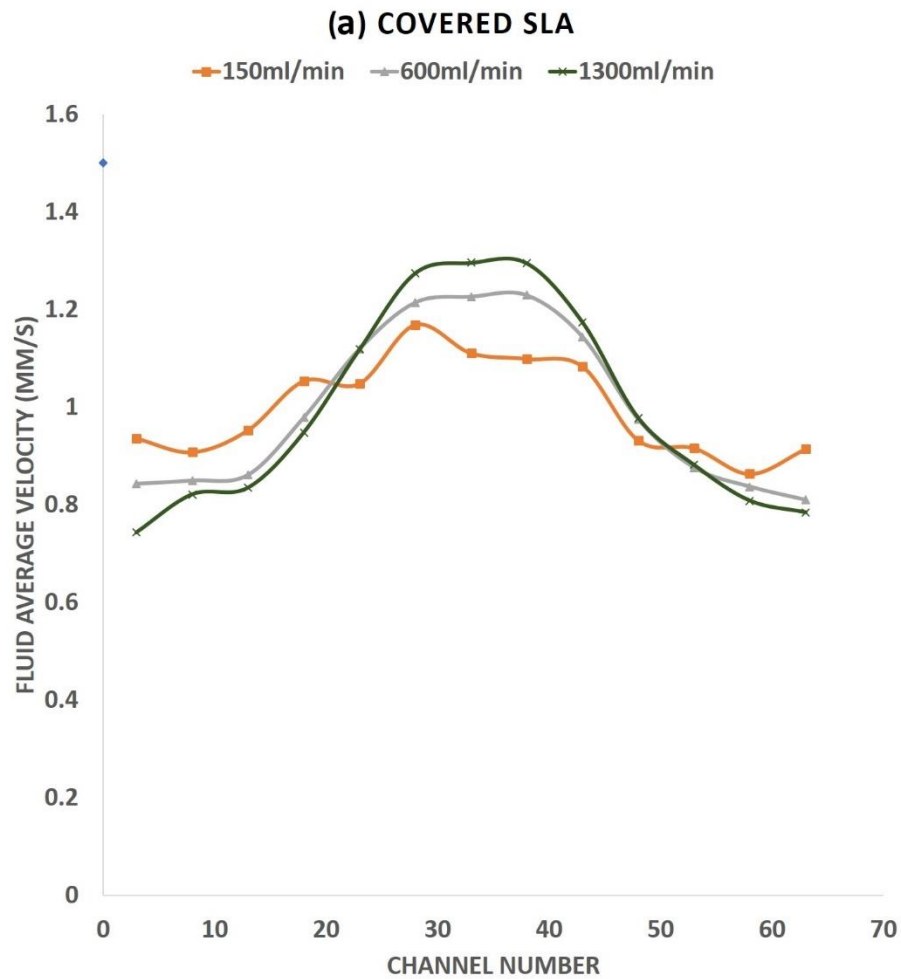


Figure 4-23: Velocity profile in cathode BPP with 0.635 mm hydraulic diameter in 150, 600, 1200 ml/min. a) Covered SLA 3D printed cathode BPP, b) Simulated cathode BPP.

Table 4-3: Statistical analysis of velocity-profile data from 6 prototype cathode BPPs versus the simulation results.

BPP #	Technology	BPP type	Number of channels	Flow rate (ml/min)	Average discrepancy from simulation (%)	Max discrepancy (%)	WLS $\times 10^{-5}$	$\beta$	COV (%)	$\frac{\bar{U}_{avg}^*}{Q/nA}$	$\bar{SE}^{**}$ (%)
2	Polyjet	Cathode	101	150	10.64	33.21	1458	1.25	0.1141	1.822	6.43
				363	9.64	35.70	1370	1.41	0.1409	1.670	5.93
				650	10.30	27.24	1450	1.32	0.1464	1.772	6.16
3	Polyjet	Cathode	64	150	7.93	19.40	754	1.23	0.1490	1.497	4.81
				600	6.54	19.98	453	1.36	0.1860	1.454	3.00
				1300	7.81	24.79	639	1.48	0.2330	1.406	3.03
4	SLA	Cathode	101	150	4.12	10.24	268	1.18	0.0819	1.328	5.02
				363	3.81	11.42	255	1.21	0.0944	1.316	5.25
				650	3.70	10.90	204	1.24	0.1148	1.241	4.67
5	SLA	Cathode (Uncovered)	64	150	4.63	19.77	639	1.17	0.1070	1.335	2.92
				600	4.43	12.67	305	1.29	0.1620	1.312	1.98
				1300	6.49	18.13	449	1.35	0.1930	1.277	2.70
6	SLA	Cathode (Covered)	64	150	4.34	12.93	238	1.18	0.1010	1.254	2.52
				600	4.10	8.93	272	1.26	0.1620	1.244	1.90
				1300	5.00	17.01	324	1.31	0.2040	1.237	2.67
7	Laser-cutter	Cathode	101	150	5.36	19.82	319	1.17	0.0776	1.041	5.12
				363	7.44	18.27	810	1.28	0.1348	1.010	4.43
				650	6.18	17.38	706	1.27	0.1512	0.910	5.51
11	Simulation 1	Cathode	64	150	0	0	0	1.10	0.0660	0.987	<0.25
				600	0	0	0	1.19	0.1200	0.983	<0.25
				1300	0	0	0	1.36	0.2420	0.976	<0.25
12	Simulation 2	Cathode	101	150	0	0	0	1.07	0.0525	0.990	<0.25
				363	0	0	0	1.09	0.0632	0.979	<0.25
				650	0	0	0	1.13	0.0854	0.971	<0.25

\* The ratio of actual mean average velocity over expected mean average velocity.

\*\*Average standard error.

#### 4.3.1.1.1 Effect of flow rate on velocity measurement precision

Comparing Figure 4-20-a, Figure 4-21-a and Figure 4-22-a, which demonstrates the velocity profile of the covered SLA BPP at flow rates of 150, 600 and 1300 ml/min, reveals that at higher flow rates, the trend of the velocity profile becomes closer to that of simulation. This is more evident in the case of uncovered SLA BPP, which can be seen from comparing Figure 4-20-b, Figure 4-21-b and Figure 4-22-b, and also is true for the Polyjet BPP, which can be seen from comparing Figure 4-20-c, Figure 4-21-c and Figure 4-22-c. Comparing the velocity profile trends between Figure 4-17, Figure 4-18 and Figure 4-19 further supports this observation.

This is because of the disturbance of dye injection to the steady flow, which is more sensible at flow rate of 150 ml/min and is alleviated at higher flow rates. Moreover, the dye is mixed better with water at higher flow rates, which lead the channels to experiencing equal dye concentration. The values of average and maximum discrepancy between experiment and simulation results, as well as the average standard error are highest in the lowest flow rate (150 ml/min), as shown in Table 4-3, which confirms the high disturbance of the tracer at low flow rates. This makes the results of the 150 ml/min flow rate less reliable than results from 600 ml/min and 1300 ml/min flow rates. The values of average and maximum discrepancy between experimental and simulation results as well as the average standard error, however, are higher in the flow rate of 1300 ml/min than 600 ml/min. This is because of the higher velocity measurement error at high flow rates, as discussed in section 3.9.3.

#### 4.3.1.1.2 Comparing the velocity profiles of prototype cathode BPPs with 0.635 mm hydraulic diameter

##### 4.3.1.1.2.1 Covered SLA

Comparing the velocity profiles of BPPs#3, #5 and #6 at each flow rate in Figure 4-14, Figure 4-22 demonstrates that enclosed cathode plate 3D printed by SLA technology (BPP#6) has the best agreement with simulation results. The trend of the velocity profile from covered SLA plate is very close to that of simulation and does not contain unexpected local deviations from expectation, as opposed to

Polyjet plate. The values of average discrepancy between velocity profile of covered SLA plate and that of simulation at flow rates of 150, 600 and 1300 ml/min are 4.3% ,4.1% and 5.0 %, respectively, as shown in Table 4-3. Moreover, the values of maximum discrepancy between velocity profile of covered SLA plate and that of simulation at flow rates of 150, 600 and 1300 ml/min are 13.0%, 9.0% and 17.0%, respectively, as shown in Table 4-3. In addition, the average standard error of the results from covered SLA plate in flow rates of 150, 600 and 1300 ml/min are 2.52%, 1.90% and 2.67%, respectively, as shown in Table 4-3. We take these errors as acceptable and attribute the discrepancies to the errors in experiment and flow visualization technique, disturbance of dye injection system, and to the non-uniformity in channels size distribution. This observation validates the simulation results and proves that our proposed method for 3D printing serves as a reliable fast screening method for promptly evaluating the design performance.

#### 4.3.1.1.2.2 Uncovered SLA

The uncovered SLA BPP (BPP#5) performs very similar to the covered SLA plate (BPP#6) and the values of maximum and average discrepancy between uncovered SLA and simulation results as well as the standard error are slightly larger in uncovered SLA plate (BPP#5). The differences between the velocity profiles of covered and uncovered SLA plate arise from the tightening of uncovered SLA plate in the transparent cell and non-uniform tension distribution over the active area. However, the differences are not significant due to the good mechanical strength of SLA 3D printing material.

The other observation from Figure 4-14 and Figure 4-22 is that velocity profiles from covered and uncovered SLA plates are more non-uniform than simulated velocity profiles at 150 ml/min and 600 ml/min, while they are slightly less non-uniform than the simulation at 1300 ml/min. One reason for this behavior is that at lower flow rates, where tracer is not mixed well with the water, the channels with higher fluid velocity (faster channels) experience a higher concentration of dye while the side channels with lower velocity receive low-concentration tracer. A threshold is used in the flow visualization

analysis such that when dye concentration in a pixel is lower than a certain amount, the entrance of dye to that pixel becomes undetectable, resulting in lower velocities obtained for side channels than actual velocity, which leads to more stretched profiles. The other reason for this could be the minor errors in simulation results.

#### 4.3.1.1.2.3 Polyjet

The values of average and maximum discrepancy between velocity profiles of Polyjet cathode plate and simulated cathode plate, as shown in Table 4-3, are greater than those of both SLA plates. The other noticeable point is that the velocity profile of Polyjet 3D printed cathode BPP shows more fluctuation around the trend line than SLA plates. This is because of the non-uniformity of channel size distribution in Polyjet plate compared to SLA plates. One reason for non-uniform channel size distribution is the inherent non-uniformity during the 3D printing. The other reason is that the Polyjet material is prone to deformation, by which the non-uniform stress distribution over the active area increases the non-uniformity in the channel size distribution.

Table 4-3 presents that the values of standard error in covered SLA and uncovered SLA plates are close to each other, and less than that of Polyjet BPP. This suggests that experimental results in covered and uncovered SLA plates are more repeatable than in Polyjet BPP. The standard error in BPPs with 0.635 mm hydraulic diameter is 2-3%, which is acceptable.

As it is evident from Figure 4-20, Figure 4-21 and Figure 4-22, one of the main differences between velocity profiles of SLA and Polyjet BPPs is that the velocity profile of Polyjet BPP is more stretched. Consistently, the COV and  $\beta$  values of Polyjet BPP are greater than those of covered and uncovered SLA BPPs, as shown in Table 4-3. This happens because the deformation by the force applied to the two sides of the transparent cell which puts more stress on the BPP side channels than middle channels, decreasing the channels cross-section surface area of side channels which, in turn, increases the channel resistance and directs more fluid to the middle channels. Such a behavior can also be observed in

uncovered SLA BPP, which has slightly more COV than covered SLA plate at flow rates of 600 ml/min and 1300 ml/min. All these observations lead us to conclude that SLA plates have better a performance than Polyjet 3D printed BPP.

#### 4.3.1.1.3 Experimentally calculated vs. actual mean average fluid velocity

As mentioned before, the velocity profiles are normalized for a better comparison, and the discrepancy between the actual and expected mean average fluid velocity could also assist us to check the flow visualization authenticity and to provide us with information about the deformation of different plates.

The values of  $\bar{U}_{avg} / (Q/nA)$ , which is the ratio of actual to expected average mean velocity, are presented for each prototype BPP at different flow rates in Table 4-3. This value does not vary significantly for each BPP at different flow rates, which suggests that this is the characteristic of each BPP and can be used to infer the degree of deformation for each plate. Based on eq. (14), it can be concluded that the ratio of actual to expected average mean velocities equals the ratio of expected to actual cross-section area, as shown in eq. (38). On the other hand, it was shown that the slope of pressure-drop curve from each BPP is reciprocally proportional to the square of the cross-section area. Combining this with eq. (38) results in eq. (39), which demonstrates that the ratio of actual to expected mean average velocities is proportional to the square root of the actual to expected slope of pressure-drop graphs.

$$\frac{\bar{U}_{avg}}{(Q/nA)} = \frac{A_{expected}}{A_{actual}} \quad (38)$$

$$\frac{\bar{U}_{avg}}{(Q/nA)} = \sqrt{\frac{m_{actual}}{m_{expected}}} \quad (39)$$

For each BPP, the ratio of actual to expected mean average fluid velocities is presented at different flow rates in Table 4-3, which is further averaged to give a single number for each BPP. The ratios of actual to expected mean average fluid velocities for covered SLA, uncovered SLA and Polyjet BPP are 1.245, 1.308 and 1.452, respectively. On the other hand, as reported in Table 4-2, the ratios of actual to expected slope of pressure-drop graphs for covered SLA, uncovered SLA and Polyjet BPP are 1.215, 1.322 and 1.582, respectively. Comparing these two sets of numbers reveals that the values of mean average fluid velocity in covered SLA, uncovered SLA and Polyjet BPP are 12.9%, 13.7% and 15.4% greater than expectation, respectively. These greater values of the mean average velocities are likely caused by the tracer dye injection, where pulse injection of a small amount of dye with a Dirac function suddenly increases the flow rate.

#### 4.3.1.1.4 Effect of flow rate on velocity distribution uniformity

Figure 4-22 shows the velocity profile in different flow rates from covered SLA and simulated cathode BPPs. Simulation results in Figure 4-22-b suggest that increasing the total flow rate increases the non-uniformity of flow distribution. The results from covered SLA plate in Figure 4-22-a are also consistent with this prediction. Simulating the velocity profiles at other flow rates over the 30-600 ml/min range, however, revealed that some flow rates do not follow the tendency that velocity profile further stretches at higher flow rates. The value of  $\beta$ , which is the ratio of fastest channel to the mean average fluid velocity, increases from 1.08 to 1.35 as the flow rate increases from 150 ml/min to 1300 ml/min, as shown in Table 4-3. This, along with the values of COV from covered SLA and simulated cathode BPP, suggests that although the non-uniformity at low flow rates is not severe, the velocity distribution among the channels of cathode BPP becomes more non-uniform at higher flow rates and the cathode BPP design should be optimized to achieve a more uniform fluid distribution.

#### 4.3.1.2 *Velocity profile in cathode BPPs with 0.4 mm hydraulic diameter*

Figure 4-24, Figure 4-25 and Figure 4-26 show the velocity profile in prototype BPPs with 0.4 mm hydraulic diameter at total fluid flow rates of 145, 338 and 651 ml/min, respectively. The tested BPPs are: SLA 3D printed cathode BPP (BPP#4,  $D_h=0.4$  mm), cathode BPP fabricated with laser cutter (BPP#7,  $D_h=0.4$  mm), Polyjet 3D printed cathode BPP (BPP#2,  $D_h=0.4$  mm). Since the curves for BPPs#2, #4 and #7 are plotted together in Figure 4-24, Figure 4-25 and Figure 4-26, and each curve consists of 101 data points, the figures are crowded which makes the comparison difficult. To improve the visualization, two groups of additional graphs are plotted using the data from Figure 4-24, Figure 4-25 and Figure 4-26. The first group contains Figure 4-27, Figure 4-28 and Figure 4-29 where the velocity of every 5 channel is averaged and represented by a single number. The second group contains Figure 4-30, Figure 4-31 and Figure 4-32 where the results from each BPP are plotted individually along with the simulation results. The results from measured velocity profiles are statistically compared with simulation results in Table 4-3.

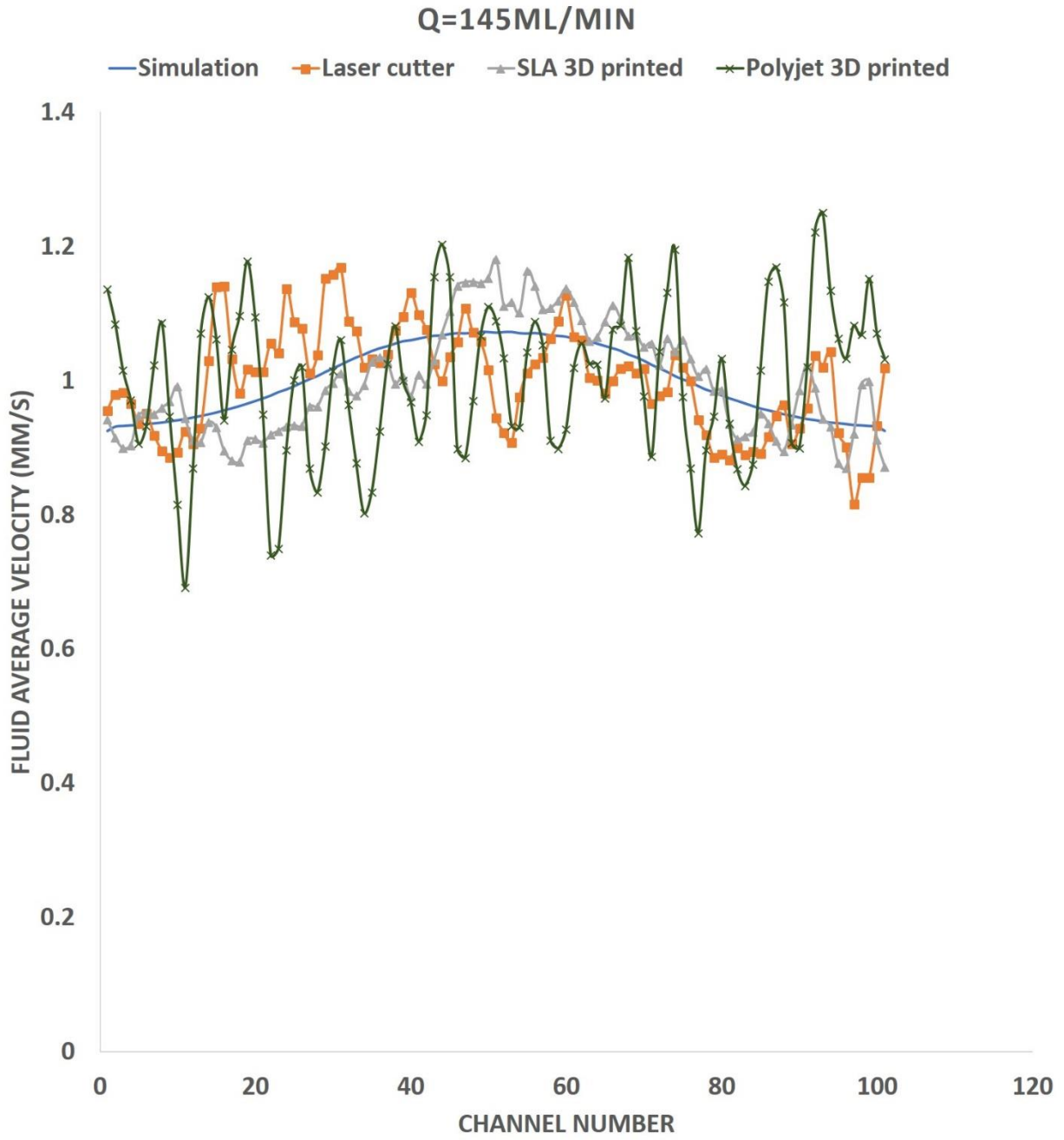


Figure 4-24: Velocity profile in cathode prototype BPPs with 0.4 mm hydraulic diameter, Q=145 ml/min.

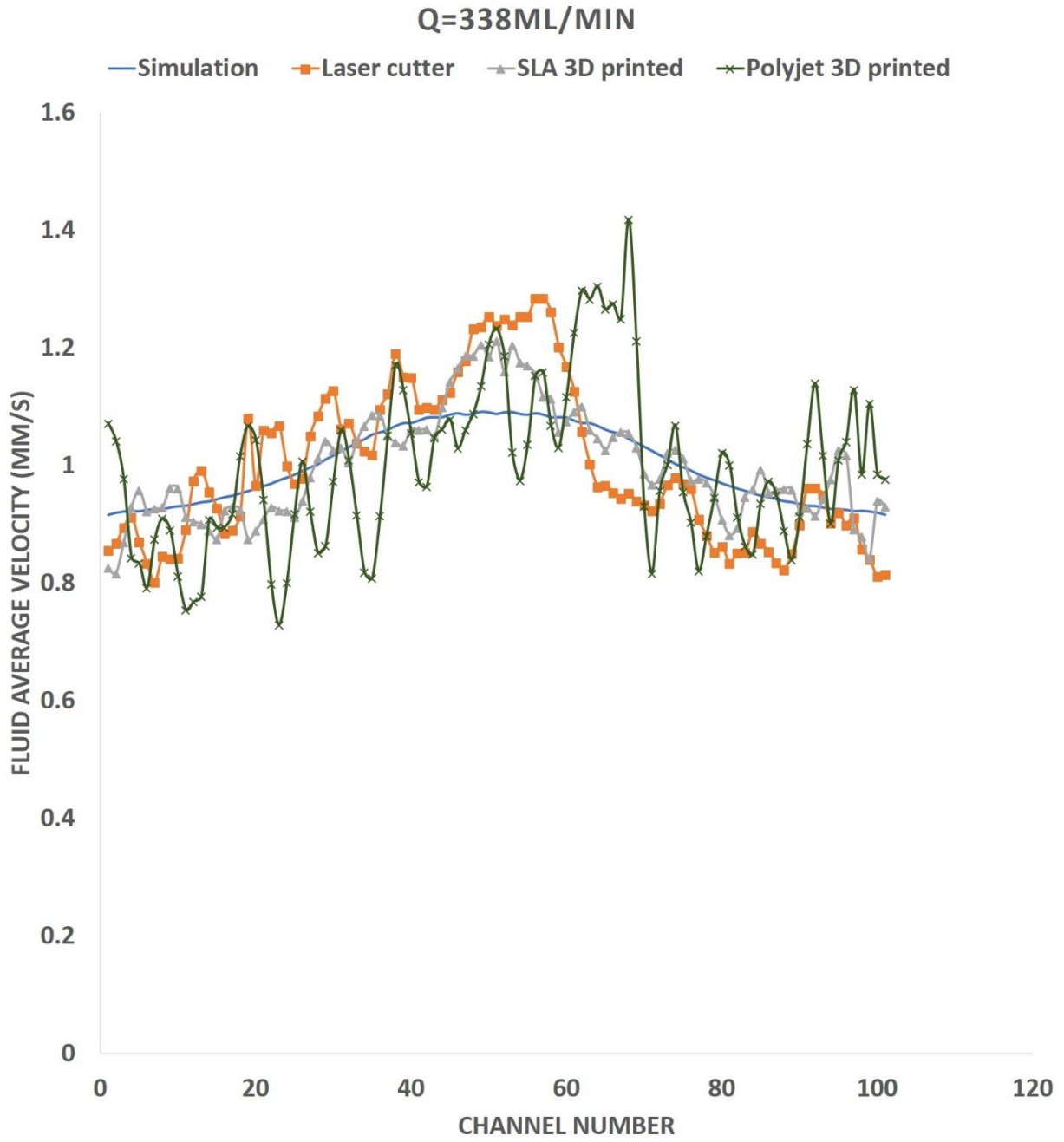


Figure 4-25: Velocity profile in cathode prototype BPPs with 0.4 mm hydraulic diameter, Q=338 ml/min.

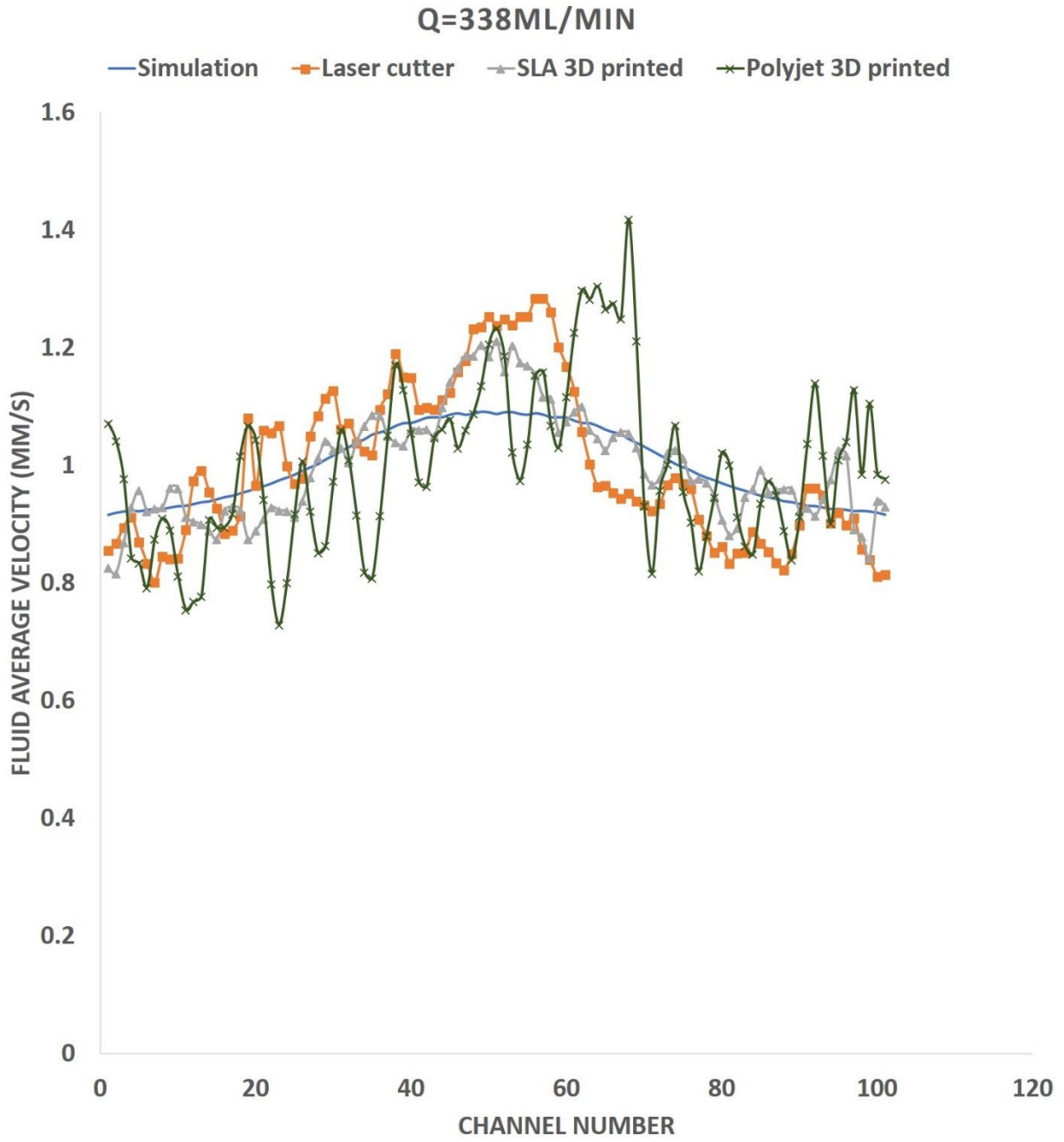


Figure 4-26: Velocity profile in cathode prototype BPPs with 0.4 mm hydraulic diameter, Q=651 ml/min.

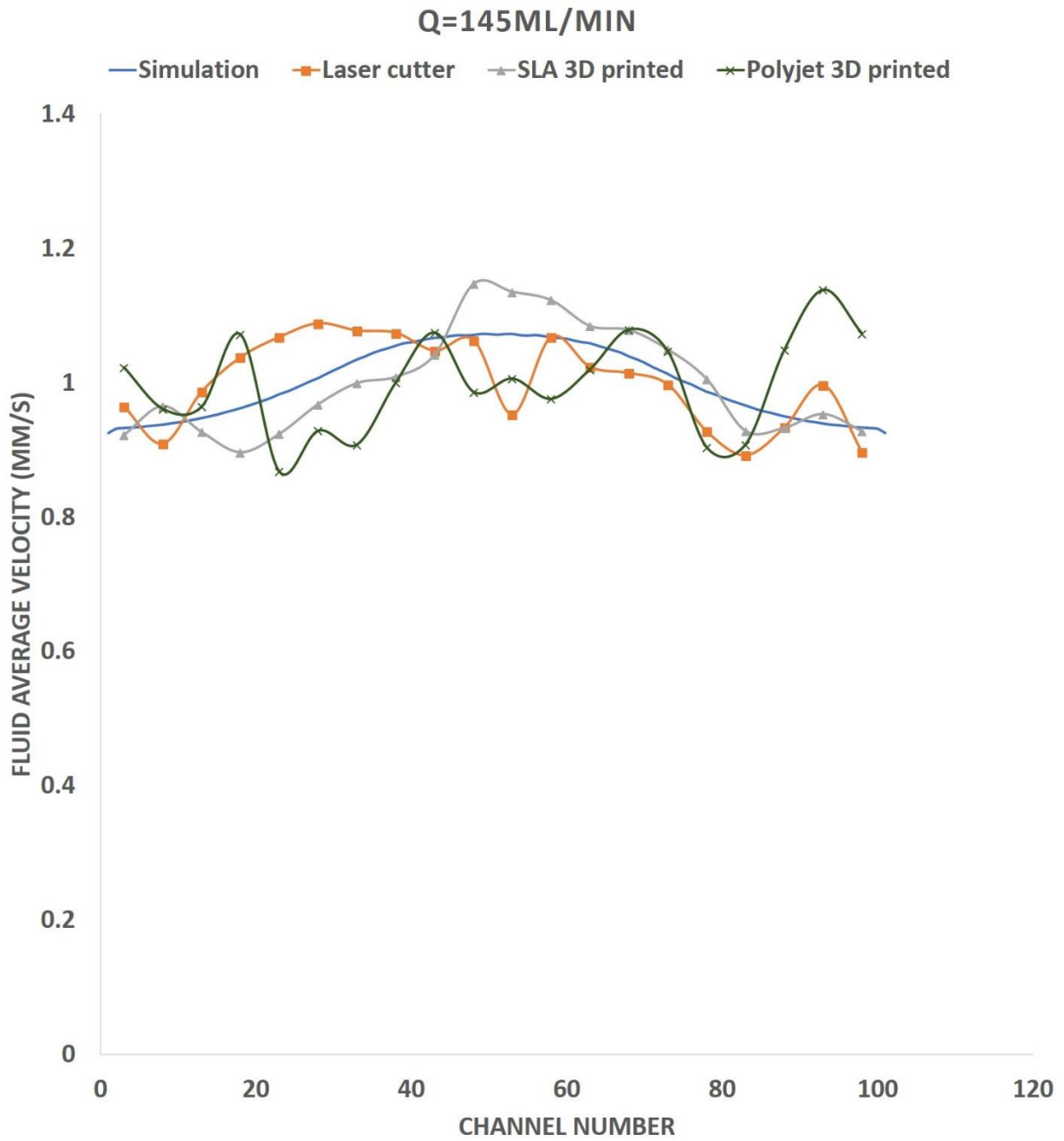


Figure 4-27: Velocity profile in cathode prototype BPPs with 0.4 mm hydraulic diameter, Q=145 ml/min. There exist 20 points on the graphs of laser cutter, SLA 3D printed and Polyjet 3D printed such that point K (K=1:20) represents the average velocity of 5 channels with channel numbers 5K-4,5K-3,5K-2,5K-1,5K.

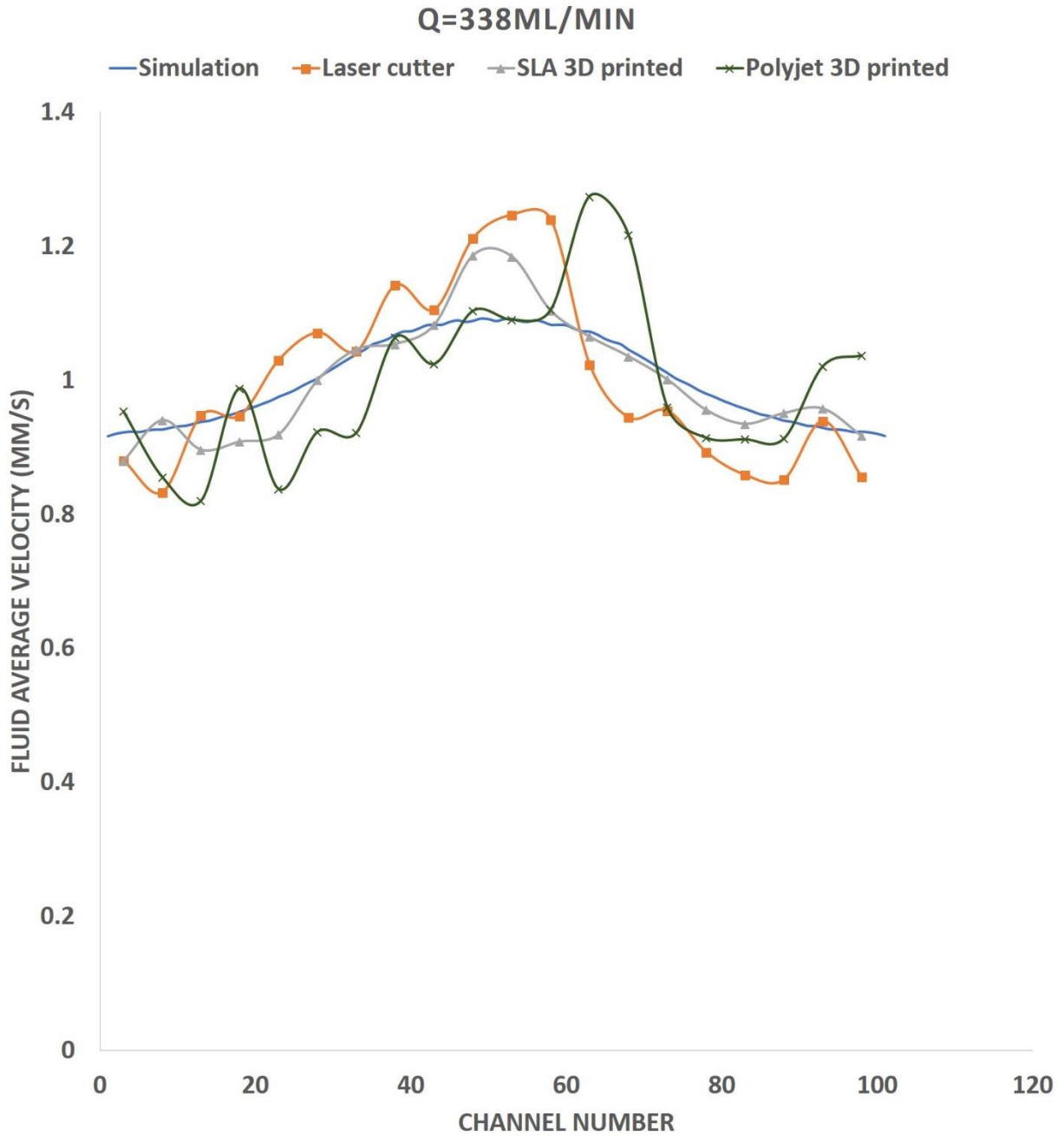


Figure 4-28: Velocity profile in cathode prototype BPPs with 0.4 mm hydraulic diameter, Q=338 ml/min. There exist 20 points on the graphs of laser cutter, SLA 3D printed and Polyjet 3D printed such that point K (K=1:20) represents the average velocity of 5 channels with channel numbers 5K-4,5K-3,5K-2,5K-1,5K.

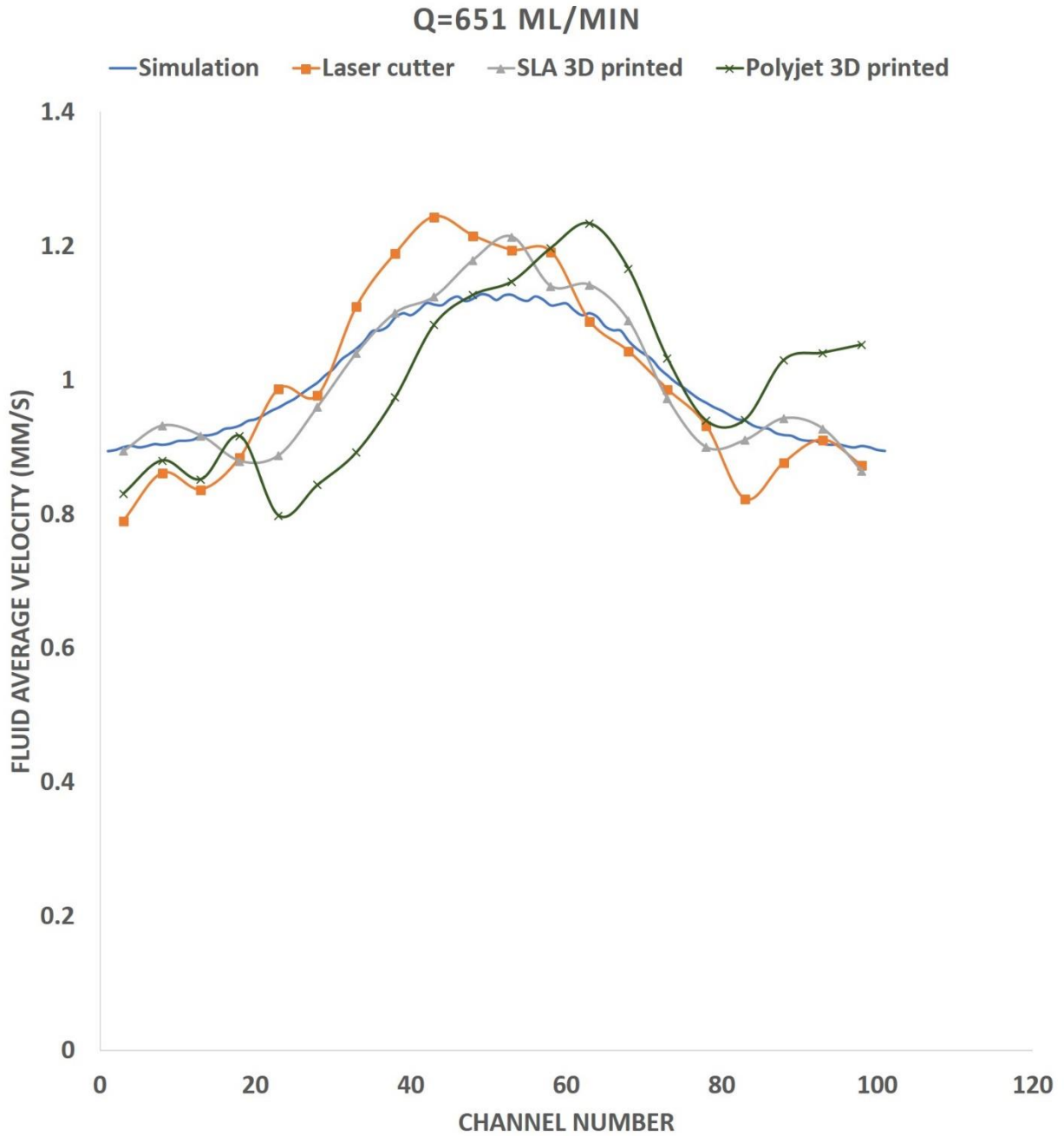


Figure 4-29: Velocity profile in cathode prototype BPPs with 0.4 mm hydraulic diameter, Q=651 ml/min. There exist 20 points on the graphs of laser cutter, SLA 3D printed and Polyjet 3D printed such that point K (K=1:20) represents the average velocity of 5 channels with channel numbers 5K-4,5K-3,5K-2,5K-1,5K.

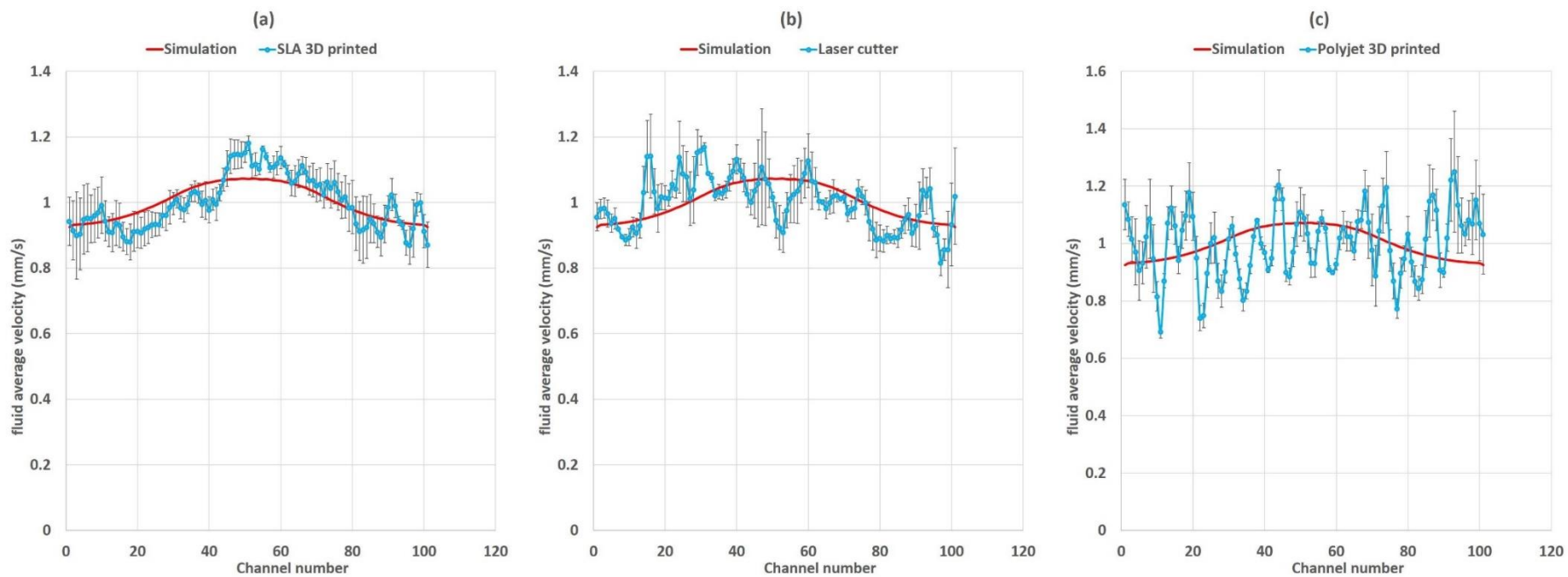


Figure 4-30: Velocity profile in cathode prototype BPPs with 0.4 mm hydraulic diameter,  $Q=145$  ml/min.

a) SLA 3D printed, b) Laser cutter, c) Polyjet 3D printed.

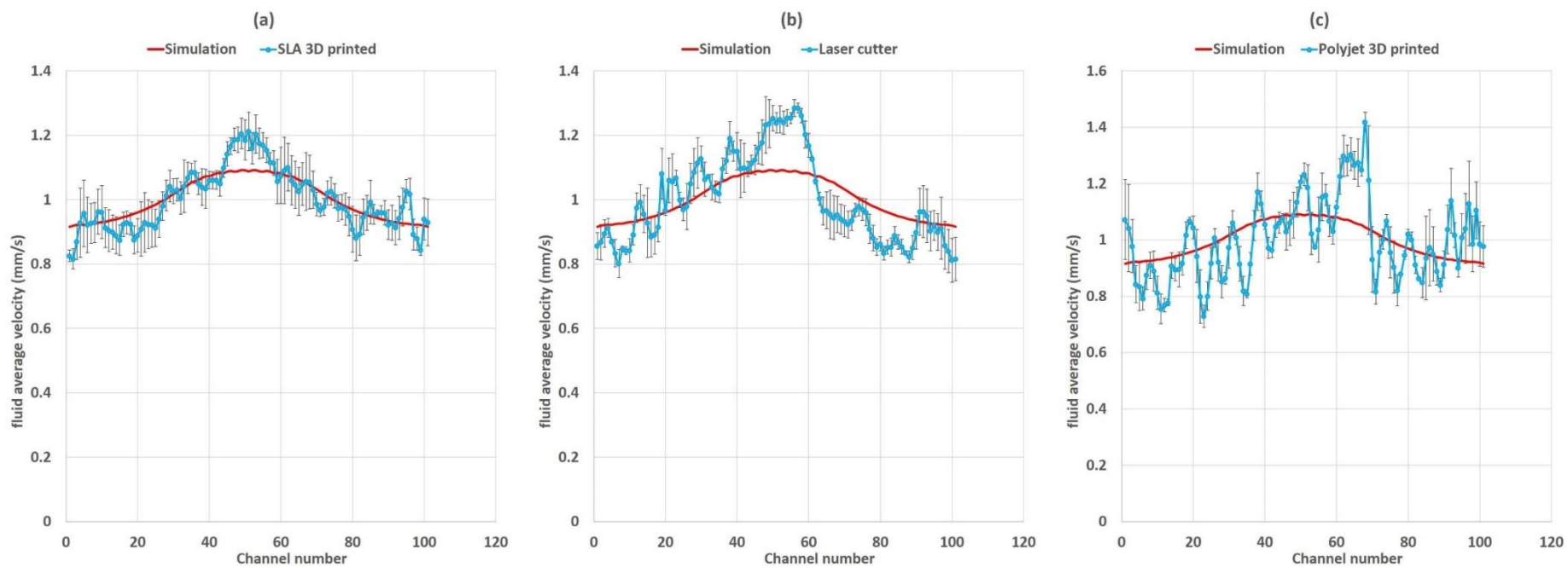


Figure 4-31: Velocity profile in cathode prototype BPPs with 0.4 mm hydraulic diameter,  $Q=338$  ml/min.

a) SLA 3D printed, b) Laser cutter, c) Polyjet 3D printed.

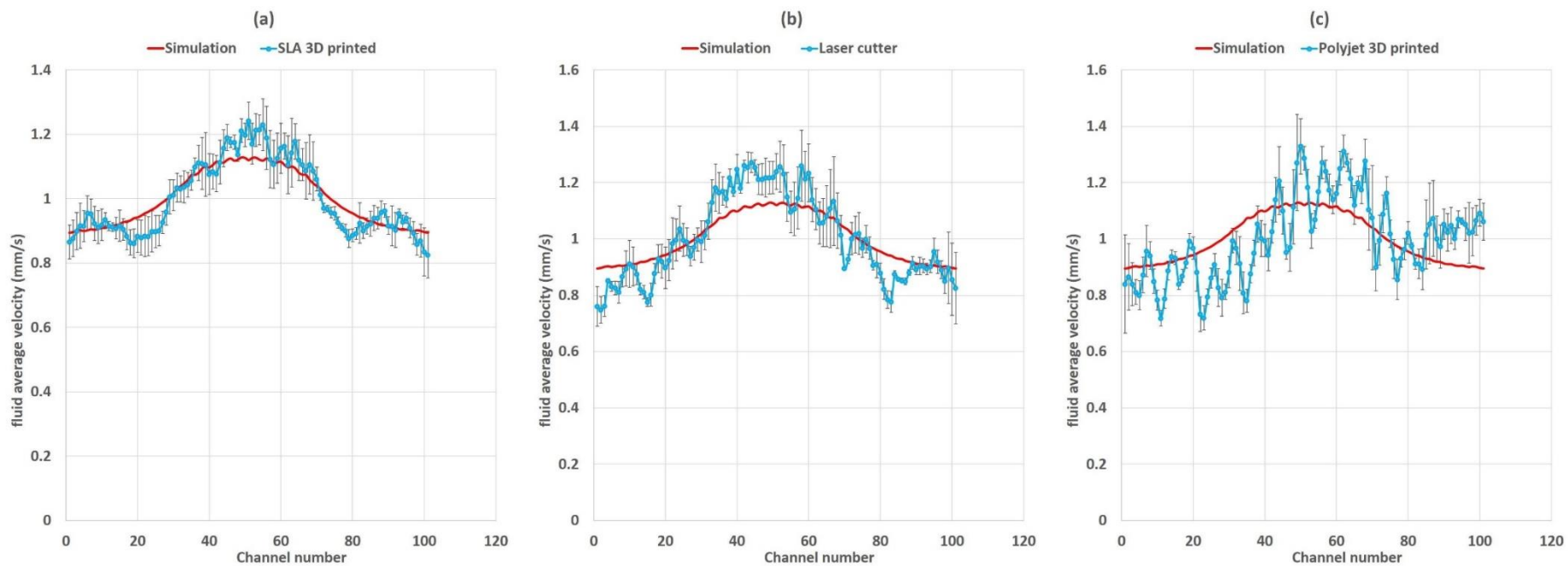


Figure 4-32: Velocity profile in cathode prototype BPPs with 0.4 mm hydraulic diameter,  $Q=651$  ml/min.

a) SLA 3D printed, b) Laser cutter, c) Polyjet 3D printed.

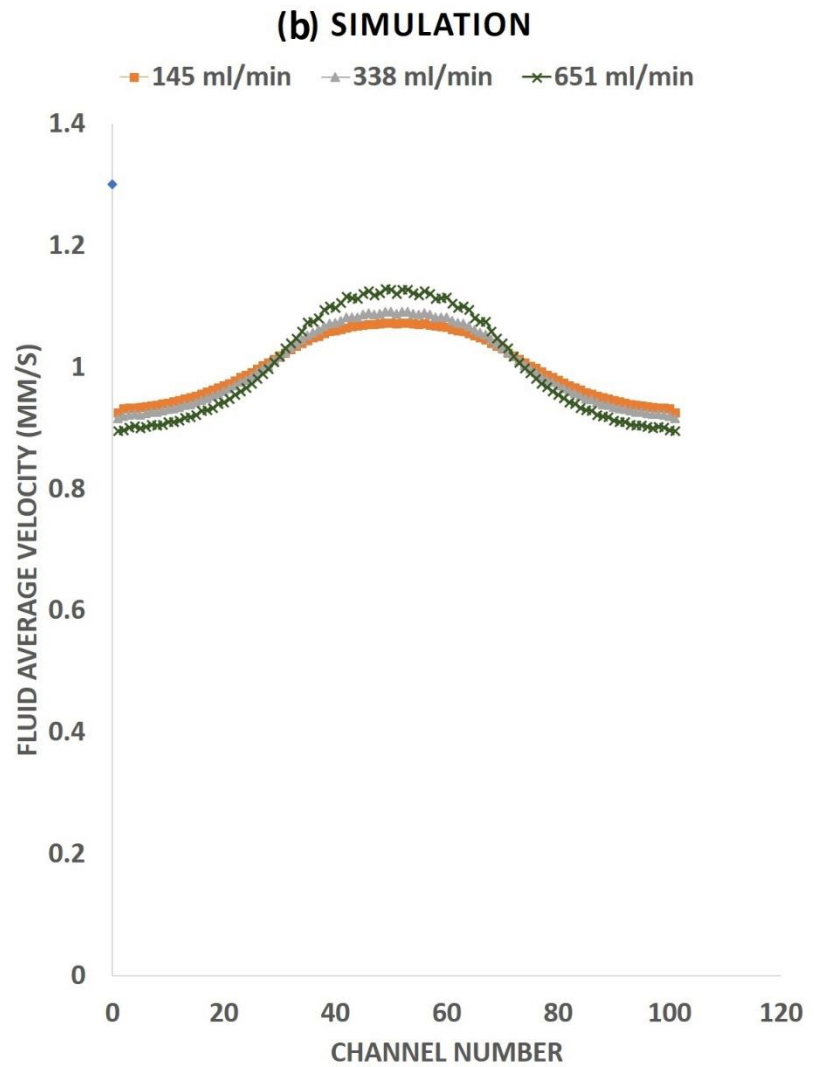
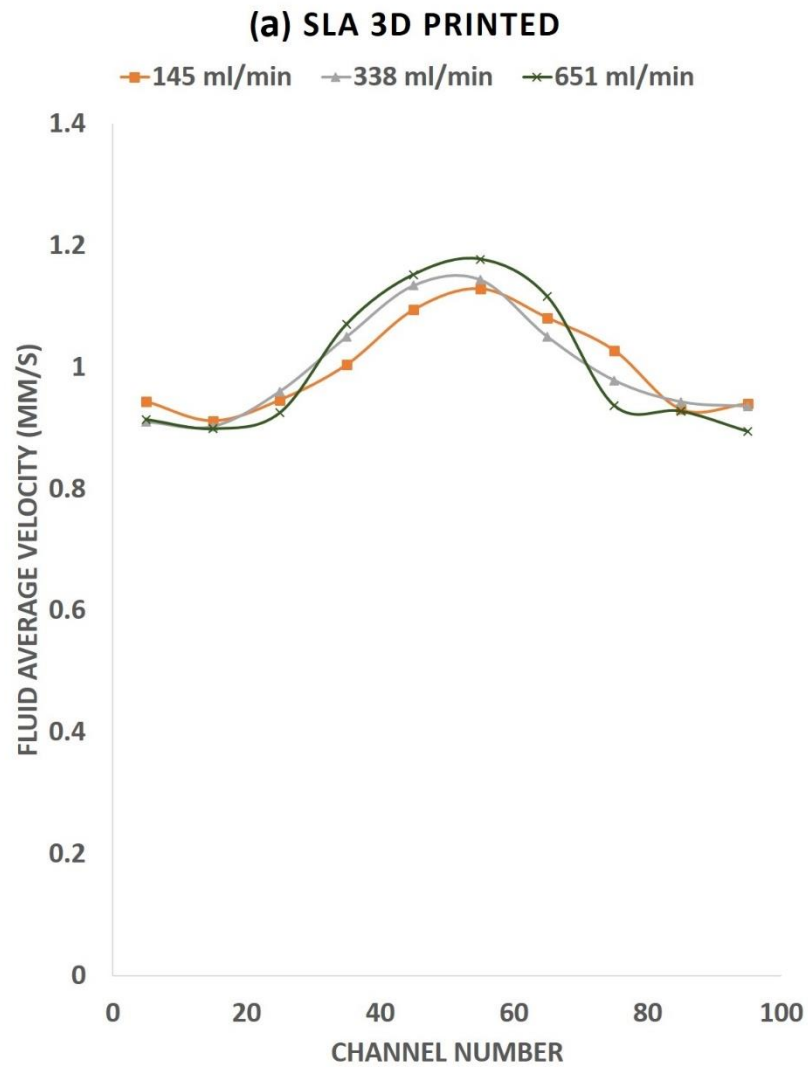


Figure 4-33: Velocity profile in cathode BPP with 0.4 mm hydraulic diameter in 145, 338, 651 ml/min. a) SLA 3D printed cathode BPP, b) Simulated cathode BPP.

#### 4.3.1.2.1 Effect of flow rate on velocity measurement precision

Comparing Figure 4-30-a, Figure 4-31-a and Figure 4-32-a, which demonstrates the velocity profile of the SLA BPP (BPP#4) at 145, 338 and 651 ml/min, reveals that at higher flow rates, the trend of the velocity profile becomes closer to that of simulation, similar to what observed in SLA BPPs with 0.635 mm diameter. This is also true for the velocity profiles of laser-cut BPP, which can be seen from comparing Figure 4-30-b, Figure 4-31-b and Figure 4-32-b. As discussed before, the closeness of the measured velocity profile to expected one at higher flow rates is a result of the disturbance and mixing effect of the tracer injection, which differs at various flow rates.

Unlike SLA and laser-cutter, the velocity profiles of Polyjet 3D printed BPP look significantly different from expectation, even at higher flow rates, as it is seen in Figure 4-30-c, Figure 4-31-c and Figure 4-32-c. One reason for such deviation from expectation could be the high non-uniformity of channel size distribution, as it was shown in Figure 4-7. The possible residual support materials could worsen the channel size distribution and make the flow distribution highly non-uniform. Moreover, it seems that the velocity profile from Polyjet 3D printed BPP skewed highly to the right-hand side, as it can be seen in Figure 4-27, Figure 4-28 and Figure 4-29. The non-symmetry of the velocity-profile can also be observed in other BPPs, but it is very severe in BPP#2. This skewness can arise from non-uniform stress distribution, which in Polyjet 3D printed BPPs could cause further deformation due to the low mechanical strength of Vero-white plastic.

#### 4.3.1.2.2 Comparing the velocity profiles of prototype cathode BPPs with 0.4 mm hydraulic diameter

##### 4.3.1.2.2.1 SLA

Comparing the velocity profiles of BPPs#2, #4 and #7 at each flow rate from Figure 4-24 and Figure 4-32 demonstrates that plate 3D printed with SLA technology (BPP#4) gives a closer velocity-profile to expectation than laser-cutter and Polyjet. The values of average and maximum discrepancies, as well as

the WLS are lowest for SLA 3D printed BPP, as shown in Table 4-3, which highlights that SLA 3D printed BPP outperforms both laser-cut and Polyjet 3D printed plates.

The values of average and maximum discrepancy, as well as WLS, are lower for SLA 3D printed BPP with 0.4 mm diameter (BPP#4) than covered SLA plate with 0.635 mm diameter (BPP#5), as shown in Table 4-3. However, the standard error is approximately 2% for BPP#5, while that of BPP#4 is approximately 5%. BPP#4 and BPP#5 have similar performance in terms of velocity profile agreement with expectation.

One reason for larger standard error in BPP#4 is the larger channel size of BPP#5 than BPP#4; Despite the good mechanical strength of SLA 3D printing material, there exists minor channel deformation that non-uniformity in stress distribution makes this channel to deform. Since both BPPs have 2 mm thickness and are fabricated with the same material, the equal stress causes equal strain in both plates. However, this strain is more sensible in BPP#4 with 0.4 mm hydraulic diameter.

The other reason of larger standard error in SLA 3D printed BPP with 0.4 mm diameter (BPP#4) than the uncovered SLA plate with 0.635 mm diameter (BPP#5) is that during the experiments, very tiny bubbles were observed in the fluid flow which were generated inside the flow fields, mostly from dead zones behind the baffles. These tiny bubbles easily flow out in 0.635mm×0.635mm channels, while they get trapped in 0.4 mm×0.4 mm channels and result in errors.

The other source of the larger error in BPPs with 0.4 mm hydraulic diameter is the error in image processing. The number of pixels across the channel is greater in a 0.635 mm channel than a 0.4 mm channel, which makes approximating the velocity profile inside a channel more accurate. Moreover, if the channel boundary in Figure 3-11 is for instance in the middle of the pixel, the change in the pixel intensity will not be sensed which in turn results in an error, and this happens more frequently in smaller channels with fewer number of pixels. Considering all, the SLA cathode BPP with 0.4 mm diameter (BPP#4) still demonstrates an acceptable performance and shows a good agreement with

simulation results, with 4% average discrepancy. This further echoes that SLA 3D printing method serves as a reliable method in fast screening of BPPs and validating the simulation results.

#### 4.3.1.2.2 Laser-cutter

Prototype laser-cut BPP has similar channel size distribution to SLA, and they both demonstrated good mechanical strength, as discussed in 4.2.1. However, the velocity-profile from laser-cut plate shows higher fluctuations around the trend line and greater deviation from the expectation. This arises from the high roughness of channel bottom in laser-cut plate, as it was shown in Figure 4-2. The channels in BPP fabricated with laser-cutter are so rough that they serve as tiny baffles all along the flow channels and highly disturb the fluid distribution and increase the pressure-drop. But the BPP fabricated with laser-cutter can still be used to quickly evaluate the BPP design and to identify the design weakness and strength points. Especially that laser-cutting costs almost one third of SLA 3D printing and could be an option when the quality is traded by cost.

#### 4.3.1.2.3 Polyjet

Although Polyjet 3D printing cost equals to that of laser-cutting, the results from this technology are not reliable in small features, as shown in Figure 4-27, Figure 4-28 and Figure 4-29. Therefore, Polyjet 3D printing is not recommended for fabricating flow channels with <0.5 mm diameter. But Polyjet offers less expensive 3D printing than SLA, which produces data with enough reliability for channels with >0.5 mm diameter.

#### 4.3.1.2.3 Experimentally calculated vs. actual mean average fluid velocity

As it is demonstrated in Table 4-3, the ratios of actual to expected mean average fluid velocity for SLA (BPP#4), laser-cutter (BPP#7) and Polyjet (BPP#2) plates are 1.295, 0.986 and 1.754, respectively. On the other hand, as it was reported in Table 4-2, the ratios of actual to expected slope of pressure-drop graphs for SLA, laser-cut and Polyjet BPPs are 1.116, 0.785 and 2.03, respectively. However, part of the pressure-drop in laser-cut plate is caused by the channel roughness, which does not affect the mean

average fluid velocity. Hence, the ratio of actual to expected slope of the pressure-drop is not a good indicator to compare the ratio of actual to expected mean average velocity. Since BPP fabricated with laser-cutter has good mechanical strength and can resist deformation, the ratio of expected to actual channel cross section, which is 0.829 for laser-cut BPP, is used from Table 4-1 to evaluate the ratio of actual to expected mean average velocity. Considering these values, the mean average fluid velocity in SLA, laser-cutter and Polyjet BPP are 22%, 19% and 23% greater than expectation, respectively. As mentioned before, these greater values are likely caused by the tracer dye pulse injection.

#### 4.3.1.2.4 Effect of flow rate on velocity distribution uniformity

Figure 4-32 shows the velocity profile at different flow rates from SLA and simulated cathode BPPs with a channel diameter of 0.4 mm. Like the simulation results from 0.635 mm BPPs, Figure 4-32-b suggests that increasing the total flow rate stretches the velocity profile. The results from SLA cathode plate with 0.4 mm diameter in Figure 4-32-a are also consistent with this prediction.

The value of  $\beta$  increases from 1.072 to 1.128 as the flow rate increases from 145 ml/min to 651 ml/min, as shown in Table 4-3. The value of  $\beta$  in similar Reynolds number is slightly smaller in BPPs with 0.4 mm hydraulic diameter than 0.635 mm BPPs, which highlights that smaller channel dimension assists flow uniformity. This is likely because the flow encounters higher resistivity in smaller flow channels, which in turn prevents higher fluid flow in middle channels and leads the flow more toward side channels.

#### 4.3.1.3 Modifying flow field design in cathode BPP using numerical simulation

To increase the flow distribution uniformity in cathode BPP, a new modified design is proposed for the transition region and cathode inlet/outlet opening. The inlet/outlet opening is converted to two-opening manifold to assist the flow movement to side channels. Moreover, the distance between the baffles in the middle region is decreased, with a gradual increase in baffle distance toward side channels. This increases the flow resistance in the middle channels and provides the side channels with more flow. Since the experimental results already validated the simulation results, here we only tested the optimized cathode BPP performance numerically.

The simulation results of the optimized design are demonstrated in Figure 4-34, Figure 4-35, Figure 4-36 and Figure 4-37. As can be seen, the optimized design directs more fluid to the side channels and results in more uniform velocity and pressure profile. Moreover, the uniformity of pressure profiles is improved in the inlet, middle, and outlet regions without increasing the total pressure-drop in cathode BPP. More interestingly, since the maximum channel velocity is lower in the optimized cathode BPP, the pressure-drop in optimized cathode BPP decreases slightly.

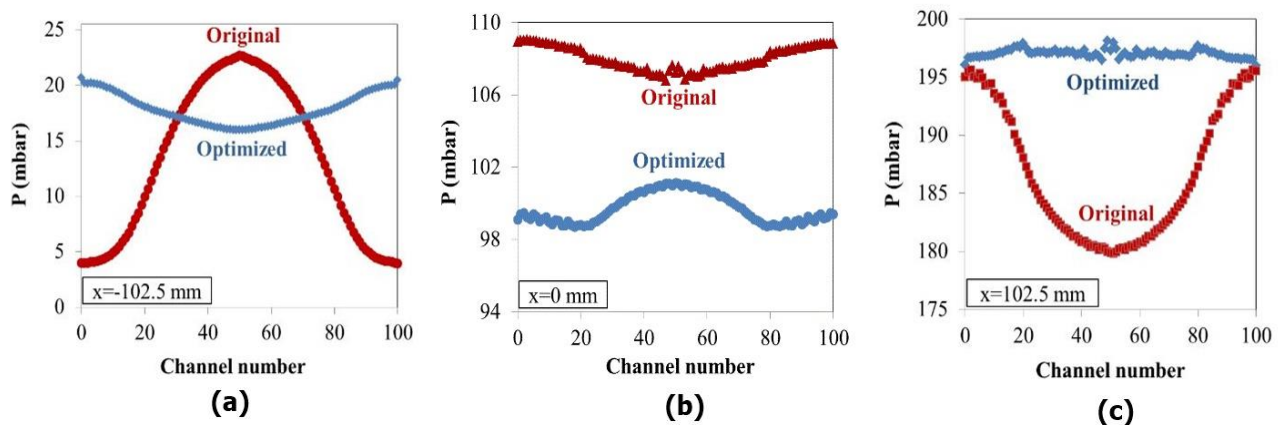
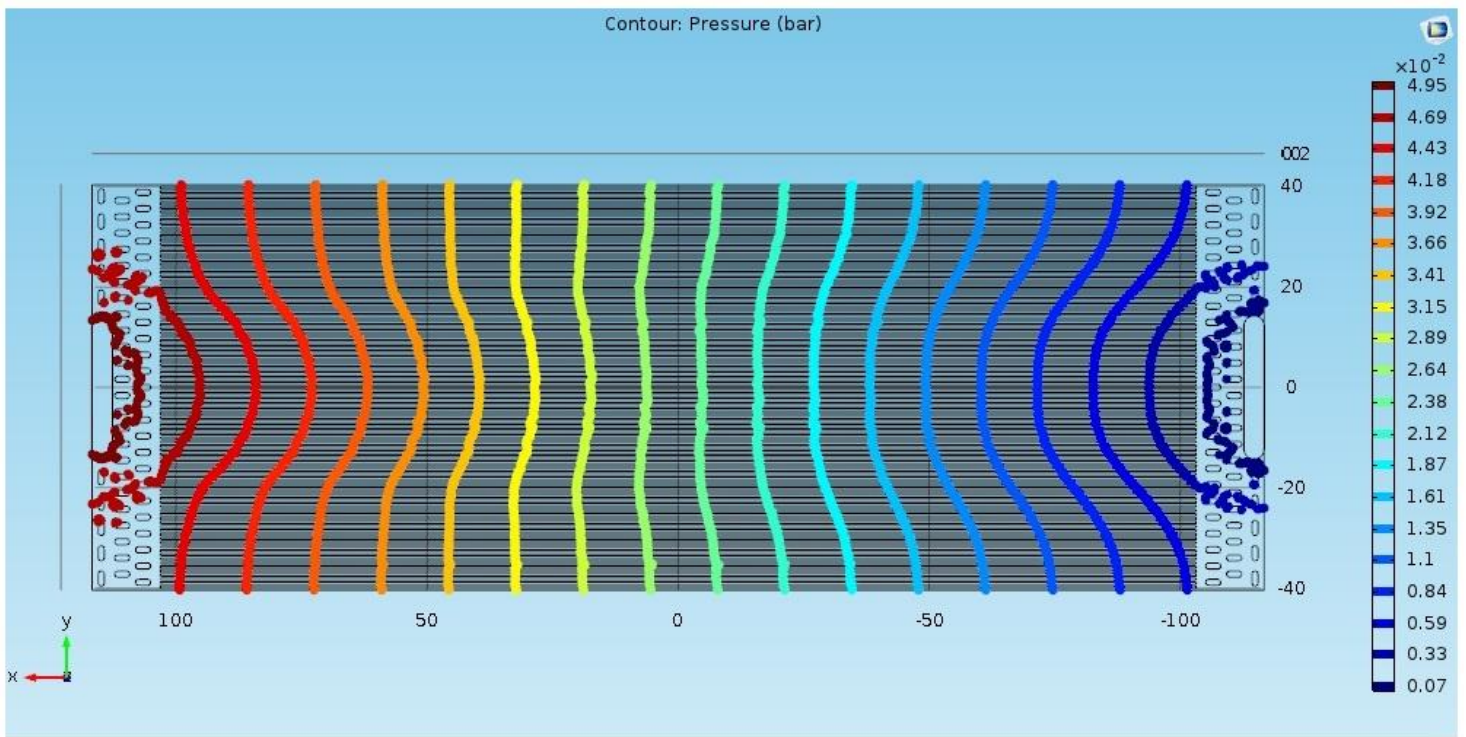
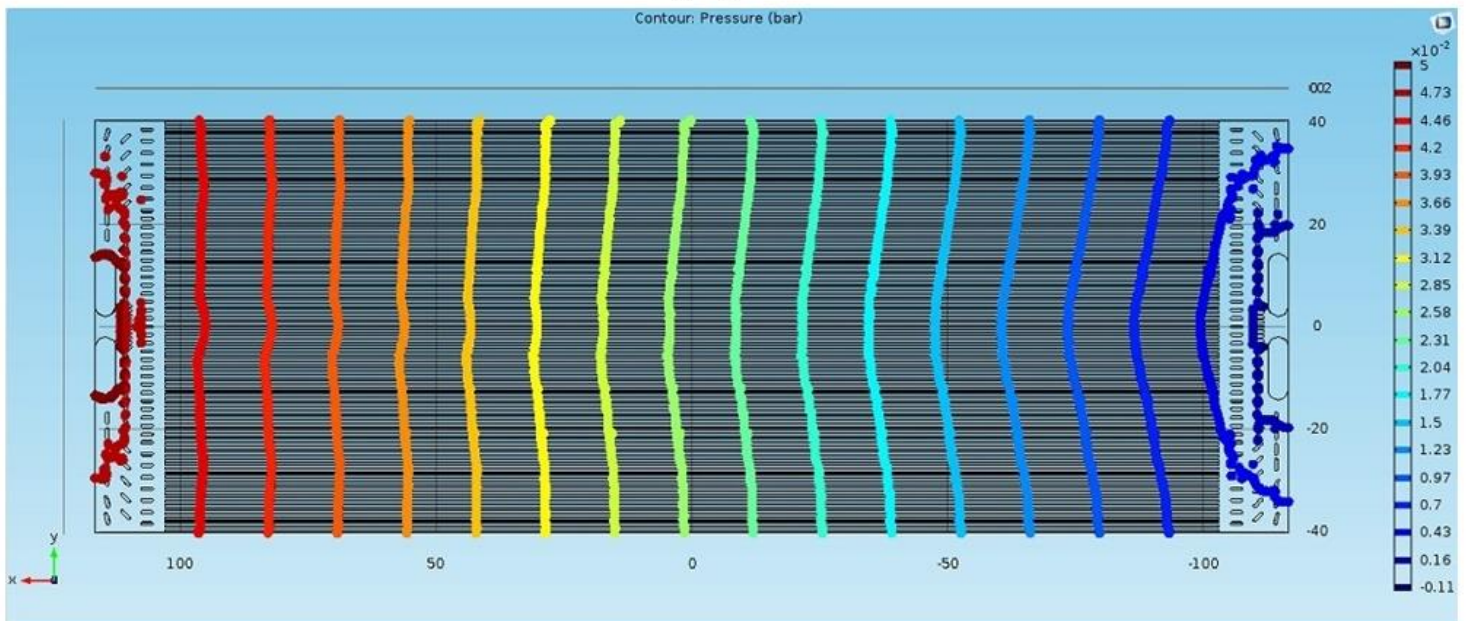


Figure 4-34: pressure-drop profile in flow channels of cathode BPP with 0.4 mm hydraulic diameter before and after optimization; a) Near inlet, b) Near middle, 3) Near outlet.



(a)



(b)

Figure 4-35: Pressure-drop contour in flow channels of cathode BPP with 0.4 mm hydraulic diameter; a) Original design, b) Optimized design

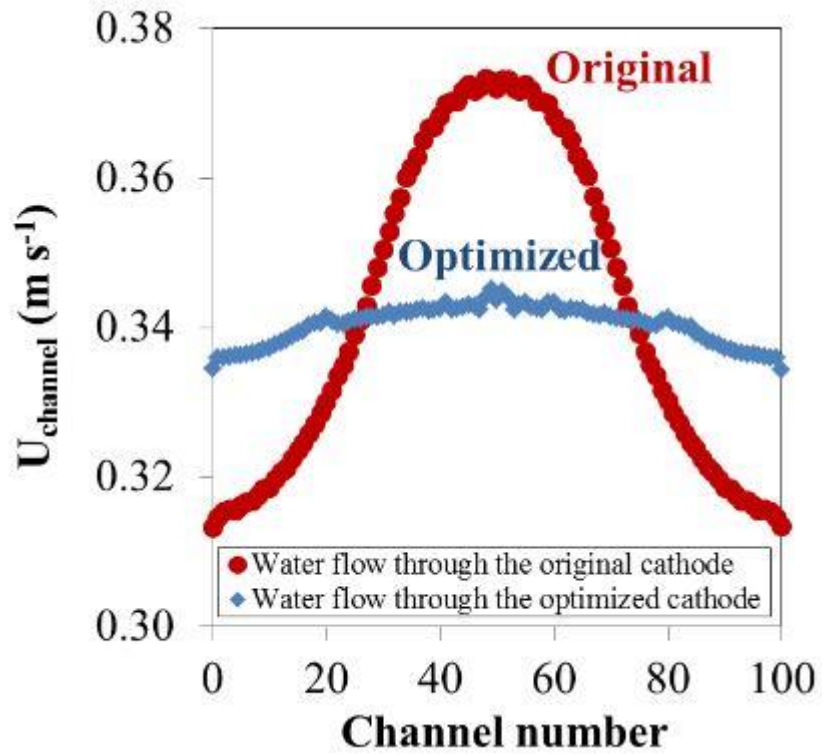


Figure 4-36: Velocity-profile in flow channels of cathode BPP with 0.4 mm hydraulic diameter before and after optimization.

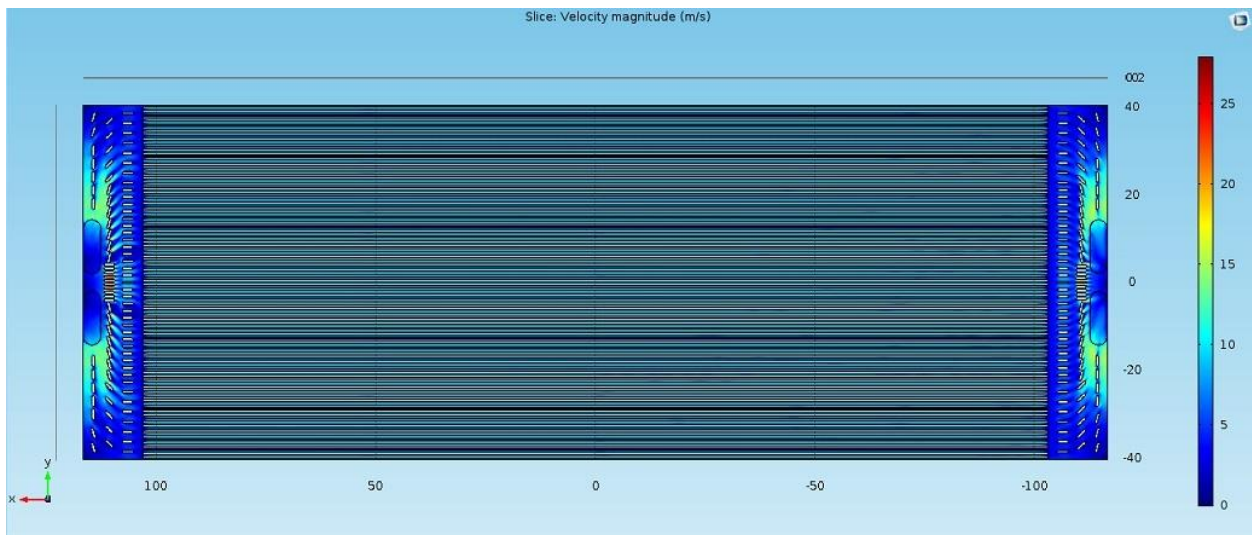


Figure 4-37 : Velocity contour in flow channels of optimized cathode BPP with 0.4 mm hydraulic diameter.

### 4.3.2 Velocity profiles in anode and water-cooling BPPs

Figure 4-38 and Figure 4-39 show the dye front evolution in anode and cooling BPPs, respectively. The images in each figure are selected randomly from among 16,000 images, which are taken from the dye distribution across the flow fields, near inlet and outlet regions. Processing the images from each experiment provided us with the velocity profiles of anode and water-cooling BPPs at different flow rates, which are demonstrated in Figure 4-40, Figure 4-41, Figure 4-42 and Figure 4-43. Please note that a water-glycerin mixture is used at the flow rates of 150, 300 and 600 ml/min, with the details given in Table 4-4. However, to compare the pressure-drop data of cathode BPPs with that of anode and water-cooling, an additional experiment is carried out with pure water at 1300 ml/min in anode and water-cooling BPPs; because the experiments in cathode BPPs were done with pure water and the flow rate of 1300 ml/min provided us with more reliable data.

Since the experiment results from cathode prototype BPPs fabricated with SLA 3D printing have proved the reliability of experimental data and demonstrated a good agreement with simulation results, only the experiments (and not the simulation) are performed for anode and water-cooling BPPs. The results suggest that in anode and water-cooling BPPs with Z-arrangement, fluid has more tendency to pass side channels than middle channels. Moreover, the channels near the inlet-side experience lower flow than the channels on the outlet-side. That the maximum values of velocity profiles from anode and water-cooling BPPs are located on two opposite ends is because anode and water-cooling BPPs have opposite inlet and outlet positions. The velocity profile results of anode and water-cooling BPPs are in agreement with the literature [35, 37, 40, 129].

#### 4.3.2.1 Comparing velocity profiles on anode, cathode and water-cooling BPPs

Like cathode BPPs, the velocity profiles of anode and water-cooling BPPs are disturbed less at higher flow rates. The values of COV and  $\beta$  suggest that anode and water-cooling BPPs possess more non-uniform velocity profiles than cathode BPP, because of the non-symmetry of inlet and outlet

position about the Y-axis. In addition, comparing Figure 4-40, Figure 4-41, Figure 4-42 and Figure 4-43 highlights that although anode and water-cooling BPPs have similar inlet and outlet positions, the velocity profile of water-cooling BPP is more stretched (non-uniform) than that of anode BPP, which is also confirmed with COV and  $\beta$  values from Table 4-4. Figure 3-1-b and c suggest that this non-uniformity is caused by the wider inlet opening, slightly shorter channels as well as the different transition region in water-cooling BPP, which consists of a single-row baffles.

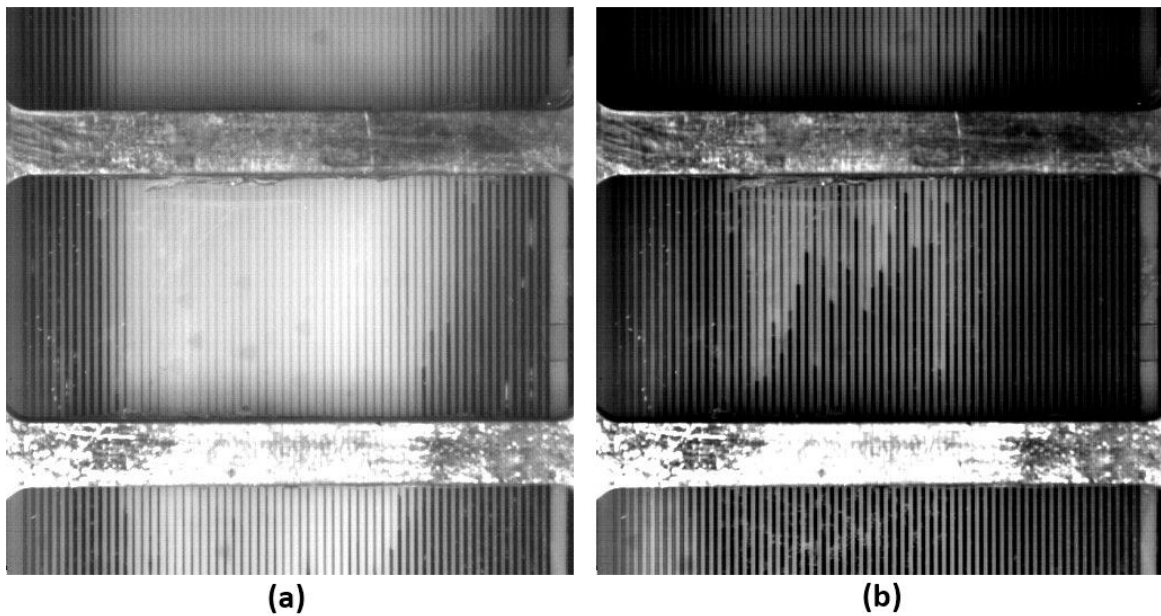
#### 4.3.2.2 *Effect of flow rate on velocity distribution uniformity*

Figure 4-44 demonstrates that the velocity distribution between flow channels of anode and water-cooling BPPs becomes more non-uniform at higher flow rates. This is in agreement with the results by Xu et al. [37], but contradicts the results by Barreras et al. [35], where they reported that the flow distribution is not dependent on Reynolds number and total flow rate. The higher flow non-uniformity at higher flow rates was also observed in the cathode BPPs in the present work. However, the values of COV and  $\beta$  from Table 4-4 suggest that the cathode BPP has less non-uniformity than water-cooling and anode BPPs. This could explain the elevated pressure-drop in anode and water-cooling BPPs, as well as the high curvature of pressure-drop graphs in water-cooling and anode BPPs, as shown in Figure 4-12. The following explains more.

#### 4.3.2.3 *Explaining different pressure-drop behavior of anode, cathode and water-cooling BPPs*

Considering the values of  $\beta$  from Table 4-4 in eq. (37) suggests that the ratio of the slope of pressure-drop should be as follow:  $m_{wc}/m_a=1.127$ ,  $m_{wc}/m_c=1.61$ ,  $m_a/m_c=1.435$ . However, the experimental values for the ratio of the slope of pressure-drop for cathode, anode and water-cooling BPPs are as follow:  $m_{wc}/m_a=1.722$ ,  $m_{wc}/m_c=3.041$ ,  $m_a/m_c=1.765$ . Hence, there exist 52%, 88% and 22% discrepancy between the expected values and actual values of  $m_{wc}/m_a$ ,  $m_{wc}/m_c$  and  $m_a/m_c$ , respectively. The discrepancy in predicting the ratio of the slope of anode to cathode is 22%, and can be attributed to the perpendicular fluid movement in transition region in anode BPP, and to the experimental error. However, the values

predicted for the slope of the pressure-drop in water-cooling BPP is significantly lower than the actual slope. Part of this discrepancy could be caused by the transition channels in water-cooling BPP, which could be responsible for a 21% increase in the slope of the pressure-drop. The other part, which could be more significant, is the number of rows of baffles in transition region of water-cooling BPP, which is one for water-cooling BPP and three for anode and cathode BPP.



*Figure 4-38: Dye evolution in SLA 3D printed anode flow field. a)  $t=1637$  ms; b)  $t=1738$  ms.*

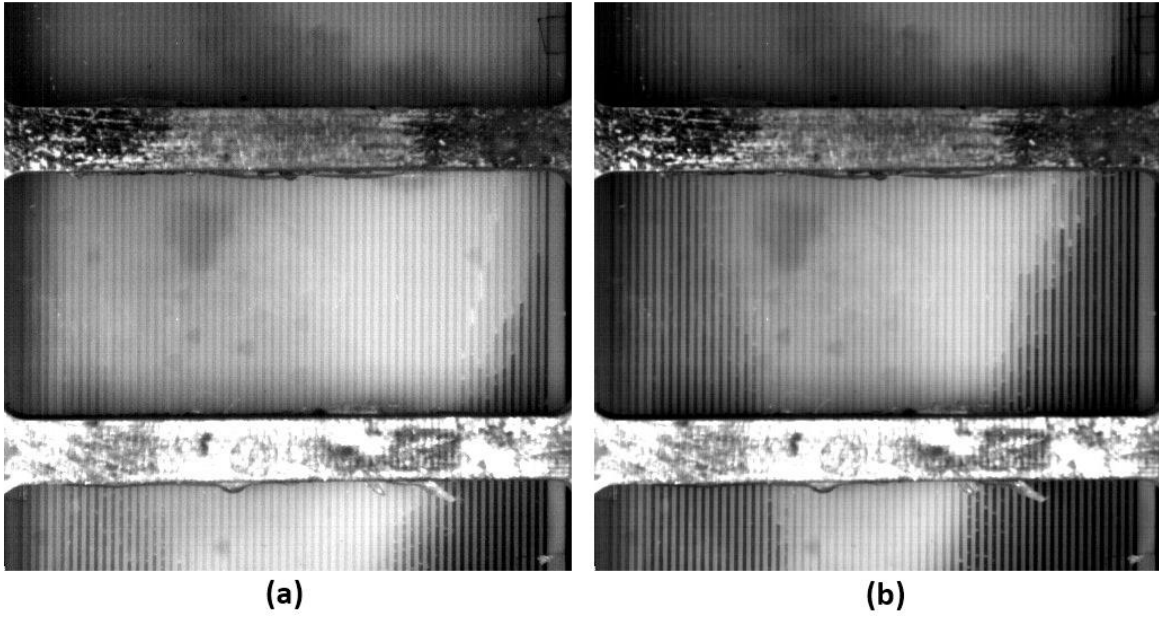


Figure 4-39: Dye evolution in SLA 3D printed water-cooling flow field. a)  $t=1717$  ms; b)  $t=1745$  ms.

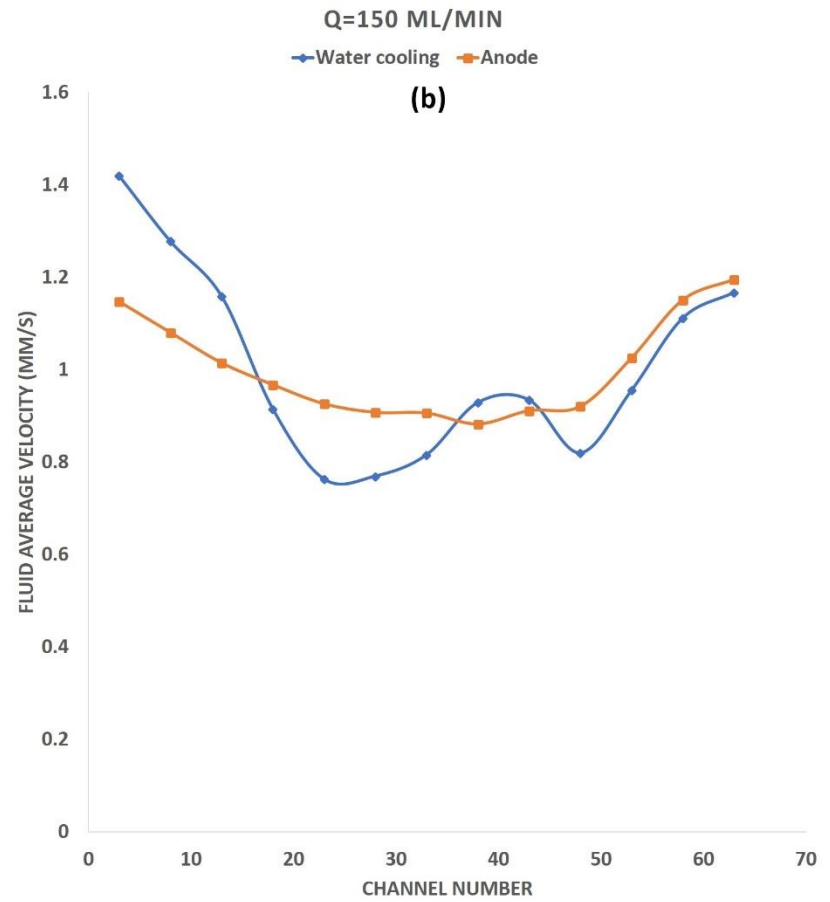
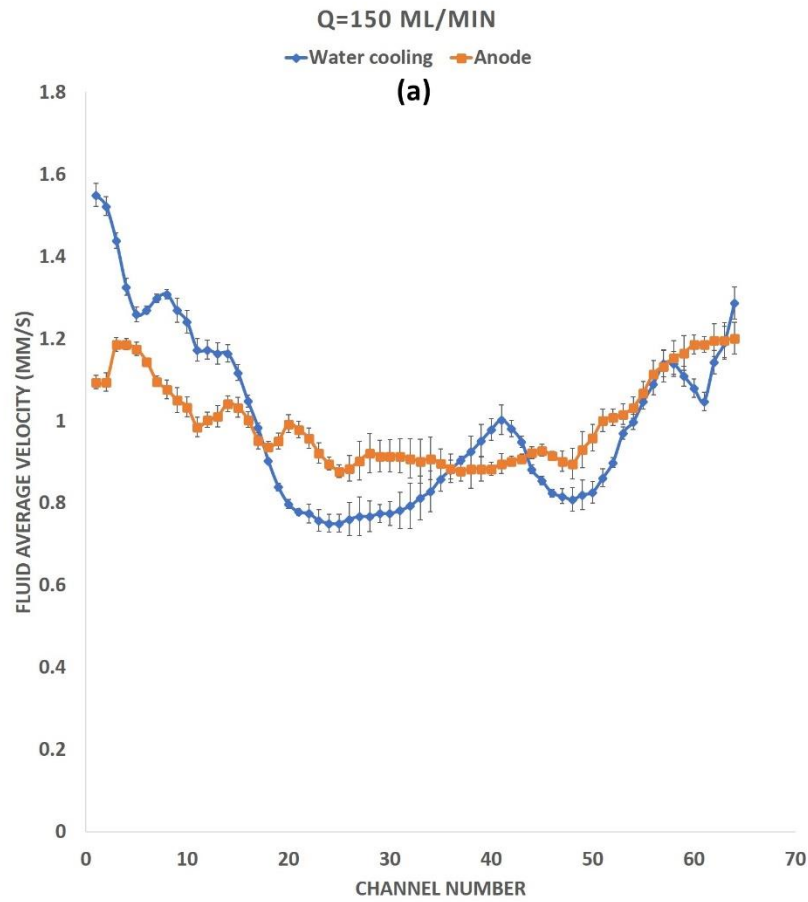


Figure 4-40: Velocity profile in anode and water-cooling prototype BPPs with 0.635 mm hydraulic diameter,  $Q=150$  ml/min;

a) Each data point on the graphs represents the velocity of a single channel,

b) Each data point on the graphs represents the average velocity of 5 adjacent channels such that point  $K$  ( $K=1:13$ ) represents the average velocity of channels  $5K-4$ ,  $5K-3$ ,  $5K-2$ ,  $5K-1$ ,  $5K$ .

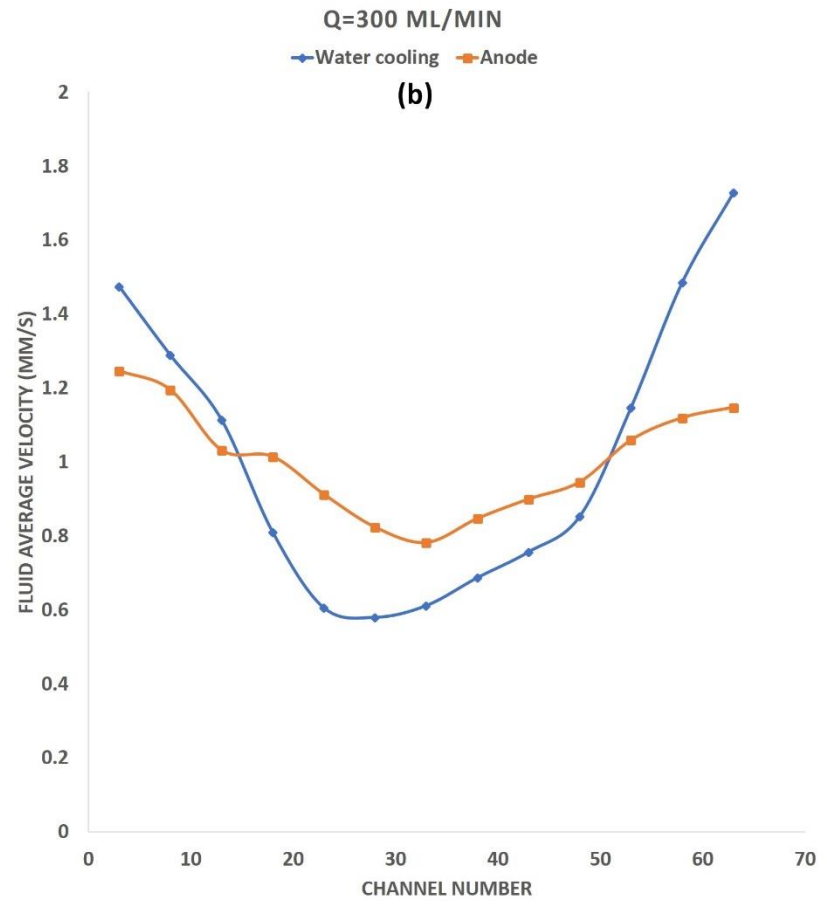
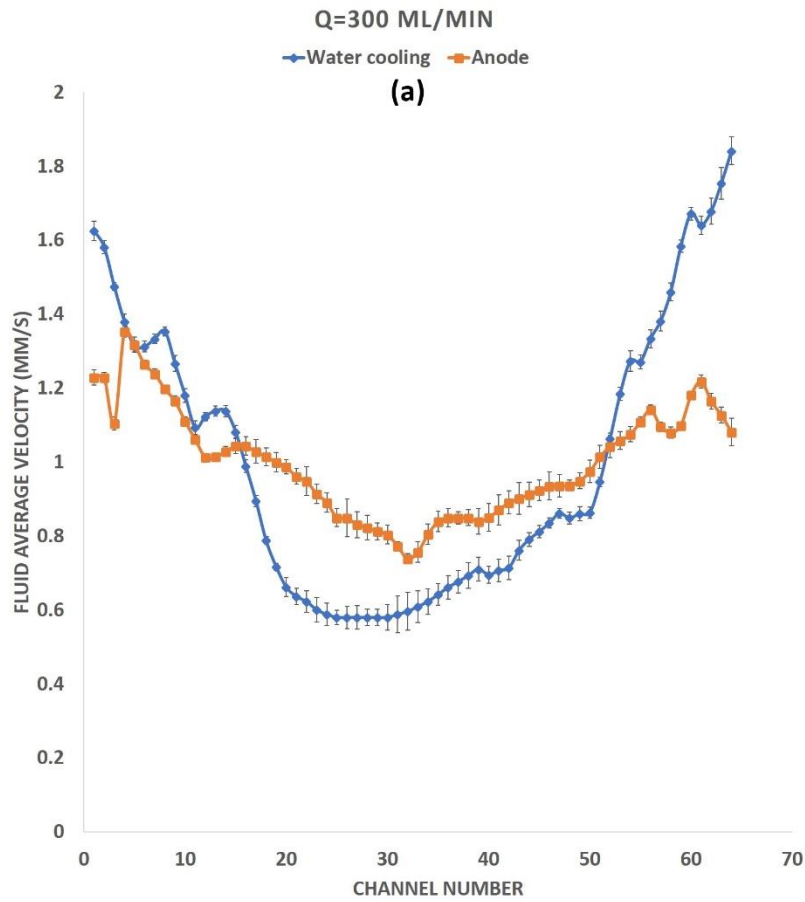


Figure 4-41: Velocity profile in anode and water-cooling prototype BPPs with 0.635 mm hydraulic diameter,  $Q=300$  ml/min;

a) Each data point on the graphs represents the velocity of a single channel,

b) Each data point on the graphs represents the average velocity of 5 adjacent channels such that point  $K$  ( $K=1:13$ ) represents the average velocity of channels  $5K-4$ ,  $5K-3$ ,  $5K-2$ ,  $5K-1$ ,  $5K$ .

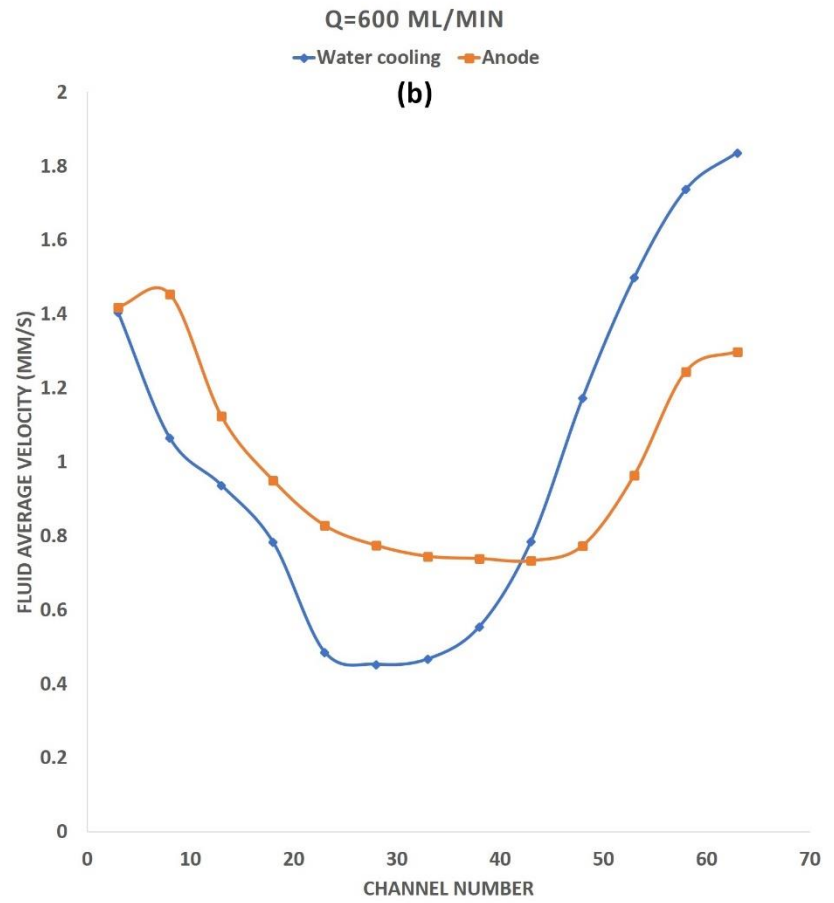
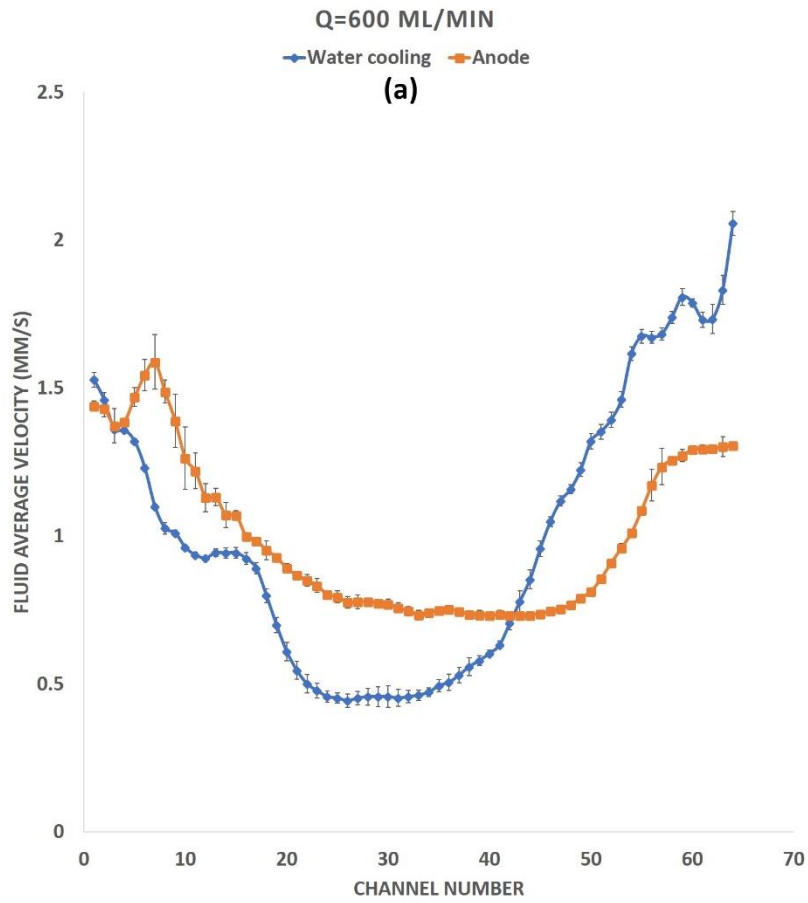


Figure 4-42: Velocity profile in anode and water-cooling prototype BPPs with 0.635 mm hydraulic diameter, Q=600 ml/min;

a) Each data point on the graphs represents the velocity of a single channel,

b) Each data point on the graphs represents the average velocity of 5 adjacent channels such that point K (K=1:13) represents the average velocity of channels 5K-4, 5K-3, 5K-2, 5K-1,5K.

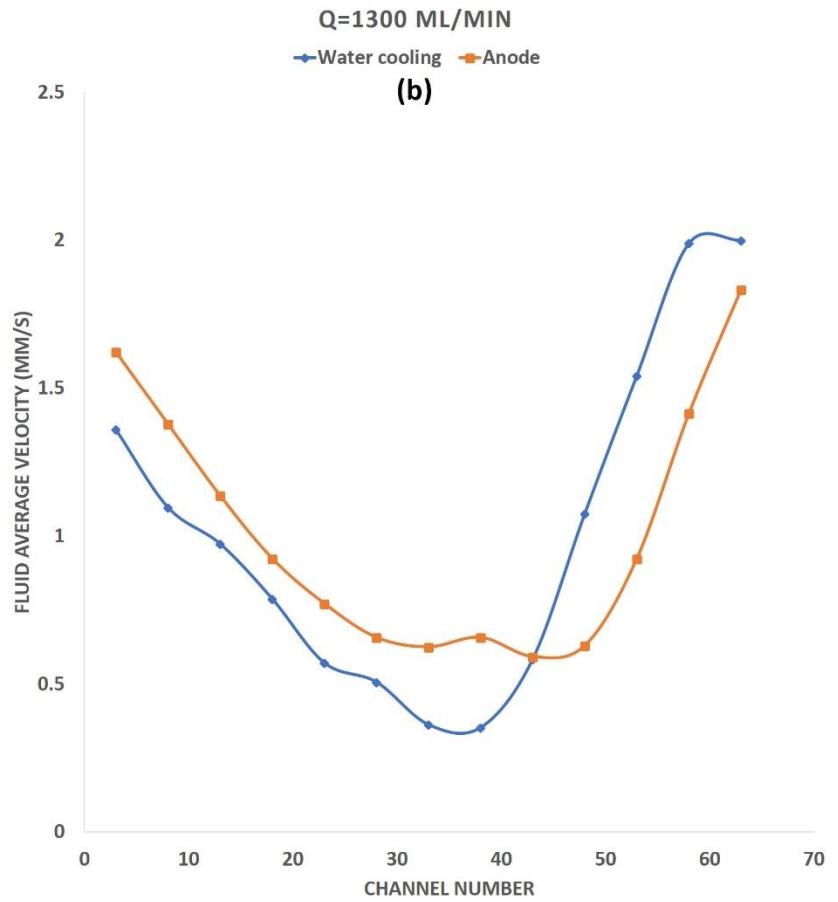
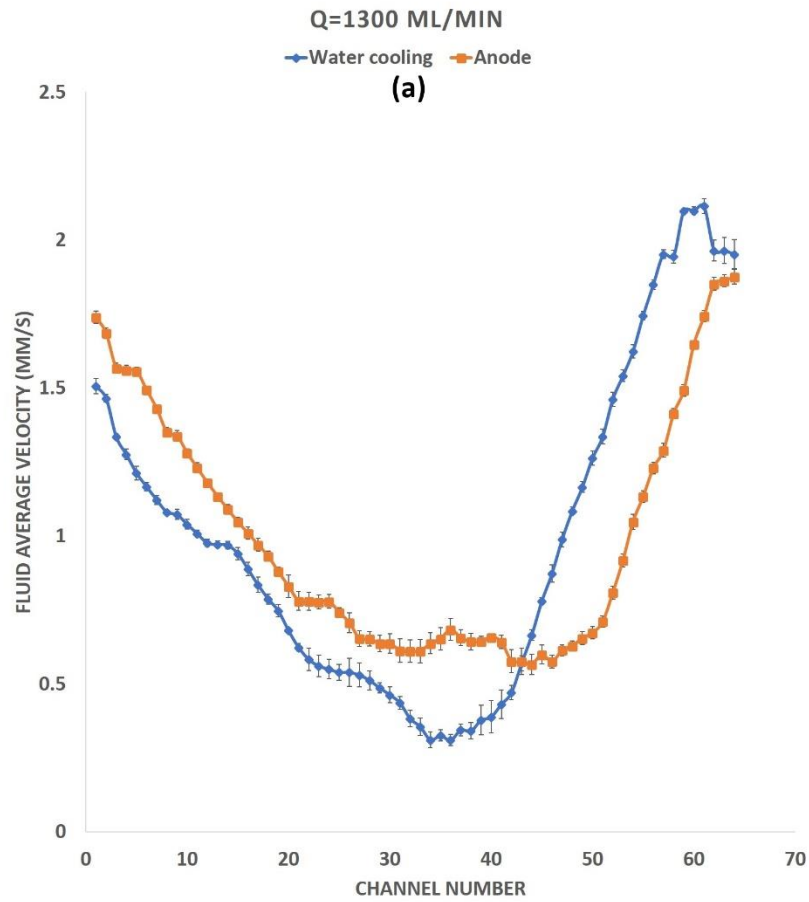


Figure 4-43: Velocity profile in anode and water-cooling prototype BPPs with 0.635 mm hydraulic diameter,  $Q=1300$  ml/min;

a) Each data point on the graphs represents the velocity of a single channel,

b) Each data point on the graphs represents the average velocity of 5 adjacent channels such that point  $K$  ( $K=1:13$ ) represents the average velocity of channels  $5K-4$ ,  $5K-3$ ,  $5K-2$ ,  $5K-1$ ,  $5K$ .

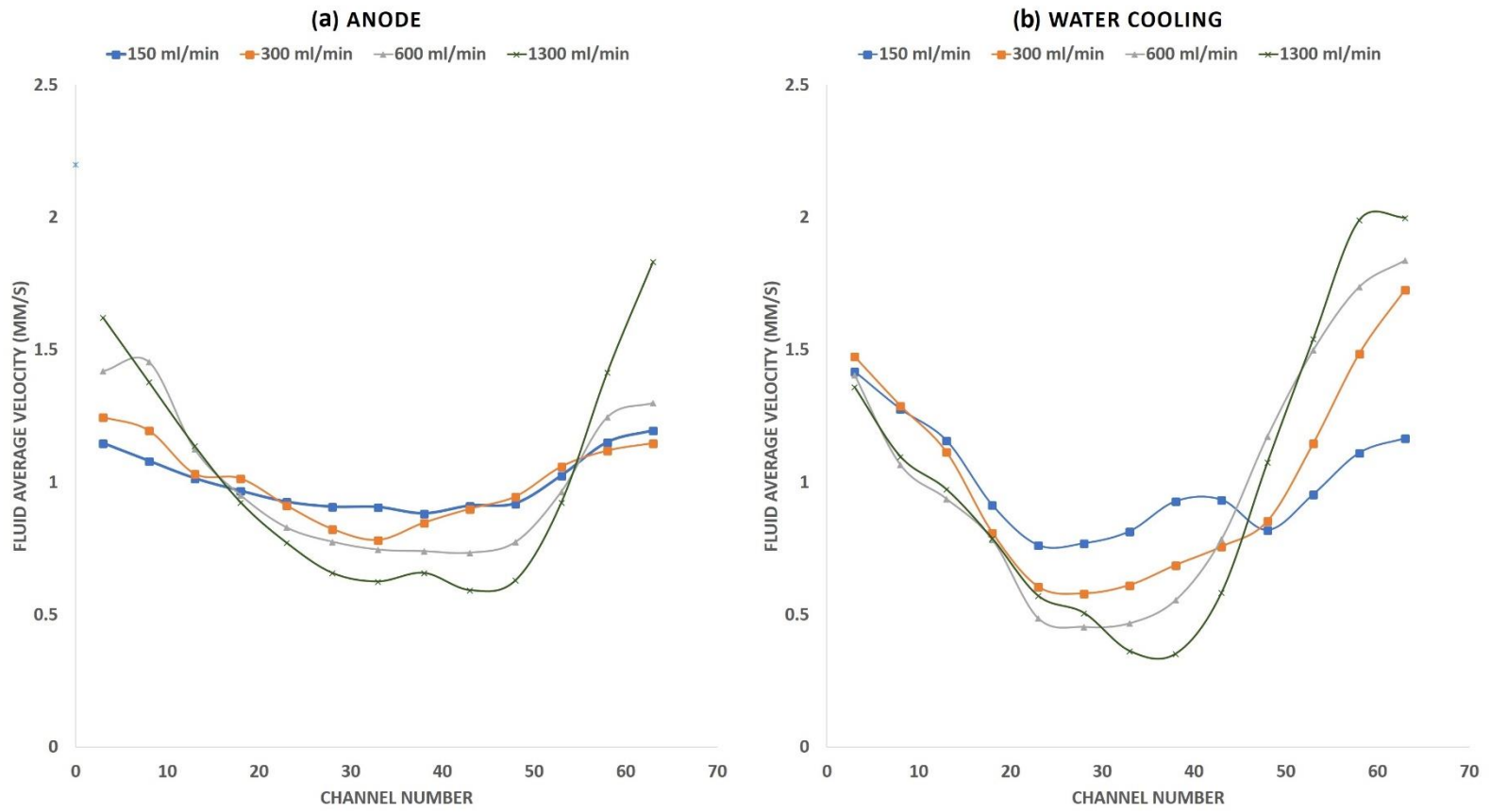


Figure 4-44: Effect of the total flow rate on the velocity profile of BPPs with 0.635 mm hydraulic diameter; a) Anode BPP, b) Water-cooling BPP.

Table 4-4: Statistical analysis of velocity-profile data from anode and water-cooling BPPs.

BPP #	Technology	BPP type	Number of channels	Flow rate (ml/min)	fluid type	$\beta$	COV (%)	$\frac{\bar{U}_{avg}}{Q/nA}$	$\overline{SE}$ (%)
8	SLA	Anode	101	150	$X_{wat}=0.53, X_{gly}=0.47$	1.20	0.106	1.338	2.72
				363	$X_{wat}=0.53, X_{gly}=0.47$	1.35	0.148	0.129	2.29
				650	$X_{wat}=0.53, X_{gly}=0.47$	1.59	0.266	1.260	2.15
				1300	$X_{wat}=1$	1.88	0.407	1.216	2.30
9	SLA	Water-cooling	64	150	$X_{wat}=0.87, X_{gly}=0.13$	1.55	0.208	1.340	2.45
				300	$X_{wat}=0.87, X_{gly}=0.13$	1.84	0.375	1.316	2.34
				600	$X_{wat}=0.87, X_{gly}=0.13$	2.05	0.470	1.287	2.21
				1300	$X_{wat}=1$	2.12	0.548	1.172	2.32
6	SLA	Cathode (Covered)	64	150	$X_{wat}=1$	1.18	0.101	1.254	2.52
				600	$X_{wat}=1$	1.26	0.162	1.244	1.90
				1300	$X_{wat}=1$	1.31	0.204	1.237	2.67

## 5 Conclusion

The main focus of the current research project at hand was to investigate the applicability of 3D printing as a rapid prototyping technique in fast screening of the flow field designs and in validating the simulation results. State-of-the-art designs for anode, cathode and water cooling BPPs were proposed and prototyped using two of the most recent 3D printing technologies, as well as laser-cutter technology, in order to:

- (1) Experimentally evaluate the fluid dynamic behavior of proposed flow field designs, and to validate the simulation results.
- (2) Compare the suitability of several novel 3D printing technologies in prototyping of the flow fields with complex designs and small feature size.
- (3) Assess the applicability and limitations of 3D printing in fabricating prototype and real BPPs.

The prototype BPPs were classified into 3 different groups as follow:

- (1) Cathode BPPs with 0.635 mm hydraulic diameter, to evaluate the rigor of SLA and Polyjet 3D printing in validating simulation results in channels with  $>0.5$  mm diameter.
- (2) Cathode BPPs with 0.400 mm hydraulic diameter, to evaluate the rigor of SLA and Polyjet 3D printing as well as laser-cutter technology in validating simulation results in channels with  $<0.5$  mm diameter.
- (3) Anode, cathode and water-cooling BPPs with 0.635 mm hydraulic diameter, with SLA 3D printed enclosed channels, to compare the velocity profile and pressure-drop in mentioned BPPs.

The cross-section imaging, pressure-drop and velocity distribution experiments were carried out in all prototype BPPs. Some of the insights gained through experiments and simulations are summarized below:

- SLA 3D printed cathode BPPs, both with 0.4 mm and 0.635 mm hydraulic diameter, demonstrated the closest agreement with simulation results, which validates the simulation results and confirms the SLA 3D printing applicability in fast-screening experiments.
- To ensure the maximum closeness to the desired geometry, to eliminate any possible gap between channel rib and acrylic glass, and to eliminate the effect of BPP tightening in experiments, a novel BPP with enclosed channels was 3D printed, named covered SLA cathode plate (BPP#6). This plate demonstrated a very good agreement with simulation results, where the average discrepancy between experimental and simulation results were 6% and 7% in velocity distribution and pressure-drop experiments, respectively.
- The SLA 3D printing technology offers a high-quality 3D printing with high precision and accuracy, with a reasonable price and very low prototyping time. SLA is capable of 3D printing complex designs and small features (<0.5 mm) with the expected geometry. We recommend this technology of 3D printing for studying the fluid dynamic behavior in complicated geometries and inter-connected flow channels. The SLA technology can 3D print smooth, robust and durable parts with enclosed geometries out of transparent materials, all of which widens its applicability in many other branches of science.
- The Polyjet technology demonstrated an acceptable channels size distribution with 15% COV, in BPPs with 0.635 mm hydraulic diameter. However, the support materials were not cleaned completely in BPPs with 0.4 mm hydraulic diameter, and the channel cross-sections were very non-uniform among different channels.
- The Polyjet 3D printing materials possess lower mechanical strength than SLA materials, which cause the Polyjet BPPs to deform under stress. This results in deviation of velocity distribution and pressure-drop from expected values, especially in BPPs with 0.4 mm hydraulic diameter.

- The high variation of velocity profile from Polyjet 3D printed BPP with 0.4 mm hydraulic diameter, and the much higher slope of pressure-drop curve than expectation, implies that Polyjet 3D printing is not suitable for printing features below 0.5 mm. However, the technology demonstrates an acceptable quality in features above 0.5 mm, and could be an option where tradeoff between price and quality is required.
- The laser-cutter technology fabricates BPPs out of plastics like acrylic glass, which has a good mechanical strength. Although the laser-cut channels are as identical as SLA 3D printed channels, the channels fabricated with laser-cutter are very rough which adds to the channel pressure-drop and disturbs the velocity distribution among the flow channels. Laser-cut channels cost one third of the SLA 3D printed channels and could serve to **qualitatively** validate the experimental results.
- The slopes of the pressure-drop graphs were in the order of: water-cooling, anode and cathode. The different pressure-drop in mentioned channels is caused by the different velocity distribution among channels and the transition region configurations.
- The velocity profile in cathode BPP is such that middle channels have higher velocity than the side channels. This is because of the centered inlet/outlet in cathode BPP, which exhibits minimum flow resistance in channels near inlet/outlet. However, in anode and water-cooling BPP, the inlet/outlet arrangement is diagonal and in turn the side channels have higher velocity than the middle channels.
- The initially proposed flow field design exhibited non-uniform velocity and pressure profiles. Using numerical simulation, the cathode BPP is modified by decreasing the gap between the baffles in the middle section of the transition region, which increases the flow resistance in middle section and directs more flow to the side channels. The simulation results demonstrated a uniform pressure and velocity profile in modified cathode flow field.

- The shallow channels (0.4 mm) in the proposed flow field design for anode, cathode and water-cooling BPPs reduce the fuel cell stack volume, weight, price and improves the power density.
- The velocity profile measurement was more precise at higher flow rates because of the disturbing effect of the tracer dye injection at lower flow rates.
- The measured mean average velocities were slightly more than expectation in all BPPs because of the pulse injection of the tracer dye.
- The image processing results were more accurate in wider channels since a higher number of pixels can be placed across the wider channels.

## 5.1 Recommendations

There are many areas of this project that should be investigated in more depth in future tests. These include:

- Performing pressure-drop and velocity distribution experiments in anode/cathode BPPs with hydrogen/air instead of water, to ensure the dynamic similarity between gas and liquid systems.
- Performing two-phase pressure-drop and velocity distribution experiments in anode/cathode BPPs.
- Prototyping BPPs with a micro-porous layer 3D printed on top of the channels to resemble the GDL. An additional layer could also be added on top of the channels with inkjet 3D printing to resemble the membrane.
- Validating the simulation results of optimized cathode BPP.
- Optimizing the flow field design in anode and water-cooling BPPs by applying 3D printing for fast screening of the baffle configurations in the transition region, without performing numerical simulation.

- Prototyping both anode and cathode BPPs with transparent 3D printing materials, assembling them in the form of a single-cell, and performing the flow visualization experiment in anode and cathode BPPs simultaneously. This allows aligning the flow channels in anode and cathode BPPs which could help better utilization of the fuel and would increase the energy output.
- Assessing the SLA 3D printing technology in printing of enclosed channels with 0.4 mm hydraulic diameter. Furthermore, evaluating the SLA 3D printing capability in printing flow channels with 0.3 mm and even 0.2 mm hydraulic diameter. The mentioned channel sizes are predicted to be the typical flow field channel size in the future.
- Prototyping state-of-the-art flow field designs with DMLS 3D printing to fabricate conductive prototype BPPs, which allows assembling the prototype BPPs in single-cell and performing fuel cell hot experiments.

## References

- [1] A. Aiyejina and M. K. S. Sastry, "PEMFC Flow Channel Geometry Optimization: A Review," *J. FC Sci. Technol.*, vol. 9, no. 1, p. 011011, 2012.
- [2] I. S. Han, J. Jeong, and H. K. Shin, "PEM fuel-cell stack design for improved fuel utilization," *Int. J. Hydrog. Energy*, vol. 38, no. 27, pp. 11996–12006, 2013.
- [3] R. Anderson, "Characterization of gas-liquid two-phase flow in a proton exchange membrane FC," University of British Columbia, 2012.
- [4] A. HERMANN, T. CHAUDHURI, and P. SPAGNOL, "Bipolar plates for PEMFCs: A review," *Int. J. Hydrog. Energy*, vol. 30, no. 12, pp. 1297–1302, 2005.
- [5] X. LI and I. SABIR, "Review of bipolar plates in PEMFCs: Flow-field designs," *Int. J. Hydrog. Energy*, vol. 30, no. 4, pp. 359–371, 2005.
- [6] A. Arvay, J. French, J.-C. Wang, X.-H. Peng, and A. M. Kannan, "Nature inspired flow field designs for proton exchange membrane FC," *Int. J. Hydrog. Energy*, vol. 38, no. 9, pp. 3717–3726, Mar. 2013.
- [7] V. Mehta and J. S. Cooper, "Review and analysis of PEMFC design and manufacturing," *J. Power Sources*, vol. 114, no. 1, pp. 32–53, 2003.
- [8] "DOE Technical Targets for Polymer Electrolyte Membrane FC Components | Department of Energy." [Online]. Available: <https://energy.gov/eere/fuelcells/doe-technical-targets-polymer-electrolyte-membrane-fuel-cell-components>. [Accessed: 24-May-2017].
- [9] J. Wang, "Flow distribution and pressure-drop in different layout configurations with z-type arrangement," *Energy Sci. Technol.*, vol. 2, no. 2, pp. 1–12, 2011.
- [10] P. J. Hamilton and B. G. Pollet, "Polymer Electrolyte Membrane FC (PEMFC) Flow Field Plate: Design, Materials and Characterisation," *FCs*, vol. 10, no. 4, pp. 489–509, Aug. 2010.

- [11] X. Li and I. Sabir, "Review of bipolar plates in PEMFCs: Flow-field designs," *Int. J. Hydrog. Energy*, vol. 30, no. 4, pp. 359–371, Mar. 2005.
- [12] J. Wang and H. Wang, "Flow-Field Designs of Bipolar Plates in PEMFCs: Theory and Applications," *FCs*, vol. 12, no. 6, pp. 989–1003, Dec. 2012.
- [13] a. P. Manso, F. F. Marzo, J. Barranco, X. Garikano, and M. Garmendia Mujika, "Influence of geometric parameters of the flow fields on the performance of a PEMFC. A review," *Int. J. Hydrog. Energy*, vol. 37, no. 20, pp. 15256–15287, 2012.
- [14] K.-S. Choi, H.-M. Kim, and S.-M. Moon, "Numerical studies on the geometrical characterization of serpentine flow-field for efficient PEMFC," *Int. J. Hydrog. Energy*, vol. 36, no. 2, pp. 1613–1627, Jan. 2011.
- [15] A. Iranzo, P. Boillat, J. Biesdorf, E. Tapia, A. Salva, and J. Guerra, "Liquid water preferential accumulation in channels of PEMFCs with multiple serpentine flow fields," *Int. J. Hydrog. Energy*, vol. 39, no. 28, pp. 15687–15695, Sep. 2014.
- [16] D. H. Jeon, S. Greenway, S. Shimpalee, and J. W. Van Zee, "The effect of serpentine flow-field designs on PEMFC performance," *Int. J. Hydrog. Energy*, vol. 33, no. 3, pp. 1052–1066, Feb. 2008.
- [17] S. Lee, T. Kim, and H. Park, "Comparison of multi-inlet and serpentine channel design on water production of PEMFCs," *Chem. Eng. Sci.*, vol. 66, no. 8, pp. 1748–1758, Apr. 2011.
- [18] X.-D. Wang, Y.-Y. Duan, W.-M. Yan, and X.-F. Peng, "Local transport phenomena and cell performance of PEMFCs with various serpentine flow field designs," *J. Power Sources*, vol. 175, no. 1, pp. 397–407, Jan. 2008.
- [19] Q. Jian, G. Ma, and X. Qiu, "Influences of gas relative humidity on the temperature of membrane in PEMFC with interdigitated flow field," *Renew. Energy*, vol. 62, pp. 129–136, Feb. 2014.

- [20] A. D. Santamaria, N. J. Cooper, M. K. Becton, and J. W. Park, "Effect of channel length on interdigitated flow-field PEMFC performance: A computational and experimental study," *Int. J. Hydrog. Energy*, vol. 38, no. 36, pp. 16253–16263, Dec. 2013.
- [21] G. Zhang, L. Guo, B. Ma, and H. Liu, "Comparison of current distributions in proton exchange membrane FCs with interdigitated and serpentine flow fields," *J. Power Sources*, vol. 188, no. 1, pp. 213–219, Mar. 2009.
- [22] S. Asghari, H. Akhgar, and B. F. Imani, "Design of thermal management subsystem for a 5 kW polymer electrolyte membrane FC system," *J. Power Sources*, vol. 196, no. 6, pp. 3141–3148, Mar. 2011.
- [23] R. Boddu, U. K. Marupakula, B. Summers, and P. Majumdar, "Development of bipolar plates with different flow channel configurations for FCs," *J. Power Sources*, vol. 189, no. 2, pp. 1083–1092, Apr. 2009.
- [24] A. Kumar and R. G. Reddy, "Effect of gas flow-field design in the bipolar/end plates on the steady and transient state performance of polymer electrolyte membrane FCs," *J. Power Sources*, vol. 155, no. 2, pp. 264–271, Apr. 2006.
- [25] Y. Vazifeshenas, K. Sedighi, and M. Shakeri, "Numerical investigation of a novel compound flow-field for PEMFC performance improvement," *Int. J. Hydrog. Energy*, vol. 40, no. 43, pp. 15032–15039, Nov. 2015.
- [26] S. M. Baek, S. H. Yu, J. H. Nam, and C.-J. Kim, "A numerical study on uniform cooling of large-scale PEMFCs with different cooling flow field designs," *Appl. Therm. Eng.*, vol. 31, no. 8–9, pp. 1427–1434, Jun. 2011.
- [27] F. c. Chen, Z. Gao, R. o. Loutfy, and M. Hecht, "Analysis of Optimal Heat Transfer in a PEMFC Cooling Plate," *FCs*, vol. 3, no. 4, pp. 181–188, Dec. 2003.

- [28] J. Choi, Y.-H. Kim, Y. Lee, K.-J. Lee, and Y. Kim, "Numerical analysis on the performance of cooling plates in a PEFC," *J. Mech. Sci. Technol.*, vol. 22, no. 7, pp. 1417–1425, Jul. 2008.
- [29] J. H. Nam, K.-J. Lee, S. Sohn, and C.-J. Kim, "Multi-pass serpentine flow-fields to enhance under-rib convection in polymer electrolyte membrane FCs: Design and geometrical characterization," *J. Power Sources*, vol. 188, no. 1, pp. 14–23, Mar. 2009.
- [30] C. Xu and T. S. Zhao, "A new flow field design for polymer electrolyte-based FCs," *Electrochem. Commun.*, vol. 9, no. 3, pp. 497–503, Mar. 2007.
- [31] S. H. Yu, S. Sohn, J. H. Nam, and C.-J. Kim, "Numerical study to examine the performance of multi-pass serpentine flow-fields for cooling plates in polymer electrolyte membrane FCs," *J. Power Sources*, vol. 194, no. 2, pp. 697–703, Dec. 2009.
- [32] A. Amirfazli, S. Asghari, and M. Koosha, "Mathematical modeling and simulation of thermal management in polymer electrolyte membrane FC stacks," *J. Power Sources*, vol. 268, pp. 533–545, Dec. 2014.
- [33] E. Alizadeh, S. M. Rahgoshay, M. Rahimi-Esbo, M. Khorshidian, and S. H. M. Saadat, "A novel cooling flow field design for polymer electrolyte membrane FC stack," *Int. J. Hydrog. Energy*, vol. 41, no. 20, pp. 8525–8532, Jun. 2016.
- [34] S. Maharudrayya, S. Jayanti, and A. P. Deshpande, "Pressure-drop and flow distribution in multiple parallel-channel configurations used in proton-exchange membrane FC stacks," *J. Power Sources*, vol. 157, no. 1, pp. 358–367, Jun. 2006.
- [35] F. Barreras, A. Lozano, L. Valiño, C. Marín, and A. Pascau, "Flow distribution in a bipolar plate of a proton exchange membrane FC: experiments and numerical simulation studies," *J. Power Sources*, vol. 144, no. 1, pp. 54–66, Jun. 2005.
- [36] B. D. Gould, R. Ramamurti, C. R. Osland, and K. E. Swider-Iyons, "ScienceDirect Assessing fuel-cell cooling flow fields with numerical models and infrared thermography," vol. 9, pp. 1–10, 2014.

- [37] Y. Xu, L. Peng, P. Yi, and X. Lai, "Analysis of the flow distribution for thin stamped bipolar plates with tapered channel shape," *Int. J. Hydrog. Energy*, vol. 41, no. 9, pp. 5084–5095, Mar. 2016.
- [38] B. H. Lim, E. H. Majlan, W. R. W. Daud, M. I. Rosli, and T. Husaini, "Numerical analysis of modified parallel flow field designs for FCs," *Int. J. Hydrog. Energy*, Apr. 2016.
- [39] H. T. Bi, P. Sauriol, and J. Stumper, "Two-phase flow distributors for FC flow channels," *Particuology*, vol. 8, no. 6, pp. 582–587, Dec. 2010.
- [40] G. M. Imbrioscia and H. J. Fasoli, "Simulation and study of proposed modifications over straight-parallel flow field design," *Int. J. Hydrog. Energy*, vol. 39, no. 16, pp. 8861–8867, May 2014.
- [41] R. D. S. C.A. Reiser, "Water evaporation for cooling and migration by hydrophilic separator plates; no collection of water on cathode side of membrane," 4,769,297.
- [42] B. D. Gould, R. Ramamurti, C. R. Osland, and K. E. Swider-Lyons, "Assessing fuel-cell cooling flow fields with numerical models and infrared thermography," *Int. J. Hydrog. Energy*, vol. 39, no. 26, pp. 14061–14070, Sep. 2014.
- [43] D. P. Wilkinson and J. St-Pierre, "In-plane gradients in FC structure and conditions for higher performance," *J. Power Sources*, vol. 113, no. 1, pp. 101–108, Jan. 2003.
- [44] D. P. Wilkinson, H. H. Voss, N. J. Fletcher, M. C. Johnson, and E. G. Pow, "Electrochemical FC stack with concurrent flow of cooling and oxidant streams and countercurrent flow of fuel and oxidant streams," US5773160 A, 30-Jun-1998.
- [45] J. Scholta, G. Escher, W. Zhang, L. Küppers, L. Jörissen, and W. Lehnert, "Investigation on the influence of channel geometries on PEMFC performance," *J. Power Sources*, vol. 155, no. 1, pp. 66–71, Apr. 2006.
- [46] X.-D. Wang, Y.-Y. Duan, and W.-M. Yan, "Numerical study of cell performance and local transport phenomena in PEMFCs with various flow channel area ratios," *J. Power Sources*, vol. 172, no. 1, pp. 265–277, Oct. 2007.

- [47] N. Zamel and X. Li, "A parametric study of multi-phase and multi-species transport in the cathode of PEMFCs," *Int. J. Energy Res.*, vol. 32, no. 8, pp. 698–721, Jun. 2008.
- [48] N. Zamel and X. Li, "Non-isothermal multi-phase modeling of PEMFC cathode," *Int. J. Energy Res.*, p. n/a-n/a, 2009.
- [49] S. SHIMPALEE and J. VANZEE, "Numerical studies on rib & channel dimension of flow-field on PEMFC performance," *Int. J. Hydrog. Energy*, vol. 32, no. 7, pp. 842–856, May 2007.
- [50] X.-D. Wang, W.-M. Yan, Y.-Y. Duan, F.-B. Weng, G.-B. Jung, and C.-Y. Lee, "Numerical study on channel size effect for proton exchange membrane FC with serpentine flow field," *Energy Convers. Manag.*, vol. 51, no. 5, pp. 959–968, May 2010.
- [51] K.-S. Choi, H.-M. Kim, and S.-M. Moon, "Numerical studies on the geometrical characterization of serpentine flow-field for efficient PEMFC," *Int. J. Hydrog. Energy*, vol. 36, no. 2, pp. 1613–1627, Jan. 2011.
- [52] A. P. Manso, F. F. Marzo, M. G. Mujika, J. Barranco, and A. Lorenzo, "Numerical analysis of the influence of the channel cross-section aspect ratio on the performance of a PEMFC with serpentine flow field design," *Int. J. Hydrog. Energy*, vol. 36, no. 11, pp. 6795–6808, Jun. 2011.
- [53] X.-D. Wang, X.-X. Zhang, T. Liu, Y.-Y. Duan, W.-M. Yan, and D.-J. Lee, "Channel Geometry Effect for Proton Exchange Membrane FC With Serpentine Flow Field Using a Three-Dimensional Two-Phase Model," *J. FC Sci. Technol.*, vol. 7, no. 5, p. 051019, Oct. 2010.
- [54] X.-D. Wang, Y.-Y. Duan, W.-M. Yan, and X.-F. Peng, "Effects of flow channel geometry on cell performance for PEMFCs with parallel and interdigitated flow fields," *Electrochimica Acta*, vol. 53, no. 16, pp. 5334–5343, Jun. 2008.
- [55] R. Anderson, L. Zhang, Y. Ding, M. Blanco, X. Bi, and D. P. Wilkinson, "A critical review of two-phase flow in gas flow channels of proton exchange membrane FCs," *J. Power Sources*, vol. 195, no. 15, pp. 4531–4553, Aug. 2010.

- [56] R. Anderson, D. P. Wilkinson, X. Bi, and L. Zhang, "Two-phase flow pressure-drop hysteresis in parallel channels of a proton exchange membrane FC," *J. Power Sources*, vol. 195, no. 13, pp. 4168–4176, Jul. 2010.
- [57] R. Anderson, D. Wilkinson, X. Bi, and L. Zhang, "Two-Phase Flow Pressure-drop Hysteresis under Typical Operating Conditions for a Proton Exchange Membrane FC," *ECS Trans.*, vol. 28, no. 30, pp. 127–137, Oct. 2010.
- [58] R. Anderson, D. P. Wilkinson, X. Bi, and L. Zhang, "Two-phase flow pressure-drop hysteresis in an operating proton exchange membrane FC," *J. Power Sources*, vol. 196, no. 19, pp. 8031–8040, Oct. 2011.
- [59] S. M. Baek, D. H. Jeon, J. H. Nam, and C.-J. Kim, "Pressure-drop and flow distribution characteristics of single and parallel serpentine flow fields for polymer electrolyte membrane FCs," *J. Mech. Sci. Technol.*, vol. 26, no. 9, pp. 2995–3006, Sep. 2012.
- [60] F. Barbir, H. Gorgun, and X. Wang, "Relationship between pressure-drop and cell resistance as a diagnostic tool for PEMFCs," *J. Power Sources*, vol. 141, no. 1, pp. 96–101, Feb. 2005.
- [61] S. G. Kandlikar, E. J. See, and R. Banerjee, "Modeling Two-Phase Pressure-drop along PEMFC Reactant Channels," *J. Electrochem. Soc.*, vol. 162, no. 7, pp. F772–F782, Jan. 2015.
- [62] L. Zhang, X. T. Bi, D. P. Wilkinson, R. Anderson, J. Stumper, and H. Wang, "Gas–liquid two-phase flow behavior in minichannels bounded with a permeable wall," *Chem. Eng. Sci.*, vol. 66, no. 14, pp. 3377–3385, Jul. 2011.
- [63] Kakac, S., Shah, R., Aung, W., *Handbook of Single-Phase Convective Heat Transfer*. New York, NY.: John Wiley & Sons, 1987.
- [64] S. Chen, D. L. Bourell, and K. L. Wood, "Fabrication of PEMFC bipolar plates by indirect SLS," in *International SFF Symposium*, Austin, TX, August, 2004, pp. 2–4.

- [65] ACE INDUSTRIAL CO., INC., "Metal and graphite bipolar plates.," 2016. [Online]. Available: [https://www.r-expo.jp/wsew2014/exhiSearch/FC/en/search\\_detail.php?id=11536](https://www.r-expo.jp/wsew2014/exhiSearch/FC/en/search_detail.php?id=11536).
- [66] M. Onischak et al., "Molded Graphite Bipolar Separator Plates for FCs," 2000.
- [67] Schunk, "Bi-Polar Plates Properties." [Online]. Available: [http://www.biservice.lv/pdfi/Schunk\\_MoldedBipolarPlates-for-FuelCells.pdf](http://www.biservice.lv/pdfi/Schunk_MoldedBipolarPlates-for-FuelCells.pdf).
- [68] "Corrosion resistant coated FC bipolar plate with filled-in fine scale porosities and method of making the same," 1999.
- [69] M. Sadler, G. O. Mepsted, D. Porter, R. A. Shatwell, and A. Loveridge, "Novel Materials and Manufacturing Processes for FC Vehicle Components," 2003.
- [70] S. Das Brett Lyons, Marat Batalov, Pranavas Mohanty, "RP of PEMFC," pp. 446–457.
- [71] P. Dudek, A. Raźniak, and B. Lis, "RP methods for the manufacture of FCs," in E3S Web of Conferences, 2016, vol. 10, p. 00127.
- [72] J. P. Kruth, "Material Incess Manufacturing by RP Techniques," CIRP Ann. - Manuf. Technol., vol. 40, no. 2, pp. 603–614, Jan. 1991.
- [73] D.W. Rosen B. Stucker and I. Gibson (last), AM technologies: RP to direct digital manufacturing,. Springer, 2010.
- [74] B. D. Gould et al., "Performance and Limitations of 3D-Printed Bipolar Plates in FCs," vol. 4, no. 4, pp. 3063–3068, 2015.
- [75] C. Bradley and B. Currie, "Advances in the Field of Reverse Engineering," Comput.-Aided Des. Appl., vol. 2, no. 5, pp. 697–706, Jan. 2005.
- [76] N. P. Kulkarni, G. Tandra, F. W. Liou, T. E. Sparks, and J. Ruan, "FC Development using AM Technologies - A Review Department of Mechanical and Aerospace Engineering , Missouri University of Science and Technology , Rolla , MO 65401 USA," pp. 686–703, 2009.

- [77] W. Zhong, F. Li, Z. Zhang, L. Song, and Z. Li, "Short fiber reinforced composites for fused deposition modeling," *Mater. Sci. Eng. A*, vol. 301, no. 2, pp. 125–130, 2001.
- [78] Stratasys, "How FDM 3D Printing Works." [Online]. Available: <http://www.stratasys.com/3d-printers/technologies/fdm-technology>. [Accessed: 22-Feb-2017].
- [79] Y. Zhuang et al., "3D-printing of materials with anisotropic heat distribution using conductive polylactic acid composites," *Mater. Des.*, vol. 126, pp. 135–140, Jul. 2017.
- [80] "Fortus 380mc and 450mc 3D Printers | FDM | Production Series | Stratasys." [Online]. Available: <http://www.stratasys.com/3d-printers/production-series/fortus-380-450mc>. [Accessed: 15-Feb-2017].
- [81] Stratasys, "Fortus 380mc and Fortus 450mc." [Online]. Available: <http://www.stratasys.com/3d-printers/technologies/fdm-technology/faqs>. [Accessed: 22-Feb-2017].
- [82] C.-Y. Chen, W.-H. Lai, B.-J. Weng, H.-J. Chuang, C.-Y. Hsieh, and C.-C. Kung, "Planar array stack design aided by RP in development of air-breathing PEMFC," *J. Power Sources*, vol. 179, no. 1, pp. 147–154, Apr. 2008.
- [83] C.-Y. Chen et al., "A New Complex Design for Air-Breathing Polymer Electrolyte Membrane FCs Aided by RP," *J. FC Sci. Technol.*, vol. 8, no. 1, pp. 014502-014502-4, Oct. 2010.
- [84] S.-S. Hsieh, S.-H. Yang, J.-K. Kuo, C.-F. Huang, and H.-H. Tsai, "Study of operational parameters on the performance of micro PEMFCs with different flow fields," *Energy Convers. Manag.*, vol. 47, no. 13–14, pp. 1868–1878, Aug. 2006.
- [85] M. Di Lorenzo, A. R. Thomson, K. Schneider, P. J. Cameron, and I. Ieropoulos, "A small-scale air-cathode microbial FC for on-line monitoring of water quality," *Biosens. Bioelectron.*, vol. 62, pp. 182–188, Dec. 2014.

- [86] G. Chisholm, P. J. Kitson, N. D. Kirkaldy, L. G. Bloor, and L. Cronin, "3D printed flow plates for the electrolysis of water: an economic and adaptable approach to device manufacture," *Energy Env. Sci*, vol. 7, no. 9, pp. 3026–3032, 2014.
- [87] Sculpteo, "LOM (Laminated Object Manufacturing): 3D Printing with Layers of Paper," 2017. [Online]. Available: <https://www.sculpteo.com/en/glossary/lom-definition/>. [Accessed: 22-Feb-2017].
- [88] M. Heynick and I. Stotz, "3D CAD, CAM and RP," in *LAPA Digital Technology Seminar Workshop*, 2006, vol. 1.
- [89] D. Ahn, J.-H. Kweon, J. Choi, and S. Lee, "Quantification of surface roughness of parts processed by laminated object manufacturing," *J. Mater. Process. Technol.*, vol. 212, no. 2, pp. 339–346, Feb. 2012.
- [90] "PolyJet Technology | Stratasys." [Online]. Available: <http://www.stratasys.com/3d-printers/technologies/polyjet-technology>. [Accessed: 22-Feb-2017].
- [91] H. Philamore, J. Rossiter, P. Walters, J. Winfield, and I. Ieropoulos, "Cast and 3D printed ion exchange membranes for monolithic microbial FC fabrication," *J. Power Sources*, vol. 289, pp. 91–99, Sep. 2015.
- [92] R. T. White et al., "3D Printed Flow Field and Fixture for Visualization of Water Distribution in FCs by X-ray Computed Tomography," *J. Electrochem. Soc.*, vol. 163, no. 13, pp. F1337–F1343, 2016.
- [93] Stratasys, "Stereolithography," *Stratasys Direct Manufacturing*, 2016. .
- [94] Stratasys, "STL File Format: How to Prepare STL Files," *Stratasys Direct Manufacturing*, 2016. .
- [95] Forecast 3D, "Forecast 3D - SLA Stereolithography for RP," 2016. [Online]. Available: <http://www.forecast3d.com/sla.html>. [Accessed: 21-Feb-2017].

- [96] G. Papaharalabos, J. Greenman, C. Melhuish, and I. Ieropoulos, "A novel small scale Microbial FC design for increased electricity generation and waste water treatment," *Int. J. Hydrog. Energy*, vol. 40, no. 11, pp. 4263–4268, Mar. 2015.
- [97] Formlabs, "3D Printing Technology Comparison: SLA vs. DLP," 2017. [Online]. Available: <https://formlabs.com/blog/3d-printing-technology-comparison-sla-dlp/>. [Accessed: 22-Feb-2017].
- [98] "Industrial 3d SLA Printers - Axis Prototypes." [Online]. Available: <https://www.axisproto.com/3d-printers.php>. [Accessed: 22-Feb-2017].
- [99] T. Grim, *Users Guide to RP*. Society of Manufacturing Engineers, 2004.
- [100] Mogan FC Inc, "AutoTech Daily News Letter."
- [101] S. Towne, V. Viswanathan, J. Holbery, and P. Rieke, "Fabrication of polymer electrolyte membrane FC MEAs utilizing inkjet print technology," *J. Power Sources*, vol. 171, no. 2, pp. 575–584, Sep. 2007.
- [102] M. Klingele, M. Breitwieser, R. Zengerle, and S. Thiele, "Direct deposition of proton exchange membranes enabling high performance hydrogen FCs," *J. Mater. Chem. A*, vol. 3, no. 21, pp. 11239–11245, May 2015.
- [103] "Laser Sintering," Stratasys Direct Manufacturing. .
- [104] "Layer Thickness : Precision of 3D Printing." [Online]. Available: <https://www.sculpteo.com/en/glossary/layer-thickness-definition/>. [Accessed: 21-Feb-2017].
- [105] N. Guo and M. C. Leu, "AM: technology, applications and research needs," *Front. Mech. Eng.*, vol. 8, no. 3, pp. 215–243, Sep. 2013.
- [106] N. Guo and M. C. Leu, "Effect of different graphite materials on the electrical conductivity and flexural strength of bipolar plates fabricated using selective laser sintering," *Int. J. Hydrog. Energy*, vol. 37, no. 4, pp. 3558–3566, 2012.

- [107] "Direct Metal Laser Sintering," Stratasys Direct Manufacturing. .
- [108] "Design Guidelines: Direct Metal Laser Sintering (DMLS)," Stratasys Direct Manufacturing. .
- [109] B. D. Gould et al., "Performance of 3D-Printed FCs and Stacks," *ECS Trans.*, vol. 64, no. 3, pp. 935–944, Aug. 2014.
- [110] B. D. Gould et al., "Performance and Limitations of 3D-Printed Bipolar Plates in FCs," *ECS J. Solid State Sci. Technol.*, vol. 4, no. 4, pp. P3063–P3068, 2015.
- [111] F. Calignano, T. Tommasi, D. Manfredi, and A. Chiolerio, "AM of a Microbial FC—A detailed study," *Sci. Rep.*, vol. 5, p. 17373, Nov. 2015.
- [112] C. J. Netwall, B. D. Gould, J. A. Rodgers, N. J. Nasello, and K. E. Swider-Lyons, "Decreasing contact resistance in proton-exchange membrane FCs with metal bipolar plates," *J. Power Sources*, vol. 227, pp. 137–144, 2013.
- [113] "DLMS feature size." [Online]. Available: [https://www.eos.info/systems\\_solutions/metal/systems\\_equipment/eosint\\_m280](https://www.eos.info/systems_solutions/metal/systems_equipment/eosint_m280).
- [114] B. D. Gould, R. Ramamurti, K. Swider-Lyons, M. Schuette, J. Rodgers, and C. Netwall, Three-dimensionally printed bipolar plate for a proton exchange membrane FC. Google Patents, 2015.
- [115] S. Y. Yoon, J. W. Ross, M. M. Mench, and K. V. Sharp, "Gas-phase particle image velocimetry (PIV) for application to the design of FC reactant flow channels," *J. Power Sources*, vol. 160, no. 2, pp. 1017–1025, Oct. 2006.
- [116] J. P. Feser, A. K. Prasad, and S. G. Advani, "Particle Image Velocimetry Measurements in a Model Proton Exchange Membrane FC," *J. FC Sci. Technol.*, vol. 4, no. 3, p. 328, 2007.
- [117] C. Hecht, N. van der Schoot, H. Kronemayer, I. Wlokas, R. Lindken, and C. Schulz, "Visualization of the gas flow in FC bipolar plates using molecular flow seeding and micro-particle image velocimetry," *Exp. Fluids*, vol. 52, no. 3, pp. 743–748, Mar. 2012.

- [118] F. Barreras, A. Lozano, L. Valiño, R. Mustata, and C. Marín, "Fluid dynamics performance of different bipolar plates: Part I. Velocity and pressure fields," *J. Power Sources*, vol. 175, no. 2, pp. 841–850, Jan. 2008.
- [119] J. Allen, "Two-Phase Flow in Small Channels and the Implications for PEMFC Operation," *ECS Trans.*, vol. 3, no. 1, pp. 1197–1206, Oct. 2006.
- [120] S. G. Kandlikar, Z. Lu, W. E. Domigan, A. D. White, and M. W. Benedict, "Measurement of flow maldistribution in parallel channels and its application to ex-situ and in-situ experiments in PEMFC water management studies," *Int. J. Heat Mass Transf.*, vol. 52, no. 7–8, pp. 1741–1752, Mar. 2009.
- [121] E. S. Lee, C. Hidrovo, K. Goodson, and J. Eaton, "Gas-Liquid Flow in Microchannels Bounded by a Porous Wall," in 6th Conference on Multiphase Flow, Leipzig, Germany, Paper, 2007.
- [122] Z. Lu, C. Rath, G. Zhang, and S. G. Kandlikar, "Water management studies in PEMFCs, part IV: Effects of channel surface wettability, geometry and orientation on the two-phase flow in parallel gas channels," *Int. J. Hydrog. Energy*, vol. 36, no. 16, pp. 9864–9875, Aug. 2011.
- [123] Forecast 3D, "Forecast 3D - FORECAST 3D - Standard Guidelines," 2016. [Online]. Available: <http://www.forecast3d.com/guidelines.html>. [Accessed: 31-Mar-2017].
- [124] "Syringe Pump Flow Rates." [Online]. Available: <http://www.kdscientific.com/technical-resources/flow-rates.html>. [Accessed: 22-Mar-2017].
- [125] D. W. G. J.O. Maloney and R.H. Perry, *Perry's Chemical Engineers Handbook*, 6th ed. McGraw-Hill, 1984.
- [126] J.F. Douglas, J.M. Gasiorek, and J.A. Swaffield, *Fluid Mechanics*, 3rd ed. England: Longman Scientific & Technical, 1995.
- [127] James Larminie and Andrew Dicks, *FC Systems Explained*. Wiley, 2002.

- [128] B. Lyons, M. Batalov, P. Mohanty, and S. Das, "RP of PEMFC Bi-Polar Plates Using 3D Printing and Thermal Spray Deposition," in Proc. SFF Symposium, Austin, TX, 2005, pp. 446–457.
- [129] K. N. Kim, D. H. Jeon, J. H. Nam, and B. M. Kim, "Numerical study of straight-parallel PEMFCs at automotive operation," *Int. J. Hydrog. Energy*, vol. 37, no. 11, pp. 9212–9227, Jun. 2012.

# Appendices

## Appendix A

MATLAB code:

```
clc;
clear;

fps=4000;
address1='G:\Experiments\EXP_RESULT\SLA_Uncovered\set2\Mar
9\SLA_uncover_600ml_4000fps\Imaging (';
N1=1;
N2=16100;
total_length_mm=80*504/(477-15);
ww=0;
wb=0;
hh=5;

total_pixels=504;
pixel_length=total_length_mm/total_pixels;

n=164;
for i=1:n

Channel_initial_x1(i)=8*(i)-round(i/2)-round(i/4);
Channel_secondary_x1=Channel_initial_x1;
Channel_initial_y1(i)=485;
Channel_secondary_y1(i)=20;

end

transfer_below=12;
transfer_above=18;
Channel_initial_x1=Channel_initial_x1+transfer_below;
Channel_secondary_x1=Channel_secondary_x1+transfer_above;

tt=74;

%%% Repairs above line totally
B=Channel_secondary_x1(1:10);
Channel_secondary_x1=-6+[B+1 B+tt-1 B+2*tt-2 B+3*tt-4 B+4*tt-6 B+5*tt-8
Channel_secondary_x1(61:n)-1];

%%%Repairs below line detailed
A=Channel_initial_x1(1:10);
Channel_initial_x1=-2+[A+1 A+tt-1 A+2*tt-3 A+3*tt-4 A+4*tt-6 A+5*tt-8
Channel_initial_x1(61:n)-1];
```

```

channel_NO=zeros(1,length(Channel_initial_x1));

% end of defining the rectangles

velocity=zeros(1,length(Channel_secondary_x1));

N=N2-N1+1;
p=zeros(1,N);
s1=zeros(length(Channel_initial_x1),N);
s2=zeros(length(Channel_initial_x1),N);

for m=1:N
S=m+N1-1;
address2=num2str(S);
address3='.bmp';
address=strcat(address1,address2,address3);
Q = imread(address);
Q=imrotate(Q,90);

    for rr=1:length(Channel_initial_x1)

square1=Q(Channel_initial_y1(rr):Channel_initial_y1(rr)+hh,Channel_initial_x1
(rr)-wb:Channel_initial_x1(rr)+ww);
square2=Q(Channel_secondary_y1(rr):Channel_secondary_y1(rr)+hh,Channel_second
ary_x1(rr)-wb:Channel_secondary_x1(rr)+ww);

        intensity1=sum(sum(square1))/( (hh+1)*abs(wb+ww+1) );
        intensity2=sum(sum(square2))/( (hh+1)*abs(wb+ww+1) );
        s1(rr,m)=intensity1;
        s2(rr,m)=intensity2;

    end

    p(m)=m;
end

for yyy=1:length(Channel_initial_x1)

loc1_s1= 1000;
loc2_s1=8000;

    s11=s1(yyy,:);

```

```

s22=s2(yyy,:);

s11(1)=mean(mean(s11(1:1000)));
s22(1)=mean(mean(s22(1:1000)));

    for kkk=1:N-1
        if abs(s11(kkk+1)-s11(kkk))>50
            s11(kkk+1)=s11(kkk);
        end
        if abs(s22(kkk+1)-s22(kkk))>50
            s22(kkk+1)=s22(kkk);
        end
    end

    end

figure;
tit1='Channel ';
tit2=num2str(yyy);
tit3=strcat(tit1,tit2);
plot(p,s11,'r'); hold on;
xlabel('frame number'); ylabel('Intensity');
plot(p,s22,'b');
xlabel('frame number'); ylabel('Intensity');

% end opf defining signals

% defining the location of peak

A=s11(loc1_s1:loc2_s1);

% end of defining the location of peak

% finding the correlation
D=zeros(1,length(s11));

    for i=1:(length(s11)-length(A))+1

        B=s22(i:i+length(A)-1);
        D(i)=corr2(A,B);

    end

% end of finding the correlation

%Finding the location of maximum correlation
maximum_corr=max(D);
for k=1:length(D)

```

```

        if D(k)==maximum_corr
            loc1_s2=k;
            break
        end
    end
end

frame_lag=loc1_s2-loc1_s1;
% end of finding the lopcation of maximum correlation

length_traveled=pixel_length*(abs(Channel_secondary_y1(yyy)-
Channel_initial_y1(yyy))+(hh/2));
time=frame_lag/fps;
    if time>0
        velocity(yyy)=length_traveled/time;
    else
        velocity(yyy)=0;
    end

channel_NO(yyy)=yyy;
end
change=velocity;
for i=1:length(velocity)

    velocity(i)=change(length(velocity)+1-i);
end

figure;
plot(channel_NO,velocity);

xlabel('Channel Number')
ylabel('Velocity (mm/s)')
title('Velocity Profile in channels')

filename='Velocity',;
A=velocity.';
xlswrite(filename,A);

```

## Appendix B

### B.1 Introduction to 3D printers

There are 4 major steps in each 3D printing method: (1) Creating the CAD model, (2) Converting CAD design to STL and Processing STL file to create G-code, (3) physically fabricating the part using G-Code, and then (4) removing support materials and finishing. Here are brief explanations of each step.

#### 1) Creating the CAD model

Computer aided design (CAD) models are prepared by either designing the part with a design software such as Solidworks, AutoCAD, CATIA, etc., or by reverse engineering the part or by reverse engineering the part by means of 3D scanning machines. Bradley et al. [73] defined the reverse engineering as “the process of duplicating an existing part, subassembly, or product without drawings, documentation, or a computer model. Reverse engineering is also defined as the process of obtaining a geometric CAD model from 3D points acquired by scanning/digitizing existing parts/products”. 3D printing software mostly uses Stereolithography (STL) format. Therefore, CAD models should be saved/converted as/to STL format. In CAD-to-STL step, the volume of the part is being meshed to series of small spatial triangles as shown in Figure B-1-b.

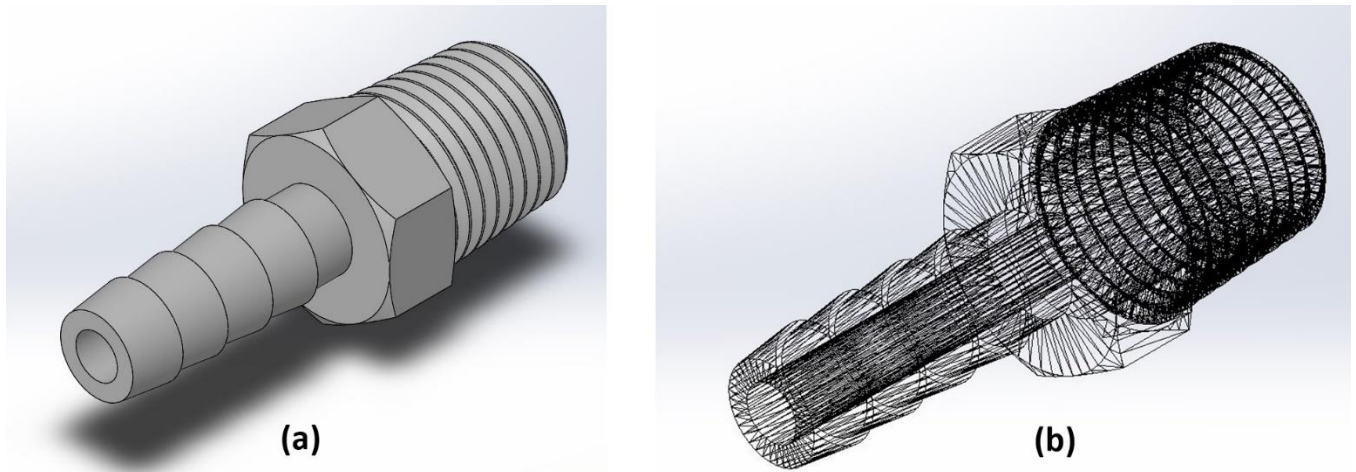


Figure B-1: (a) A solid CAD mode; (b) Meshed CAD file in .STL format.

## 2) Processing STL file to create G-code

At this step, the 3D printing software processes the STL file using a slicing program. The slicing program creates slices of the model and translates them into control actions of the 3D printer. This control language is called G-code that orders the machine how to move to certain points and how to control the material curing.

## 3) Physical fabrication of parts

The physical part fabrication occurs by one-layer at a time strategy to create the part layer by layer. Using one of the below mentioned 3D printing techniques, 3D printer fabricates the part from a plastic polymer, metal, curable resin, plastic powder etc. Most 3D printers (except possibly FDM) perform autonomously and do not need interference of a human during the fabrication [69].

## 4) Finishing

The last step of 3D printing is finishing, which removes, if any, support materials, unused powder and unused resin. Finishing steps are intended to increase the smoothness and applicability of parts. Some

3D printing techniques require some extra step before being functionally applied that will be mentioned below. The following discusses different 3D printing technologies.

## B.2 Different 3D printing technologies

One of the early works that has tried to review the different 3D printing techniques is done by Kulkarni et al. [74], who reviewed three different AM techniques: 1) FDM 3D printing 2) Inkjet head printing 3) Selective laser sintering. The paper gives very basic introduction about each method and mentions FC components that can be fabricated using each method. We believe that a more helpful approach could be analyzing different fabrication methods for each component and investigating advantages and disadvantages of each method, which have been used in the current research.

The review by Kulkarni et al. [74] summarized (not criticized) one or two research in each 3D printing method, but did not reflect pros and cons of each method following a critical approach. Moreover, the review [74] provides just very elementary information about each 3D printing method, with a focus on methodology and experiments used by each group, making the paper to be less informative in its main scope. The review of Kulkarni et al. [74] just captures the viewpoint of the author(s) presented in each paper, but did not compare each paper with similar works nor criticize it. For instance, Kulkarni et al. [74] asserted in their conclusion that components fabricated by AM techniques gave equal or better performance than those fabricated by conventional techniques. Although this might be true in the case of MEA fabricated by inkjet head printing method, we now know that FDM method for instance has much lower accuracy than CNC and is not capable of 3D printing real BPPs.

In terms of categorizing 3D printing methods, there are different classifications, one of which is based on the type of starting material, as suggested by [69]. In the sense of starting material, there are three categories of 3D printing: solid based, liquid based and powder based.

## B.2.1 Solid based

### B.2.1.1 Fused deposition modelling (FDM)

Fused deposition modelling is one of the earliest, most popular and most basic 3D printing technologies. This technology was invented by Scott Crump, founder of Stratasys, Ltd. more than 20 years ago. As shown in Figure B-2, a heated nuzzle melts the thermoplastic filament to a semi-solid state and extrudes out the plastic in the form of melted beads. The plastics gets deposited on the surface of built layer and then cooled down, providing the surface for depositing next layer of material. Hollow parts can be 3D printed using support materials, which are soluble materials, and can be removed after 3D printing by soaking the part into hot water, detergent or other recommended solutions [75] [76]. FDM 3D printers have 7° of self-retaining angles, which enables fabricating some angled features without using support underneath, as shown in Figure B-3.

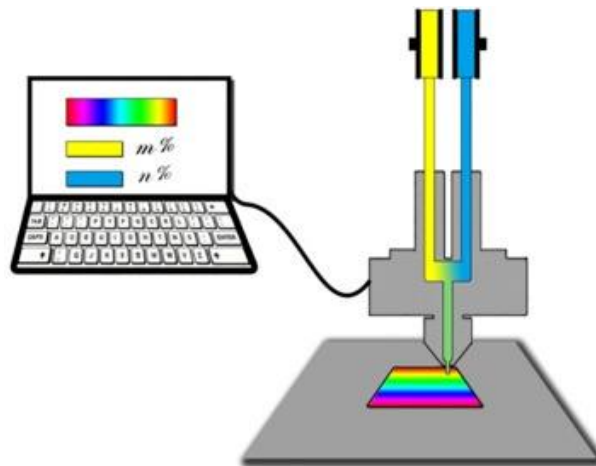


*Figure B-2: Schematic representation of the fabrication process in FDM 3D printer; Mixed fabrication process with two types of different filaments (yellow and blue) (reprinted from [77] with modified image caption, with permission from Elsevier).*

The fabrication time in 3D printing depends on accuracy and part size. As a rough estimation, it takes 2-4 hours to fabricate prototype BPPs with FDM technology. Prototyping with FDM 3D printer costs around US\$ 0.075per gram. FDM 3D printer is the least expensive 3D printing apparatus and could cost from 1,000 to 8,000 US\$.

FDM 3D printers' feature accuracy can be controlled by changing the extrusion speed (i.e. the melted plastic Debi) from the software that runs the 3D printer. The layer thickness (Z direction accuracy) of FDM 3D printers ranges from 0.005" to 0.02" (0.127-0.508 mm), and the XY plane accuracy ranges from 0.005" to 0.008" (0.127-0.2 mm), depending on the FDM 3D printer type [78],[79]. Recommended minimum feature size for FDM technology is 1 mm. FDM 3D-printed parts are not usually smooth, and require an extra step of warm acetone bath for a few second to suppress the small rugged parts.

Two common FDM 3D printer materials are Acrylonitrile Butadiene Styrene (ABS) polymer and Polylactic Acid (PLA), as well as some soluble materials to be used as support materials. ABS and PLA possess good mechanical strength, durability and chemical resistivity. The glass transition temperature of ABS and PLA is 105 °C and 65 °C, respectively. Therefore, ABS is mostly applicable in PEMFC researches where the operating temperature is below 100 °C. In terms of prototyping complexity, FDM 3D printers are more challenging to work with than other 3D printing techniques. For instance, Polyjet 3D printers can be cleaned by regular water, and support materials can be removed with regular brushes. While in FDM 3D printers, care must be taken to make sure that the part will stick to the surface during fabrication. Thermoplastic nature of ABS would result in part warpage that makes the fabrication process more difficult; When adding a new layer of melted plastic, the newly added layers of plastic have higher temperature than previous layers, that creates a vertical temperature gradient and shrinkage of previously added layers, which causes part to warp. It is thus suggested that the fabrication bed be warmed up before starting 3D printing in order to maintain the overall part temperature relatively high during fabrication. Another method to overcome part warpage is to create a glue with dissolving ABS fragments in acetone solution and applying it on fabrication bed before starting 3D printing. This makes the part stick to the fabrication bed and prevents warpage.

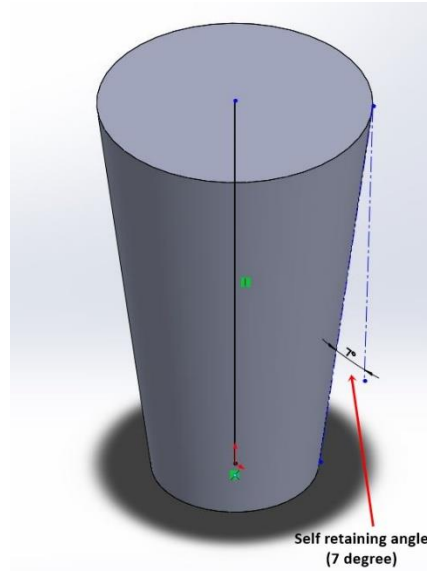


Figure B-3: Self-retaining angle in FDM 3D printing.

#### ***B.2.1.1 Laminated object manufacturing (LOM)***

LOM 3D printing is the least expensive and least popular 3D printing technique. LOM is not as widely used by researchers as other RP techniques. Like other 3D printing techniques, fabrication of the part is by one-layer-at-a-time strategy. A very thin plastic sheet is rolled on the building platform, and is cut into the desired geometry with a laser or blade. The material (sheet) is usually coated with an adhesive material and the feeding roller heats the material while rolling, which activates the adhesive material. After the first layer is cut, the roller provides a new layer of the rolling material. The new layer is glued to previous one and the laser (blade) cuts the new layer. This procedure continues until all the layers are fabricated [85]. Figure B-4 illustrates how LOM 3D printer functions. The LOM 3D printing layer thickness is 0.1-0.15 mm, and commonly used materials are paper and plastic sheets [86].

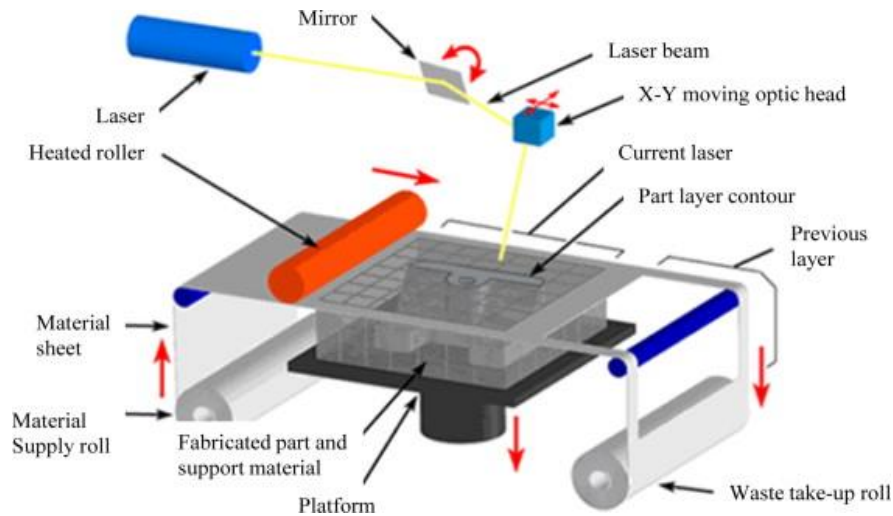


Figure B-4: A typical type of laminated object manufacturing process (reprinted from [87] with permission from Elsevier).

## B.2.2 Liquid Based

### B.2.2.1 Polyjet

Polyjet 3D printing is relatively new generation of 3D printing technology that performs similar to inkjet paper printer. Instead of jetting the ink droplets on a paper, Polyjet 3D printer jets droplets of photo-reactive polymer on the build platform. After jetting the photopolymer, a UV light source instantly cures the photopolymer to have it solidified. The 3D printing continues with one-layer-at-a-time strategy until all the layers of part are fabricated. Figure B-5 demonstrates how Polyjet 3D printer works. Whenever it is required for fabricating hollow parts, the nozzle jets a removable support material [88]. Unlike FDM 3D printing, Polyjet 3D printing could not provide any self-retaining angle. Polyjet 3D printing can create minimum layer thickness of 16 microns (0.016 mm). The XY plane accuracy is 0.1 mm, and the printing resolution is 600 dpi in X-axis, 600 dpi in Y-axis and 1600 dpi in z-axis. 3D printing with Polyjet costs around US\$0.75 per gram. Polyjet 3D printers cost from US\$ 24,000 to 300,000.

Philamore et al. [89] applied Polyjet technology for the first time for 3D printing of ion exchange membrane of microbial FCs. They compared the power-density of 3D printed ion exchange membrane MFC, with that of the conventional planar membrane MFC, and reported that 3D printed cation

exchange membrane results in higher power-density with lowered fabrication cost. Philamore et al. [89] made a quantitative comparison between membrane fabrication costs of conventional and 3D printing techniques and reported the following: US\$ 0.16 (Stratasys 3D printing) compared to US\$ 0.22-40 (Conventional membrane) for the equivalent active area of material. The results of Philamore et al. [89] demonstrate that 3D printed ion exchange membrane possesses a higher surface area in comparison with conventional membranes, resulting in higher power-density and more compact MFCs. 3D printing of membranes provides the platform for geometric flexibility and miniaturization of MFCs. Philamore et al. [89] suggested that 3D printed molds and dyes could be fabricated to form ion exchange membranes into complex and novel geometries with a high surface area than planar membrane materials.

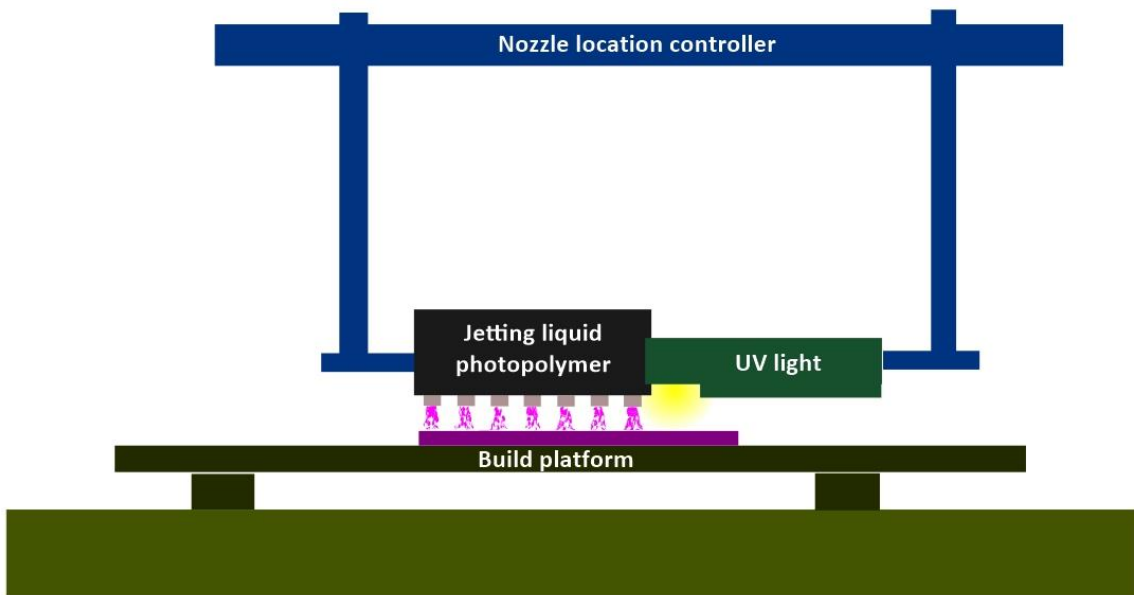


Figure B-5: Schematic of the 3D printing process in Polyjet 3D printer.

### B.2.2.2 Stereolithography (SLA)

SLA 3D printing filed as a patent in 1986 by Charles Hull, co-founder of 3D Systems, Inc. Within this process, the stereolithographic apparatus (SLA) fabricates parts by using a precise beam of UV laser to consolidate a photo-reactive resin. SLA is one of the most precise technologies of 3D printing and is

suggested for conceptual models, laboratory prototypes and investment casting designs [91]. As shown in Figure B-6 [69], there exists a tank that is filled with resin and the part is built on the surface of a perforated platform as follows. UV laser is aimed across the print area and cures the resin as it goes along, creating the first layer of the part. Then, the perforated platform is lowered a few tens of millimeters so that the next layer can be fabricated on top of the previous layer, and this process continues. After all the layers are printed and the so-called green part is formed, the platform is raised to its initial height and the green part is being rinsed using a resin solvent. In the last stage, the green part is baked with a UV light oven to strengthen the resin and to break the support. Photo-reactives used in SLA 3D printer are epoxy resins and acrylic. Researchers are trying to further reinforce SLA 3D printed parts with addition of carbon fibers and ceramics [69].

SLA 3D printed parts are usually smooth. The thickness of SLA 3D printed layers is 0.002"-0.004" (0.0508-0.1016 mm), and the XY plane accuracy is 0.005" (0.127 mm) for the first inch and 0.002" (0.0508 mm) for each additional inch. The minimum feature size with SLA 3D printing is 0.025" (0.635 mm) [93, 94]. 3D printing with SLA is almost twice as expensive as Polyjet. For instance, a 3D printed part costed US\$79 using Polyjet technology, and US\$165 using SLA technology. High-resolution SLA is said to increase both accuracy and the minimum feature size (0.002" layer thickness) [93]. However, this will limit the part length to be 10" (254 mm) and will also increase the part cost drastically. The mentioned part that costed US\$165 with regular SLA technology could cost US\$496 with high-resolution SLA, based on a quote from the company. The SLA 3D printer machine could cost from US\$2,000 (Desktop SLA 3D printers) to more than US\$250k (Professional SLA 3D printers).

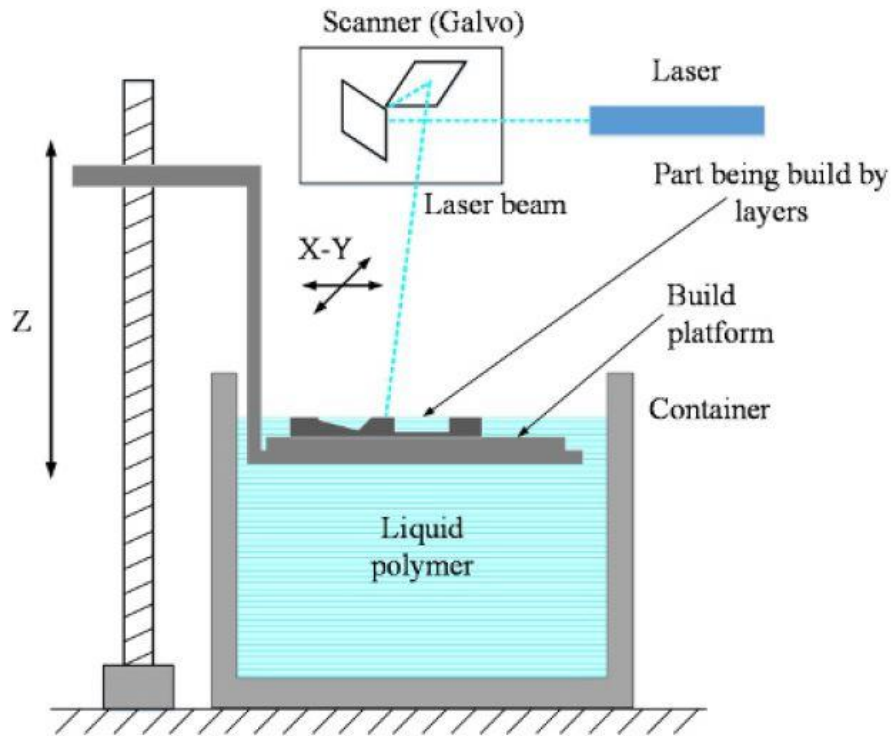


Figure B-6: Schematic of the 3D printing process in SLA 3D printer (reprinted from [69], open access article).

### B.2.2.3 Digital light processing (DLP)

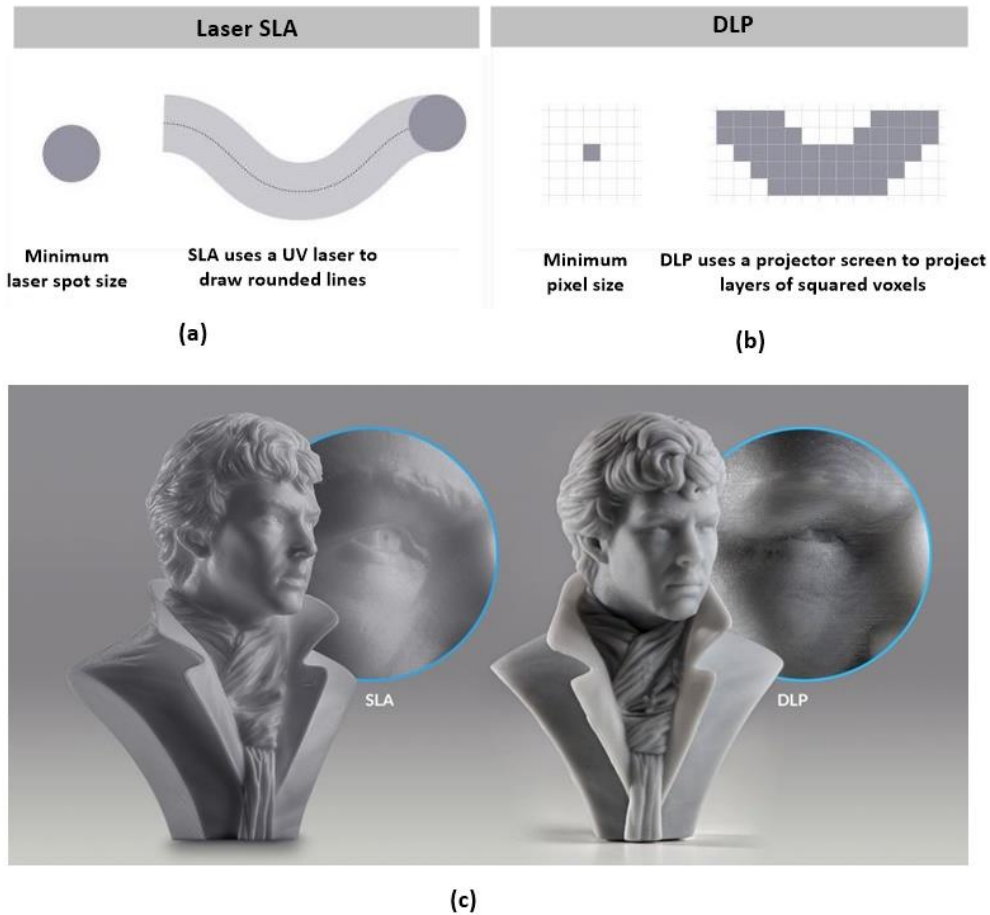


Figure B-7: Stereolithography VS Digital light processing 3D printing (reprinted from [95]).

DLP performs very similar to SLA; SLA uses a laser beam to draw the pattern of each layer, while DLP projects a single image of each layer across the entire platform using a digital projector. Figure B-7-a,b [95] illustrates how two technologies differ. It can be inferred that DLP can offer faster 3D printing since for each layer it only applies single image projection at once. However, the practical 3D printing accuracy is higher with SLA. Figure B-7-c [95] illustrates how two technologies result in different part accuracy [95].

DLP 3D printing layer thickness is similar to that of SLA, which is 0.025-0.15 mm. The theoretical X-Y resolution is 0.025-0.065 mm, but, as illustrated in Figure B-7-c [95], SLA provides us with more accurate

parts. Since SLA uses laser for drawing the pattern, the minimum feature size would be the thickness of the laser beam plus other factors. However, we are not having such limitation in DLP and the minimum feature size equals the resolution. The maximum printing size with DLP is 31"×13"×16" [96]. DLP 3D printers could cost from US\$2,000 (for desktop DLP) up to > US\$250K. DLP is less popular than and is not employed as widely as SLA. Although the printing resin cost is equal for SLA and DLP, SLA 3D printing costs more since it requires more hours to print the part.

### **B.2.3 Powder based**

#### ***B.2.3.1 Powder bed and inkjet head 3D printing***

Although in the sense of being Inkjet head, this technique of 3D printing can be the subset of liquid based category, we have discussed this technique as a subset of powder based because of the powder form bed being utilized in this technique.

Inkjet 3D printers use drop-on-demand technology [74]. As its name reveals, drop-on-demand means depositing the colloidal ink wherever there is a demand, based on the CAD model. There is a capability of switching between inks which would result in 3D printing a multi-color multi-material part. The prototyping accuracy depends on the droplet size which is proportional to the nozzle size. Inkjet 3D printers are categorized based on the method they utilize for driving out the droplets; One type uses piezoelectric transducers and the other uses thermal resistors [74].

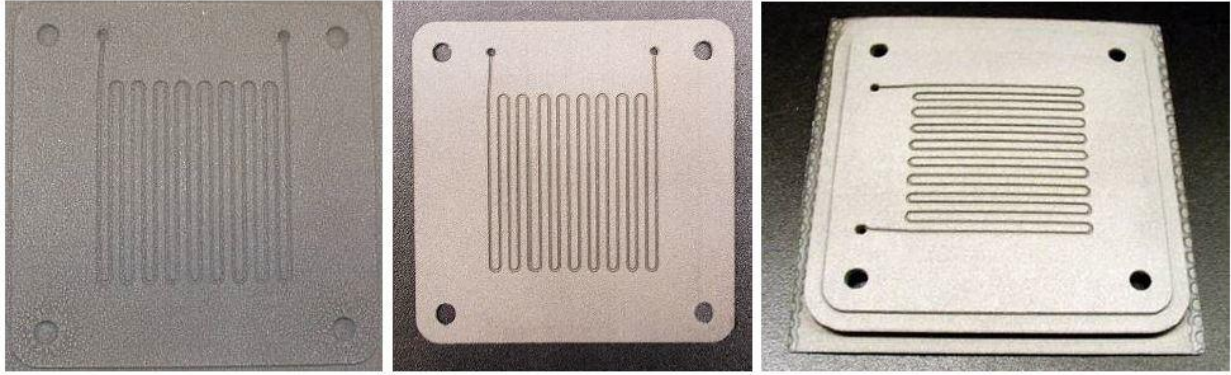


*Figure B-8: Samples plates created with the TS-3DP by Lyons et.al [68] (reprinted from [68]).*

#### B.2.3.1.1 Inkjet head 3D printing in MEA fabrication

Please note that MEA fabrication is beyond the scope of current research. However, since we are giving a review about application of different 3D printing techniques in FC development, we shortly introduce the applicability of 3D printing in MEA fabrication and we include the references which could be useful for other researchers.

The Inkjet technology can be used in MEA fabrication with applying catalyst solution instead of 3D printing ink. One of the early works on MEA fabrication with inkjet technology is fulfilled by Towne et al. [99], within which they have introduced the protocol for catalyst ink preparation to be used in inkjet printer. In comparison with conventional catalyst deposition techniques like screen printing and hand printing, inkjet 3D printing provides high accuracy and control over platinum loading that causes more efficient platinum utilization, which in turn reduces the required platinum loading and cost. It has been reported that Inkjet printing could be 4-5 times faster than screen printing [100], [81]. Moreover, inkjet reduces the number of fabrication steps (like drying and massing) which makes the process more reproducible [74]. By using inkjet technology for MEA fabrication, Towne et al. [99] reduced the platinum loading by 33% while only 7% decrease in power-density was experienced, which proves that inkjet printed MEAs are comparable to the commercial ones. Inkjet 3D printing enables us to grade the platinum loading after print which can further increase the platinum usage efficiency [74].

### *B.2.3.2 Selective laser sintering (SLS)*

This 3D printing technology was patented by a University of Texas undergraduate student, Carl Deckard, in 1980s. SLS uses a high-powered CO<sub>2</sub> laser to sinter thermoplastics like nylon, that are accumulated on top of the building platform. As shown in Figure B-9, the laser beam fuses a thin layer of the plastic and creates the first layer of the part. Thereafter, the building platform is lowered and powder is re-applied by a leveling drum, and the next layer is fabricated. The important advantage of SLS 3D printing is that the part is buried in powder. This deletes the need for any support and enables fabrication of more complex parts that might be impossible with other 3D printing techniques. The building chamber is warmed up to prevent part warpage and is filled with an inert gas (nitrogen) to prevent plastic aging. There are two different types of SLS technology: direct and indirect SLS. In direct SLS method, the fabrication procedure is just laser sintering of powder, while indirect SLS includes several post processing procedures. SLS printed parts are stronger than SLA, FDM and Polyjet parts. SLS parts are heat resistant, and show better performance against water and air leakage. They are fabricated with exceptional materials including polyamide, polyethylene, elastomers, ceramics, aluminum-filled Nylon 12 and metals. The part structure can be further increased in density using liquid state fusion[69], [101]. The SLS can produce layer thickness of 0.004"-0.006" (0.1016-0.152 mm), and the X-Y plane tolerance is 0.030"-0.050" (0.762-1.27 mm). Although it has been asserted that the theoretical minimum feature size of SLS technology is 125 μm (0.125 mm), in practice it is recommended to have a minimum feature size of 0.040" (1 mm) to ensure an acceptable strength of the feature. The building platform for the largest SLS machine is 26.5"×13.5"×20" and parts larger than that should be fabricated in sections [104, 103] . In terms of price, SLS would cost around 1.4 times more than Polyjet, and SLA would cost around 1.5 time more than SLS. The SLS 3D printer apparatus is more expensive than a SLA or Polyjet 3D printer with equal performance, ranging from US\$ 10K (desktop SLS 3D printers) to > US\$ 250K.

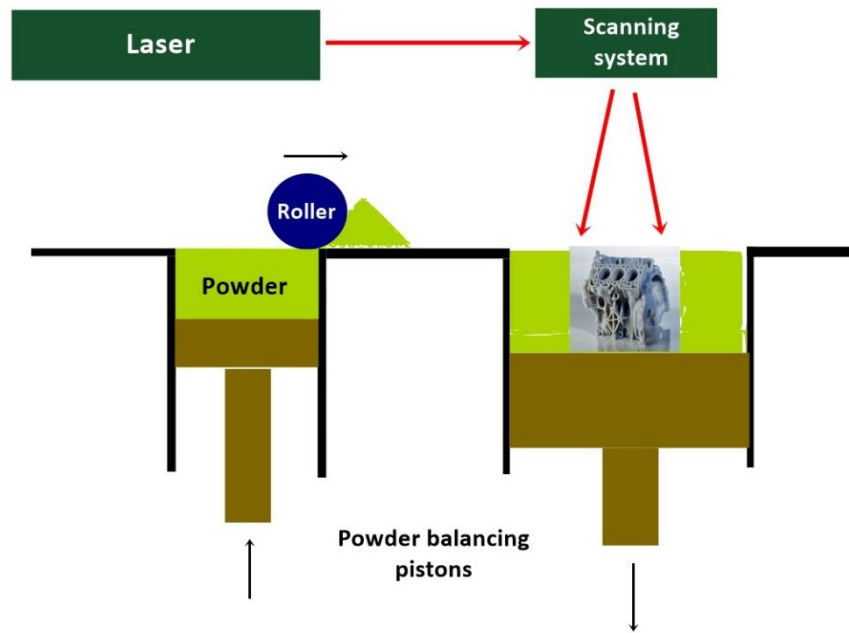


Figure B-9: Schematic of 3D printing process in SLS 3D printer.

SLS can be used in selective laser sintering of graphite composite BPPs, which is a fast prototyping technique that could be an alternative technique to injection or compression molding of composites.

### *B.2.3.3 Direct metal laser sintering (DMLS)*

DMLS performs very similar to SLS method, except that DMLS sinters a metal powder rather than a plastic powder. DMLS 3D printing uses a precise Yb fiber laser to micro-weld metal powders and to create strong, durable, functional metal parts. As shown in Figure B-10 [69], DMLS method applies a high wattage laser to locally sinter the metal powders in the focused area and creates the first layer of the part. The build platform is then lowered and a levelling drum adds a fresh layer of metal powder, after which laser creates the next layer of the part. This process continues until the part is fully fabricated. Unlike SLS techniques, supports are needed to keep the part in its initial position and to prevent the part warpage that might be a result of the residual stresses within cooling down of each

layer after melting. After fabricating the part, supports are removed and finishing steps are followed. Finishing steps are selected based on special requirements for the part, such as cleaning of the surfaces, that were in contact with supports, tumbling, bead blasting etc. Despite the similarity with SLS 3D printing, DMLS usually takes extra effort and requires special design requirement and post-processing steps [69],[105]. Materials are being used in DMLS are Aluminum, Titanium, Stainless Steel, Inconel etc. Ti-6Al-4V titanium alloy is one of the most conventional materials being used in DMLS for research applications. This Ti-alloy benefits from a high strength-to-power ratio that makes it ideal for aerospace applications [72] . Furthermore, the low thermal conductivity of Ti-alloy makes it a useful material for IR thermography since it holds any problem in heat transfer [42].

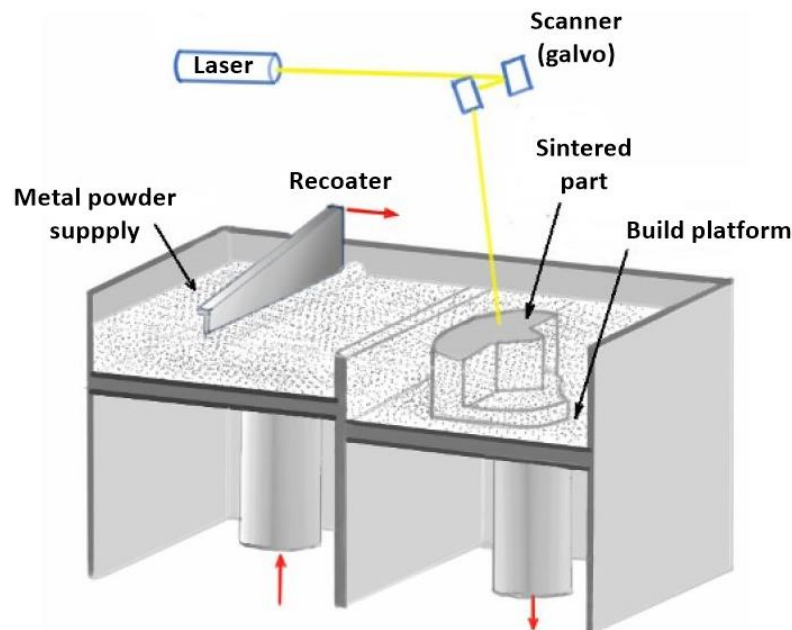


Figure B-10: Schematic of 3D printing process in DMLS 3D printer (reprinted from [69] , open access article).

The layer thickness at highest resolution is 0.0008"-0.0015" (0.02-0.04 mm) and the XY plane resolutions is 0.012"-0.016" (0.30-0.40 mm). The minimum hole diameter is 0.035"-0.045" (0.89-1.14 mm) and parts

can reach up to 99.5% density [107,108]. DMLS is the most expensive method of 3D printing and costs 12 times more than SLA. For instance, a part that costed US\$ 165 with SLA, would cost US\$ 2,000 with DMLS, based on a quote from the company. The DMLS 3D printer machine is the most expensive 3D printing apparatus; The cheapest available machine costs US\$ 250K, and the conventional DMLS 3D printer costs more than US\$ 500K. DMLS is a very beneficial technique for prototyping of BPPs and other FC components. DMLS enables fabricating hollow parts and complex ideas for flow field design in one-piece without the need for welding [109, 110] , and has great potential for end-use products in the near future. DMLS has drawn researchers' attention in developments of microbial FCs since it brings the chance for tailoring inter-connected porosities which favors the attachment of bacteria [85, 91, 96, 111]. Calignano et al. [85, 91, 96, 111] employed three different AM techniques including DMLS 3D printing in the development of an additive-manufacturing-based microbial FC. They used DMLS 3D printing with aluminum-alloy material for fabricating bio-inspired diamond lattice to create a macro porous structure with a high specific surface area, high conductivity, high chemical stability, and a tailored surface roughness that benefits microbial growth. They took advantage of the self-supportive feature of diamond structure and 3D printed the part without the use of supports in design. They reported the DMLS 3D printed anode structure density to be 0.54 g/cm<sup>3</sup>, with regular spherical shape particles with a mean size of 20 μm. Calignano et al. [85, 91, 96, 111] treated the anode structure with two more post-processing steps after DMLS 3D printing. They put the part in a furnace for 2h for stress relieving, and then further post-processed the part with shot peening. They reported that their 3D printed anode structure showed good biocompatibility with bacteria. Calignano et al. [85, 91, 96, 111] advised that balling phenomena that occurs during laser melting of metal powder in DMLS 3D printing could cause surface discontinuity, cracks and partially bonded particles. Although it seems problematic, it could be quite beneficial in some applications such as biomedical engineering.

To further prepare their cell, Calignano et al. [85, 91, 96, 111] used FDM 3D printing for fabricating external structures and outer packaging for easier assembly and a better cell seal. Thereafter, for tailoring the bacteria network formation on anode structure, they used spray-coating which is another AM technique. Calignano et al. [85, 91, 96, 111] ran their setup for 5 months and reported a stable and reproducible cell performance with  $2500 \text{ mW m}^{-2}$  power-density, which is almost 3 times more than previous studies. They reported that AM anodes boost the attachment of bacteria, which allows faster retention time (6 days) than MFCs (15-40 days). They confirmed that additive manufactured MFC is fast and prompt in responding to varying power demand and concluded that this elevated performance represents the promises of AM for energy generation in remote environments. Calignano et al. [85, 91, 96, 111] suggested that long-term application of AM MFC essences a modified cathode design.

## Appendix C

### C.1 Pumping system

A pumping system is required to circulate the flow through the flow fields. As it was discussed in section 2.1.3, we need to measure the pressure-drop at various flow rates to acquire the relationship between pressure-drop and fluid average velocity in the designed BPPs. Based on eq. (4) because of the linear relationship between the pressure-drop and the fluid flow rate in a single channel, we need a stable fluid flow to precisely measure the pressure-drop at each flow rate. In addition, since small changes in the fluid flow rate would result in deviation from steady state, and might perturb the fluid flow distribution, we need stable fluid flow to assure constant experiment conditions. Stable fluid flow means that the flow rate is not changing neither in short-term nor long term, and it is pulse-less.

To achieve such a stable flow, we set the following requirements for the fluid flow at different rates, after steady state: (1) The rotameter indicator should show the same flow for at least 5 min (long-term stability), (2) The indicator should show the same flow rate in 30s intervals (short-term stability), (3) The rotameter indicator should not shake nor fluctuate rapidly (flow pulse-less-ness). The first option used for circulating the flow was LAING SM-909-NTW-26 circulating pump. It did not meet any of the three mentioned requirements. Then a magnet pump by PAN WORLD CO., LTD. MODEL: NH-15P1-Z-D was used which did not meet any of the three requirements. As another method, an 8-gallon pressure vessel, PAINTED-STEEL EXPANSION TANK by McMASTER-CARR was filled with deaerated water and pressurized using nitrogen cylinder, and the outlet was connected to two needle valves in series to control the fluid flow. This system met the pulse-less-ness and short-term stability requirements, but failed to meet the long-term stability requirement and we observed flow rate decrease after 3 min. It was also fraught with high safety issues because of the high-pressurized system. The other option we considered to acquire a stable flow was syringe pump. Although stability is one of the important

features of syringe pumps, syringe pumps are appropriate for low flow rates: 500 nano liter per min up to maximum 215 milliliter per min [124].

Peristaltic pump was the other option we tested for running the fluid through flow channels. A COLE-PARMER 7553-20 pump drive, with COLE-PARMER 7518-00 pump head, with COLE-PARMER 7553-71 speed controller, with "C-Flex tubing (50 A), L/S 15,25ft "tube was used. In the high flow rates (>200 ml/min), the system could meet the three mentioned requirements successfully. However, in low flow rates (<100 ml/min), we observed that rotameter indicator was shaking very fast, which is due to the rotational nature of the fluid pumping in peristaltic pumps. To overcome this problem, we fabricated a house-made pulse dampener with inspiration from the industrial pulse dampeners. To damp the pulse, a compressible medium is needed in the flow up-stream that could damp the flow fluctuations. We let the trapped air in a plastic chamber to act as the compressible medium and to damp the flow fluctuations. Figure C-1 exhibits the house-made pulse dampener. This pumping system provided the 30-1200 ml/min flow rate.

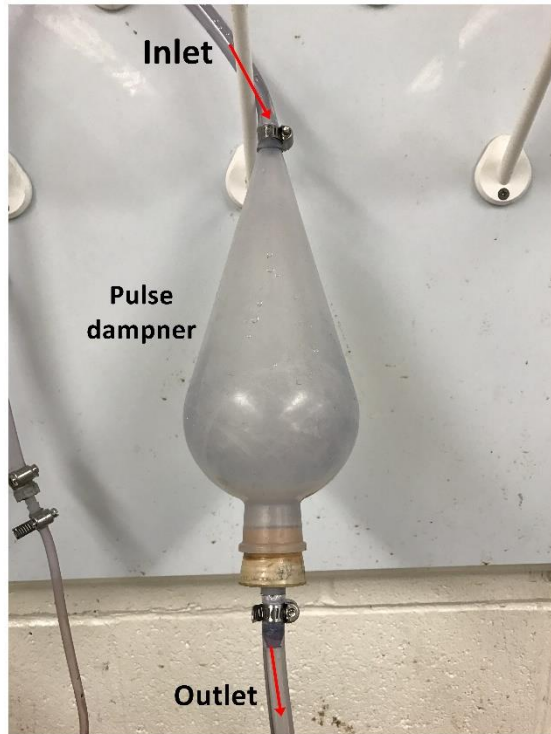


*Figure C-1: House-made pulse dampener. The trapped air in the chamfer is a compressible medium and acts as a pulse dampener.*